Weak gravitational lensing cross-correlations

by

Tilman Tröster

A THESIS SUBMITTED IN PARTIAL FULFILLMENT

OF THE REQUIREMENTS FOR THE DEGREE OF

Doctor of Philosophy

in

THE FACULTY OF GRADUATE AND POSTDOCTORAL STUDIES

(Physics)

The University of British Columbia

(Vancouver)

August 2017

Abstract

The matter content of the Universe is dominated by dark matter. Beyond its abundance and its lack of non-gravitational interactions with standard model matter, little is known about the nature of dark matter. This thesis attempts to illuminate different aspects of dark matter by using gravitational lensing in conjunction with other cosmological probes. Gravitational lensing describes the deflection of light by gravitational potentials and is a direct and unbiased probe of the matter distribution in the Universe.

We investigate the weakly interacting massive particle (WIMP) model of dark matter by performing a tomographic and spectral cross-correlation between weak gravitational lensing from the Canada-France-Hawaii Telescope Lensing Survey (CFHTLenS), Red Cluster Sequence Lensing Survey (RCSLenS), and Kilo-Degree Survey (KiDS), and gamma rays from Fermi-LAT. The non-detection of a correlation allows us to constrain the allowed masses, annihilation cross-sections, and decay rates of WIMP dark matter.

Even though most matter in the Universe is dark matter, about 16% is baryonic matter. To make precision measurements of the dark matter distribution with gravitational lensing, it is therefore necessary to understand the behaviour and distribution of baryonic matter. We measure and analyse the cross-correlation between weak gravitational lensing from RCSLenS and the thermal Sunyaev-Zeldovich (tSZ) effect from the Planck satellite to constrain the effect of baryon physics on the matter distribution.

Models of gravitational lensing often make use of a range of approximations. We study the effect of dropping these approximations on the cross-correlation between gravitational lensing and tSZ by performing a detailed calculation up to fourth order in the gravitational potential. We find that the common approximations are sufficiently accurate even for future surveys.

Finally, we explore the growth of structure and the effect of residual weak lensing systematics in a tomographic cross-correlation between weak gravitational lensing from KiDS and lensing of the cosmic microwave background (CMB) from Planck.

Lay summary

This thesis aims to illuminate various aspects of dark matter, a mysterious substance that makes up the majority of matter in the Universe. The existence and behaviour of dark matter can only be inferred from its gravitational effect on its surroundings since it is impossible to observe directly. The distribution of dark matter can be measured with gravitational lensing, which is caused by the deflection of light rays by matter in the Universe and can be observed by studying the distortion of the images of faraway galaxies. Using gravitational lensing by itself and in conjunction with other observations, we shed light on: whether dark matter could be a hitherto unobserved elementary particle; how the distribution of dark matter compares to that of normal matter; and if the evolution of the dark matter distribution with time is in agreement with that predicted by the standard model of cosmology.

Preface

Chapters 2 and 4 have been adapted from articles published in peer-reviewed journals, while Chapters 3 and 5 have been adapted from submitted but not yet published articles. The articles on which Chapters 2 and 5 are based were written as part of the KiDS collaboration, while the one on which Chapters 3 is based on was written as part of the RCSLenS collaboration. Both collaborations have a publication policy that breaks the author list into three groups: the first group consists of the primary authors who conducted the main analysis and wrote the manuscript; the second group consists of members who provided infrastructure work on which the analysis was based *and* contributed significantly to the final manuscript; and the third group consists of members who provided infrastructure work *or* contributed significantly to the final manuscript.

Chapter 2 is adapted from the article *'Cross-correlation of weak lensing and gamma rays: implications for the nature of dark matter'* by T. Tröster, S. Camera, M. Fornasa, M. Regis, L. van Waerbeke, J. Harnois-Déraps, S. Ando, M. Bilicki, T. Erben, N. Fornengo, C. Heymans, H. Hildebrandt, H. Hoekstra, K. Kuijken, and M. Viola, published in Monthly Notices of the Royal Astronomical Society, 467, 3, 2706-2722 (2017). The primary authors are T. Tröster, S. Camera, M. Fornasa, M. Regis, and L. van Waerbeke. T. Tröster led the project, conducted the measurement and analysis, wrote the measurement and analysis code, produced all figures, and drafted the manuscript. S. Camera, M. Fornasa, and M. Regis provided the modelling and analytical covariance matrices and contributed to the writing of Section 2.2. Both the modelling and analytical covariances were validated by comparing it to an independent code by T. Tröster. L. van Waerbeke (thesis advisor) provided guidance and comments. All authors provided comments on the final manuscript.

Chapter 3 is based on the article *'Cross-correlating Planck tSZ with RCSLenS weak lensing: Implications for cosmology and AGN feedback'* by A. Hojjati, T. Tröster, J. Harnois-Déraps, I. G. McCarthy, L. van Waerbeke, A. Choi, T. Erben, C. Heymans, H. Hildebrandt, G. Hinshaw, Y. Z. Ma, L. Miller, M. Viola, and H. Tanimura, accepted for publication in Monthly Notices of the Royal Astronomical Society. The primary authors are A. Hojjati, T. Tröster, J. Harnois-Déraps, I. G. McCarthy, L. van Waerbeke. T. Tröster conducted the configuration-space measurements, performed the analysis, wrote the measurement and analysis code, produced all figures except Figs. 3.1, B.5, and B.4, provided extensive comments on the manuscript, and addressed the second round of referee comments. Postdoctoral researcher A. Hojjati led the project, conducted initial measurements, produced Figs. 3.1, B.5, and B.4, and drafted parts of the manuscript. J. Harnois-Déraps conducted the Fourier-space measurements. I. G. McCarthy provided the simulation products. L. van Waerbeke (thesis advisor) provided the con-

vergence maps. All authors provided comments on the final manuscript.

Chapter 4 is adapted from the article *'Weak lensing corrections to tSZ-lensing cross correlation'* by T. Tröster and L. van Waerbeke, published in the Journal for Cosmology and Astroparticle Physics, 11, 008, 8 (2014), doi:10.1088/1475-7516/2014/11/008. T. Tröster did all calculations, produced the plots, and wrote the manuscript. L. van Waerbeke (thesis advisor) provided guidance and comments.

Chapter 5 is based on the article *'KiDS-450: Tomographic Cross-Correlation of Galaxy Shear with Planck Lensing'* by J. Harnois-Déraps, T. Tröster, N. E. Chisari, C. Heymans, L. van Waerbeke, M. Asgari, M. Bilicki, A. Choi, H. Hildebrandt, H. Hoekstra, S. Joudaki, K. Kuijken, J. Merten, L. Miller, N. Robertson, P. Schneider, and M. Viola, accepted for publication in Monthly Notices of the Royal Astronomical Society. The primary authors are J. Harnois-Déraps, T. Tröster, and N. E. Chisari. T. Tröster conducted all measurements and provided comments on the manuscript. Postdoctoral researcher J. Harnois-Déraps led the project, conducted the analysis, produced the plots, and drafted the manuscript. N. E. Chisari provided the modelling of intrinsic alignment. All authors provided comments on the final manuscript.

Table of Contents

List of Tables

List of Figures

Chapter 1

Introduction

According to the Copernican principle, we do not observe the Universe from any special vantage point. In more technical terms, this means that on sufficiently large scales the Universe is statistically homogeneous (the same everywhere) and isotropic (the same in all directions). On these large scales the dynamics are expected to be dominated by gravity. The most accurate theory of gravity to date is Einstein's general relativity (GR). Its field equations are notoriously difficult to solve in general. However, as is often the case in physics, imposing symmetries allows one to simplify the field equations to a point where they become tractable. Specifically, upon imposing homogeneity and isotropy on Einstein's field equations of GR, one arrives at a solution for an expanding universe, the Friedmann-Lemaître-Robertson-Walker (FLRW) metric.

The expansion history is determined by the energy content of the Universe, specifically by the abundances of non-relativistic matter Ω_{M}, radiation Ω_{R}, and the cosmological constant Ω_{Λ}, and is described by the Friedmann equation. The abundances change with time; relativistic massive particles in the early Universe behave like radiation but the expansion of the Universe causes them to adiabatically cool down to non-relativistic speeds later on and contribute to the non-relativistic (cold) matter budget. Furthermore, while the density of non-relativistic matter decreases proportional to the volume of the expanding space, the radiation density experiences an additional decrease due to the shifting of the radiation field to longer wavelengths – the redshift – such that the density of radiation decays quicker than the density of matter.

At early times, matter was in the form of a relativistic plasma of elementary particles. As the Universe expanded, the plasma cooled, allowing the formation of baryons and light nuclei. At the end of this process, called big bang nucleosynthesis (BBN), the baryon content Universe consisted of about three quarters hydrogen, one quarter helium, and small amounts of deuterium, tritium, and lithium.

When the Universe had cooled enough for electrons to be able to combine with the hydrogen and helium nuclei to form neutral atoms, the Universe became transparent to the photons. Released from the primordial plasma, these photons have since travelled the Universe essentially unimpeded and form today's cosmic microwave background (CMB), an isotropic, thermal radiation bath with a temperature of 2.73 K.

Quantum fluctuations of the quantum fields of the elementary particles sourced inhomogeneities in

the primordial plasma. The inhomogeneities expanded as acoustic waves – the baryon acoustic oscillations (BAO) – in the plasma until recombination, when the Universe became transparent to photons. The inhomogeneities left an imprint on the free streaming photons, observable as small anisotropies in the CMB. These anisotropies have a characteristic length scale corresponding to the distance the acoustic waves travelled in the primordial plasma.

Unlike the pressure-supported inhomogeneities in the primordial plasma, the dark matter inhomogeneities had been free to collapse under the influence of gravity. Once the baryonic inhomogeneities are free from the photon-pressure that supported them, they too begin to collapse, aided by the existing potential wells of dark matter structures. The characteristic correlation length of the BAO is preserved by the growth of structure and is observable in the distribution of galaxies in the large-scale structure (LSS) of the Universe. In cosmological recent times, the expansion of the Universe has been accelerating, driven by dark energy. This late time accelerated expansion of the Universe can be observed in cosmological distance measures, such as supernovae (SNe) and BAO, and in the suppression of the growth of structure in the Universe.

The expansion history of the Universe, the primordial abundances of elements, the temperature and anisotropies of the CMB, and the growth of the LSS and its clustering properties form the core of the standard model of cosmology, called ΛCDM after the two main contribution to today's energy content of the Universe: dark energy (Λ) and cold dark matter (CDM).

While ΛCDM has been remarkably successful in describing cosmological observations, it posits the existence of dark matter and dark energy. To date, there is no satisfactory explanation in terms of fundamental physics for either of the two. The work presented in this thesis seeks to illuminate the nature of dark matter by employing gravitational lensing, the deflection of light by matter, in conjunction with other probes. In Chapter 2 the correlation of gamma rays with gravitational lensing is used to constrain particle models of dark matter. Chapters 3 and 4 investigate the relationship between baryons and dark matter by probing their distributions through the cross-correlation of gravitational lensing and the thermal Sunyaev-Zeldovich (tSZ) effect. The evolution of structure in Universe and systematics inherent to the measurement of gravitational lensing are analysed in Chapter 5.

The following sections give an introductory exposure to the some of the tools used in this thesis, namely gravitational lensing, its two-point statistics, and its application to LSS.

1.1 Gravitational lensing

Gravitational lensing describes the deflection of light rays by gravitational potentials. The general relativistic solution for the deflection angle of a light ray by a mass M and impact parameter d is $\alpha = 4\frac{GM}{d}$ (see, e.g., Wald, 1984; Carroll, 2004). Remarkably, this expression differs only by an overall factor of 2 from a classical calculation.

A gravitational lensing system consists of an observer, a source, and one or more, potentially extended, lenses. A simple system with a single lens plane is shown in Fig. 1.1. The photon path from the source, S, to the observer, O, is shown in blue. In the absence of a lens, the source would be observed at a angular position $\vec{\beta}$ on the sky. The deflection of light by the lens instead causes the source to appear

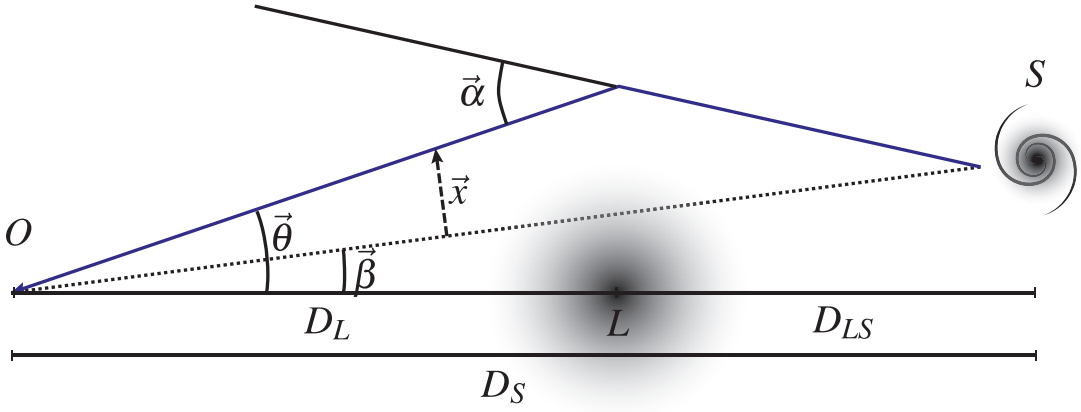

Figure 1.1: Geometry of a lensing system. The observer O is on the left and observes a source S at an angular position $\vec{\theta}$. The (deflected) light path from the source to the observer is shown in blue while the undeflected path is denoted by the dotted line. In the absence of the lens L, the source would be observed at an angular position $\vec{\beta}$.

at a position $\vec{\theta}$. If the lens deflects the light ray by a deflection angle $\vec{\alpha}$, then the geometry of Fig. 1.1 suggests that $\vec{\theta}$ and $\vec{\beta}$ are related by

$$\vec{\beta} = \vec{\theta} - \frac{D_{\mathrm{LS}}}{D_{\mathrm{S}}}\vec{\alpha}\,, \tag{1.1}$$

where D_{LS} is the distance between the lens and the source and D_{S} is the distance between the observer and the source. Here we have assumed that the deflection angle is small enough that the small angle approximation is applicable. In astrophysical situations, the deflection angle is indeed very small, reaching only a few arcmin in the case of lensing of the CMB. The small angle approximation is therefore well justified. For multiple, localised lenses L_i, the lens equation becomes

$$\vec{\beta} = \vec{\theta} - \sum_i \frac{D_{\mathrm{L_iS}}}{D_{\mathrm{S}}}\vec{\alpha}_i\,. \tag{1.2}$$

We will now give a heuristic derivation of this lens equation and then justify the result by sketching the formal derivation based on GR, where we will also present the general lens equation Eq. (1.19).

1.1.1 Heuristic derivation of the lens equation

In the following section we will forgo mathematical rigour in favour of heuristic and physical arguments. We parametrise the transverse deviation of a light ray from the undeflected path by $\vec{x}(\chi)$, where χ denotes the (comoving) distance from the observer, as illustrated in Fig. 1.1. We assume that all angles are small such that the deviation is well described by a vector perpendicular to the undeflected path. At the observer, the angle between the deflected and undeflected paths is $\vec{\hat{\alpha}} = \vec{\theta} - \vec{\beta}$. The deflection is obtained by integrating the equation of motion of the transverse deviation. The deviation $\vec{x}(\chi)$ can be written as

$$\begin{aligned}\vec{x}(\chi) &= \int_0^{t(\chi)} \mathrm{d}t' \dot{\vec{x}}(t') = \chi\vec{\hat{\alpha}} + \int_0^t \mathrm{d}t' \int_0^{t'} \mathrm{d}t'' \ddot{\vec{x}}(t'') \\ &= \chi\vec{\hat{\alpha}} + \frac{1}{c^2}\int_0^{\chi} \mathrm{d}\chi' \int_0^{\chi'} \mathrm{d}\chi'' \ddot{\vec{x}}(\chi'') = \chi\vec{\hat{\alpha}} + \frac{1}{c^2}\int_0^{\chi} \mathrm{d}\chi' (\chi - \chi') \ddot{\vec{x}}(\chi') \,,\end{aligned} \tag{1.3}$$

where we used that $\vec{x}(0) = 0$ and $\frac{\mathrm{d}\chi}{\mathrm{d}t} = c$, c being the speed of light. The transverse acceleration $\ddot{\vec{x}}$ can be expressed in terms of the transverse gradient of the Newtonian potential as

$$\ddot{\vec{x}}(\chi) = -\vec{\nabla}_\perp \phi(\vec{\gamma}_0(\chi) + \vec{x}(\chi)) \,, \tag{1.4}$$

where $\vec{\gamma}_0(\chi)$ denotes the location of the undeflected light ray at a distance χ from the observer and the transverse gradient $\vec{\nabla}_\perp$ is taken with respect to the direction of the undeflected ray $\vec{\gamma}_0$. Equation (1.4) applies for classical, massive particles. In the following, we include an extra factor of 2, anticipating that the deflection angle of light in GR is twice that of the classical derivation, such that the acceleration is $\ddot{\vec{x}}(\chi) = -2\vec{\nabla}_\perp \phi(\vec{\gamma}_0(\chi) + \vec{x}(\chi))$. The classical derivation essentially ignores the spatial part of the metric, whereas in GR the spatial and temporal components contribute equally to the deflection of a massless particle. Since the deflections are small, evaluating the potential along the unperturbed path, i.e., $\phi(\vec{\gamma}_0(\chi) + \vec{x}(\chi)) \approx \phi(\vec{\gamma}_0(\chi))$, is a good approximation. This is the so called Born-approximation and the effects of dropping it are investigated in Chapter 4 (see also Krause et al., 2010; Bernardeau et al., 2012). At the source S, the deviation $\vec{x}(\chi_\mathrm{S})$ is zero. At a distance χ_S from the observer we therefore have

$$0 = \chi_\mathrm{S}\vec{\theta} - \chi_\mathrm{S}\vec{\beta} - \frac{2}{c^2}\int_0^{\chi_\mathrm{S}} \mathrm{d}\chi' (\chi_\mathrm{S} - \chi')\vec{\nabla}_\perp \phi(\vec{\gamma}_0(\chi')) \,, \tag{1.5}$$

or, rearranging the terms and dividing by χ_S,

$$\vec{\beta} = \vec{\theta} - \frac{2}{c^2}\int_0^{\chi_\mathrm{S}} \mathrm{d}\chi' \frac{(\chi_\mathrm{S} - \chi')}{\chi_\mathrm{S}} \vec{\nabla}_\perp \phi(\vec{\gamma}_0(\chi')) \,. \tag{1.6}$$

If the lenses are well localised, i.e., if their extent along the line-of-sight is small compared to the distances between lenses, the source, and the observer, then we can break the integral up into small segments centred on each lens i: $\int_0^{\chi_\mathrm{S}} \mathrm{d}\chi \approx \sum_i \int_{\chi_i-\varepsilon}^{\chi_i+\varepsilon} \mathrm{d}\chi$. Since the potential varies on much smaller scales than the factor $\frac{(\chi_\mathrm{S}-\chi)}{\chi_\mathrm{S}}$, we can take this factor out of the integral. We are left with integrals of the

form

$$\int_{\chi_i-\varepsilon}^{\chi_i+\varepsilon} \mathrm{d}\chi \vec{\nabla}_\perp \phi(\vec{\gamma}_0(\chi)) \,. \tag{1.7}$$

We will now assume that the potential is sufficiently spherically symmetric at the distance $\vec{d}$ from the centre of the mass distribution. The potential is then simply $\phi(d,\chi) = -\frac{GM}{r} = -\frac{GM}{\sqrt{d^2+(\chi-\chi_i)^2}}$. Inserting the potential into Eq. (1.7) we find

$$\int_{\chi_i-\varepsilon}^{\chi_i+\varepsilon} \mathrm{d}\chi \vec{\nabla}_\perp \phi(\vec{\gamma}_0(\chi)) = -2GM\vec{\nabla}_\perp \mathrm{arsinh}\left(\frac{\varepsilon}{d}\right) = 2GM\frac{\vec{d}}{d^2}\frac{1}{\sqrt{1+\frac{d^2}{\varepsilon^2}}} \,. \tag{1.8}$$

The distance ε along the line-of-sight is much larger than the impact parameter d, thus reducing Eq. (1.8) to $\frac{2GM}{c^2}\frac{\vec{d}}{d^2}$. Equation (1.6) can now be written as

$$\vec{\beta} = \theta - \sum_i \frac{(\chi_\mathrm{S}-\chi_i)}{\chi_\mathrm{S}} \frac{4GM}{c^2}\frac{\vec{d}_i}{d_i^2} \,. \tag{1.9}$$

Noting that $\chi_\mathrm{S}-\chi_i = D_{\mathrm{L_i S}}$, $\chi_\mathrm{S} = D_\mathrm{S}$, and $\frac{4GM}{c^2}\frac{\vec{d}_i}{d_i^2}$ is the deflection angle $\vec{\alpha}_i$, we have therefore derived Eq. (1.2).

1.1.2 Derivation of the lens equation based on general relativity

There are a number of ways to derive the lensing equations in GR, for example through geodesic deviation equation, Fermat's theorem, or geodesic congruences. Here we sketch a derivation based on geodesic deviation. For detailed derivations, see, e.g., Blandford et al. (1991), Seitz et al. (1994), Sachs (1961), Pyne et al. (1996), and reviews by Bartelmann et al. (2001) and Bartelmann (2010).

We wish to study the evolution of a bundle of light rays. We choose one ray as our fiducial ray $\gamma_0^\mu(\lambda)$, parameterised by the affine parameter λ. The tangent vector along this ray is given by

$$\tilde{k}^\mu = \frac{\mathrm{d}\ \gamma_0(\lambda)^\mu}{\mathrm{d}\lambda} \,. \tag{1.10}$$

We want to describe the evolution of the deviation between the fiducial ray γ_0^μ and some adjacent ray γ^μ, as illustrated in Fig. 1.2. We choose a two-dimensional screen spanned by the vectors E_1^μ and E_2^μ. The two vectors $E_{1,2}^\mu$ are chosen such that they are perpendicular to observer u^μ and the direction of the ray $\tilde{k}^\mu$, i.e., $E_i^\mu u_\mu = E_i^\mu \tilde{k}_\mu = 0$. Imposing orthonormality further sets $E_i^\mu E_{j\mu} = \delta_{ij}$. We can now define a deviation vector Y^μ that connects the fiducial ray γ_0^μ to the adjacent ray γ^μ as

$$Y^\mu = -\xi^1 E_1^\mu - \xi^2 E_2^\mu - \xi^0 \tilde{k}^\mu \,, \tag{1.11}$$

where $\xi^{1,2}$ parametrises the transversal components of the deviation and ξ^0 the deviation along the ray.

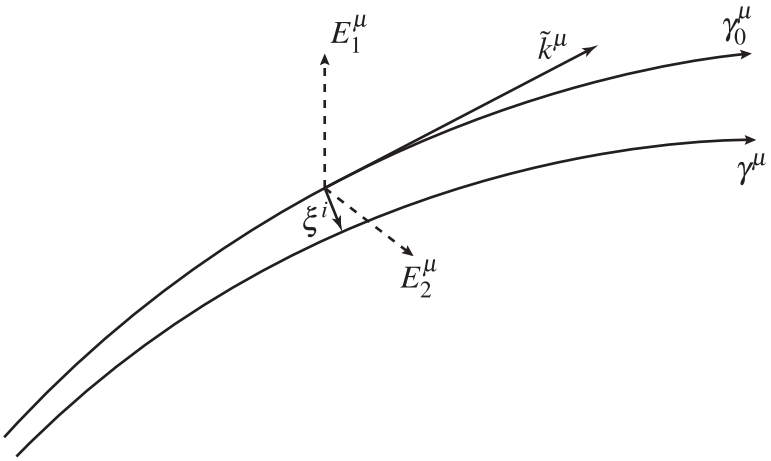

Figure 1.2: Illustration geodesic deviation. From a bundle of light rays we choose a fiducial ray γ_0^μ and some adjacent ray γ^μ. The tangent of γ_0^μ is given by $\tilde{k}^\mu$. We can define a two-dimensional screen perpendicular to the fiducial ray and the observer spanned by E_1^μ and E_2^μ. The deviation between γ_0^μ and γ^μ projected on this screen is then given by ξ^i.

The evolution of the transverse components is then given by

$$\frac{\mathrm{d}^2\xi^i}{\mathrm{d}\lambda^2} = \mathscr{T}\xi^i \,, \tag{1.12}$$

where $\mathscr{T}(\lambda)$ is the optical tidal matrix. This matrix can be written in the form

$$\mathscr{T} = \begin{pmatrix} \mathscr{R} + \Re[\mathscr{F}] & \Im[\mathscr{F}] \\ \Im[\mathscr{F}] & \mathscr{R} - \Re[\mathscr{F}] \end{pmatrix} \,, \tag{1.13}$$

where $\mathscr{R}$ describes the isotropic expansion or contraction of the bundle and depends on the Ricci tensor. Anisotropic shearing of the bundle is described by $\mathscr{F}$, which depends on the Weyl curvature tensor.

We are interested in the propagation of light in an expanding Universe described by the FLRW metric with matter inhomogeneities. If the Newtonian potential is small in the sense that $\frac{\phi}{c^2} \ll 1$, the metric can be perturbed around the FLRW background as

$$\mathrm{d}s^2 = -\left(1+\frac{2\phi}{c^2}\right)c^2\mathrm{d}t^2 + a(t)^2\left(1-\frac{2\phi}{c^2}\right)\left(\mathrm{d}\chi^2 + f_\mathrm{K}(\chi)^2\mathrm{d}\Omega^2\right) \,. \tag{1.14}$$

Here a denotes the scale factor and f_K depends on the global curvature K and comoving distance χ as

$$f_\mathrm{K}(\chi) = \begin{cases} \frac{1}{\sqrt{K}}\sin\left(\sqrt{K}\chi\right) & K > 0 \\ \chi & K = 0 \\ \frac{1}{\sqrt{-K}}\sinh\left(\sqrt{-K}\chi\right) & K < 0 \end{cases} \,. \tag{1.15}$$

Given the metric, the Ricci and Weyl curvature tensors can be calculated, yielding expressions for $\mathscr{R}$ and $\mathscr{F}$. Expressing the deviations equation Eq. (1.12) in terms of the comoving distance χ and the comoving bundle dimension x^i, we finally find

$$\left(\frac{\mathrm{d}^2}{\mathrm{d}\chi^2}+K\right)x^i=-\frac{2\partial^i\phi}{c^2}\ . \tag{1.16}$$

The Green's function of this differential equation is

$$G(\chi,\chi')=\frac{1}{\sqrt{K}}\sin\left(\sqrt{K}(\chi-\chi')\right)\Theta(\chi-\chi')=f_{\mathrm{K}}(\chi-\chi')\Theta(\chi-\chi')\ , \tag{1.17}$$

where Θ denotes the Heaviside step function. The initial conditions are given by

$$x^i(0)=0\ ,\quad \frac{\mathrm{d}x^i}{\mathrm{d}\chi}(0)=\theta^i-\beta^i\ , \tag{1.18}$$

where θ^i is again the observed position of the source on the sky and β^i the position if no deflection had occured. The solution for the evolution of the comoving bundle dimension is

$$x^i(\chi)=f_{\mathrm{K}}(\chi)(\theta^i-\beta^i)-\frac{2}{c^2}\int_0^\chi \mathrm{d}\chi' f_{\mathrm{K}}(\chi-\chi')\partial^i\phi(\vec{\gamma}_0(\chi')+\vec{x}(\chi'))\ . \tag{1.19}$$

Considering the case of a flat Universe, i.e., $K=0$ such that $f_{\mathrm{K}}(\chi)=\chi$, applying the Born approximation such that $\phi(\vec{\gamma}_0(\chi')+\vec{x}(\chi'))\approx\phi(\vec{\gamma}_0(\chi'))$, and evaluating Eq. (1.19) at χ_{S}, we recover Eq. (1.5) from the heuristic derivation.

1.1.3 Image distortions

The deflection angle and transverse deviation are not observable, as we do not know the true position of the source. We instead observe distortions of the source. This distortion is given by the Jacobi map which describes the infinitesimal change across the image as the source position is varied. Taking the derivative of $\vec{\beta}$ with respect to the image position $\vec{\theta}$ we find to first order

$$\mathscr{A}_{ij}=\frac{\partial\beta_i}{\partial\theta_j}=\delta_{ij}-\frac{2}{c^2}\int_0^{\chi_{\mathrm{S}}}\mathrm{d}\chi'\frac{f_{\mathrm{K}}(\chi_{\mathrm{S}}-\chi')f_{\mathrm{K}}(\chi')}{f_{\mathrm{K}}(\chi_{\mathrm{S}})}\partial_i\partial_j\phi(\vec{\gamma}_0(\chi'))\ , \tag{1.20}$$

where the coordinate system is chosen such that the spatial derivatives ∂_i are along directions perpendicular to the direction of the ray $\vec{\gamma}_0$. In Eq. (1.20) we applied the Born approximation and used the approximation $\frac{\partial}{\partial\theta^i}\phi(\vec{\gamma}_0(\chi'))=f_{\mathrm{K}}(\chi')\partial_i\phi(\vec{\gamma}_0(\chi'))$. The general expression without these approximations is given by Eq. (4.3). The Jacobi map is usually split into trace and trace-free parts and parametrised by the convergence κ and the shear components γ_1 and γ_2:

$$\mathscr{A}_{ij}=\begin{pmatrix}1-\kappa & 0\\ 0 & 1-\kappa\end{pmatrix}-\begin{pmatrix}\gamma_1 & \gamma_2\\ \gamma_2 & -\gamma_1\end{pmatrix}\ . \tag{1.21}$$

The convergence causes isotropic stretching of the source image, whereas the shear causes anisotropic shearing. The effects of the convergence and shear on a circular source image are demonstrated in Fig. 1.3. Since the two partial derivatives in Eq. (1.20) commute, the Jacobi map is symmetric at first order. The general expression for the Jacobi map Eq. (4.3) does not have this symmetry, however, and thus allows for a rotational component in addition to the convergence and shear.

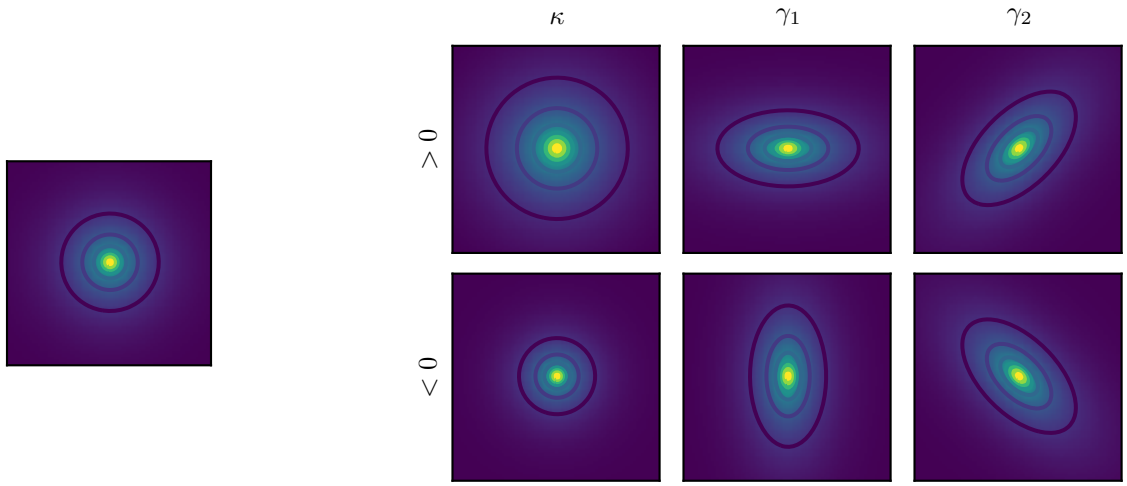

Figure 1.3: Lensing-induced distortions of a circular source image. The undistorted image is shown on the left. The three columns on the right show the effects of the convergence κ and shear components γ_1 and γ_2.

In the following, we will focus on the convergence, as it can be simply related to the matter distribution in the Universe. It is, however, not a direct observable. Galaxy lensing surveys measure the ellipticities of large numbers of galaxies. In this thesis we make use of the currently best available galaxy lensing data sets Canada-France-Hawaii Telescope Lensing Survey (CFHTLenS), Red Cluster Sequence Lensing Survey (RCSLenS), and Kilo-Degree Survey (KiDS), each of which contains ellipticity estimates for millions of galaxies over a combined area of $\gtrsim 1000\,\mathrm{deg}^2$. In the absence of intrinsic alignments of these source galaxies, the observed ellipticities serve as an estimator of the 'reduced shear' g_i, defined as

$$g_i = \frac{\gamma_i}{1-\kappa}\,. \tag{1.22}$$

In weak lensing, the shear and convergence are small so that the reduced shear can be used as an estimator of the shear. Magnification, as observed, e.g., through excess galaxy number counts, measures the determinant of the Jacobi map Eq. (1.21), which is a combination of shear and convergence. In CMB lensing, usually the lensing potential is estimated instead, such as through the quadratic estimator of Hu et al. (2002). Both the shear and the lensing potential can be related to the convergence, so that we can

restrict ourselves to the convergence in the following without loss of generality.

From Eq. (1.21) we see that the convergence is given by $\kappa = 1 - \frac{1}{2}\mathrm{tr}\mathscr{A}$. It is therefore proportional to some (weighted) integral over $(\partial_1^2 + \partial_2^2)\phi(\vec{\gamma}_0(\chi))$. If the potential is localised, we replace the two-dimensional Laplacian with the three-dimensional one. This allows us to insert the Poisson equation:

$$\vec{\nabla}^2\phi = \frac{3}{2}\frac{H_0^2}{c^2}\frac{\Omega_\mathrm{M}}{a}\delta \,, \tag{1.23}$$

where H_0 is the Hubble constant today. The convergence at a position $\vec{\theta}$ on the sky can now be expressed in terms of the line-of-sight integral over the density contrast as

$$\kappa(\vec{\theta}, \chi_\mathrm{S}) = \frac{3}{2}\frac{H_0^2\Omega_\mathrm{M}}{c^2}\int_0^{\chi_\mathrm{S}} \mathrm{d}\chi' \frac{f_\mathrm{K}(\chi_\mathrm{S} - \chi')f_\mathrm{K}(\chi')}{a(\chi')f_\mathrm{K}(\chi_\mathrm{S})}\delta(f_\mathrm{K}(\chi')\vec{\theta}, \chi') \,, \tag{1.24}$$

where we set the undeflected path to $\vec{\gamma}_0(\chi') = (f_\mathrm{K}(\chi')\vec{\theta}, \chi')$. The response of lensing to the density contrast is encapsulated into a window function

$$\tilde{W}^\kappa(\chi, \chi_\mathrm{S}) = \frac{3}{2}\frac{H_0^2\Omega_\mathrm{M}}{c^2}\frac{f_\mathrm{K}(\chi_\mathrm{S} - \chi)f_\mathrm{K}(\chi)}{a(\chi)f_\mathrm{K}(\chi_\mathrm{S})} \,. \tag{1.25}$$

So far we have only worked with a single source at a comoving distance χ_S. This is a valid assumption in the case of lensing of the CMB, where the source plane is located at the surface of last scattering at $z \approx 1100$. In galaxy lensing, we derive the shear and convergence from many source galaxies instead. If the source galaxies follow a distribution $p(\chi_\mathrm{S})$ then the convergence due to this source sample is

$$\kappa(\vec{\theta}) = \int_0^{\chi_H} \mathrm{d}\chi_\mathrm{S} p(\chi_\mathrm{S})\kappa(\vec{\theta}, \chi_\mathrm{S}) \,. \tag{1.26}$$

This dependence on the source distribution can be absorbed into the window function

$$W^\kappa(\chi) = \int_\chi^{\chi_H} \mathrm{d}\chi' p(\chi')\tilde{W}^\kappa(\chi, \chi') \,. \tag{1.27}$$

Using this general window function, the expression Eq. (1.24) for the convergence can then be be written as

$$\kappa(\vec{\theta}) = \int_0^{\chi_H} \mathrm{d}\chi' W^\kappa(\chi')\delta(f_\mathrm{K}(\chi')\vec{\theta}, \chi') \,. \tag{1.28}$$

1.1.4 Two-point statistics

In cosmology, we are often interested in the two-point statistics of fields, such as: the angular power spectrum of CMB temperature and polarisation anisotropies; the correlation function of galaxies; or cosmic shear – the correlation of galaxy shapes. This is motivated by the fact that at early times the matter field is a Gaussian random field whose statistics are completely described by two-point statistics. While the fields evolve linearly, they remain Gaussian, such that two-point statistics remain an excellent

description. Once the fields evolve non-linearly and deviate from Gaussianity, two-point statistics are not sufficient anymore to completely describe the statistical properties of the fields. Even though they do not capture all information contained within the fields, two-point statistics are still valid statistics, however, and provide useful information about the physical processes we wish to measure. Furthermore, the estimation and modelling of higher-order n-point statistics of cosmological observables is a challenge in itself and still a topic of current research. As the Fourier modes of a Gaussian random field are independent and remain so under linear evolution of LSS, it is often advantageous to work in Fourier space with the power spectrum instead of the configuration space correlation function.

The convergence field is defined on the sphere. We therefore decompose it in terms of spherical harmonics Y_{lm} as

$$\kappa(\vec{\theta}) = \sum_{l=0}^{\infty} \sum_{m=-l}^{l} \kappa_{lm} Y_{lm}(\vec{\theta}) \,, \quad \kappa_{lm} = \int \mathrm{d}\Omega \kappa(\vec{\theta}) Y^*_{lm}(\vec{\theta}) \,. \tag{1.29}$$

The integral is over the whole sphere with $\mathrm{d}\Omega = \mathrm{d}\phi \mathrm{d}\vartheta \sin\vartheta$ where (ϕ, ϑ) correspond to the position $\vec{\theta}$ on the sphere. If the regions of interest on the sky are small, they can be approximated by tangent planes and it is not necessary to employ spherical harmonics. We follow the more general full-sky treatment for now. For a derivation using the flat-sky approximation, see Section 4.2.

Expanding the correlation function $\xi_{\kappa\kappa}(|\vec{\theta} - \vec{\theta}'|) = \langle \kappa(\vec{\theta}) \kappa(\vec{\theta}') \rangle$ in terms of spherical harmonics we find

$$\langle \kappa(\vec{\theta}) \kappa(\vec{\theta}') \rangle = \sum_{lml'm'} \langle \kappa_{lm} \kappa^*_{l'm'} \rangle Y_{lm}(\vec{\theta}) Y^*_{l'm'}(\vec{\theta}') = \sum_{lm} C_l^{\kappa\kappa} Y_{lm}(\vec{\theta}) Y^*_{lm}(\vec{\theta}') \,, \tag{1.30}$$

where the angular power spectrum $C_l^{\kappa\kappa}$ is defined as $\langle \kappa_{lm} \kappa^*_{l'm'} \rangle = \delta_{ll'} \delta_{mm'} C_l^{\kappa\kappa}$. Taking the definition of the convergence Eq. (1.28) the correlation function can be expressed as

$$\langle \kappa(\vec{\theta}) \kappa(\vec{\theta}') \rangle = \int \mathrm{d}\chi \mathrm{d}\chi' W^{\kappa}(\chi) W^{\kappa}(\chi') \langle \delta(\chi\vec{\theta}, \chi) \delta(\chi'\vec{\theta}', \chi') \rangle \,, \tag{1.31}$$

where we have assumed that the Universe is flat, i.e., $f_{\mathrm{K}}(\chi) = \chi$. Measurements of the CMB anisotropies and the BAO scale have strongly constrained the curvature of the Universe (Planck Collaboration XIII, 2016), such that this is a justified assumption. We write the density contrast $\delta(\chi\vec{\theta}, \chi)$ in term of its Fourier transform

$$\delta(\vec{x}, \chi) = \int \frac{\mathrm{d}^3 k}{(2\pi)^3} \mathrm{e}^{\mathrm{i}\vec{k}\vec{x}} \hat{\delta}(\vec{k}, \chi) \,, \tag{1.32}$$

where we denoted the three-dimensional position by $\vec{x}$. Note that χ sets the time at which the density contrast is evaluated at position $\vec{x}$. The power spectrum of the density contrast is defined as

$$\langle \hat{\delta}(\vec{k}, \chi) \hat{\delta}^*(\vec{k}', \chi') \rangle = (2\pi)^3 \delta_{\mathrm{D}}(\vec{k} - \vec{k}') P_{\delta\delta}(|\vec{k}|, \chi, \chi') \,. \tag{1.33}$$

The correlation function of the density contrast $\langle \delta(\chi\vec{\theta}, \chi) \delta(\chi'\vec{\theta}', \chi') \rangle$ is then related to the density

contrast power spectrum $P_{\delta\delta}(|\vec{k}|,\chi,\chi')$ by

$$\langle\delta(\vec{x},\chi)\delta(\vec{x}',\chi')\rangle = \int \frac{\mathrm{d}^3k}{(2\pi)^3} \mathrm{e}^{\mathrm{i}\vec{k}(\vec{x}-\vec{x}')} P_{\delta\delta}(|\vec{k}|,\chi,\chi') \; . \tag{1.34}$$

The Fourier basis $\mathrm{e}^{\mathrm{i}\vec{k}\vec{x}}$ can be expanded in terms of spherical Bessel functions j_l and spherical harmonics Y_{lm} as

$$\mathrm{e}^{\mathrm{i}\vec{k}\vec{x}} = 4\pi \sum_{lm} \mathrm{i}^l j_l(k\chi) Y^*_{lm}(\vec{\theta}) Y_{lm}(\vec{\omega}) \; , \tag{1.35}$$

where $\vec{\theta}$ is the angular direction of vector $\vec{x}$ and $\vec{\omega}$ the angular direction of the wave vector $\vec{k}$. Inserting this expansion into Eq. (1.34), we find that

$$\langle\delta(\vec{x},\chi)\delta(\vec{x}',\chi')\rangle = \frac{2}{\pi} \sum_{lm} \int \mathrm{d}k k^2 j_l(k\chi) j_l(k\chi') Y^*_{lm}(\vec{\theta}) Y_{lm}(\vec{\theta}') P_{\delta\delta}(k,\chi,\chi') \; , \tag{1.36}$$

where we used the orthogonality relation of the spherical harmonics

$$\int \mathrm{d}\Omega Y_{lm}(\vec{\theta}) Y^*_{l'm'}(\vec{\theta}) = \delta_{ll'}\delta_{mm'} \; . \tag{1.37}$$

The spherical Bessel functions in Eq. (1.34) oscillate with a period of $\sim \frac{2\pi}{\chi}$ as a function of k. For cosmological distances χ, this causes the Bessel functions to vary rapidly compared to the power spectrum $P_{\delta\delta}(k)$. The power spectrum can then be approximated by evaluating it at the peak of the spherical Bessel function $k \sim \frac{l}{\chi}$ and taking it out of the integral. Applying the orthogonality relation of the spherical Bessel function we thus arrive at

$$\int_0^\infty \mathrm{d}k k^2 j_l(k\chi) j_l(k\chi') P_{\delta\delta}(k,\chi,\chi') \approx \frac{\pi}{2\chi^2} \delta_\mathrm{D}(\chi-\chi') P_{\delta\delta}\left(\frac{l}{\chi},\chi\right) \; . \tag{1.38}$$

This is the so called Limber approximation (Limber, 1953), which is sufficiently accurate for all current practical applications. The deviations from the exact treatment are less than 1% for $l \gtrsim 50$. For a detailed analysis of the effects of the Limber and other approximations on the convergence power spectrum, see Kilbinger et al. (2017). The double line-of-sight integral in Eq (1.31) can now be reduced to one. Comparing to Eq. (1.31) we finally arrive at the angular power spectrum of the convergence:

$$C_l^{\kappa\kappa} \approx \int_0^{\chi_H} \mathrm{d}\chi \frac{W^\kappa(\chi)^2}{\chi^2} P_{\delta\delta}\left(\frac{l}{\chi},\chi\right) \; . \tag{1.39}$$

This result can be easily generalised to any field that can be written in terms of a line-of-sight integral. For two fields on the sphere A and B, sourced by three-dimensional fields $\tilde{A}$ and $\tilde{B}$, with window functions W^A and W^B, the angular (cross) power spectrum reads

$$C_l^{AB} \approx \int_0^{\chi_H} \mathrm{d}\chi \frac{W^A(\chi) W^B(\chi)}{\chi^2} P_{\tilde{A}\tilde{B}}\left(\frac{l}{\chi},\chi\right) \; . \tag{1.40}$$

All probes studied in this thesis are of this form, allowing a single framework to handle cross-correlations between weak lensing, gamma rays, tSZ, and CMB lensing.

While power spectra are more natural from a theoretical perspective, it is often easier to measure correlation functions in configuration space, since estimators for correlation functions consist of simple sums over products of the quantities that are being correlated, see, e.g, Eq. (2.11). Power spectrum estimators are more complicated: the estimator in Chapter 2 relies on an integral over the measured correlation function while the pseudo-C_ℓ estimator in Chapter 3 explicitly needs to account for masks.

In this thesis we consider two types of correlation functions: two-point correlation functions $\xi^{\kappa X}$ between the convergence κ and some other scalar field X, such as the tSZ y parameter or CMB lensing convergence; and the two-point correlation function $\xi^{\gamma_t X}$ between the tangential shear γ_t and a scalar field X. The tangential shear γ_t describes the tangential component of the shear with respect to some reference point (see, e.g, Viola et al., 2015, for a technical definition). The tangential shear two-point correlation function is estimated by measuring the tangential component of the source galaxy ellipticities around all pixel positions of the map of the scalar field X. The tangential shear two-point correlation function $\xi^{\gamma_t X}$ has the advantage that it operates directly on the raw data sets – the galaxy shape catalogues, such as those from CFHTLenS, RCSLenS, or KiDS and scalar maps, such as those provided by the Planck team – and thus does not require additional processing steps that could introduce systematics. The correlation functions can be related to the power spectrum Eq. (1.40) by

$$\xi^{\kappa X}(\vartheta) = \frac{1}{2\pi}\int_0^\infty \mathrm{d}\ell\ell J_0(\ell\vartheta) C_\ell^{\kappa X} \quad \text{and} \quad \xi^{\gamma_t X}(\vartheta) = \frac{1}{2\pi}\int_0^\infty \mathrm{d}\ell\ell J_2(\ell\vartheta) C_\ell^{\kappa X} \,, \tag{1.41}$$

where ϑ denotes the angular separation on the sky and J_0 and J_2 are the Bessel functions of the first kind of order zero and two, respectively. Note that both $\xi^{\kappa X}$ and $\xi^{\gamma_t X}$ are related to the angular cross-power spectrum $C_\ell^{\kappa X}$, such that the underlying modelling is the same for the two estimators.

1.2 Large-scale structure

The convergence power spectrum Eq. (1.39) probes the matter power spectrum at different epochs. In the linear regime, the time evolution of the Fourier coefficients of the matter field can be separated into a growth factor $D_+(t)$ and the Fourier coefficients of the linear density contrast at some initial time as

$$\hat{\delta}^{\mathrm{lin}}(\vec{k},t) = D_+(t)\hat{\delta}_0^{\mathrm{lin}}(\vec{k}) \,. \tag{1.42}$$

The differential equation governing the growth of structure has two solutions, a growing mode D_+ and a decaying mode D_-. Since we are interested in the matter distribution at late times, the decaying mode can be neglected in our discussion. Because the time evolution separates from the spatial dependence, the time evolution of the linear power spectrum is therefore simply

$$P_{\delta\delta}^{\mathrm{lin}}(k,t) = D_+(t)^2 P_{\delta_0\delta_0}^{\mathrm{lin}}(k) \,. \tag{1.43}$$

The linear evolution breaks down at scales where $\Delta^{2,\mathrm{lin}}(k,t) = \frac{k^3}{4\pi^2} P^{\mathrm{lin}}_{\delta\delta}(k,t) \gtrsim 1$. At small scales $\Delta^{2,\mathrm{lin}}$ has a $\sim \log k^2$ dependence, such that small scales become non-linear before large scales. These scales are then subject to non-linear gravitational collapse. Describing the non-linear evolution of the matter field has proven difficult. Extending the perturbative treatment to higher orders allows us to describe the power spectrum accurately into the mildly non-linear regime. However, to model the power spectrum down to small, truly non-linear scales, it is necessary to rely on N-body simulations or phenomenological models, such as the halo model.

1.2.1 Halo model

In the halo model it is assumed that all matter has collapsed into haloes. The matter distribution can then be written as (see, e.g., Scherrer et al., 1991; Scoccimarro et al., 2001)

$$\rho(\vec{x}) = \sum_i \rho_i(\vec{x} - \vec{x}_i) \ , \tag{1.44}$$

where the sum runs over all haloes i, and ρ_i is the density profile of halo i with centre $\vec{x}_i$. It has been shown in N-body simulations that dark matter haloes on average are well described by a spherically symmetric profile $\rho_{\mathrm{h}}(r|M,z)$ that only depends on the mass and redshift (Navarro et al., 1997). The density profiles in Eq. 1.44 can thus be written as $\rho_{\mathrm{h}}(\vec{x} - \vec{x}_i|M_i,z) = \rho_{\mathrm{h}}(|\vec{x} - \vec{x}_i||M_i,z)$. In the following, we will investigate statistics of the density field. In order to calculate the expectation values, it is useful to separate the mass and position dependence of the haloes from their profile:

$$\rho(\vec{x}) = \int \mathrm{d}M \mathrm{d}^3y \sum_i \delta_{\mathrm{D}}(M - M_i)\delta_{\mathrm{D}}(\vec{y} - \vec{x}_i)\rho_{\mathrm{h}}(|\vec{x} - \vec{y}||M,z) \ . \tag{1.45}$$

The expectation value of the density field can then be expressed as

$$\langle\rho\rangle = \int \mathrm{d}M \mathrm{d}^3y \ \langle\sum_i \delta_{\mathrm{D}}(M - M_i)\delta_{\mathrm{D}}(\vec{y} - \vec{x}_i)\rangle \, \rho_{\mathrm{h}}(|\vec{x} - \vec{y}||M,z) \ . \tag{1.46}$$

The term in the brackets describes the mass and position of haloes and has dimensions of $M^{-1}L^{-3}$ (inverse mass times inverse length cubed). The expectation value of this term should therefore be a number density per mass. We hence set

$$\langle\sum_i \delta_{\mathrm{D}}(M - M_i)\delta_{\mathrm{D}}(\vec{y} - \vec{x}_i)\rangle = \frac{\mathrm{d}n(M,z)}{\mathrm{d}M} \ , \tag{1.47}$$

where $\frac{\mathrm{d}n(M,z)}{\mathrm{d}M}$ is the mass function, which describes the number density of haloes at redshift z with masses between M and $M + \mathrm{d}M$. Equation (1.46) can now be simplified to

$$\langle\rho\rangle = \int \mathrm{d}M \frac{\mathrm{d}n(M,z)}{\mathrm{d}M} \int \mathrm{d}^3y \ \rho_{\mathrm{h}}(|\vec{x} - \vec{y}||M,z) = \bar{\rho} \ , \tag{1.48}$$

such that we indeed recover the average density of the Universe $\bar{\rho}$. In the second equality we have used that the spatial integral over the density profile is just the mass M of the halo and that the mass integral over $M\frac{\mathrm{d}n(M,z)}{\mathrm{d}M}$ is the average matter density.

The quantities of interest in this thesis are two-point statistics, such as two-point correlation functions and power spectra. The two-point correlation function of the density field is $\xi_{\rho\rho}(\vec{x},\vec{x}-\vec{r}) = \langle\rho(\vec{x})\rho(\vec{x}-\vec{r})\rangle$. Since the Universe is assumed to be statistically homogeneous, the correlation function only depends on the separation: $\xi_{\rho\rho}(\vec{x},\vec{x}-\vec{r}) = \xi_{\rho\rho}(\vec{r})$. Furthermore, isotropy demands that the correlation function only depends on the modulus of the separation, not its direction, i.e., $\xi_{\rho\rho}(\vec{r}) = \xi_{\rho\rho}(|\vec{r}|)$. Using the formalism from Eq. (1.44), the correlation function $\xi_{\rho\rho}(|\vec{r}|)$ can be separated into two terms:

$$\begin{aligned}\xi_{\rho\rho}(|\vec{r}|) = \langle\rho(\vec{x})\rho(\vec{x}-\vec{r})\rangle = \langle\sum_i \rho_{\mathrm{h}}(|\vec{x}-\vec{x}_i||M_i,z)\rho_{\mathrm{h}}(|\vec{x}-\vec{r}-\vec{x}_i||M_i,z)\rangle \\ + \langle\sum_{i\neq j} \rho_{\mathrm{h}}(|\vec{x}-\vec{x}_i||M_i,z)\rho_{\mathrm{h}}(|\vec{x}-\vec{r}-\vec{x}_j||M_j,z)\rangle \ .\end{aligned} \tag{1.49}$$

The first term describes the correlation within haloes and is called the 'one-halo' term. The second term, called the 'two-halo' term, describes the correlation between different haloes.

Following the same steps as in the derivation of the mean density in Eq. (1.48), we can write the one-halo term as

$$\langle\rho(\vec{x})\rho(\vec{x}-\vec{r})\rangle_{1\mathrm{h}} = \int \mathrm{d}M \frac{\mathrm{d}n(M,z)}{\mathrm{d}M} \int \mathrm{d}^3y \rho_{\mathrm{h}}(|\vec{x}-\vec{y}||M,z)\rho_{\mathrm{h}}(|\vec{x}-\vec{r}-\vec{y}||M,z) \ . \tag{1.50}$$

The two-halo term can be treated analogously:

$$\begin{aligned}\langle\rho(\vec{x})\rho(\vec{x}-\vec{r})\rangle_{2\mathrm{h}} = \int \mathrm{d}M_1\mathrm{d}M_2 \int \mathrm{d}^3y_1\mathrm{d}^3y_2 \\ \times \langle\sum_{i\neq j} \delta_{\mathrm{D}}(M_1-M_i)\delta_{\mathrm{D}}(M_2-M_j)\delta_{\mathrm{D}}(\vec{y}_1-\vec{x}_i)\delta_{\mathrm{D}}(\vec{y}_2-\vec{x}_j)\rangle \\ \times \rho_{\mathrm{h}}(|\vec{x}-\vec{y}_1||M_1,z)\rho_{\mathrm{h}}(|\vec{x}-\vec{r}-\vec{y}_2||M_2,z) \ .\end{aligned} \tag{1.51}$$

The interpretation of the term in the second line is similar to that of Eq. (1.47): it should describe the number densities of haloes of masses M_1 and M_2. Furthermore, since it deals with separate haloes, it should account for the correlation between them. We therefore define

$$\begin{aligned}\langle\sum_{i\neq j} \delta_{\mathrm{D}}(M_1-M_i)\delta_{\mathrm{D}}(M_2-M_j)\delta_{\mathrm{D}}(\vec{y}_1-\vec{x}_i)\delta_{\mathrm{D}}(\vec{y}_2-\vec{x}_j)\rangle = \\ \frac{\mathrm{d}n(M_1,z)}{\mathrm{d}M}\frac{\mathrm{d}n(M_2,z)}{\mathrm{d}M}\xi_{\mathrm{hh}}(|\vec{y}_1-\vec{y}_2|,M_1,M_2) \ ,\end{aligned} \tag{1.52}$$

where $\xi_{\mathrm{hh}}(|\vec{y}_1-\vec{y}_2|,M_1,M_2)$ is the halo correlation function of haloes of masses M_1 and M_2, separated by $|\vec{y}_1-\vec{y}_2|$. Putting things together, we are left with the expression for the two-halo contribution to the

matter density correlation function:

$$\begin{aligned}\langle\rho(\vec{x})\rho(\vec{x}-\vec{r})\rangle_{2\mathrm{h}} = \int \mathrm{d}M_1\mathrm{d}M_2 \frac{\mathrm{d}n(M_1,z)}{\mathrm{d}M}\frac{\mathrm{d}n(M_2,z)}{\mathrm{d}M}\int \mathrm{d}^3y_1\mathrm{d}^3y_2 \\ \times \rho_{\mathrm{h}}(|\vec{x}-\vec{y}_1||M_1,z)\rho_{\mathrm{h}}(|\vec{x}-\vec{r}-\vec{y}_2||M_2,z)\xi_{\mathrm{hh}}(|\vec{y}_1-\vec{y}_2|,M_1,M_2)\ .\end{aligned} \tag{1.53}$$

The integrals over $\mathbb{R}^3$ in Eq. (1.50) and Eq. (1.53) are convolutions and it is therefore advantageous to proceed in Fourier space, where they can be represented as simple products (see Appendix C.1). The Fourier transform of the correlation function is the power spectrum and is defined as

$$\langle\hat{\rho}(\vec{k})\hat{\rho}(\vec{k}')\rangle = (2\pi)^3\delta_{\mathrm{D}}(\vec{k}-\vec{k}')P_{\rho\rho}(|\vec{k}|)\ , \tag{1.54}$$

where we have again assumed statistical homogeneity and isotropy. The one-halo and two-halo terms of the matter density power spectrum are then

$$\begin{aligned}P^{1\mathrm{h}}_{\rho\rho}(k,z) &= \int \mathrm{d}M\frac{\mathrm{d}n(M,z)}{\mathrm{d}M}|\hat{\rho}(k,M,z)|^2\ , \\ P^{2\mathrm{h}}_{\rho\rho}(k,z) &= \int \mathrm{d}M_1\mathrm{d}M_2\frac{\mathrm{d}n(M_1,z)}{\mathrm{d}M}\frac{\mathrm{d}n(M_2,z)}{\mathrm{d}M}\hat{\rho}(k,M_1,z)\hat{\rho}(k,M_2,z)P_{\mathrm{hh}}(k,M_1,M_2,z)\ .\end{aligned} \tag{1.55}$$

The correlation function and power spectrum of the density contrast are shown in Fig. 1.4, demonstrating the scale dependence of one-halo and two-halo terms. Except at the transition scale of around 2 Mpc h^{-1}, the correlation is clearly dominated by either the intra-halo correlation, described by the one-halo term, or the inter-halo correlation, described by the two-halo term. The separation into the two contributions is thus sensible.

It is conventional in cosmology to work with the matter density contrast $\delta(\vec{x}) = \frac{\rho(\vec{x})-\bar{\rho}}{\bar{\rho}}$ instead of the matter density itself. The correlation function of the density contrast $\xi_{\delta\delta}$ is related to the correlation function of the matter density by $\xi_{\delta\delta} = \frac{1}{\bar{\rho}^2}\xi_{\rho\rho} - 1$. The density contrast power spectrum $P_{\delta\delta}$ in terms of the matter density power spectrum is therefore given by $P_{\delta\delta} = \frac{1}{\bar{\rho}^2}P_{\rho\rho} - (2\pi)^3\delta_{\mathrm{D}}(0)$. The second term only applies for $k = 0$, which is not observable, since it corresponds to infinitely large scales. We will thus not include it explicitly in the rest of this discussion.

The halo power spectrum $P_{\mathrm{hh}}(k,M_1,M_2,z)$ describes the clustering of haloes, i.e., it is the power spectrum of the halo number density contrast δ^{h}. The halo number density is biased with respect to the matter distribution. At large scales, where the two-halo term dominates, the bias is linear and scale-independent such that we can write $\hat{\delta}^{\mathrm{h}}(\vec{k},M,z) = b(M,z)\hat{\delta}(\vec{k},z)$ (Mo et al., 1996; Sheth et al., 1999). It follows that the halo power spectrum can be expressed in terms of the matter power spectrum as $P_{\mathrm{hh}}(k,M_1,M_2,z) \approx b(M_1,z)b(M_2,z)P_{\delta\delta}(k,z)$. At intermediary and small scales this overestimates the halo power spectrum, however (Cooray et al., 2002). To resolve this overestimation, a common approximation is to estimate the halo power spectrum as

$$P_{\mathrm{hh}}(k,M_1,M_2,z) \approx b(M_1,z)b(M_2,z)P^{\mathrm{lin}}_{\delta\delta}(k,z)\ , \tag{1.56}$$

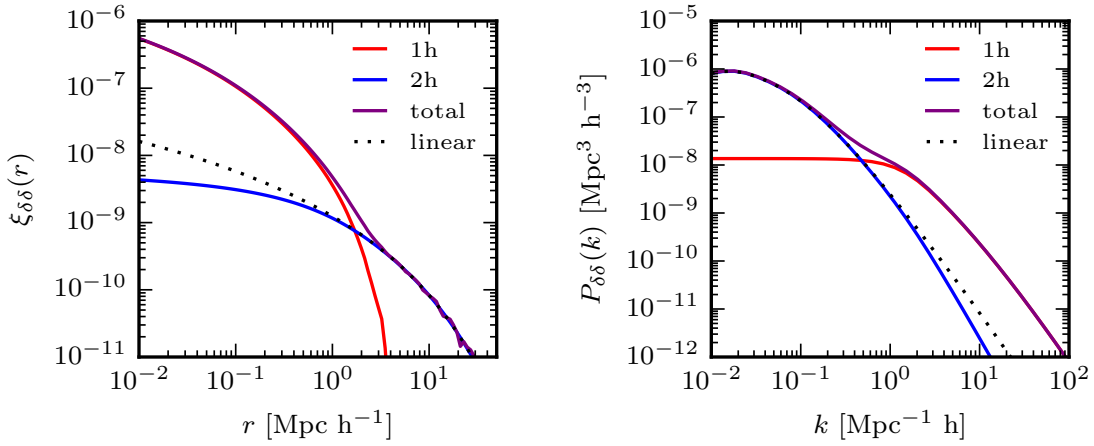

Figure 1.4: *Left:* Two-point correlation function of the density contrast. The one-halo term is shown in red, the two-halo term in blue, the total in purple, and the prediction from linear theory as black dotted line. On small scales, the one-halo term dominates, while at scales larger than a few Mpc the two-halo term determines the correlation. At these large scales the correlation is well described by linear theory. *Right:* Power spectrum of the density contrast. The formatting is analogous to that of the correlation function.

where $P_{\delta\delta}^{\rm lin}$ is the linear matter (density contrast) power spectrum. This allows us to separate the two integrals of the two-halo term in Eq. (1.55). Since the bias parameter obeys the consistency relation

$$\int \mathrm{d}M\, M \frac{\mathrm{d}n(M,z)}{\mathrm{d}M} b(M,z) = \bar{\rho}\ , \tag{1.57}$$

the two-halo terms takes an especially simple form at large scales: $P_{\delta\delta}^{\rm 2h} \approx P_{\delta\delta}^{\rm lin}$. This can be clearly seen in Fig. 1.4, where the two-halo term and linear prediction match up to scales within the one-halo regime.

In the literature, the halo density profile $\rho_{\rm h}(r)$ is often written in terms of a normalised profile

$$u(r,M) = \frac{\rho(r,M)}{\int \mathrm{d}^3 r \rho(r,M)} = \frac{\rho(r,M)}{M}\ . \tag{1.58}$$

The Fourier transform of the normalised profile $\hat{u}(k,M)$ then has the property that $\hat{u}(k,M) \to 1$ for $k \to 0$. The one-halo term therefore goes to a constant as $k \to 0$, as shown in Fig. 1.4. Writing the expressions in Eq. (1.55) in terms of the density contrast and normalised halo profile, as well as approximating the halo power spectrum by the linear power spectrum times the bias parameter, we recover the standard results from the literature:

$$\begin{aligned} P_{\delta\delta}^{\rm 1h}(k,z) &= \frac{1}{\bar{\rho}^2} \int \mathrm{d}M\, M^2 \frac{\mathrm{d}n(M,z)}{\mathrm{d}M} |\hat{u}(k,M,z)|^2\ ; \\ P_{\delta\delta}^{\rm 2h}(k,z) &= \frac{1}{\bar{\rho}^2} \left(\int \mathrm{d}M\, M \frac{\mathrm{d}n(M,z)}{\mathrm{d}M} b(M,z) \hat{u}(k,M,z) \right)^2 P_{\delta\delta}^{\rm lin}(k,z)\ . \end{aligned} \tag{1.59}$$

Halo model for cross-correlations

The formalism presented in the previous section can be straightforwardly generalised to describe the cross-correlation between two different fields. For example, the cross-correlation between gravitational lensing and gamma rays in Chapter 2 seeks to constrain the contribution of weakly interacting massive particle (WIMP) dark matter annihilation to the extragalactic gamma-ray flux. The gamma-ray flux due to dark matter annihilations is proportional to the dark matter density squared, since each annihilation event requires two dark matter particles. Gravitational lensing depends on the density contrast instead (cf. Section 1.1). We therefore wish to model the quantity $\langle \rho_{\rm DM}^2 \delta \rangle$. This can be accomplished by just replacing one factor of the halo density profile in Eq. (1.55) with the square of the density profile. The mass function and halo power spectrum do not have to be changed since the square of the density is still described by the same halo distribution. The resulting cross-power spectrum between the density contrast and density contrast squared is given by Eq. (2.9), although note the different definition of u there.

The cross-correlation between gravitational lensing and the tSZ effect can be treated similarly: here one factor of the density is instead replaced by the electron pressure profile. The resulting (angular) cross-power spectrum Eq. (3.14) is therefore only a minor modification of that derived in the previous section. This versatility is one of the great advantages of the halo model formalism.

It should be noted that the halo model is not without its downsides. It is a purely phenomenological model, making it difficult to extract physical information. Moreover, while it is quite accurate at large and small scales, this is not the case in the transition regime between the one and two-halo term. There have been efforts to ameliorate these inaccuracies by replacing certain terms in the halo model description with fitting functions tuned to N-body simulations (see, e.g., Smith et al., 2003; Takahashi et al., 2012; Mead et al., 2015, 2016). These tuned halo models remain computationally very simple, making it possible to include them in likelihoods sampled by Markov chain Monte Carlo (MCMC) methods, while retaining most of the information content of the simulations on two-points statistics. This computational simplicity is especially beneficial in cases where cosmological hydrodynamical simulations are required, such as for modelling the tSZ effect, since these simulations are still very computationally expensive to run.

1.3 Cross-correlations

This thesis investigates the correlations between weak gravitational lensing and other cosmological probes. Specifically, we are interested in two-point statistics, such as correlation functions and power spectra. In general, we measure two fields $\hat{A}$ and $\hat{B}$, which consist of the physical signals of interest A, B and noise components n_A, n_B:

$$\hat{A} = A + n_A \; ; \qquad \hat{B} = B + n_B \; . \tag{1.60}$$

The noise components encompass any contributions to the measurements that are not the signal of interest, e.g., measurement noise or systematics. In the cases we are considering in this thesis, it is

assumed that the noise components do not correlate with the primary signals, i.e., $\langle An_A\rangle = \langle An_B\rangle = \langle Bn_B\rangle = \langle Bn_A\rangle = 0$, nor do the noise components of the different fields correlate: $\langle n_A n_B\rangle = 0$. For example, in the cross-correlation between gravitational lensing and gamma rays in Chapter 2, the noise component of gravitational lensing comes from the uncertainty in the measurement of galaxy shapes, while the noise component of the extra-galactic gamma ray flux consists of shot-noise due to the finite observed photon counts and contamination due to Galactic gamma-ray emissions. Gravitational lensing probes the extra-galactic matter distribution, while the shape measurement uncertainties are dominated by the effects of the atmosphere, telescope, and detector on the observed galaxy image. It is therefore well justified to assume that these two effect are uncorrelated. Similarly, shot-noise of the gamma-ray observations and Galactic foregrounds are neither expected to correlate with the extra-galactic nature of gravitational lensing nor with shape measurement effects.

The cross-correlation between the two measured fields is therefore given by

$$\langle \hat{A}\hat{B}\rangle = \langle AB\rangle \ , \tag{1.61}$$

i.e., the measured cross-correlation is an unbiased estimator of the cross-correlation of the true signals. This is in contrast to the auto-correlation $\langle \hat{A}\hat{A}\rangle = \langle AA\rangle + \langle n_A n_A\rangle$, which is biased by the noise auto-correlation $\langle n_A n_A\rangle$. The absence of this noise bias is an important advantage of cross-correlations over auto-correlations, since the noise auto-correlation often dominates the true auto-correlation signal, sometimes by orders of magnitude, and can be difficult to remove accurately.

Even though the cross-correlation measurement is unbiased by the noise, the noise auto-correlations still contributes to the error budget and need to be accounted for there. To demonstrate this, we consider the angular power spectrum C_ℓ^{AB} between the two two-dimensional fields A and B defined on the whole sphere. The estimator for C_ℓ^{AB} is

$$\hat{C}_\ell^{AB} = \frac{1}{2\ell+1}\sum_{m=-\ell}^{\ell} \hat{A}_{\ell m}\hat{B}^*_{\ell m} \ , \tag{1.62}$$

where $\hat{A}_{\ell m}$ and $\hat{B}_{\ell m}$ are the spherical harmonic coefficients of the observed fields $\hat{A}$ and $\hat{B}$. The covariance of the measured angular cross-power spectrum $\hat{C}_\ell^{AB}$ is then

$$\mathrm{Cov}\left[\hat{C}_\ell^{AB}, \hat{C}_{\ell'}^{AB}\right] = \langle \hat{C}_\ell^{AB}\hat{C}_{\ell'}^{AB}\rangle - \langle \hat{C}_\ell^{AB}\rangle \langle \hat{C}_{\ell'}^{AB}\rangle \ . \tag{1.63}$$

Inserting the definition of the estimator Eq. (1.62) into the first term we find

$$\begin{aligned}
\langle \hat{C}_\ell^{AB}\hat{C}_{\ell'}^{AB}\rangle &= \frac{1}{(2\ell+1)(2\ell'+1)}\sum_{mm'} \langle \hat{A}_{\ell m}\hat{B}^*_{\ell m}\hat{A}_{\ell' m'}\hat{B}^*_{\ell' m'}\rangle \\
&= \frac{1}{(2\ell+1)(2\ell'+1)}\sum_{mm'} \Big(\langle \hat{A}_{\ell m}\hat{B}^*_{\ell m}\hat{A}_{\ell' m'}\hat{B}^*_{\ell' m'}\rangle_c + \langle \hat{A}_{\ell m}\hat{B}^*_{\ell m}\rangle \langle \hat{A}_{\ell' m'}\hat{B}^*_{\ell' m'}\rangle \\
&\qquad + \langle \hat{A}_{\ell m}\hat{A}_{\ell' m'}\rangle \langle \hat{B}^*_{\ell m}\hat{B}^*_{\ell' m'}\rangle + \langle \hat{A}_{\ell m}\hat{B}^*_{\ell' m'}\rangle \langle \hat{A}_{\ell m}\hat{B}^*_{\ell' m'}\rangle\Big) \ .
\end{aligned} \tag{1.64}$$

Using the definition of the angular power spectrum $\langle A_{\ell m} B^*_{\ell' m'} \rangle = \delta_{\ell\ell'} \delta_{mm'} C_\ell^{AB}$ and noting that the the second term on the second line in Eq. (1.64) cancels the second term in Eq. (1.63), we can write the covariance of $\hat{C}_\ell^{AB}$ as

$$\mathrm{Cov}\left[\hat{C}_\ell^{AB}, \hat{C}_{\ell'}^{AB}\right] = \frac{\delta_{\ell\ell'}}{2\ell+1}\left(\hat{C}_\ell^{AA}\hat{C}_\ell^{BB} + \left(\hat{C}_\ell^{AB}\right)^2\right) + \hat{T}_{\ell\ell'}^{AB}\,, \tag{1.65}$$

with the trispectrum term $\hat{T}_{\ell\ell'}^{AB}$ defined as

$$\hat{T}_{\ell\ell'}^{AB} = \frac{1}{(2\ell+1)(2\ell'+1)} \sum_{mm'} \langle \hat{A}_{\ell m} \hat{B}^*_{\ell m} \hat{A}_{\ell' m'} \hat{B}^*_{\ell' m'} \rangle_c \ . \tag{1.66}$$

We now split the observed fields again into the true signal and noise component such that we can write $\hat{C}_\ell^{AA} = C_\ell^{AA} + N_\ell^A$, where C_ℓ^{AA} is the angular power spectrum of the true signal A and N_ℓ^A is the auto spectrum of the noise n_A. Since the noise terms n_A and n_B do not correlate with the signals nor with each other, we again have $\hat{C}_\ell^{AB} = C_\ell^{AB}$ and $\hat{T}_{\ell\ell'}^{AB} = T_{\ell\ell'}^{AB}$. The covariance in terms of the true signal power spectra and noise spectra is

$$\mathrm{Cov}\left[\hat{C}_\ell^{AB}, \hat{C}_{\ell'}^{AB}\right] = \frac{\delta_{\ell\ell'}}{2\ell+1}\left(C_\ell^{AA}C_\ell^{BB} + \left(C_\ell^{AB}\right)^2 + C_\ell^{AA}N_\ell^B + C_\ell^{BB}N_\ell^A + N_\ell^A N_\ell^B\right) + T_{\ell\ell'}^{AB}\,. \tag{1.67}$$

The errors and covariance of the cross-correlation $\hat{C}_\ell^{AB}$ therefore do not only depend on the noise spectra N_ℓ^A and N_ℓ^B but also on the auto spectra C_ℓ^{AA} and C_ℓ^{BB}, the cross-spectrum C_ℓ^{AB}, and the trispectrum $T_{\ell\ell'}^{AB}$. The terms in the covariance that depend on the true signals A and B constitute the sampling variance. The sampling variance describes the uncertainty of our measurements due to the finite volume we have observed.

Broadly speaking, there are three approaches to estimate the covariance in practice: modelling of the covariance according to Eq. (1.67); creating many realisations of the data from simulations and estimating the covariance between these realisations; and internal estimates such as bootstrap (Efron, 1979) and jackknife (Tukey, 1958) that estimate the covariance by resampling the data. The three approaches suffer from different shortcomings. Modelling the covariance can be difficult, especially when contributions from the sampling variance are non-negligible, since the covariance depends on the signal we wish to measure and for which we might not have an adequate model. Using simulations to create realisations of the data can become very computationally expensive if the signal is produced by non-linear processes. Finally, covariances of correlated data estimated using bootstrap or jackknife methods can be biased and need to be checked and calibrated against other covariance estimates.

1.4 Thesis overview

The following chapters of this thesis concern themselves with various aspects of probing the nature of dark matter with gravitational lensing. Specifically, they cover the cross-correlation of gravitational lensing with three other probes: gamma rays; the tSZ effect; and CMB lensing.

1.4.1 Gamma rays

The analysis presented in Chapter 2 attempts to answer the question of the microscopic nature of dark matter. A popular hypothesis for the nature of dark matter is a WIMP. Such a particle would have been in thermal equilibrium with standard model matter at early times. An attractive feature of the WIMP scenario is that an annihilation cross-section at the weak scale yields the correct dark matter abundance $\Omega_{\rm DM}$ today. This annihilation cross-section is about $\langle \sigma_{\rm ann} v \rangle \sim 3 \times 10^{-26}\,{\rm cm}^3{\rm s}^{-1}$ and is called the thermal relic cross-section (see, e.g., Jungman et al., 1996).

The study of the cross-correlation between gravitational lensing and gamma rays in Chapter 2 is motivated by the rather generic prediction that the annihilation or decay products of WIMP dark matter will include gamma rays (Bergström et al., 2001; Ullio et al., 2002). If dark matter is a WIMP, then regions of the Universe with high dark matter content are expected to show excesses in gamma rays emission. Gravitational lensing probes the matter distribution in the Universe and, since the matter content is dominated by dark matter, it is also a good probe of the dark matter distribution. A correlation between gamma rays and gravitational lensing would therefore support the hypothesis that dark matter is a WIMP with annihilation or decay channels into gamma rays. Conversely, a lack of correlation would constrain the parameter space of WIMP dark matter, restricting the allowed masses, annihilation cross-sections, and decay rates. This reasoning is complicated by the fact that there are known astrophysical gamma-ray sources in the Universe that also trace the matter distribution (Xia et al., 2015). Furthermore, the gamma-ray flux due to dark matter annihilations is strongly dependent on the small-scale clustering of dark matter. We model different populations of astrophysical gamma-ray emitters and consider a range of small-scale dark matter clustering models to address these uncertainties.

1.4.2 tSZ

Most of matter in the Universe, 84% (Planck Collaboration XIII, 2016), is dark matter. The remaining 16% is in the form of baryons, which closely trace the dark matter distribution at large scales but can deviate strongly at small scales where baryon physics become important. Unlike dark matter, baryons are able to cool radiatively, allowing them to form much denser structures, such as stars and galaxies. These cooling processes increase the clustering of matter at small scales. Other processes, such as stellar winds, super novea, and active galactic nuclei (AGN) feedback cause gas to be redistributed and possibly expelled from its host galaxy (van Daalen et al., 2011). These processes are highly non-linear, making their modelling complicated. The physical processes typically originate on scales much smaller than the resolution of cosmological simulations, thus requiring separate sub-grid modelling to include these astrophysical processes. It is therefore necessary to provide observational data to calibrate these simulations.

In Chapter 3 we provide such data by comparing the distribution of gas inferred from the tSZ effect to that of the total matter distribution measured by gravitational lensing. The tSZ effect is caused by the inverse Compton scattering of CMB photons off hot electrons (Sunyaev et al., 1972). The resulting spectral distortion of the CMB can be imaged, yielding a map of the distribution of hot, free electrons which traces the diffuse gas in the Universe. The tSZ effect is therefore ideal to statistically measure the

effect of violent processes, such as AGN feedback, on gas.

The first-order derivation of the convergence power spectrum in Eq. (1.39) has been shown to be sufficiently accurate for current and upcoming surveys. However, it is a priori not evident that the same is true for cross-correlations between the convergence and other fields. To ensure that models used in Chapter 3 are not biased by neglecting terms of higher order in the potential, we check in Chapter 4 the effect of terms that are third and fourth order in the gravitational potential on the cross-power spectrum between lensing and tSZ.

1.4.3 CMB lensing

The analyses in Chapters 2 and 3 made the implicit assumption that the growth of structure proceeds as predicted by the ΛCDM concordance model of cosmology and that the measurement of weak gravitational lensing are accurate and not biased by systematics. Chapter 5 tests these assumptions by combining two different realisations of gravitational lensing: galaxy lensing; and lensing of the CMB. Galaxy lensing from surveys such as CFHTLenS, RCSLenS, and KiDS measures the ellipticities of galaxies to obtain an estimate of the shear field. This kind of lensing was employed in the analyses of Chapters 2 and 3. If the galaxy sample has redshift estimates, we can in principle select galaxies to follow a source distribution $p(\chi_{\rm S})$ of our choosing. This allows us to optimise the window function W^{κ} in Eq. (1.27) to be sensitive to a certain redshift range. Using different galaxy selections to probe different redshift ranges, a technique called tomography, we have a tool to probe the evolution of the matter distribution. Lensing of the CMB manifests itself in coherent distortions of the CMB anisotropies. By analysing these distortions we are able to directly estimate the lensing potential. Since the source plane for CMB lensing is the surface of last scattering, it probes the matter distribution of the whole observable Universe. However, since there is only one source plane, it is not possible to do tomographic measurements with just CMB lensing alone. Cross-correlating galaxy lensing with CMB lensing in redshift slices allows for a tomographic measurements of the matter distribution while enjoying the advantages of cross-correlations laid out in Section 1.3. Chapter 5 presents such a cross-correlation and analyses it for deviations from the expected growth rate of structure and residual systematics in the galaxy lensing data. The measurements build on previous work presented in Harnois-Déraps et al. (2016), to which the author of this thesis provided the measurements, covariances, and analysis of the configuration space estimators.

Chapter 2

Cross-correlation of weak lensing and gamma rays: implications for the nature of dark matter

We measure the cross-correlation between Fermi-LAT gamma-ray photons and over 1000 deg^2 of weak lensing data from the Canada-France-Hawaii Telescope Lensing Survey (CFHTLenS), the Red Cluster Sequence Lensing Survey (RCSLenS), and the Kilo-Degree Survey (KiDS). We present the first measurement of tomographic weak lensing cross-correlations and the first application of spectral binning to cross-correlations between gamma rays and weak lensing. The measurements are performed using an angular power spectrum estimator, while the covariance is estimated using an analytical prescription. We verify the accuracy of our covariance estimate by comparing it to two internal covariance estimators. Based on the non-detection of a cross-correlation signal, we derive constraints on weakly interacting massive particle (WIMP) dark matter. We compute exclusion limits on the dark matter annihilation cross-section $\langle\sigma_{\rm ann}v\rangle$, decay rate $\Gamma_{\rm dec}$, and particle mass $m_{\rm DM}$. We find that in the absence of a cross-correlation signal, tomography does not significantly improve the constraining power of the analysis compared to a non-tomographic measurement. Assuming a strong contribution to the gamma-ray flux due to small-scale clustering of dark matter and accounting for known astrophysical sources of gamma rays, we exclude the thermal relic cross-section for particle masses of $m_{\rm DM} \lesssim 20$ GeV. These constraints are comparable to those derived from other analyses of the extra-galactic gamma-ray flux but somewhat weaker than those from local probes, such as from dwarf spheroidal galaxies (dSphs) and the Galactic centre.

2.1 Introduction

The matter content of the Universe is dominated by so called dark matter, whose cosmological abundance and large-scale clustering properties have been measured to high precision (e.g. Hinshaw et al., 2013; Planck Collaboration XIII, 2016; Ross et al., 2015; Anderson et al., 2014; Mantz et al., 2015; Hoekstra et al., 2015; Hildebrandt et al., 2017). However, little is known about its microscopic nature,

beyond its lack of – or at most weak – non-gravitational interactions with standard model matter.

WIMPs thermally produced in the early Universe are among the leading dark matter candidates. With a mass of the order of GeV or TeV, their decoupling from thermal equilibrium occurs in the non-relativistic regime. The weak interaction rate with lighter standard model particles furthermore ensures that their thermal relic density is naturally of the order of the measured cosmological dark matter abundance (Lee et al., 1977; Gunn et al., 1978).

Many extensions of the standard model of particle physics predict the existence of new massive particles at the weak scale; some of these extra states can indeed be 'dark', i.e., be colour and electromagnetic neutral, with the weak force and gravity as the only relevant coupling to ordinary matter (for reviews, see e.g., Jungman et al., 1996; Bertone et al., 2005; Schmaltz et al., 2005; Hooper et al., 2007; Feng, 2010).

The weak coupling allows us to test the hypothesis of WIMP dark matter: supposing that WIMPs are indeed the building blocks of large-scale structure (LSS) in the Universe, there is a small but finite probability that WIMPs in dark matter haloes annihilate or decay into detectable particles. These standard model particles produced by these annihilations or decays would manifest as cosmic rays, which can be observed. In particular, since the WIMP mass is around the electroweak scale, gamma rays can be produced, which can be observed with ground-based or space-borne telescopes, e.g., the Large Area Telescope on the Fermi gamma-ray space telescope (Fermi-LAT, Atwood et al., 2009). Indeed, analyses of the gamma-ray sky have already been widely used to put constraints on WIMP dark matter, see e.g. Charles et al. (2016) for a recent review.

The currently strongest constraints on the annihilation cross-section and WIMP mass come from the analysis of local regions with high dark matter content, such as dSphs (Ackermann et al., 2015c). These analyses exclude annihilation cross-sections larger than $\sim 3 \times 10^{-26}$ cm^{3}s^{-1} for dark matter candidates lighter than 100 GeV. This value for the annihilation cross-section is known as the thermal cross-section, below which many models of new physics predict dark matter candidates that yield a relic dark matter density in agreement with cosmological measurements of the dark matter abundance (Jungman et al., 1996).

Instead of these local probes of dark matter properties, one could consider the unresolved gamma-ray background (UGRB), i.e., the cumulative radiation produced by all sources that are not bright enough to be resolved individually. Correctly modelling the contribution of astrophysical sources, such as blazars, star-forming, and radio galaxies, allows the measurement of the UGRB to be used to constrain the component associated with dark matter (Fornasa et al., 2015). Indeed, the study of the energy spectrum of the UGRB (Ackermann et al., 2015d), as well as of its anisotropies (Ando et al., 2013; Fornasa et al., 2016) and correlation with tracers of LSS (Ando et al., 2014; Shirasaki et al., 2014; Fornengo et al., 2015; Regis et al., 2015; Cuoco et al., 2015; Shirasaki et al., 2015; Ando et al., 2016; Shirasaki et al., 2016; Feng et al., 2017) have yielded independent and competitive constraints on the nature of dark matter.

In this chapter, we focus on the cross-correlation of the UGRB with weak gravitational lensing. Gravitational lensing is an unbiased tracer of matter and thus closely probes the distribution of dark

matter in the Universe. This makes it an ideal probe to cross-correlate with gamma rays to investigate the particle nature of dark matter (Camera et al., 2013).

We extend previous analyses of cross-correlations of gamma rays and weak lensing of Shirasaki et al. (2014, 2016) by adding weak lensing data from the Kilo-Degree Survey (KiDS, de Jong et al., 2013b; Kuijken et al., 2015) and making use of the spectral and redshift information contained within the data sets. This chapter presents the first tomographic weak lensing cross-correlation measurement and the first application of spectral binning to the cross-correlation between gamma rays and galaxy lensing. Exploiting tomography and the information contained in the energy spectrum of the dark matter annihilation signal has been shown to greatly increase the constraining power compared to the case where no binning in redshift or energy is performed (Camera et al., 2015).

The structure of this chapter is as follows: in Section 2.2 we introduce the formalism and theory; the data sets are described in Section 2.3; Section 2.4 introduces the measurement methods and estimators; the results are presented in Section 2.5; and we draw our conclusions in Section 2.6.

2.2 Formalism

Our theoretical predictions are obtained by computing the angular cross-power spectrum $C_\ell^{g\kappa}$ between the lensing convergence κ and gamma-ray emissions for different classes of gamma-ray sources, denoted by g. In the Limber approximation (Limber, 1953), it takes the form

$$\begin{aligned} C_\ell^{g\kappa} = &\int_{\Delta E} \mathrm{d}E \int_0^\infty \mathrm{d}z \, \frac{c}{H(z)} \frac{1}{\chi(z)^2} \\ &\times W^g(E,z)\, W^\kappa(z)\, P_{g\delta}\left(k = \frac{\ell}{\chi(z)}, z\right) , \end{aligned} \tag{2.1}$$

where z is the redshift, E is the gamma-ray energy and ΔE the energy bin that is being integrated over, c is the speed of light in the vacuum, $H(z)$ is the Hubble rate, and $\chi(z)$ is the comoving distance. We employ a flat ΛCDM cosmological model with parameters taken from Planck Collaboration XIII (2016).

W^g and W^κ are the window functions that characterize the redshift and energy dependence of the gamma-ray emitters and the efficiency of gravitational lensing, respectively. $P_{g\delta}(k,z)$ is the three-dimensional cross-power spectrum between the gamma-ray emission for a gamma-ray source class and the matter density δ, with k being the modulus of the wavenumber and ℓ the angular multipole. The functional form of the window functions and power spectra depend on the populations of gamma-ray emitters and source galaxy distributions under consideration and are described in the following subsections.

The quantity measured from the data is the tangential shear cross-correlation function $\xi^{g\gamma_t}(\vartheta)$. This correlation function is related to the angular cross-power spectrum by a Hankel transformation:

$$\xi^{g\gamma_t}(\vartheta) = \frac{1}{2\pi} \int_0^\infty \mathrm{d}\ell \; \ell J_2(\ell\vartheta) C_\ell^{g\kappa} , \tag{2.2}$$

where ϑ is the angular separation in the sky and J_2 is the Bessel function of the first kind of order two.

2.2.1 Window functions

The window function describes the distribution of the signal along the line of sight, averaged over all lines of sight.

Gravitational lensing

For gravitational lensing the window function is given by (see, e.g., Bartelmann, 2010)

$$W^{\kappa}(z) = \frac{3}{2} H_0^2 \Omega_{\rm M} (1+z) \chi(z) \int_z^{\infty} {\rm d}z' \, \frac{\chi(z') - \chi(z)}{\chi(z')} n(z') \, , \tag{2.3}$$

where H_0 is the Hubble rate today, $\Omega_{\rm M}$ is the current matter abundance in the Universe, and $n(z)$ is the redshift distribution of background galaxies in the lensing data set. The galaxy distribution depends on the data set and redshift selection, as described in Section 2.3.1. The redshift distribution function $n(z)$ is binned in redshift bins of width $\Delta_z = 0.05$. To compute the window function in Eq. (2.3), $n(z)$ is interpolated linearly between those bins. The resulting window functions for KiDS are shown in the bottom panel of Fig. 2.1. The width of the window function in Fig. 2.1, especially for the 0.1–0.3 redshift bin, is due to the leakage of the photometric redshift distribution outside the redshift selection range.

Gamma-ray emission from dark matter

We consider two processes by which dark matter can create gamma rays: annihilation and decay.

The window function for annihilating dark matter reads (Ando et al., 2006; Fornengo et al., 2014)

$$\begin{aligned} W^{g_{\rm ann}}(z, E) = & \frac{(\Omega_{\rm DM} \rho_{\rm c})^2}{4\pi} \frac{\langle \sigma_{\rm ann} v \rangle}{2 {m_{\rm DM}}^2} (1+z)^3 \Delta^2(z) \\ & \times \frac{{\rm d}N_{\rm ann}}{{\rm d}E} [E(1+z)] \, {\rm e}^{-\tau[z, E(1+z)]} \, , \end{aligned} \tag{2.4}$$

where $\Omega_{\rm DM}$ is the cosmological abundance of dark matter, $\rho_{\rm c}$ is today's critical density of the Universe, $m_{\rm DM}$ is the rest mass of the dark matter particle, and $\langle \sigma_{\rm ann} v \rangle$ denotes the velocity-averaged annihilation cross-section, assumed here to be the same in all haloes. The optical depth of gamma rays is given by τ. ${\rm d}N_{\rm ann}/{\rm d}E$ indicates the number of photons produced per annihilation as a function of photon energy, and sets the gamma-ray energy spectrum. We will consider it to be given by the sum of two contributions: prompt gamma-ray production from dark matter annihilation, which provides the bulk of the emission at low masses; and inverse Compton scattering of highly energetic dark matter-produced electrons and positrons on CMB photons, which upscatter in the gamma-ray band. The final states of dark matter annihilation are computed by means of the PYTHIA Monte Carlo package v8.160 (Sjöstrand et al., 2008). The inverse Compton scattering contribution is calculated as in Fornasa et al. (2013), which assumes negligible magnetic field and no spatial diffusion for the produced electrons and positrons.

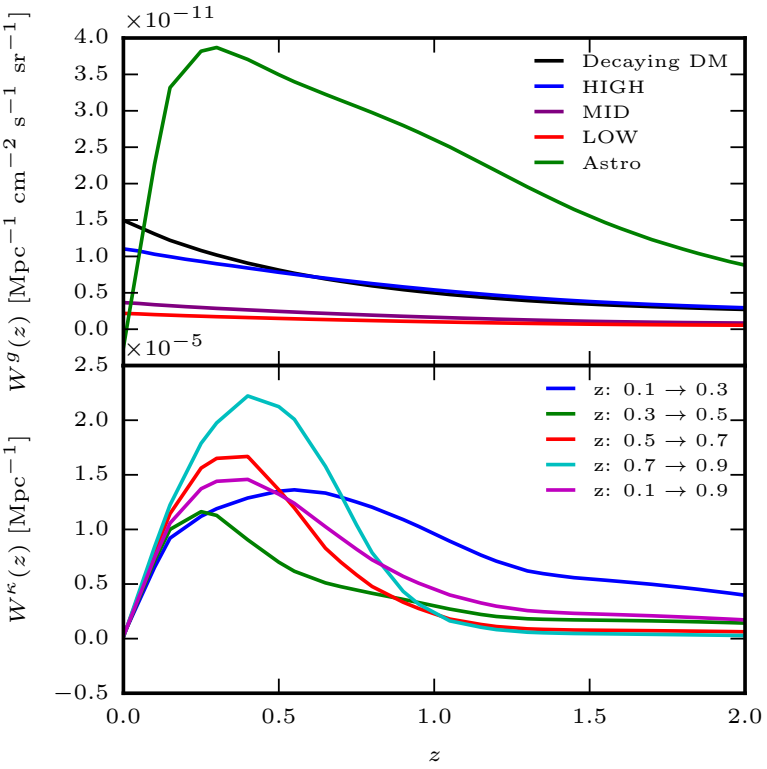

Figure 2.1: *Top:* window functions for the gamma-ray emissions W^g for the energy range 0.5–500 GeV and redshift selection of 0.1–0.9. Shown are the window functions for the three annihilating dark matter scenarios considered, i.e., HIGH (blue), MID (purple), LOW (red); decaying dark matter (black); and the sum of the astrophysical sources (green). The annihilation scenarios assume $m_{\rm DM} = 100$ GeV and $\langle\sigma_{\rm ann} v\rangle = 3 \times 10^{-26}$ cm^{3}s^{-1}. For decaying dark matter, $m_{\rm DM} = 200$ GeV and $\Gamma_{\rm dec} = 5 \times 10^{-28}$ s^{-1}. The predictions for annihilating and decaying dark matter are for the $b\bar{b}$ channel. We consider three populations of astrophysical sources that contribute to the UGRB: blazars, mAGN, and SFG, described in Section 2.2.1. *Bottom:* the lensing window functions for the five tomographic bins chosen for KiDS.

Results will be shown for three final states of the annihilation: $b\bar{b}$ pairs, which yields a relatively soft spectrum of photons and electrons, mostly associated with hadronisation into pions and their subsequent decay; $\mu^+\mu^-$, which provides a relatively hard spectrum, mostly associated with final state radiation of photons and direct decay of the muons into electrons; and $\tau^+\tau^-$, which lies between the first two cases, being a leptonic final state, but with semi-hadronic decay into pions (Fornengo et al., 2004; Cembranos et al., 2011; Cirelli et al., 2011).

The optical depth τ in Eq. (2.4) accounts for attenuation of gamma rays due to scattering off the extragalactic background light (EBL), and is taken from Franceschini et al. (2008).

The clumping factor Δ^2 is related to how dark matter density is clustered in haloes and subhaloes. Its definition depends on the square of the dark matter density; therefore, it is a measure of the amount

of annihilations happening and, thus, the expected gamma-ray flux. The clumping factor is defined as (see, e.g., Fornengo et al., 2014)

$$\Delta^2(z) \equiv \frac{\langle \rho^2_{\rm DM} \rangle}{\bar{\rho}^2_{\rm DM}} = \int_{M_{\rm min}}^{M_{\rm max}} {\rm d}M \frac{{\rm d}n_{\rm h}}{{\rm d}M}(M,z)\,[1+b_{\rm sub}(M,z)] \times \int {\rm d}^3x \frac{\rho^2_{\rm h}(\vec{x}|M,z)}{\bar{\rho}^2_{\rm DM}}\,, \tag{2.5}$$

where $\bar{\rho}_{\rm DM}$ is the current mean dark matter density, ${\rm d}n_{\rm h}/{\rm d}M$ is the halo mass function (Sheth et al., 1999), $M_{\rm min}$ is the minimal halo mass, $M_{\rm max}$ is the maximal mass of haloes (for definiteness, we use 10^{18} $\mathrm{M}_\odot$, but the results are insensitive to the precise value assumed), $\rho_{\rm h}(\mathbf{x}|M,z)$ is the dark matter density profile of a halo with mass M at redshift z, taken to follow a Navarro-Frenk-White (NFW) profile (Navarro et al., 1997), and $b_{\rm sub}$ is the boost factor that encodes the 'boost' to the halo emission provided by subhaloes. To characterize the halo profile and the subhalo contribution, we need to specify their mass concentration. Modelling the concentration parameter $c(M,z)$ at such small masses and for subhaloes is an ongoing topic of research and is the largest source of uncertainty of the models in this analysis. We consider three cases: LOW, which uses the concentration parameter derived in Prada et al. (2012), (see also Sánchez-Conde et al., 2014); HIGH, based on Gao et al. (2012); and MID, following the recent analysis of Moliné et al. (2017). The last one represents our reference case, with predictions that are normally intermediate between those of the LOW and HIGH. The authors in Moliné et al. (2017) refined the estimation of the boost factor of Sánchez-Conde et al. (2014) by modelling the dependence of the concentration of the subhaloes on their position in the host halo. Accounting for this dependence and related effects, such as tidal stripping, leads to an increase of a factor 1.7 in the overall boost factor over the LOW model. Predictions for the dark matter clumping factor for the three models are shown in Fig. 2.2.

Since the number of subhaloes and, therefore, the boost factor, increases with increasing host halo mass, the integral in Eq. (2.5) is dominated group and cluster-sized haloes (Ando et al., 2013). However, in the absence of subhaloes, the clumping factor in Eq. (2.5) strongly depends on the low-mass cutoff $M_{\rm min}$, since the mass integral in Eq. (2.5) diverges as $M_{\rm min} \to 0$ (Ando et al., 2006). The minimum halo mass $M_{\rm min}$ depends on the free-streaming scale of dark matter, which is assumed to be in the range of 10^{-12}–10^{-3} $\mathrm{M}_\odot$ (Profumo et al., 2006; Bringmann, 2009). We therefore choose an intermediary mass cutoff of $M_{\rm min} = 10^{-6}$ $\mathrm{M}_\odot$. As all our models include substructure, the dependence on $M_{\rm min}$ is at most $\mathscr{O}(1)$. Specifically, the changes to clumping factor due to varying $M_{\rm min}$ in the range 10^{-12}–10^{-2} $\mathrm{M}_\odot$ are less than the uncertainty in the concentration parameter (Regis et al., 2015).

The window function of decaying dark matter is given by (Ando et al., 2006; Ibarra et al., 2013; Fornengo et al., 2014)

$$W^{g_{\rm dec}}(z,E) = \frac{\Omega_{\rm DM}\rho_{\rm c}}{4\pi}\frac{\Gamma_{\rm dec}}{m_{\rm DM}}\frac{{\rm d}N_{\rm dec}}{{\rm d}E}\,[E(1+z)]\,{\rm e}^{-\tau[z,E(1+z)]}\,, \tag{2.6}$$

where $\Gamma_{\rm dec}$ is the decay rate and $\frac{{\rm d}N_{\rm dec}}{{\rm d}E}(E) = \frac{{\rm d}N_{\rm ann}}{{\rm d}E}(2E)$, i.e., the energy spectrum for decaying dark matter

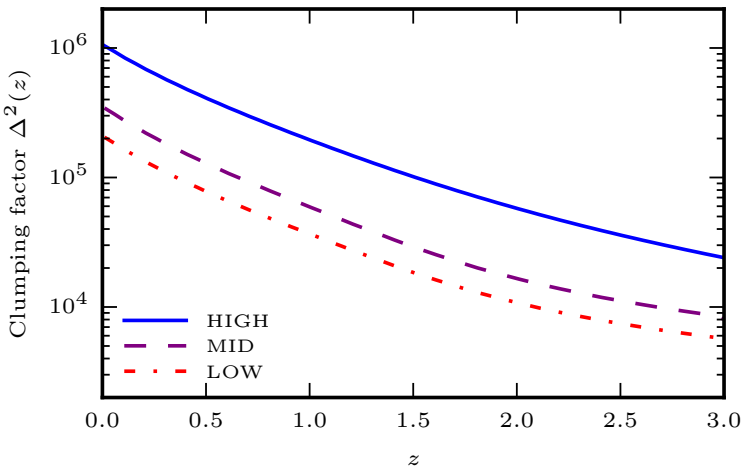

Figure 2.2: Dark matter clumping factor Δ^2, as defined in Eq. (2.5), as a function of redshift for the LOW (dash-dotted red), MID (dashed purple) and HIGH (solid blue) scenarios of dark matter clustering. The MID model is built from its expression at $z = 0$ in Moliné et al. (2017), assuming the same redshift scaling as in Prada et al. (2012).

is the same as that for annihilating dark matter described above, at twice the energy (Cirelli et al., 2011). Unlike annihilating dark matter, decaying dark matter does not depend on the clumping factor and the expected emission is thus much less uncertain. A set of representative window functions for annihilating and decaying dark matter is shown in the top panel of Fig. 2.1. In Fig. 2.3 we show the average all-sky gamma-ray emission expected from annihilating dark matter for the three clumping scenarios described above and from decaying dark matter.

Gamma-ray emission from astrophysical sources

Besides dark matter, gamma rays are produced by astrophysical sources, which will contaminate, and even dominate over the expected dark matter signal. Indeed, astrophysical sources have been shown to be able to fully explain the observed cross-correlations between gamma rays and tracers of LSS, like galaxy catalogues (Xia et al., 2015; Cuoco et al., 2015). For this analysis, we model three populations of astrophysical sources of gamma rays: blazars; misaligned AGN (mAGN); and star forming galaxies (SFGs). Blazars are likely AGN with their jets directly pointed towards us, while mAGN have jets pointed in our general direction, resulting in lower luminosities than blazars. The sum of the gamma-ray emissions produced by the three extragalactic astrophysical populations described above approximately accounts for all the UGRB measured (see Fornasa et al., 2015), as shown in Fig. 2.3, where the emissions from the three astrophysical source classes are compared to the most recent measurement of the UGRB energy spectrum from Ackermann et al. (2015a). For each of these astrophysical gamma-ray sources,

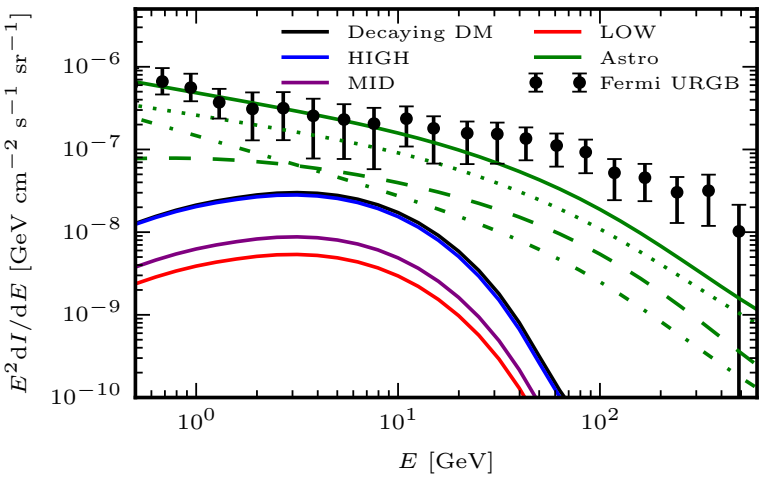

Figure 2.3: Intensities of the gamma-ray source classes considered in this work: annihilating dark matter assuming HIGH (solid blue), MID (solid purple), LOW (solid red) clustering models; decaying dark matter (solid black); and astrophysical sources ('Astro', solid green). The dark matter particle properties are the same as in Fig. 2.1. The astrophysical sources are further divided into blazars (dashed green), mAGN (dotted green), and SFG (dash-dotted green). The black data points represents the observed isotropic component of the UGRB (Ackermann et al., 2015a).

we consider a window function of the form

$$W^{gs}(z,E) = \chi(z)^2 \int_{\mathscr{L}_{\min}}^{\mathscr{L}_{\max}(F_{\rm sens},z)} \mathrm{d}\mathscr{L}\, \frac{\mathrm{d}F}{\mathrm{d}E}(\mathscr{L},z)\, \Phi(\mathscr{L},z)\,, \tag{2.7}$$

where $\mathscr{L}$ is the gamma-ray luminosity in the energy interval 0.1–100 GeV, and Φ is the gamma-ray luminosity function (GLF) corresponding to one of the source classes of astrophysical emitters included in our analysis. The upper bound, $\mathscr{L}_{\max}(F_{\rm sens},z)$, is the luminosity above which an object can be resolved, given the detector sensitivity $F_{\rm sens}$, taken from Ackermann et al. (2015b). As we are interested in the contribution from unresolved astrophysical sources, only sources with luminosities smaller than $\mathscr{L}_{\max}$ are included. Conversely, the minimum luminosity $\mathscr{L}_{\min}$ depends on the properties of the source class under investigation. The differential photon flux is given by $\mathrm{d}F/\mathrm{d}E = \mathrm{d}N_{\rm S}/\mathrm{d}E \times \mathrm{e}^{-\tau[z,E(1+z)]}$, where $\mathrm{d}N_{\rm S}/\mathrm{d}E$ is the observed energy spectrum of the specific source class and the exponential factor again accounts for the attenuation of high-energy photons by the EBL.

We consider a unified blazar model combining BL Lacertae and flat-spectrum radio quasars as a single source class. The GLF and energy spectrum are taken from Ajello et al. (2015) where they are derived from a fit to the properties of resolved blazars in the third Fermi-LAT catalogue (Acero et al., 2015).

In the case of mAGN, we follow Di Mauro et al. (2014), who studied the correlation between the gamma-ray and radio luminosity of mAGN, and derived the GLF from the radio luminosity function.

We consider their best-fitting $\mathscr{L}$–$L_{r,\mathrm{core}}$ relation and assume a power-law spectrum with index $\alpha_{\mathrm{mAGN}} = 2.37$.

To build the GLF of SFG, we start from the IR luminosity function of Gruppioni et al. (2013), adding up spiral, starburst, and SF-AGN populations of their table 8, and adopt the best-fitting $\mathscr{L}$–L_{IR} relation from Ackermann et al. (2012). The energy spectrum is taken to be a power law with spectral index $\alpha_{\mathrm{SFG}} = 2.7$.

The window function and average all-sky emission expected from the astrophysical sources are shown as green lines in the top panel of Fig. 2.1 and Fig. 2.3, respectively.

2.2.2 Three-dimensional power spectrum

The three-dimensional cross-power spectrum $P_{g\delta}$ between the gamma-ray emission of a source class g and the matter density is defined as

$$\langle \hat{f}_g(z,\vec{k})\hat{f}^*_\delta(z',\vec{k}')\rangle = (2\pi)^3\delta^3(\vec{k}+\vec{k}')P_{g\delta}(k,z,z') \;, \tag{2.8}$$

where $\hat{f}_g$ and $\hat{f}_\delta$ denote the Fourier transform of the emission of the specific class of gamma-ray emitters and matter density, respectively, and $\langle\,.\,\rangle$ indicates the average over the survey volume. Using the Limber approximation, one can set $z = z'$ in Eq. 2.8. The density of gamma-ray emission due to decaying dark matter traces the dark matter density contrast δ_{DM}, while the emission associated with annihilating dark matter traces δ^2_{DM}. Astrophysical sources are assumed to be point-like biased tracers of the matter distribution. Finally, lensing directly probes the matter contrast δ_{M}. To compute $P_{g\delta}$, we follow the halo model formalism (for a review, see, e.g., Cooray et al., 2002), and write $P = P^{1\mathrm{h}} + P^{2\mathrm{h}}$. We derive the 1-halo term $P^{1\mathrm{h}}$ and the two-halo term $P^{2\mathrm{h}}$ as in Fornengo et al. (2015) and in Camera et al. (2015).

Dark matter gamma-ray sources

The 3D cross-power spectrum between dark matter sources of gamma rays and matter density is given by

$$\begin{aligned}
P^{1\mathrm{h}}_{g_{\mathrm{DM}}\kappa}(k,z) &= \int_{M_{\mathrm{min}}}^{M_{\mathrm{max}}} \mathrm{d}M\, \frac{\mathrm{d}n_{\mathrm{h}}}{\mathrm{d}M}(M,z)\, \hat{v}_{g_{\mathrm{DM}}}(k|M,z)\, \hat{u}_\kappa(k|M,z) \;, \\
P^{2\mathrm{h}}_{g_{\mathrm{DM}}\kappa}(k,z) &= \left[\int_{M_{\mathrm{min}}}^{M_{\mathrm{max}}} \mathrm{d}M\, \frac{\mathrm{d}n_{\mathrm{h}}}{\mathrm{d}M}(M,z)\, b_{\mathrm{h}}(M,z)\, \hat{v}_{g_{\mathrm{DM}}}(k|M,z)\right] \\
&\quad \times \left[\int_{M_{\mathrm{min}}}^{M_{\mathrm{max}}} \mathrm{d}M\, \frac{\mathrm{d}n_{\mathrm{h}}}{\mathrm{d}M}(M,z)\, b_{\mathrm{h}}(M,z)\hat{u}_\kappa(k|M,z)\right] \\
&\quad \times P^{\mathrm{lin}}_{\delta\delta}(k,z) \;,
\end{aligned} \tag{2.9}$$

where $P^{\mathrm{lin}}_{\delta\delta}$ is the linear matter power spectrum, b_{h} is the linear bias (taken from the model of Sheth et al., 1999), and $\hat{u}_\kappa(k|M,z)$ is the Fourier transform of the matter halo density profile, i.e., $\rho_{\mathrm{h}}(\vec{x}|M,z)/\bar{\rho}_{DM}$. The Fourier transform of the gamma-ray emission profile for dark matter haloes is described by $\hat{v}_{g_{\mathrm{DM}}}(k|M,z)$. For decaying dark matter, $\hat{v}_{g_{\mathrm{DM}}} = \hat{u}_\kappa$, i.e., the emission follows the dark matter density

profile. Conversely, the emission for annihilating dark matter follows the square of the dark matter density profile: $\hat{v}_{g_{\rm DM}}(k|M,z) = \hat{u}_{\rm ann}(k|M,z)/\Delta(z)^2$, where $\hat{u}_{\rm ann}$ is the Fourier transform of the square of the main halo density profile plus its substructure contribution, and $\Delta(z)^2$ is the clumping factor. The mass limits are $M_{\rm min} = 10^{-6}$ M$_\odot$ and $M_{\rm max} = 10^{18}$ M$_\odot$ again.

Astrophysical gamma-ray sources

The cross-correlation of the convergence with astrophysical sources is sourced by the 3D power spectrum

$$\begin{aligned} P^{\rm 1h}_{g_{\rm S}\kappa}(k,z) &= \int_{\mathscr{L}_{\rm min}}^{\mathscr{L}_{\rm max}} {\rm d}\mathscr{L}\, \frac{\Phi(\mathscr{L},z)}{\langle f_{\rm S}\rangle} \frac{{\rm d}F}{{\rm d}E}(\mathscr{L},z)\, \hat{u}_\kappa(k|M(\mathscr{L},z),z)\ , \\ P^{\rm 2h}_{g_{\rm S}\kappa}(k,z) &= \left[\int_{\mathscr{L}_{\rm min}}^{\mathscr{L}_{\rm max}} {\rm d}\mathscr{L}\, b_{\rm S}(\mathscr{L},z)\, \frac{\Phi_i(\mathscr{L},z)}{\langle f_{\rm S}\rangle} \frac{{\rm d}F}{{\rm d}E}(\mathscr{L},z)\right] \\ &\quad \times \left[\int_{M_{\rm min}}^{M_{\rm max}} {\rm d}M\, \frac{{\rm d}n_{\rm h}}{{\rm d}M} b_{\rm h}(M,z) \hat{u}_\kappa(k|M,z)\right] \\ &\quad \times P^{\rm lin}_{\delta\delta}(k,z)\ , \end{aligned} \tag{2.10}$$

where $b_{\rm S}$ is the bias of gamma-ray astrophysical sources with respect to the matter density, for which we adopt $b_{\rm S}(\mathscr{L},z) = b_{\rm h}(M(\mathscr{L},z))$. That is, a source with luminosity $\mathscr{L}$ has the same bias $b_{\rm h}$ as a halo with mass M, with the relation $M(\mathscr{L},z)$ between the mass of the host halo M and the luminosity of the hosted object $\mathscr{L}$ taken from Camera et al. (2015). The mean flux $\langle f_{\rm S}\rangle$ is defined as $\langle f_{\rm S}\rangle = \int {\rm d}\mathscr{L} \frac{{\rm d}F}{{\rm d}E}\Phi$.

2.3 Data

2.3.1 Weak lensing data sets

For this study we combine CFHTLenS[1] and RCSLenS[2] data sets from the Canada France Hawaii Telescope (CFHT) and KiDS[3] from the VLT Survey Telescope (VST), all of which have been optimised for weak lensing analyses. The same photometric redshift and shape measurement algorithms have been used in the analysis of the three surveys. However, there are slight differences in the algorithm implementation and in the shear and photometric redshift calibration, as described in the following subsections.

The sensitivity of the measurement depends inversely on the overlap area between the gamma-ray map and the lensing data, with a weaker dependence on the parameters characterizing the lensing sensitivity, i.e., the galaxy number density and ellipticity dispersion. This is due to the fact that at large scales, sampling variance dominates the contribution of lensing to the covariance and reducing the shape noise does not result in an improvement of the overall covariance. This point is further discussed in Section 2.4.2.

[1] http://www.cfhtlens.org/
[2] http://www.rcslens.org/
[3] http://kids.strw.leidenuniv.nl/

Of the three surveys, only CFHTLenS and KiDS have full photometric redshift coverage. We choose to restrict the tomographic analysis to KiDS, as the much smaller area of CFHTLenS is expected to yield a much lower sensitivity for this measurement. In Section 2.5.2 we find that tomography does not appreciably improve the exclusion limits on the dark matter parameters. We thus do not lose sensitivity by restricting the tomographic analysis to KiDS in this work.

CFHTLenS

CFHTLenS spans a total area of 154 deg^2 from a mosaic of 171 individual MEGACAM pointings, divided into four compact regions (Heymans et al., 2012). Details of the data reduction are described in Erben et al. (2013). The observations in the five bands *ugriz* of the survey allow for the precise measurement of photometric redshifts (Hildebrandt et al., 2012). The shape measurement with LENSFIT is described in detail in Miller et al. (2013). We make use of all fields in the data set as we are not affected by the systematics that lead to field rejections in the cosmic shear analyses (Kilbinger et al., 2013). We correct for the additive shear bias for each galaxy individually, while the multiplicative bias is accounted for on an ensemble basis, as described in Section 2.4.1.

Individual galaxies are selected based on the Bayesian photometric redshift z_B being in the range [0.2, 1.1]. The resulting redshift distribution of the selected galaxies is obtained by stacking the redshift probability distribution function of individual galaxies, weighted by the LENSFIT weight. As a result of the stacking of the individual redshift PDFs, the true redshift distribution leaks outside the z_B selection range. Stacking the redshift PDFs can lead to biased estimates of the true redshift distribution of the source galaxies (Choi et al., 2016) but in light of the large statistical and modelling uncertainties in this analysis these biases can be safely neglected here.

RCSLenS

The RCSLenS data consist of 14 disconnected regions whose combined total area reaches 785 deg^2. A full survey and lensing analysis description is given in Hildebrandt et al. (2016). RCSLenS uses the same LENSFIT version as CFHTLenS but with a different size prior, as galaxy shapes are measured from *i*-band images in CFHTLenS, whereas RCSLenS uses the *r*-band. The additive and multiplicative shear biases are accounted for in the same fashion as in CFHTLenS.

Multi-band photometric information is not available for the whole RCSLenS footprint, therefore we use the redshift distribution estimation technique described in Harnois-Déraps et al. (2016) and Hojjati et al. (2016). Of the three magnitude cuts considered in Hojjati et al. (2016), we choose to select the source galaxies such that $18 < \mathrm{mag_r} < 26$, as this selection yielded the strongest cross-correlation signal in Hojjati et al. (2016). This cut is close to the $18 < \mathrm{mag_r} < 24$ in Harnois-Déraps et al. (2016) but with the faint cutoff determined by the shape measurement algorithm. The redshift distribution is derived from the CFHTLenS-VIPERS sample (Coupon et al., 2015), a UV and IR extension of CFHTLenS. We stack the redshift PDF in the CFHTLenS-VIPERS sample, accounting for the RCSLenS magnitude selection, *r*-band completeness, and galaxy shape measurement (LENSFIT) weights.

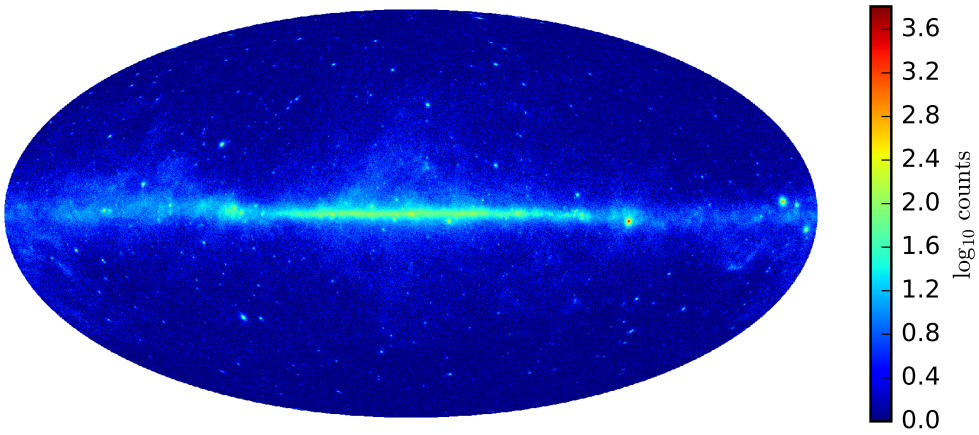

Figure 2.4: Photon count map of the gamma-ray sky for the energy range 0.5–500 GeV for `ultracleanveto` photons.

KiDS

The third data set considered here comes from KiDS, which currently covers 450 deg^2, with complete *ugri* four band photometry in five patches. Galaxy shapes are measured in the *r*-band using the new self-calibrating LENSFIT (Fenech Conti et al., 2017). Cross-correlation studies such as this work are only weakly sensitive to additive biases and, being linear in the shear, are less affected by multiplicative biases than cosmic shear studies. Nonetheless, the analysis still benefits from well-calibrated shape measurements. The residual multiplicative shear bias is accounted for on an ensemble basis, as for CFHTLenS and RCSLenS. To correct for the additive bias we subtract the LENSFIT weighted ellipticity means in each tomographic bin. A full description of the survey and data products is given in Hildebrandt et al. (2017).

We select galaxies with $0.1 \leq z_{\rm B} < 0.9$ and then further split the data into four redshift bins [0.1, 0.3], [0.3, 0.5], [0.5, 0.7], and [0.7, 0.9]. We derive the effective $n(z)$ following the DIR method introduced in Hildebrandt et al. (2017).

2.3.2 Fermi-LAT

For this work we use Fermi-LAT data gathered until 2016 September 1, spanning over eight years of observations. We use Pass 8 event reconstruction and reduce the data using FERMI SCIENCE TOOLS version `v10r0p5`. We select `FRONT+BACK` converting events (`evtype=3`) between energies of 0.5 and 500 GeV. We restrict our main analysis to `ultracleanveto` photons (`evclass=1024`). We verify that selecting `clean` photons (`evclass=256`) does not change the results of the analysis. Furthermore, we apply the cuts `(DATA_QUAL>0)&&(LAT_CONFIG==1)` on the data quality. We then create full sky HEALPIX[4] photon count and exposure maps with `nside=1024` (Górski et al.,

[4] http://healpix.sourceforge.net/

2005) in 20 logarithmically spaced energy bins in the range mentioned above. The photon count map for the whole energy range is shown in Fig. 2.4.

The flux map used in the cross-correlation analysis is obtained by dividing the count maps by the exposure maps in each energy bin before adding them. We have confirmed that the energy spectrum of the individual flux maps follows a broken power law with an index of 2.34 ± 0.02, consistent with that obtained in previous studies of the UGRB (Ackermann et al., 2015d).

We also create maps for four energy bins 0.5–0.766 GeV, 0.766–1.393 GeV, 1.393–3.827 GeV, and 3.827–500 GeV. The bins are chosen such that they would contain equal photon counts for a power law spectrum with index 2.5. The flux maps for the four energy bins are computed by first dividing each energy bin into three logarithmically spaced bins, creating flux maps for these fine bins, and then adding them up.

The total flux is dominated by resolved point sources and, to a lesser extent, by diffuse Galactic emission. To probe the unresolved component of the gamma-ray sky, we mask the 500 brightest point sources in the third Fermi point source catalogue Acero et al. (2015) with circular masks having a radius of two degrees. The remaining point sources are masked with one degree circular masks. We checked that the analysis is robust with respect to other masking strategies. The effect of the diffuse Galactic emission is minimized by subtracting the `gll_iem_v06` model. Furthermore, we employ a 20° cut in Galactic latitude. It has been shown in Shirasaki et al. (2016) that this cross-correlation analysis is robust against the choice made for the model of diffuse Galactic emission. We have confirmed that our results are not significantly affected even in the extreme scenario of not removing the diffuse Galactic emission at all. This represents an important benefit of using cross-correlations to study the UGRB over studies of the energy spectrum alone, as in Ackermann et al. (2015d).

The robustness of these selection and cleaning choices is demonstrated in Fig. 2.6, where the impact of the event selection, point source masks, and cleaning of the diffuse Galactic emission on the cross-correlation signal is shown. None of these choices lead to a significant change in the measured correlation signal, highlighting the attractive feature of cross-correlation analyses that uncorrelated quantities, such as Galactic emissions and extragalactic effects like lensing, do not bias the signal.

The point spread function (PSF) of Fermi-LAT is energy dependent and, especially at low energies, significantly reduces the cross-correlation signal power at small angular scales, as demonstrated in Fig. 2.5. The pixelation of the gamma-ray sky has a similar but much weaker effect. In this analysis, we choose to account for this suppression of power by forward modelling. That is, rather than correcting the measurements, the predicted angular power spectra $C_\ell^{g\kappa}$ are modified to account for the effect of the PSF and pixel window function. The PSF provided by FERMI SCIENCE TOOLS takes into account all our photon selection criteria and is sufficiently accurate for the sensitivity in this analysis.[5]

The gamma-ray data used in the analysis are obtained by cutting out regions around the lensing footprints. To increase the sensitivity at large angular scales, we include an additional four degree wide band around each of the 23 lensing patches.

[5]Systematic uncertainty on the PSF: https://fermi.gsfc.nasa.gov/ssc/data/analysis/LAT_caveats.html

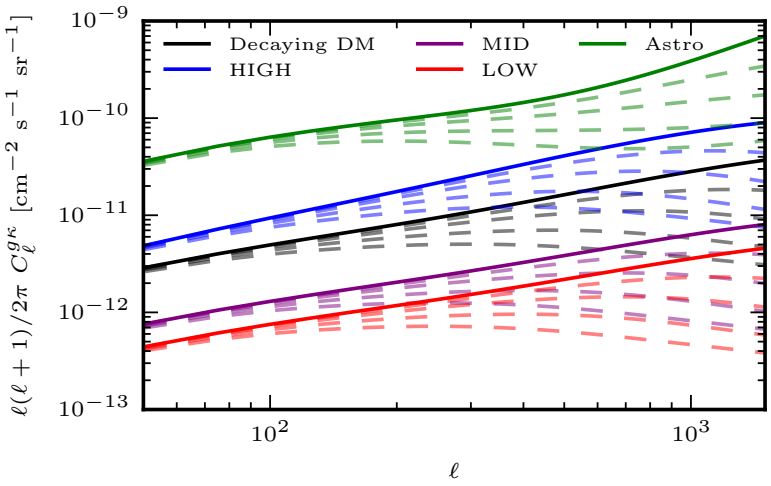

Figure 2.5: Model $C_\ell^{g\kappa}$ for three annihilating dark matter scenarios (HIGH, MID, and LOW), decaying dark matter, and astrophysical sources ('Astro'). The models and formatting are the same as in Figs. 2.1 and 2.3. The models assume the $n(z)$ for the $z \in [0.1, 0.9]$ bin for KiDS and the energy range 0.5–500 GeV. The effect of the Fermi-LAT PSF on the cross-power spectrum is illustrated by dashed lines for the four energy bins, with the lowest energy bin having the strongest suppression of power at small scales.

2.4 Methods

2.4.1 Estimators

To measure the cross-correlation function between gamma rays and lensing, we employ the tangential shear estimator (see also Shirasaki et al., 2014; Harnois-Déraps et al., 2016; Hojjati et al., 2016):

$$\begin{aligned} \hat{\xi}^{g\gamma_{t/x}}(\vartheta) &= \frac{\sum_{ij} w_i e_{ij}^{t/x} g_j \Delta_{ij}(\vartheta)}{\sum_{ij} w_i \Delta_{ij}(\vartheta)} \frac{1}{1+K(\vartheta)} \,, \\ \frac{1}{1+K(\vartheta)} &= \frac{\sum_{ij} w_i \Delta_{ij}(\vartheta)}{\sum_{ij} w_i (1+m_i) \Delta_{ij}(\vartheta)} \,, \end{aligned} \tag{2.11}$$

where the sum runs over all galaxies i and pixels j of the gamma-ray flux map, w_i is the LENSFIT-weight of galaxy i and $e_{ij}^{t/x}$ is the tangential (t) or cross (x) component of the shear with respect to the position of pixel j, g_j is the flux at pixel j, and $\Delta_{ij}(\vartheta)$ accounts for the angular binning, being equal to 1 if the distance between galaxy i and pixel j falls within the angular bin centred on ϑ and 0 otherwise. The factor of $\frac{1}{1+K}$ accounts for the multiplicative shear bias, with m_i being the multiplicative shear bias of galaxy i. We choose to work with the gamma-ray flux instead of its contrast $(g - \langle g \rangle) / \langle g \rangle$, since the mean flux $\langle g \rangle$ would be encumbered by large systematic uncertainties due to to imperfect subtraction of large-scale Galactic emission and leakage of flux from masked resolved point sources.

The $\hat{\xi}^{g\gamma_{t/x}}(\vartheta)$ measurement described in Eq. (2.11) exhibits strong correlation between the angular

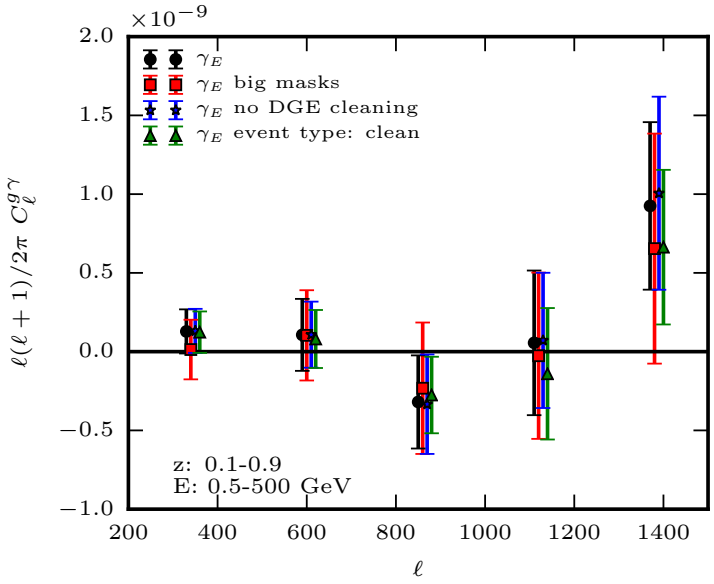

Figure 2.6: Measurement of the cross-spectrum $\hat{C}_\ell^{g\kappa}$ between Fermi-LAT gamma rays in the energy range 0.5–500 GeV and KiDS weak lensing data in the redshift range 0.1–0.9 for different gamma-ray data preparation choices: fiducial, as described in Section 2.3.2 (black points); using two-degree radius circular masks for all point sources (red squares); no cleaning of the diffuse Galactic emission (DGE) (blue stars); and using the `clean` event selection (green triangles).

bins at all scales. This complicates the estimation of the covariance matrix, as the off-diagonal elements have to be estimated accurately. On the other hand, the covariance of the angular cross-power spectrum $\hat{C}_\ell^{g\kappa}$ is largely diagonal since the measurement is noise-dominated. We thus choose to work with the angular power spectrum $\hat{C}_\ell^{g\kappa}$ instead of the correlation function $\hat{\xi}^{g\gamma_t}(\vartheta)$. Inverting the relation in Eq. (2.2), one can construct an estimator for the angular cross-power spectrum $\hat{C}_\ell^{g\kappa}$ based on the measurement of $\hat{\xi}^{g\gamma_t}(\vartheta)$ (Schneider et al., 2002; Szapudi et al., 2001b). Specifically, working in the flat-sky approximation, one can write

$$\hat{C}_\ell^{g\kappa} = 2\pi \int_0^\infty \mathrm{d}\vartheta \; \vartheta J_2(\ell\vartheta)\hat{\xi}^{g\gamma_t}(\vartheta) \; . \tag{2.12}$$

This estimator yields an estimate for the cross-power spectrum between the gamma rays and the E-mode of the shear field. Replacing the tangential shear γ_t in Eq. (2.12) with the cross component of the shear γ_x results in an estimate of the cross-power spectrum between the gamma rays and the B-mode of the shear field, which is expected to vanish in the absence of lensing systematics. In Appendix A.1, we check that this estimator indeed accurately recovers the underlying power spectrum.

To estimate the power spectrum using the estimator in Eq. (2.12), we measure the tangential shear between 1 and 301 arc minutes, in 300 linearly spaced bins. The resulting power spectrum is then

binned in five linearly spaced bins between ℓ of 200 and 1500. At smaller scales the Fermi-LAT PSF suppresses power, especially at low energies. At very large scales of $\ell \lesssim 100$, the covariance is affected by residuals from imperfect foreground subtraction, hence we restrict ourselves to scales of $\ell > 200$.

2.4.2 Covariances

Our primary method to estimate the covariance relies on a Gaussian analytical prescription. This is justified because the covariance is dominated by photon and shape noise, both of which can be modelled accurately. To verify that this analytical prescription is a good estimate of the true covariance, we compare it to two internal covariance estimators that estimate the covariance from the data. In the first approach, we select random patches on the gamma-ray flux map and correlate them with the lensing data, as described in Section 2.4.2. For the second method we randomise the pixels of the gamma-ray flux map within the patches used in the cross-correlation measurement, described in Section 2.4.2. Both of these internal estimators ignore the correlation between gamma rays and lensing, i.e., they implicitly assume that the $C_\ell^{g\kappa}$ term in Eq. (2.13) is zero. Since we do not observe a correlation, this approach is justified.

Unlike an analytical covariance, inverting covariances estimated from a finite number of realizations incurs a bias (Kaufman, 1967; Hartlap et al., 2007; Taylor et al., 2013; Sellentin et al., 2016). The bias is dependent on the number of degrees of freedom in the measurement. Combining measurements of multiple energy or redshift bins increases the size of the measurement vector. Specifically, in the case of no binning in redshift or energy, the data vector here has five elements, when binning in either redshift or energy, it contains 20 elements, and when binning in both redshift and energy, its length is 80. For a fixed number of realizations, the bias therefore changes depending on which data are used in the analysis, diminishing the advantage gained by combining multiple energy or redshift bins and making comparisons between different binning strategies harder. For this reason, we choose the analytical prescription as our primary method to estimate the covariance.

The diagonal elements of the three covariance estimates are shown in Fig. 2.7 for the case of KiDS, showing good agreement between all three approaches. The limits derived from the three covariance estimations agree as well. Choosing the analytical prescription as our primary method is thus justified.

Analytical covariance

We model the covariance $\mathbf{C}$ as

$$\mathbf{C}[C_\ell^{g\kappa}] = \frac{1}{f_{\rm sky}(2\ell+1)\Delta_\ell}\left(\hat{C}_\ell^{gg}\hat{C}_\ell^{\kappa\kappa} + \left(\hat{C}_\ell^{g\kappa}\right)^2\right) , \tag{2.13}$$

where $f_{\rm sky}$ denotes the fraction of the sky that is covered by the effective area of the survey, Δ_ℓ is the ℓ-bin width, $\hat{C}_\ell^{gg}$ is an estimate of the gamma-ray auto-power spectrum, $\hat{C}_\ell^{\kappa\kappa}$ is the convergence auto-power spectrum, and $\hat{C}_\ell^{g\kappa}$ is the cross-spectrum between gamma rays and the convergence, calculated as described in Section 2.2. The effective area for the cross-correlation is given by the product of the masks of the gamma-ray map and lensing data, which corresponds to 99, 308, and 362 deg^2 for CFHTLenS,

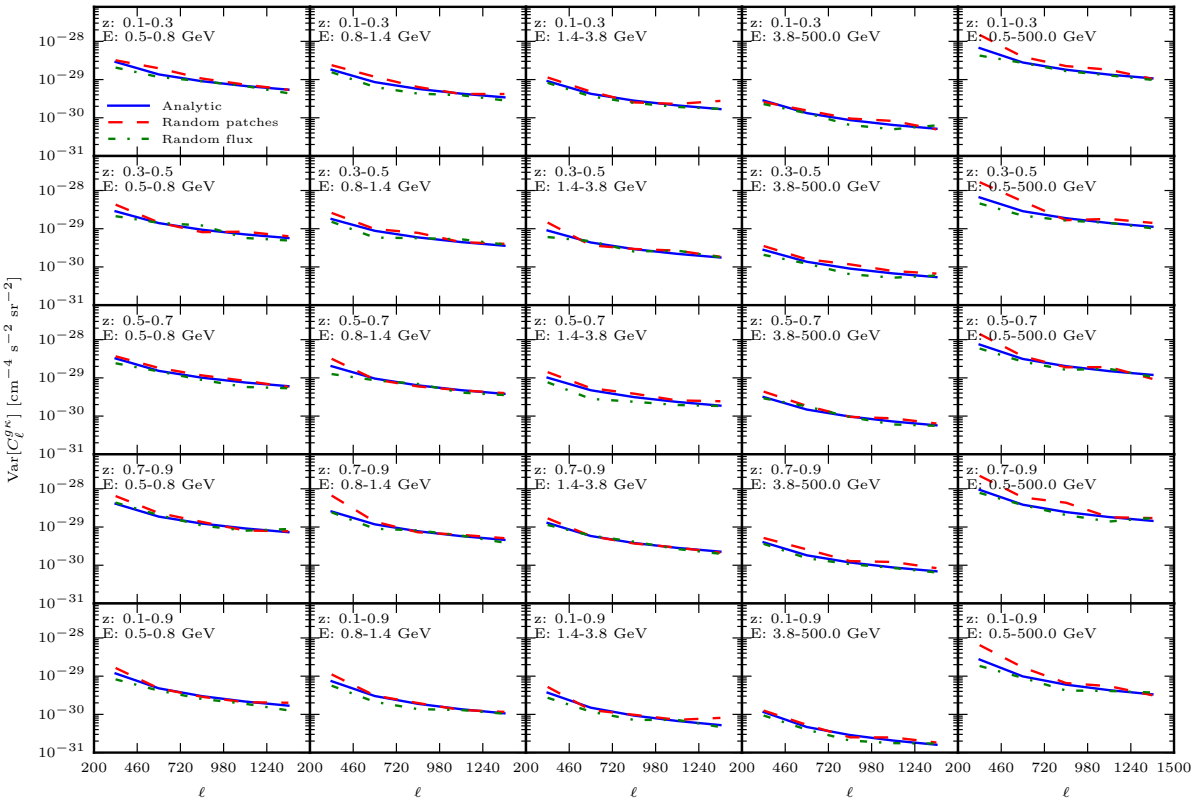

Figure 2.7: Diagonal elements of the analytical covariance (solid blue), covariance from random patches (dashed red), and covariance from randomized flux (dot-dashed green) for the five energy and redshift bins for KiDS. All three estimates agree at small scales, while the covariance derived from random patches shows a slight excess of variance at large scales.

RCSLenS, and KiDS, respectively.

The gamma-ray auto-power spectrum $\hat{C}_\ell^{gg}$ is estimated from the same gamma-ray flux maps as used in the cross-correlation. We measure the auto-spectra of the five energy bins and the cross-spectra between the energy bins using POLSPICE[6] in 15 logarithmically spaced ℓ-bins between ℓ of 30 and 2000. Because the measurement is very noisy at large scales, we fit the measured spectra with a spectrum of the form

$$\hat{C}_\ell^{gg} = C_\mathrm{P} + c\,\ell^\alpha\,, \tag{2.14}$$

where C_P is the Poisson noise term, and c and α describe a power-law contribution to account for a possible increase of power at very large scales. The values of the intercept c is consistent with zero in all cases, while best-fitting Poisson noise terms are consistent with a direct estimate based on the mean

[6] http://www2.iap.fr/users/hivon/software/PolSpice/

Table 2.1: Total number of galaxies with shape measurements $n_{\rm gal}$, effective galaxy number density $n_{\rm eff}$, and ellipticity dispersion $\sigma_{\rm e}$ for CFHTLenS, RCSLenS, and KiDS for the cuts employed in this analysis. We follow the prescription in Heymans et al. (2012) to calculate $n_{\rm eff}$ and $\sigma_{\rm e}$.

	$n_{\rm gal}$	$n_{\rm eff}$ [arcmin^{-2}]	$\sigma_{\rm e}$
CFHTLenS	4760606	9.44	0.279
RCSLenS	14490842	5.84	0.277
KiDS $0.1 \leq z_{\rm B} < 0.3$	3769174	2.23	0.290
KiDS $0.3 \leq z_{\rm B} < 0.5$	3249574	2.03	0.282
KiDS $0.5 \leq z_{\rm B} < 0.7$	2941861	1.81	0.273
KiDS $0.7 \leq z_{\rm B} < 0.9$	2640577	1.49	0.276
KiDS $0.1 \leq z_{\rm B} < 0.9$	12601186	7.54	0.281

number of photon counts, i.e.,

$$C_{\rm P} = \frac{\langle n_{\rm g}/\varepsilon^2 \rangle}{\Omega_{\rm pix}} \,, \tag{2.15}$$

where $n_{\rm g}$ is the number of observed photons per pixel, ε the exposure per pixel, and $\Omega_{\rm pix}$ the solid angle covered by each pixel (Fornasa et al., 2016). Except for the lowest energies, the observed intrinsic angular auto-power spectrum is sub-dominant to the photon shot noise (Fornasa et al., 2016).

The lensing auto-power spectrum is given by

$$\hat{C}_\ell^{\kappa\kappa} = C_\ell^{\kappa\kappa} + \frac{\sigma_{\rm e}^2}{n_{\rm eff}} \,, \tag{2.16}$$

where $C_\ell^{\kappa\kappa}$ is the cosmic shear signal and $\frac{\sigma_{\rm e}^2}{n_{\rm eff}}$ is the shape noise term, with $\sigma_{\rm e}^2$ being the dispersion per ellipticity component and $n_{\rm eff}$ the galaxy number density. These parameters are listed in Table 2.1. The cosmic shear term $C_\ell^{\kappa\kappa}$ is calculated using the halo-model. The two terms in Eq. (2.16) are of similar magnitude, with the shape noise dominating at small scales and sampling variance dominating at large scales. Decreasing $\sigma_{\rm e}$ or increasing $n_{\rm eff}$ thus only improves the covariance at scales where the shape noise makes a significant contribution to Eq. (2.16). However, increasing the area of the lensing survey and thus the overlap with the gamma-ray map directly decreases the covariance inversely proportional to the overlap area. For this reason CFHTLenS has a low sensitivity in this analysis, even though it is the deepest survey of the three. Although RCSLenS has the largest effective area, the covariance for KiDS is slightly smaller, since the increase in depth is large enough to overcome the area advantage of RCSLenS.

Random patches

We select 100 random patches from the gamma-ray map as an approximation of independent realizations of the gamma-ray sky. The patches match the shape of the original gamma-ray cutouts, i.e., the lensing

footprints plus a four degree wide band, but have their positions and orientations randomised. The patches are chosen such that they do not lie within the Galactic latitude cut.

These random patches are uncorrelated with the lensing data but preserve the auto-correlation of the gamma rays and hence account for sampling variance in the gamma-ray sky, including residuals of the foreground subtraction.

For small patches, the assumption of independence is quite accurate, as the probability of two random patches overlapping is low. Larger patches will correlate to a certain degree. This lack of independence might lead to an underestimation of the covariance. This correlation is minimized by rotating each random patch, making the probability of having two very similar patches low.

The diagonal elements of the resulting covariance are shown in Fig. 2.7. While the agreement with the Gaussian covariance is good at small scales, there is an excess of variance at large scales for some energy and redshift bins. This excess can be explained by a large-scale modulation of the power in the gamma-ray map, which would be sampled by the random patches. This interpretation is consistent with the strong growth of the error bars of the gamma-ray auto-correlation towards large scales. However, the results of the analysis are not affected significantly by this.

Randomized flux

In a further test of the analytical covariance in Eq. (2.13), we randomize the gamma-ray pixel positions within each patch. This preserves the one-point statistics of the flux while destroying any spatial correlations. This approach is similar to the random Poisson realizations used in Shirasaki et al. (2014), but we use the actual one-point distribution of the data themselves instead of assuming a Poisson distribution.

Because the pixel values are not correlated anymore, contributions to the large-scale variance due to imperfect foreground subtraction or leakage of flux from point sources outside of their masks are removed.

The covariance derived from 100 such random flux maps is in good agreement with both the analytical covariance and the covariance estimated from random patches, as shown in Fig. 2.7.

2.4.3 Statistical methods

The likelihood function we employ to find exclusion limits on the annihilation cross-section $\langle\sigma_{\rm ann}v\rangle$ or decay rate $\Gamma_{\rm dec}$ and WIMP mass $m_{\rm DM}$ is given by

$$\mathscr{L}(\vec{\alpha}|\vec{d}) \propto \mathrm{e}^{-\frac{1}{2}\chi^2(\vec{d},\vec{\alpha})} \,, \tag{2.17}$$

with

$$\chi^2(\vec{d},\vec{\alpha}) = \left(\vec{d}-\vec{\mu}(\vec{\alpha})\right)^{\mathrm{T}} \mathbf{C}^{-1} \left(\vec{d}-\vec{\mu}(\vec{\alpha})\right) \,, \tag{2.18}$$

where $\vec{d}$ denotes the data vector, $\vec{\mu}(\vec{\alpha})$ the model vector, $\vec{\alpha}$ the parameters considered in the fit, i.e., either the cross-section $\langle\sigma_{\rm ann}v\rangle$ and the particle mass $m_{\rm DM}$ or the decay rate $\Gamma_{\rm dec}$ and $m_{\rm DM}$. The ampli-

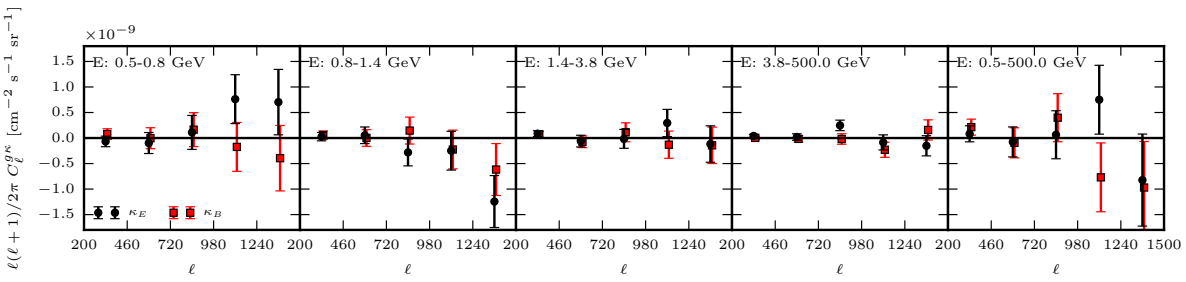

Figure 2.8: Measurement of the cross-spectrum $\hat{C}_\ell^{g\kappa}$ between Fermi-LAT gamma rays and weak lensing data from CFHTLenS for five energy bins for gamma-ray photons (black points). The cross-spectrum of the gamma rays and CFHTLenS B-modes are depicted as red data points.

tude of the cross-correlation signal expected from astrophysical sources is kept fixed and thus does not contribute as an extra free parameter. Finally, $\mathbf{C}^{-1}$ is the inverse of the data covariance.

The limits on $\langle\sigma_{\rm ann}v\rangle$ and $\Gamma_{\rm dec}$ correspond to contours of the likelihood surface described by Eq. (2.17). Specifically, for a given confidence interval p, the contours are given by the set of parameters $\vec{\alpha}_{\rm cont.}$ for which

$$\chi^2(\vec{d},\vec{\alpha}_{\rm cont.}) = \chi^2(\vec{d},\vec{\alpha}_{\rm ML}) + \Delta_{\chi^2}(p)\ , \tag{2.19}$$

where $\vec{\alpha}_{\rm ML}$ is the maximum likelihood estimate of the parameters $\langle\sigma_{\rm ann}v\rangle$ or $\Gamma_{\rm dec}$ and $m_{\rm DM}$, χ^2 is given by Eq. (2.18), and $\Delta_{\chi^2}(p)$ corresponds to the quantile function of the χ^2-distribution. For this analysis we are dealing with two degrees of freedom and require 2σ contours, hence $\Delta_{\chi^2}(0.95) = 6.18$.

This approach to estimate the exclusion limits follows recent studies, such as Shirasaki et al. (2016). It should be noted that deriving the limits on $\langle\sigma_{\rm ann}v\rangle$ or $\Gamma_{\rm dec}$ for a fixed mass $m_{\rm DM}$ is also common in the literature, see e.g., Fornasa et al. (2016) for a recent example. This corresponds to calculating the quantile function $\Delta_{\chi^2}(p)$ for only one degree of freedom.

Care has to be taken when using data-based covariances, such as the random patches and randomized flux, as the inverse of these covariances is biased (Kaufman, 1967; Hartlap et al., 2007). To account for the effect of a finite number of realizations, the Gaussian likelihood in Eq. (2.17) should be replaced by a modified t-distribution (Sellentin et al., 2016). Alternatively, the effect of this bias on the uncertainties of inferred parameter can be approximately corrected (Hartlap et al., 2007; Taylor et al., 2014). In light of the large systematic uncertainties in this analysis we opt for the latter approach when using the data-based covariances.

2.5 Results

2.5.1 Cross-correlation measurements

We present the measurement of the cross-correlation of Fermi-LAT gamma rays with CFHTLenS, RCSLenS, and KiDS weak lensing data in Figs. 2.8, 2.9, and 2.10, respectively. The measurements for

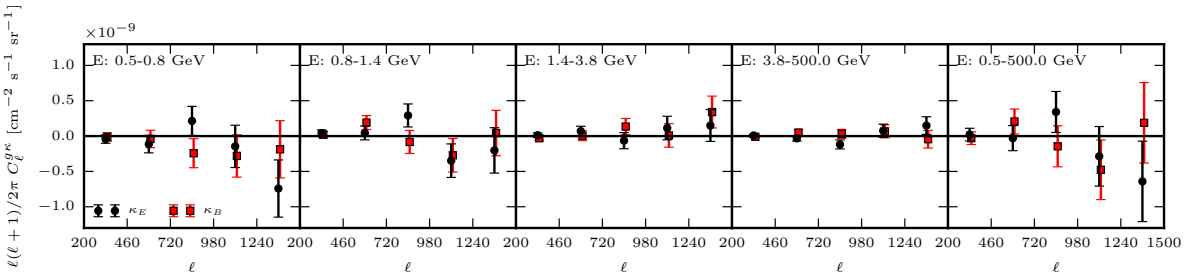

Figure 2.9: Measurement of the cross-spectrum $\hat{C}_\ell^{g\kappa}$ between Fermi-LAT gamma rays and weak lensing data from RCSLenS for five energy bins for gamma-ray photons (black points). The cross-spectrum of the gamma rays and RCSLenS B-modes are depicted as red data points.

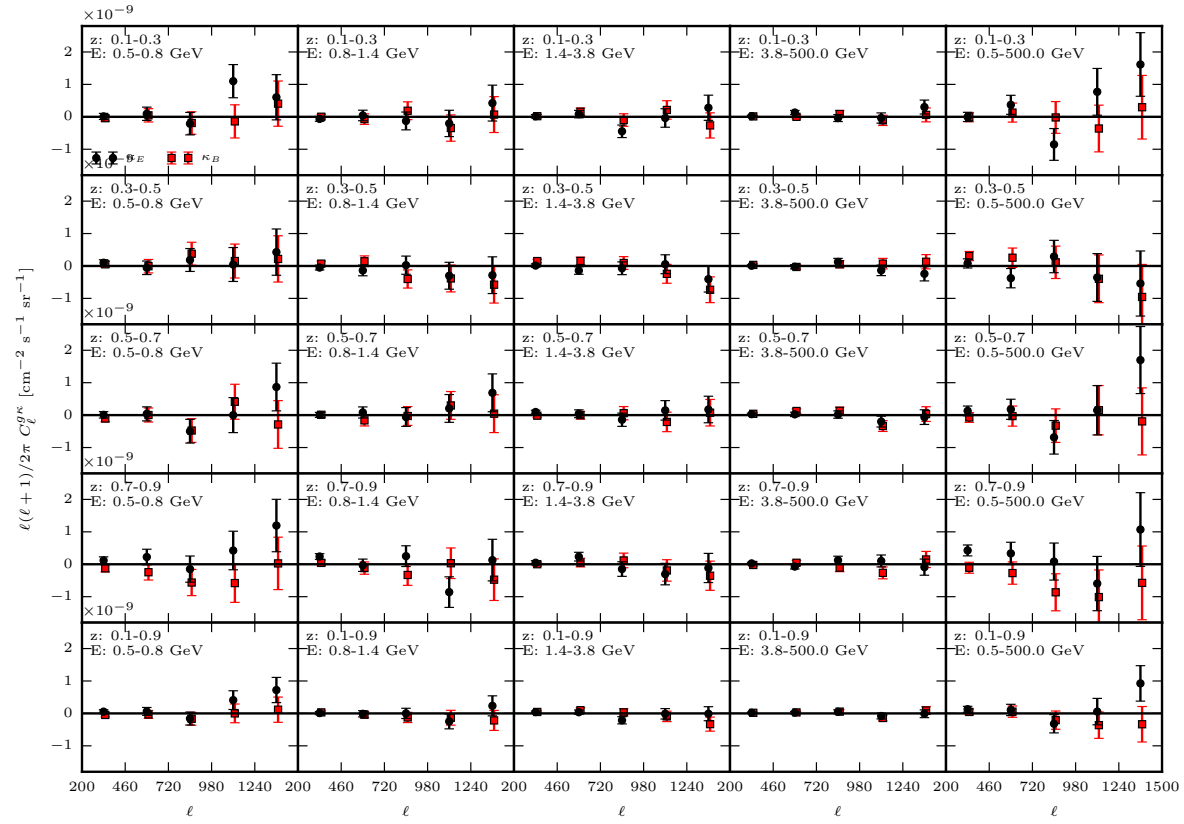

Figure 2.10: Measurement of the cross-spectrum $\hat{C}_\ell^{g\kappa}$ between Fermi-LAT gamma rays and weak lensing data from KiDS for five energy bins for gamma-ray photons and five redshift bins for KiDS galaxies (black points). The cross-spectrum of the gamma rays and KiDS B-modes are depicted as red data points.

Table 2.2: χ_0^2 values with respect to the hypothesis of a null signal for the measurements of $\hat{C}_\ell^{g\kappa}$ shown in Figs. 2.8, 2.9, and 2.10. The number of degrees of freedom is the number of multipole bins, i.e., $\nu = 5$ for all measurements.

	$\chi_0^2\left(\hat{C}_\ell^{g\kappa}, \nu = 5\right)$				
Energy bin [GeV]	0.5–0.8	0.8–1.4	1.4–3.8	3.8–500.0	0.5–500.0
CFHTLenS	4.49	7.77	3.78	8.43	2.43
RCSLenS	6.06	6.75	2.39	6.47	3.19
KiDS $0.1 \leq z_\mathrm{B} < 0.3$	5.96	1.85	6.53	6.89	8.47
KiDS $0.3 \leq z_\mathrm{B} < 0.5$	1.84	1.94	2.75	3.42	2.77
KiDS $0.5 \leq z_\mathrm{B} < 0.7$	3.27	1.89	4.02	2.56	5.57
KiDS $0.7 \leq z_\mathrm{B} < 0.9$	4.82	11.42	4.98	2.88	8.76
KiDS $0.1 \leq z_\mathrm{B} < 0.9$	7.16	1.81	5.42	3.05	6.55

CFHTLenS and RCSLenS use a single redshift bin and the five energy bins described in Section 2.3.2. The measurements for KiDS use the same energy bins but are further divided into the five redshift bins given in Section 2.3.1.

Beside the cross-correlation of the gamma rays and shear due to gravitational lensing (denoted by black circles), we also show the cross-correlation between gamma rays and the B-mode of the shear as red squares. The B-mode of the shear is obtained by rotating the galaxy orientations by 45°, which destroys the gravitational lensing signal. Any significant B-mode signal would be indicative of spurious systematics in the lensing data.

The χ_0^2 values of the measurements with respect to the hypothesis of a null signal, i.e., $\vec{\mu} = 0$, are listed in Table 2.2. The χ_0^2 values are consistent with a non-detection of a cross-correlation for all measurements. This finding is in agreement with the previous studies Shirasaki et al. (2014, 2016) of cross-correlations between gamma rays and galaxy lensing. For a 3 σ detection of the cross-correlation with astrophysical sources,[7] the error bars would have to shrink by a factor of 3 with respect to the current error bars for KiDS. This corresponds to a $\sim$4000 deg^2 survey with KiDS characteristics, comparable in size to the galaxy surveys used in Xia et al. (2015). This is further illustrated in Fig. 2.11, which shows the measurement for KiDS for the unbinned case in comparison with the expected correlation signal from astrophysical sources and annihilating dark matter for the HIGH scenario and $\langle \sigma_\mathrm{ann} v \rangle = 3 \times 10^{-26}$ cm^{3}s^{-1} for $m_\mathrm{DM} = 100$ GeV and the $b\bar{b}$ channel. While these signals are not observable at current sensitivities, they are within reach of upcoming surveys, such as DES.[8]

The B-mode signal is consistent with zero for all measurements. This suggests that the systematics that could introduce B-modes into the measurement are under control. At very small scales, lens-source clustering can cause a suppression of the lensing signal (van Uitert et al., 2011; Hoekstra et al., 2015). The angular scales we are probing in this analysis are however not affected by this.

[7] Cross-correlations between tracers of LSS and gamma rays have already been detected in Xia et al. (2015). A significant signal in the case of future weak lensing surveys is therefore a reasonable expectation.

[8] https://www.darkenergysurvey.org/

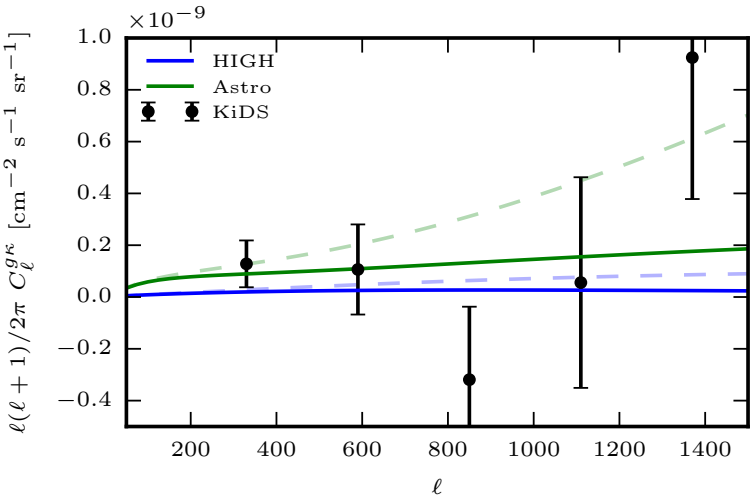

Figure 2.11: Measurement of the cross-spectrum $\hat{C}_\ell^{g\kappa}$ between Fermi-LAT gamma rays in the energy range 0.5–500 GeV and KiDS weak lensing data in the redshift range 0.1–0.9 (black data points), compared to the expected signal from the sum of astrophysical sources ('Astro', solid green) and annihilating dark matter for the HIGH scenario (solid blue). The astrophysical sources considered are blazars, mAGN, and SFGs. The annihilating dark matter model assumes the HIGH scenario, $m_{\rm DM} = 100$ GeV, and $\langle\sigma_{\rm ann}v\rangle = 3\times10^{-26}$ cm^{3}s^{-1}. The dashed lines show the same models but without correcting for the Fermi-LAT PSF.

2.5.2 Interpretation

We wish to exploit the measurements presented in the previous subsection to derive constraints on WIMP dark matter annihilation or decay. To derive the exclusion limits on the annihilation cross-section $\langle\sigma_{\rm ann}v\rangle$ and WIMP mass $m_{\rm DM}$, and the decay rate $\Gamma_{\rm dec}$ and $m_{\rm DM}$, we apply the formalism described in Section 2.4.3.

In Camera et al. (2015) it was shown that the spectral and tomographic information contained within the gamma-ray and lensing data can improve the limits on $\langle\sigma_{\rm ann}v\rangle$ and $\Gamma_{\rm dec}$. We show the effect of different combinations of spectral and tomographic binning for the case of KiDS and annihilations into $b\bar{b}$ pairs under the HIGH scenario in Fig. 2.12 and for dark matter decay in Fig. 2.13. For these limits we adopt the conservative assumption that all gamma rays are sourced by dark matter, i.e., no astrophysical contributions are included. There is a significant improvement of the limits when using four energy bins over a single energy bin, especially at high particle masses $m_{\rm DM}$. This is due to the fact that the UGRB scales roughly as $E^{-2.3}$ (Ackermann et al., 2015a). The vast majority of the photons in the 0.5–500 GeV bin therefore come from low energies. However, the peak in the prompt gamma-ray emission induced by dark matter occurs at energy around $m_{\rm DM}/20$ (annihilating) or $m_{\rm DM}/40$ (decaying) for $b\bar{b}$ and at higher energies for the other channels. Thus, for high $m_{\rm DM}$, a single energy bin of 0.5–500 GeV largely increases the noise without significantly increasing the expected dark matter signal with respect to the 3.8–500 GeV bin.

The improvement due to tomographic binning is only marginal. Two factors contribute to this lack of

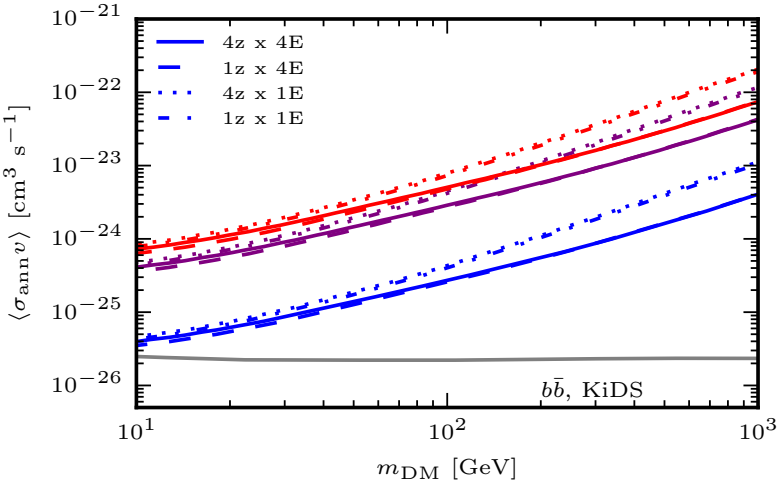

Figure 2.12: Exclusion limits on the annihilation cross-section $\langle\sigma_{\rm ann}v\rangle$ and WIMP mass $m_{\rm DM}$ for the clustering scenarios HIGH (blue), MID (purple), and LOW (red) and for different binning strategies for the KiDS data. The lines correspond to 2σ upper limits on $\langle\sigma_{\rm ann}v\rangle$ and $m_{\rm DM}$, assuming a 100% branching ratio into $b\bar{b}$. No binning in redshift or energy (1z×1E) is denoted by dash-dotted lines. The case of binning in redshift but not energy (4z×1E) is plotted as dotted lines, while binning in energy but not redshift (1z×4E) is plotted as dashed lines. Finally, binning in both redshift and energy (4z×4E) is shown as solid lines. The thermal relic cross-section, from Steigman et al. (2012), is shown in grey.

improvement. Firstly, in the case of no observed correlation signal – as is the case here – the differences in the redshift dependence of the astrophysical and dark matter sources do not come to bear because there is no signal to disentangle. Secondly, the lensing window functions are quite broad and thus insensitive to the featureless window function of the dark matter gamma-ray emissions, as depicted in Fig. 2.1. This is due to the cumulative nature of lensing on the one hand and the fact that photo-z cause the true $n(z)$ to be broader than the redshift cuts we impose on the other hand. This is in contrast with spectral binning, which allows us to sharply probe the characteristic gamma-ray spectrum induced by dark matter. As shown in Fig. 2.3, annihilating dark matter shows a pronounced pion bump when annihilating into $b\bar{b}$ and a cutoff corresponding to the dark matter mass $m_{\rm DM}$, while for decaying dark matter the cutoff appears at half the dark matter mass. For this reason we refrain from a tomographic analysis for CFHTLenS and RCSLenS, as we expect little to no improvements of the limits.

The limits can be further tightened by taking into account known astrophysical sources of gamma rays. This comes, however, at the expense of introducing new uncertainties in the modelling of said astrophysical sources. Going forward, we include the astrophysical sources to show the sensitivity reach of such analyses but also show the conservative limits derived under the assumption that all gamma rays are sourced by dark matter.

To account for the astrophysical sources, we subtract the combination of the three populations (blazars, mAGN, and SFG) described in Section 2.2 from the observed cross-correlation signal. The dark matter limits are then obtained by proceeding as before but using the residuals between the cross-

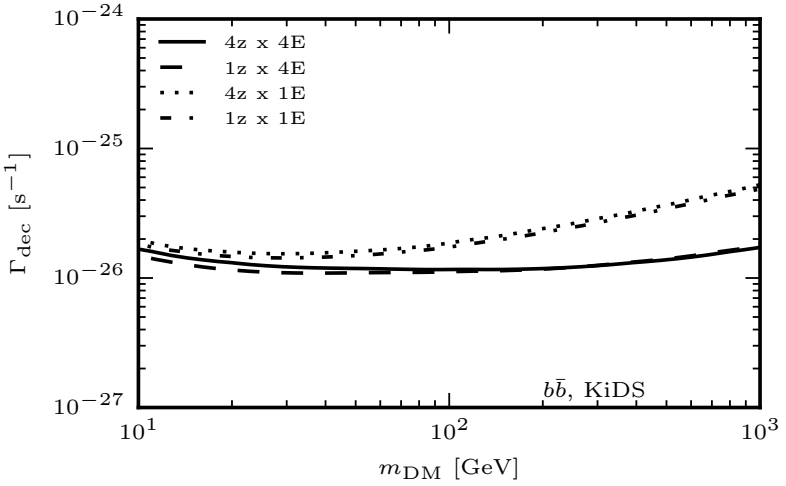

Figure 2.13: Exclusion limits on the decay rate $\Gamma_{\rm dec}$ and WIMP mass $m_{\rm DM}$ for the $b\bar{b}$ channel for different binning strategies for the KiDS data. The style of the lines is analogous to Fig. 2.12.

correlation measurement and the astrophysical contribution. Since we assume no error on the astrophysical models, the limits obtained by including blazars, mAGN, and SFG contributions should be considered as a sensitivity forecast for a future situation where gamma-ray emission from these astrophysical sources will be perfectly understood.

The resulting 2σ exclusion limits on the dark matter annihilation cross-section $\langle\sigma_{\rm ann}v\rangle$ for the $b\bar{b}$, $\mu^-\mu^+$, and $\tau^-\tau^+$ channels are shown in Fig. 2.14. Finally, the combined exclusion limits for CFHTLenS, RCSLenS, and KiDS are shown in Fig. 2.15 and Fig. 2.16 for annihilating and decaying WIMP dark matter, respectively. The exclusion limits for annihilating dark matter should be compared to the thermal relic cross-section (Steigman et al., 2012), shown in grey. Under optimistic assumptions about the clustering of dark matter, i.e., the HIGH model, and accounting for contributions from astrophysical sources (dashed blue line), we can exclude the thermal relic cross-section for masses $m_{\rm DM} \lesssim 20$ GeV for the $b\bar{b}$ channel. In the case of annihilations or decays into muons or tau leptons, the exclusion limits change shape and become stronger for large dark matter masses, compared to the b channel. This is due to the fact that, for heavy dark matter candidates, inverse Compton scattering produces a significant amount of gamma-ray emission in the upper energy range probed by our measurement (Ando et al., 2016). If we make the conservative assumption that only dark matter contributes to the UGRB, i.e., we do not account for the astrophysical sources of gamma rays, the exclusion limits weaken slightly, as seen in the difference between the dashed and solid blue lines in Fig. 2.15. In this case the thermal relic cross-section can be excluded for $m_{\rm DM} \lesssim 10$ GeV for the $b\bar{b}$ channel. These limits are consistent with those forecasted in Camera et al. (2015).

The exclusion limits when dark matter is assumed to be the only contributor to the UGRB are comparable to those derived from the energy spectrum of the UGRB in Ackermann et al. (2015d). However, when the contribution from astrophysical sources is accounted for, the limits in Ackermann

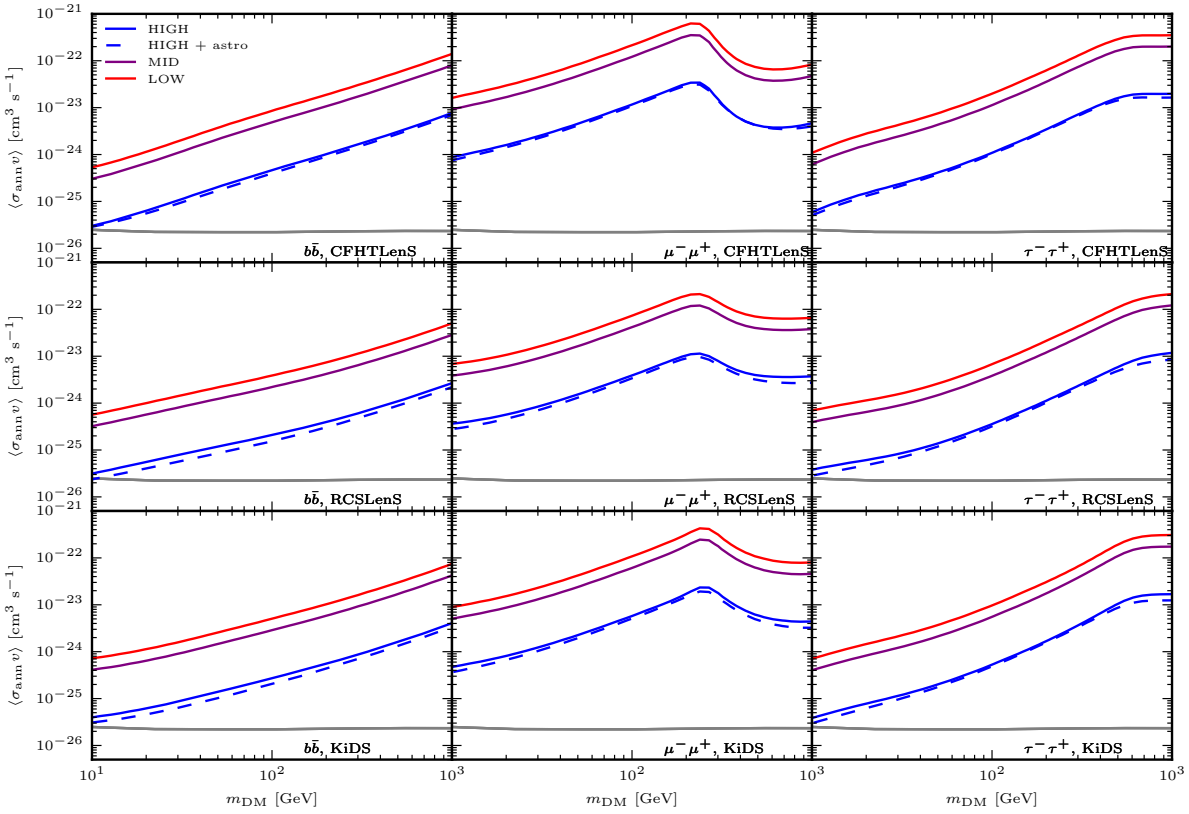

Figure 2.14: Exclusion limits on the annihilation cross-section $\langle\sigma_{\rm ann}v\rangle$ and WIMP mass $m_{\rm DM}$ at 2σ significance for CFHTLenS, RCSLenS, and KiDS and annihilation channels $b\bar{b}$, $\mu^-\mu^+$, and $\tau^-\tau^+$. CFHTLenS and RCSLenS use four energy bins while KiDS additionally makes use of four redshift bins. The exclusion limits are for the three clustering scenarios HIGH (blue), MID (purple), and LOW (red). The dashed blue line indicates the improvement of the limits for the HIGH scenario when including the astrophysical sources in the analysis.

et al. (2015d) improve by approximately one order of magnitude, while our limits see only modest improvements. This is due to the fact that we do not observe a cross-correlation signal. The constraining power therefore largely depends on the size of the error bars. The contribution from astrophysical sources is small compared to the size of our error bars, as shown in Fig. 2.11, explaining the modest gain in constraining power when including the astrophysical sources compared to probes that observe a signal. The exclusion limits obtained in Fornasa et al. (2016) from the measurement of the UGRB angular auto-power spectrum are stronger than the ones presented here. Those limits are dominated by the emission from dark matter subhaloes in the Milky Way, a component that is not considered in our analysis since it does not correlate with weak lensing. When restricting the analysis of the auto-spectrum in Fornasa et al. (2016) to only the extragalactic components, our cross-correlation analysis yields more stringent limits. The limits presented here are comparable to those of similar analyses of the cross-correlation between gamma rays and weak lensing (Shirasaki et al., 2014, 2016) but weaker than those derived from cross-correlations between gamma rays and galaxy surveys (Cuoco et al., 2015;

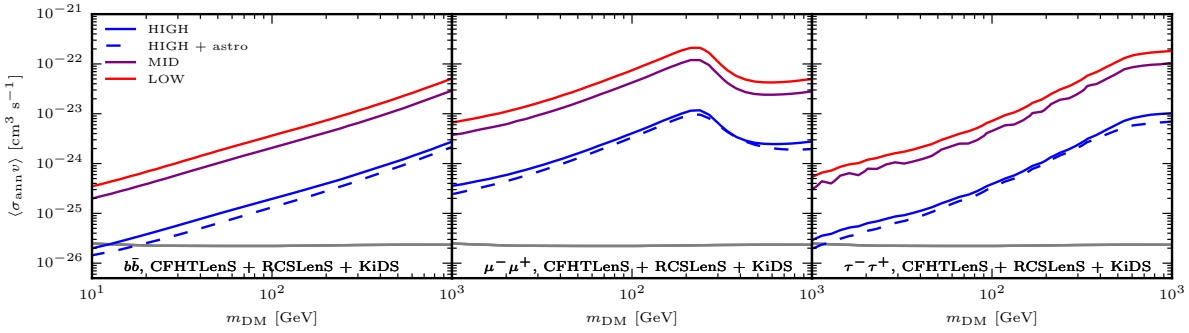

Figure 2.15: Exclusion limits on the annihilation cross-section $\langle\sigma_{\rm ann}v\rangle$ and WIMP mass $m_{\rm DM}$ at 2σ significance for the combination of CFHTLenS, RCSLenS, and KiDS. The style of the lines is the same as for Fig. 2.14.

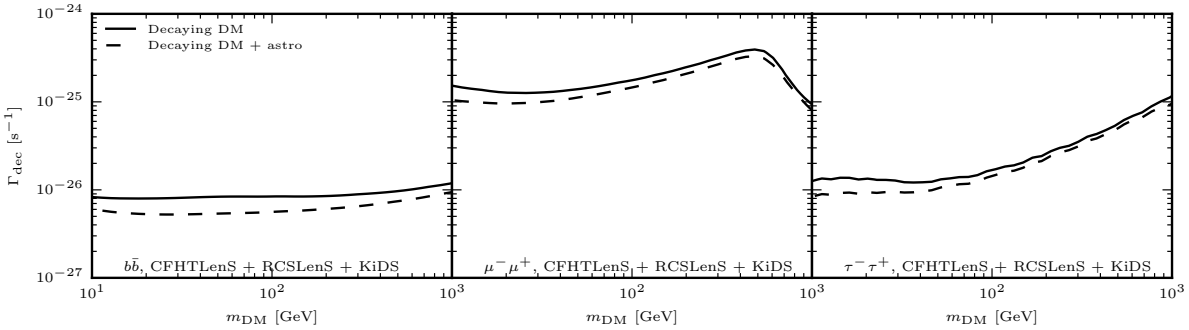

Figure 2.16: Exclusion limits on the decay rate $\Gamma_{\rm dec}$ and WIMP mass $m_{\rm DM}$ at 2σ significance for the combination of CFHTLenS, RCSLenS, and KiDS (solid black). Including the astrophysical sources in the analysis results in the more stringent exclusion limits denoted by the black dashed line.

Regis et al., 2015). The exclusion limits from all these extragalactic probes are somewhat weaker than those derived from dSphs (Ackermann et al., 2015c; Baring et al., 2016).

The weaker limits obtained when using KiDS data, compared to those obtained from RCSLenS data, can be traced to the high data point at small scales in the low energy bins. Restricting the analysis to the ℓ-range of 200 to 1240, i.e., removing the last data point, improves the limits derived from the KiDS to exceed those derived from RCSLenS, as one would expect from the covariances of the two measurements. To check whether the high data point is part of a trend that might become significant at even smaller scales, we extend the measurement to higher ℓ modes. Doing so reveals a high scatter of the data points around zero beyond $\ell \gtrsim 1500$, and no further excess of power at smaller scales. It should be noted that at these small scales, we are probing close to the pixel scale and are within the Fermi-LAT PSF, so the signal is expected to be consistent with zero there. Including astrophysical sources absorbs some of the effect of the high data point at small scales. The limits including astrophysical sources of gamma rays are thus closer to those obtained from RCSLenS than those assuming only dark matter as the source of gamma rays.

2.6 Conclusion

We have measured the angular cross-power spectrum of Fermi-LAT gamma rays and weak gravitational lensing data from CFHTLenS, RCSLenS, and KiDS. Combined together, the three surveys span a total area of more than 1000 deg^2. We made use of eight years of Pass 8 Fermi-LAT data in the energy range 0.5–500 GeV which was divided further into four energy bins. For CFHTLenS and RCSLenS, the measurement was done for a single redshift bin, while the KiDS data were further split into five redshift bins, making this the first measurement of tomographic weak lensing cross-correlation. We find no evidence of a cross-correlation signal in the multipole range $200 \leq \ell < 1500$, consistent with previous studies and forecasts based on the expected signal and current error bars.

Using these measurements we constrain the WIMP dark matter annihilation cross-section $\langle \sigma_{\rm ann} v \rangle$ and decay rate $\Gamma_{\rm dec}$ for WIMP masses between 10 GeV and 1 TeV. Assuming the HIGH model for small-scale clustering of dark matter and accounting for astrophysical sources, we are able to exclude the thermal annihilation cross-section for WIMPs of masses up to 20 GeV for the $b\bar{b}$ channel. Not accounting for the astrophysical contribution weakens the limits only slightly, while the exclusion limits for the more conservative clustering models MID and LOW are a factor of about 10 weaker. We find that tomography does not significantly improve the constraints. However, exploiting the spectral information of the gamma rays strengthens the limits by up to a factor 3 at high masses.

The exclusion limits derived in this work are competitive with others derived from the UGBR, such as its intensity energy spectrum (Ackermann et al., 2015d), auto-power spectrum (Fornasa et al., 2016), cross-correlation with weak lensing (Shirasaki et al., 2014, 2016) or galaxy surveys (Regis et al., 2015; Cuoco et al., 2015). Exclusion limits derived from local probes, such as dSphs, are stronger, however (Ackermann et al., 2015c).

Future avenues to build upon this analysis include the use of upcoming large area lensing data sets, such as future KiDS data, Dark Energy Survey (DES), Hyper Suprime-Cam (HSC)[9], Large Synoptic Survey Telescope (LSST)[10], and Euclid[11], which will make it possible to detect a cross-correlation signal between gamma rays and gravitational lensing. The analysis would also benefit from extending the range of the gamma-ray energies covered, by making use of measurements from atmospheric Cherenkov telescopes, which are more sensitive to high-energy photons (Ripken et al., 2014).

Instead of treating the astrophysical contributions as a contamination to a dark matter signal, the measurements presented in this work could be used to investigate the astrophysical extragalactic gamma-ray populations that are thought to be responsible for the UGRB. We defer this to a future analysis.

[9] http://www.naoj.org/Projects/HSC/
[10] http://www.lsst.org/
[11] http://sci.esa.int/euclid/

Chapter 3

Cross-correlating Planck tSZ with RCSLenS weak lensing: implications for cosmology and AGN feedback

We present measurements of the spatial mapping between (hot) baryons and the total matter in the Universe, via the cross-correlation between the thermal Sunyaev-Zeldovich (tSZ) map from Planck and the weak gravitational lensing maps from the Red Sequence Cluster Survey (RCSLenS). The cross-correlations are performed at the map level where all the sources (including diffuse intergalactic gas) contribute to the signal. We consider two configuration-space correlation function estimators, $\xi^{y-\kappa}$ and $\xi^{y-\gamma_t}$, and a Fourier space estimator, $C_\ell^{y-\kappa}$, in our analysis. We detect a significant correlation out to three degrees of angular separation on the sky. Based on statistical noise only, we can report 13σ and 17σ detections of the cross-correlation using the configuration-space y–κ and y–γ_t estimators, respectively. Including a heuristic estimate of the sampling variance yields a detection significance of 7σ and 8σ, respectively. A similar level of detection is obtained from the Fourier-space estimator, $C_\ell^{y-\kappa}$. As each estimator probes different dynamical ranges, their combination improves the significance of the detection. We compare our measurements with predictions from the cosmo-OWLS suite of cosmological hydrodynamical simulations, where different galaxy feedback models are implemented. We find that a model with considerable AGN feedback that removes large quantities of hot gas from galaxy groups provides the best match to the measurements.

3.1 Introduction

Weak gravitational lensing has matured into a precision tool. The fact that it is insensitive to galaxy bias has made lensing a powerful probe of large-scale structure. However, our lack of a complete understanding of small-scale astrophysical processes has been identified as a major source of uncertainty for the interpretation of the lensing signal. For example, baryonic physics has a significant impact on the matter power spectrum at intermediate and small scales with $k \gtrsim 1h\mathrm{Mpc}^{-1}$ (van Daalen et al., 2011) and ignoring such effects can lead to significant biases in our cosmological inference (Semboloni et al.,

2011; Harnois-Déraps et al., 2015b). On the other hand, if modelled accurately, these effects can be used as a powerful way to probe the role of baryons in structure formation without affecting the ability of lensing to probe cosmological parameters and the dark matter distribution.

One can gain insights into the effects of baryons on the total mass distribution by studying the cross-correlation of weak lensing with baryonic probes. In this way, one can acquire information that is otherwise inaccessible, or very difficult to obtain, from the lensing or baryon probes individually. Cross-correlation measurements also have the advantage that they are immune to residual systematics that do not correlate with the respective signals. This enables the clean extraction of information from different probes.

Recent detections of the cross-correlation between the tSZ signal and gravitational lensing has already revealed interesting insights about the evolution of the density and temperature of baryons around galaxies and clusters. van Waerbeke et al. (2014) found a 6 σ detection of the cross-correlation between the galaxy lensing convergence, κ, from the Canada-France-Hawaii Telescope Lensing Survey (CFHTLenS) and the tSZ signal (y) from Planck. Further theoretical investigations using the halo model (Ma et al., 2015) and hydrodynamical simulations (Hojjati et al. 2015; Battaglia et al. 2015) demonstrated that about 20% of the cross-correlation signal arises from low-mass haloes $M_{\rm halo} \leq 10^{14}{\rm M}_{\odot}$, and that about a third of the signal originates from the diffuse gas beyond the virial radius of haloes. While the majority of the signal comes from a small fraction of baryons within haloes, about half of all baryons reside outside haloes and are too cool ($T \sim 10^5$ K) to contribute to the measured signal significantly. We also note that Hill et al. (2014) presented a correlation between weak lensing of the CMB (as opposed to background galaxies) and the tSZ with a similar significance of detection, whose signal is dominated by higher-redshift ($z > 2$) sources than the galaxy lensing-tSZ signal.

The galaxy lensing-tSZ cross-correlation studies described above were limited. In van Waerbeke et al. (2014), for example, statistical uncertainty dominates due to the relatively small area of the CFHTLenS survey ($\sim$150 deg^2). The tSZ maps were constructed from the first release of the Planck data. And finally, the theoretical modelling of the cross-correlation signal was not as reliable for comparison with data as it is today.

In this chapter, we use the Red Cluster Survey Lensing (RCSLenS) data (Hildebrandt et al., 2016) and the recently released tSZ maps by the Planck team (Planck Collaboration XXII, 2016). RCSLenS covers an effective area of approximately 560 deg^2, which is roughly four times the area covered by CFHTLenS (although the RCSLenS data is somewhat shallower). Combined with the high-quality tSZ maps from Planck, we demonstrate a significant improvement in our measurement uncertainties compared to the previous measurements in van Waerbeke et al. (2014). In this chapter, we also utilize an estimator of lensing mass-tSZ correlations where the tangential shear is used in place of the convergence. As discussed in Section 3.2.1, this estimator avoids introducing potential systematic errors to the measurements during the mass map making process and we also show that it leads to an improvement in the detection significance.

We compare our measurements to the predictions from the cosmo-OWLS suite of cosmological hydrodynamical simulations for a wide range of baryon feedback models. We show that models with

considerable AGN feedback reproduce our measurements best when a WMAP-7yr cosmology is employed. Interestingly, we find that all of the models over-predict the observed signal when a Planck cosmology is adopted. In addition, we also compare our measurements to predictions from the halo model with the baryonic gas pressure modelled using the so-called 'universal pressure profile' (UPP). We find consistency in the cosmological conclusions drawn from the halo model approach with that deduced from comparisons to the hydrodynamical simulations.

The organization of the chapter is as follows. We present the theoretical background and the data in Section 3.2. The measurements are presented in Section 3.3 and the covariance matrix reconstruction is described in Section 3.4. The implication of our measurements for cosmology and baryonic physics are described in Section 3.5 and we summarize in Section 3.6.

3.2 Observational data and theoretical models

3.2.1 Cross-correlation

Formalism

We work with two lensing quantities in this chapter, the gravitational lensing convergence, κ, and the tangential shear, γ_t. The convergence, $\kappa(\vec{\theta})$ is given by

$$\kappa(\vec{\theta}) = \int_0^{w_{\rm H}} {\rm d}w\, W^{\kappa}(w)\, \delta_{\rm m}(\vec{\theta} f_K(w), w)\ , \tag{3.1}$$

where $\vec{\theta}$ is the position on the sky, $w(z)$ is the comoving radial distance to redshift z, $w_{\rm H}$ is the distance to the horizon, and $W^{\kappa}(w)$ is the lensing kernel (van Waerbeke et al., 2014),

$$W^{\kappa}(w) = \frac{3}{2}\Omega_{\rm m}\left(\frac{H_0}{c}\right)^2 g(w)\,\frac{f_K(w)}{a}\ , \tag{3.2}$$

with $\delta_{\rm m}(\vec{\theta} f_K(w), w)$ representing the 3D mass density contrast, $f_K(w)$ is the angular diameter distance at comoving distance w, and the function $g(w)$ depends on the source redshift distribution $n(w)$ as

$$g(w) = \int_w^{w_{\rm H}} {\rm d}w'\, n(w')\,\frac{f_K(w'-w)}{f_K(w')}\ , \tag{3.3}$$

where we choose the following normalization for $n(w)$:

$$\int_0^{\infty} {\rm d}w'\, n(w') = 1. \tag{3.4}$$

The tSZ signal is due to the inverse Compton scattering of CMB photons off hot electrons along the line-of-sight which results in a frequency-dependent variation in the CMB temperature (Sunyaev et al., 1970),

$$\frac{\Delta T}{T_0} = y\, S_{\rm SZ}(x), \tag{3.5}$$

where $S_{\rm SZ}(x) = x\coth(x/2) - 4$ is the tSZ spectral dependence, given in terms of $x = h\nu/k_{\rm B}T_0$. Here h is the Planck constant and should not be confused with the parametrization of the Hubble rate H_0, $k_{\rm B}$ is the Boltzmann constant, and $T_0 = 2.725$ K is the CMB temperature. The quantity of interest in the calculations here is the Comptonization parameter, y, given by the line-of-sight integral of the electron pressure:

$$y(\vec{\theta}) = \int_0^{w_{\rm H}} a\,{\rm d}w\,\frac{k_{\rm B}\sigma_{\rm T}}{m_{\rm e}c^2}\,n_{\rm e}T_{\rm e}, \tag{3.6}$$

where $\sigma_{\rm T}$ is the Thomson cross-section, $k_{\rm B}$ is the Boltzmann constant, and $n_{\rm e}[\vec{\theta}f_K(w), w]$ and $T_{\rm e}[\vec{\theta}f_K(w), w]$ are the 3D electron number density and temperature, respectively.

The first estimator of the tSZ-lensing cross-correlation that we use for the analysis in this chapter is the configuration-space two-point cross-correlation function, $\xi^{y-\kappa}(\vartheta)$:

$$\xi^{y-\kappa}(\vartheta) = \sum_\ell \left(\frac{2\ell+1}{4\pi}\right) C_\ell^{y-\kappa} P_\ell(\cos(\vartheta))\, b_\ell^y b_\ell^\kappa, \tag{3.7}$$

where P_ℓ are the Legendre polynomials. Note that ϑ represents the angular separation and should not be confused with the sky coordinate $\vec{\theta}$. The y–κ angular cross-power spectrum is

$$C_\ell^{y-\kappa} = \frac{1}{2\ell+1}\sum_m y_{\ell m}\kappa_{\ell m}^*, \tag{3.8}$$

where $y_{\ell m}$ and $\kappa_{\ell m}$ are the spherical harmonic transforms of the y and κ maps, respectively (see Ma et al. 2015 for details), and b_ℓ^y and b_ℓ^κ are the smoothing kernels of the y and κ maps, respectively. Note that we ignore higher-order lensing corrections to our cross-correlation estimator. It was shown in Tröster et al. (2014, Chapter 4) that corrections due to the Born approximation, lens-lens coupling, and higher-order reduced shear estimations have a negligible contribution to our measurement signal. We also ignore relativistic corrections to the tSZ signal.

Another estimator of lensing-tSZ correlations is constructed using the tangential shear, γ_t, which is defined as

$$\gamma_t(\vec{\theta}) = -\gamma_1\cos(2\phi) - \gamma_2\sin(2\phi), \tag{3.9}$$

where (γ_1,γ_2) are the shear components relative to Cartesian coordinates, $\vec{\theta} = [\vartheta\ \cos(\phi), \vartheta\ \sin(\phi)]$ where ϕ is the polar angle of $\vec{\theta}$ with respect to the coordinate system. In the flat sky approximation, the Fourier transform of γ_t can be written in terms of the Fourier transform of the convergence as (Jeong et al., 2009):

$$\gamma_t(\vec{\theta}) = -\int \frac{d^2l}{(2\pi)^2}\kappa(\vec{l})\cos[2(\phi-\varphi)]e^{il\theta\cos(\phi-\varphi)}. \tag{3.10}$$

where φ is the angle between $\vec{l}$ and the cartesian coordinate system. We use the above expression to derive the y–γ_t cross-correlation function as

$$\xi^{y-\gamma_t}(\vartheta) = \langle y\ \gamma_t\rangle(\vartheta) = \int_0^{2\pi}\frac{d\phi}{2\pi}\int\frac{d^2l}{(2\pi)^2}C_l^{y-\kappa}\cos[2(\phi-\varphi)]e^{il\vartheta\cos(\phi-\varphi)}. \tag{3.11}$$

Note that the correlation function that we have introduced in Eq. 3.11 differs from what is commonly used in galaxy-galaxy lensing studies, where the average shear profile of haloes $\langle \gamma_t \rangle$ is measured. Here, we take every point in the y map, compute the corresponding tangential shear from every galaxy at angular separation ϑ in the shear catalogue and then take the average (instead of computing the signal around identified haloes). Working with the shear directly in this way, instead of convergence, has the advantage that we skip the mass map reconstruction process and any noise and systematic issues that might be introduced during the process. We have successfully applied similar estimators previously to compute the cross-correlation of galaxy lensing with CMB lensing in Harnois-Déraps et al. (2016). In principle, this estimator can be used for cross-correlations with any other scalar quantity.

Fourier-space versus configuration-space analysis

In addition to the configuration-space analysis described above, we also study the cross-correlation in the Fourier space. A configuration-space analysis has the advantage that there are no complications introduced by the presence of masks, which significantly simplifies the analysis. As described in Harnois-Déraps et al. (2016), a Fourier analysis requires extra considerations to account for the impact of several factors, including the convolution of the mask power spectrum and mode-mixing. On the other hand, a Fourier space analysis can be useful in distinguishing between different physical effects at different scales (e.g., the impact of baryon physics and AGN feedback). We choose a forward modelling approach as described in Harnois-Déraps et al. (2016) and discussed further in Section 3.3.

3.2.2 Observational data

RCSLenS lensing maps

The Red Sequence Cluster Lensing Survey (Hildebrandt et al., 2016) is part of the second Red-sequence Cluster Survey (RCS2; Gilbank et al. (2011)).[1] Data were acquired from the MegaCAM camera from 14 separate fields and covers a total area of 785 deg^2 on the sky. The pipeline used to process RCSLenS data includes a reduction algorithm (Erben et al., 2013), followed by photometric redshift estimation (Hildebrandt et al., 2012; Benítez, 2000) and a shape measurement algorithm (Miller et al., 2013). For a complete description see Heymans et al. (2012) and Hildebrandt et al. (2016).

For some of the RCSLenS fields the photometric information is incomplete, so we use external data to estimate the galaxy source redshift distribution, $n(z)$. The CFHTLenS-VIPERS photometric sample is used which contains near-UV and near-IR data combined with the CFHTLenS photometric sample and is calibrated against 60'000 spectroscopic redshifts (Coupon et al., 2015). The source redshift distribution, $n(z)$, is then obtained by stacking the posterior distribution function of the CFHTLenS-VIPERS galaxies with predefined magnitude cuts and applying the following fitting function (using the

[1] The RCSLenS data are public and can be found at: www.rcslens.org

procedure outlined in Section 3.1.2 of Harnois-Déraps et al. (2016)):

$$n_{\rm RCSLenS}(z) = a\,z\,\exp\left[\frac{-(z-b)^2}{c^2}\right] + d\,z\,\exp\left[\frac{-(z-e)^2}{f^2}\right] + g\,z\,\exp\left[\frac{-(z-h)^2}{i^2}\right]. \quad (3.12)$$

As described in the Appendix B.1, we experimented with several different magnitude cuts to find the range where the SNR for our measurements is maximized. We find that selecting galaxies with $\mathrm{mag_r} > 18$ yields the highest SNR with the best-fit values of (a,b,c,d,e,f,g,h,i) = (2.94, −0.44, 1.03, 1.58, 0.40, 0.25, 0.38, 0.81, 0.12). This cut leaves us with approximately 10 million galaxies from the 14 RCSLenS fields, yielding an effective galaxy number density of $\bar{n} = 5.8$ gal/arcmin^2 and an ellipticity dispersion of $\sigma_\epsilon = 0.277$ (see Heymans et al. (2012) for details).

Fig. 3.1 shows the source redshift distributions $n(z)$ for the three different magnitude cuts we have examined. The double-bump structure in $n(z)$ for the 18–24 and > 18 $\mathrm{mag_r}$ selection is due to the interplay of the galaxy selection function and the shapes of the posterior redshift distribution function of the CFHTLenS-VIPERS galaxies. Note that the lensing signal is most sensitive in the redshift range approximately half way between the sources and the observer. RCSLenS is shallower than the CFHTLenS (see the analysis in van Waerbeke et al., 2013) but, as we demonstrate later, the larger area coverage of RCSLenS (more than) compensates for the lower number density of the source galaxies, in terms of the measurement of the cross-correlation with the tSZ signal.

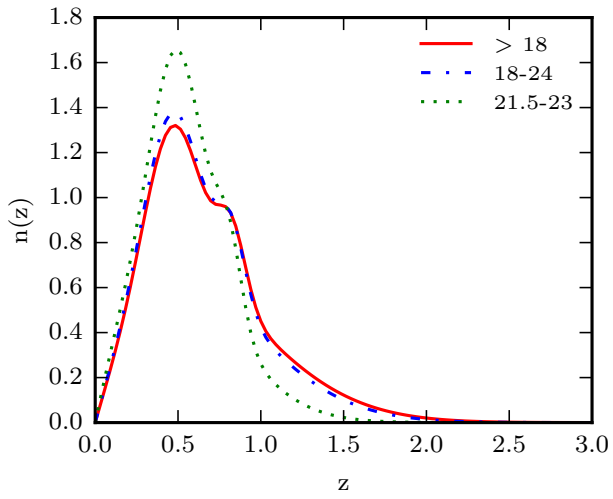

Figure 3.1: Redshift distribution, $n(z)$, of the RCSLenS sources for different r-magnitude cuts. We work with the $\mathrm{mag_r} > 18$ cut (which includes all the objects in the survey).

For our analysis we use the shear data as well as the reconstructed projected mass maps (convergence maps) from RCSLenS. For the tSZ-tangential shear cross-correlation (y–γ_t), we work at the

catalogue level where each pixel in the y map is correlated with the average tangential shear from the corresponding shear data in an annular bin around that point, as described in Section 3.3.1. To construct the convergence maps, we follow the method described in van Waerbeke et al. (2013). In Appendix B.1 we study the impact of map smoothing on the signal to noise ratio (SNR) we determine for the y–κ cross-correlation analysis. We demonstrate that the best SNR is obtained when the maps are smoothed with a kernel that roughly matches the beam scale of the corresponding y maps from Planck survey (FWHM = 10 arcmin).

The noise properties of the constructed maps are studied in detail in Appendix B.2.

Planck tSZ y maps

For the cross-correlation with the tSZ signal, we use the full sky maps provided in the Planck 2015 public data release (Planck Collaboration XXII, 2016). We use the `MILCA` map that has been constructed from multiple frequency channels of the survey. Since we are using the public data from the Planck collaboration, there is no significant processing involved. Our map preparation procedure is limited to masking the map and cutting the patches matching the RCSLenS footprint.

Note that in performing the cross-correlations we are limited by the footprint area of the lensing surveys. In the case of RCSLenS, we have 14 separate compact patches with different sizes. In contrast, the tSZ y maps are full-sky (except for masked regions). We therefore have the flexibility to cut out larger regions around the RCSLenS fields, in order to provide a larger cross-correlation area that helps suppress the statistical noise, leading to an improvement in the SNR. We cut out y maps so that there is complete overlap with RCSLenS up to the largest angular separation in our cross-correlation measurements.

Templates have also been released by the Planck collaboration to remove various contaminating sources. We use their templates to mask Galactic emission and point sources, which amounts to removing about 40% of the sky. We have compared our cross-correlation measurements with and without the templates and checked that our signal is robust. We have also separately checked that the masking of point sources has a negligible impact on our cross-correlation signal (see Appendix B.1). These sources of contamination do not bias our cross-correlation signal and contribute only to the noise level.

In addition to using the tSZ map from the Planck collaboration, we have also tested our cross-correlation results with the maps made independently following the procedure described in van Waerbeke et al. (2014), where several full-sky y maps were constructed from the second release of Planck CMB maps. To construct the maps, a linear combination of the four HFI frequency band maps (100, 143, 217, and 353 GHz) were used and smoothed with a Gaussian beam profile with $\theta_{\rm SZ,FWHM} = 10$ arcmin. To combine the band maps, band coefficients were chosen such that the primary CMB signal is removed, and the dust emission with a spectral index $\beta_{\rm d}$ is nulled. A range of models with different $\beta_{\rm d}$ values were employed to construct a set of y maps that were used as diagnostics of residual contamination. The resulting cross-correlation measurements vary by roughly 10% between the different y maps, but are consistent within the errors with the measurements from the public Planck map.

3.2.3 Theoretical models

We compare our measurements with theoretical predictions based on the halo model and from full cosmological hydrodynamical simulations. Below we describe the important aspects of these models.

Halo model

We use the halo model description for the tSZ - lensing cross-correlation developed in Ma et al. (2015). In the framework of the halo model as introduced in Chapter 1, the y–κ cross-correlation power spectrum is:

$$C_\ell^{y-\kappa} = C_\ell^{y-\kappa,1\mathrm{h}} + C_\ell^{y-\kappa,2\mathrm{h}}, \tag{3.13}$$

where the 1-halo and 2-halo terms are defined as

$$\begin{aligned} C_\ell^{y-\kappa,1\mathrm{h}} &= \int_0^{z_{\max}} \mathrm{d}z \frac{\mathrm{d}V}{\mathrm{d}z\mathrm{d}\Omega} \int_{M_{\min}}^{M_{\max}} \mathrm{d}M \frac{\mathrm{d}n}{\mathrm{d}M} y_\ell(M,z)\, \kappa_\ell(M,z), \\ C_\ell^{y-\kappa,2\mathrm{h}} &= \int_0^{z_{\max}} \mathrm{d}z \frac{\mathrm{d}V}{\mathrm{d}z\mathrm{d}\Omega} P_{\mathrm{m}}^{\mathrm{lin}}(k=\ell/\chi,z) \\ &\times \left[\int_{M_{\min}}^{M_{\max}} \mathrm{d}M \frac{\mathrm{d}n}{\mathrm{d}M} b(M,z) \kappa_\ell(M,z)\right] \\ &\times \left[\int_{M_{\min}}^{M_{\max}} \mathrm{d}M \frac{\mathrm{d}n}{\mathrm{d}M} b(M,z) y_\ell(M,z)\right]. \end{aligned} \tag{3.14}$$

In the above equations $P_{\mathrm{m}}^{\mathrm{lin}}(k,z)$ is the 3D linear matter power spectrum at redshift z, $\kappa_\ell(M,z)$ is the Fourier transform of the convergence profile of a single halo of mass M at redshift z with the NFW profile:

$$\kappa_\ell = \frac{W^\kappa(z)}{\chi^2(z)} \frac{1}{\bar{\rho}_{\mathrm{m}}} \int_0^{r_{\mathrm{vir}}} \mathrm{d}r (4\pi r^2) \frac{\sin(\ell r/\chi)}{\ell r/\chi} \rho(r;M,z), \tag{3.15}$$

and $y_\ell(M,z)$ is the Fourier transform of the projected gas pressure profile of a single halo:

$$y_\ell = \frac{4\pi r_{\mathrm{s}}}{\ell_{\mathrm{s}}^2} \frac{\sigma_{\mathrm{T}}}{m_{\mathrm{e}}c^2} \int_0^\infty \mathrm{d}x x^2 \frac{\sin(\ell x/\ell_s)}{\ell x/\ell_s} P_{\mathrm{e}}(x;M,z). \tag{3.16}$$

Here $x \equiv a(z) r/r_{\mathrm{s}}$ and $\ell_{\mathrm{s}} = a\chi/r_{\mathrm{s}}$, where r_{s} is the scale radius of the 3D pressure profile, and P_{e} is the 3D electron pressure. The ratio $r_{\mathrm{vir}}/r_{\mathrm{s}}$ is the concentration parameter (see e.g Ma et al. (2015) for details).

For the electron pressure of the gas in haloes, we adopt the so-called 'universal pressure profile' (UPP; Arnaud et al. 2010):

$$\begin{aligned} P(x \equiv r/R_{500}) &= 1.65 \times 10^{-3} E(z)^{\frac{8}{3}} \left(\frac{M_{500}}{3\times 10^{14} h_{70}^{-1} \mathrm{M}_\odot}\right)^{\frac{2}{3}+0.12} \\ &\times \mathbb{P}(x)\, h_{70}^2 \ \left[\mathrm{keV\ cm^{-3}}\right], \end{aligned} \tag{3.17}$$

Table 3.1: Sub-grid physics of the baryon feedback models in the cosmo-OWLS runs. Each model has been run adopting both the WMAP-7yr and Planck cosmologies.

Simulation	UV/X-ray background	Cooling	Star formation	SN feedback	AGN feedback	$\Delta T_{\rm heat}$
NOCOOL	Yes	No	No	No	No	...
REF	Yes	Yes	Yes	Yes	No	...
AGN 8.0	Yes	Yes	Yes	Yes	Yes	$10^{8.0}$ K
AGN 8.5	Yes	Yes	Yes	Yes	Yes	$10^{8.5}$ K
AGN 8.7	Yes	Yes	Yes	Yes	Yes	$10^{8.7}$ K

where $\mathbb{P}(x)$ is the generalized NFW model (Nagai et al., 2007):

$$\mathbb{P}(x) = \frac{P_0}{(c_{500}x)^{\gamma}[1+(c_{500}x)^{\alpha}]^{(\beta-\gamma)/\alpha}}. \tag{3.18}$$

We use the best-fit parameter values from Planck Collaboration Int. V (2013): $\{P_0, c_{500}, \alpha, \beta, \gamma\} = \{6.41, 1.81, 1.33, 4.13, 0.31\}$. Since we ultimately only fit for a single amplitude parameter $A_{\rm tSZ}$ (defined in Eq. 3.24), we choose not to marginalise over the individual UPP parameters but instead fix them to the values provided in Planck Collaboration Int. V (2013). To compute the configuration-space correlation functions, we use Eqs. 3.7 and 3.11 for $\xi^{y-\kappa}$ and $\xi^{y-\gamma_t}$, respectively. We present the halo model predictions for two sets of cosmological parameters: the maximum-likelihood Planck 2013 cosmology (Planck Collaboration XVI, 2014) and the maximum-likelihood WMAP-7yr cosmology (Komatsu et al., 2011) with $\{\Omega_{\rm m}, \Omega_{\rm b}, \Omega_{\Lambda}, \sigma_8, n_{\rm s}, h\}$ = 0.3175, 0.0490, 0.6825, 0.834, 0.9624, 0.6711 and $\{$0.272, 0.0455, 0.728, 0.81, 0.967, 0.704$\}$, respectively.

There are several factors that have an impact on these predictions; the choice of the gas pressure profile, the adopted cosmological parameters, and the $n(z)$ distribution of sources in the lensing survey. In addition, the hydrostatic mass bias parameter, b (defined as $M_{\rm obs,500} = (1-b)M_{\rm true,500}$), alters the relation between the adopted pressure profile and the true halo mass. Typically, it has been suggested that $1-b \approx 0.8$. Note that the impact of the hydrostatic mass bias in real groups and clusters will be absorbed into our amplitude fitting parameter $A_{\rm tSZ}$.

3.2.4 The cosmo-OWLS hydrodynamical simulations

We also compare our measurements to predictions from the cosmo-OWLS suite of hydrodynamical simulations. In Hojjati et al. (2015) we compared these simulations to measurements using CFHTLenS data and we also demonstrated that high resolution tSZ-lensing cross-correlations have the potential to simultaneously constrain cosmological parameters and baryon physics. Here we build on our previous work and employ the cosmo-OWLS simulations in the modelling of RCSLenS data.

The cosmo-OWLS suite is an extension of the OverWhelmingly Large Simulations project (OWLS; Schaye et al. 2010). The suite consists of box-periodic hydrodynamical simulations with volumes of $(400\ h^{-1}\ {\rm Mpc})^3$ and 1024^3 baryon and dark matter particles. The initial conditions are based on either

the WMAP-7yr or Planck 2013 cosmologies. We quantify the agreement of our measurements with the predictions from each cosmology in Section 3.5 .

We use five different baryon models from the suite as summarized in Table 3.1 and described in detail in Le Brun et al. (2014) and McCarthy et al. (2014) and references therein. NOCOOL is a standard non-radiative ('adiabatic') model. REF is the OWLS reference model and includes sub-grid prescriptions for star formation (Schaye et al., 2008), metal-dependent radiative cooling (Wiersma et al., 2009a), stellar evolution, mass loss, chemical enrichment (Wiersma et al., 2009b), and a kinetic supernova feedback prescription (Dalla Vecchia et al., 2008). The AGN models are built on the REF model and additionally include a prescription for black hole growth and feedback from active galactic nuclei (Booth et al., 2009). The three AGN models differ only in their choice of the key parameter of the AGN feedback model $\Delta T_{\rm heat}$, which is the temperature by which neighbouring gas is raised due to feedback. Increasing the value of $\Delta T_{\rm heat}$ results in more energetic feedback events, and also leads to more bursty feedback, since the black holes must accrete more matter in order to heat neighbouring gas to a higher adiabat.

Following McCarthy et al. (2014), we produce light cones of the simulations by stacking randomly rotated and translated simulation snapshots (redshift slices) along the line-of-sight back to $z = 3$. Note that we use 15 snapshots at fixed redshift intervals between $z = 0$ and $z = 3$ in the construction of the light cones. This ensures a good comoving distance resolution, which is required to capture the evolution of the halo mass function and the tSZ signal. The light cones are used to produce $5^\circ \times 5^\circ$ maps of the y, shear (γ_1, γ_2) and convergence (κ) fields. We construct 10 different light cone realizations for each feedback model and for the two background cosmologies. Note that in the production of the lensing maps we adopt the source redshift distribution, $n(z)$, from the RCSLenS survey to produce a consistent comparison with the observations.

From our previous comparisons to the cross-correlation of CFHTLenS weak lensing data with the initial public Planck data in Hojjati et al. (2015), we found that the data mildly preferred a WMAP-7yr cosmology to the Planck 2013 cosmology. We will revisit this in Section 3.5 in the context of the new RCSLenS data.

3.3 Observed cross-correlation

Below we describe our cross-correlation measurements between tSZ y and galaxy lensing quantities using the configuration-space and Fourier-space estimators described in Section 3.2.1.

3.3.1 Configuration-space analysis

We perform the cross-correlations on the 14 RCSLenS fields. The measurements from the fields converge around the mean values at each bin of angular separation with a scatter that is due to statistical noise and sampling variance. To combine the fields, we take the weighted mean of the field measurements, where the weights are determined by the total LENSFIT weight (see Miller et al. 2013 for technical definitions).

As described earlier, to improve the SNR and suppress statistical noise, we use 'extended' y maps around each RCSLenS field to increase the cross-correlation area. For RCSLenS, we extend our mea-

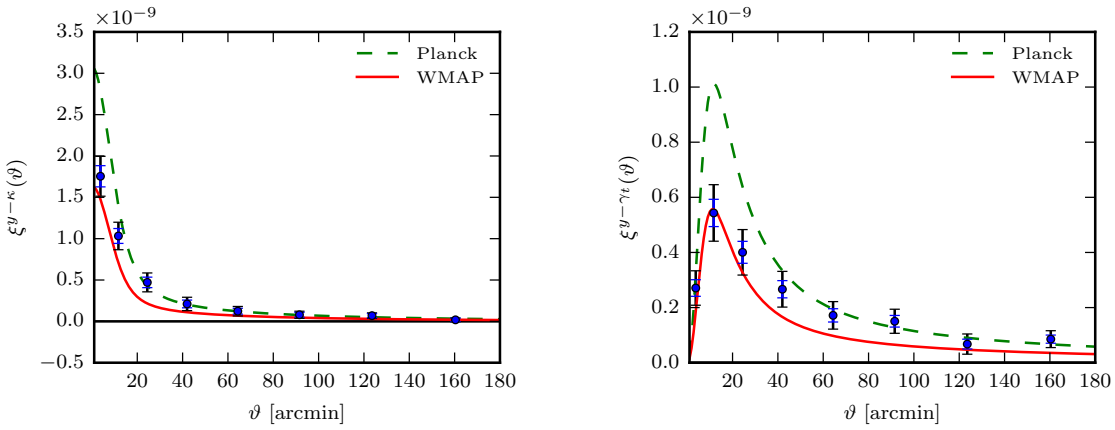

Figure 3.2: Cross-correlation measurements of y–κ (left) and y–γ_t (right) from RCSLenS. The larger (smaller) error bars represent uncertainties after (before) including our estimate of the sampling variance contribution (see Section 3.4). Halo model predictions using UPP with WMAP-7yr and Planck cosmologies are also over-plotted for comparison.

surements to an angular separation of 3°, and hence include 4° wide bands around the RCSLenS fields.

We compute our configuration-space estimators as described below. For y–γ_t, we work at the catalogue level and compute the two-point correlation function as

$$\xi^{y-\gamma_t}(\vartheta) = \frac{\sum_{ij} y^i e_t^{ij} w^j \Delta_{ij}(\vartheta)}{\sum_{ij} w^j \Delta_{ij}(\vartheta)} \frac{1}{1+K(\vartheta)}, \tag{3.19}$$

where y^i is the value of pixel i of the tSZ map, e_t^{ij} is the tangential ellipticity of galaxy j in the catalog with respect to pixel i, and w^j is the LENSFIT weight. The $(1+K(\vartheta))^{-1}$ factor accounts for the multiplicative calibration correction (see Hildebrandt et al. (2016) for details):

$$\frac{1}{1+K(\vartheta)} = \frac{\sum_{ij} w^j \Delta_{ij}(\vartheta)}{\sum_{ij} w^j (1+m^j) \Delta_{ij}(\vartheta)}. \tag{3.20}$$

Finally, $\Delta_{ij}(\vartheta)$ is imposes our binning scheme and is 1 if the angular separation is inside the bin centred at ϑ and zero otherwise.

For the y–κ cross-correlation, we use the corresponding mass maps for each field and compute the correlation function as

$$\xi^{y-\kappa}(\vartheta) = \frac{\sum_{ij} y^i \kappa^j \Delta_{ij}(\vartheta)}{\sum_{ij} \Delta_{ij}(\vartheta)}, \tag{3.21}$$

where κ^j is the convergence value at pixel j and includes the necessary weighting, w^j.

Fig. 3.2 presents our configuration-space measurement of the RCSLenS cross-correlation with Planck tSZ. Our measurements are performed within 8 bins of angular separation, square-root-spaced between 1 and 180 arcmin. That is, the bins are uniformly spaced between $\sqrt{1'}$ and $\sqrt{180'}$. The filled circle data points show the y–κ (left) and y–γ_t (right) cross-correlations. To guide the eye, the solid

red curves and dashed green curves represent the predictions of the halo model for WMAP-7yr and Planck 2013 cosmologies, respectively.

3.3.2 Fourier-space measurements

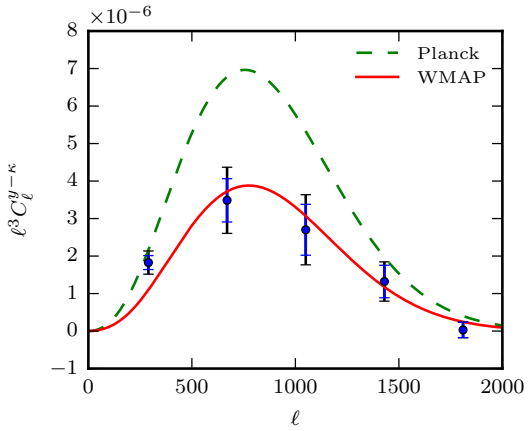

Figure 3.3: Similar to Fig. 3.2 but for Fourier-space estimator, $C_\ell^{y-\kappa}$.

In the Fourier-space analysis, we work with the convergence and tSZ maps. As detailed in Harnois-Déraps et al. (2016), it is important to account for a number of numerical and observational effects when performing the Fourier-space analysis. These effects include data binning, map smoothing, masking, zero-padding and apodization. Failing to take such effects into account will bias the cross-correlation measurements significantly.

Here we adopt the forward modelling approach described in Harnois-Déraps et al. (2016), where theoretical predictions are turned into 'pseudo-C_ℓ', as summarized below. First, we obtain the theoretical C_ℓ predictions from Eqs. (3.13) and (3.14) as described in Section 3.2.3. We then multiply the predictions by a Gaussian smoothing kernel that matches the Gaussian filter used in constructing the κ maps in the mass map making process, and another smoothing kernel that accounts for the beam effect of the Planck satellite.

Next we include the effects of observational masks on our power spectra which breaks down into three components (see Harnois-Déraps et al. (2016) for details): i) an overall downward shift of power due to the masked pixels which can be corrected for with a rescaling by the number of masked pixels; ii) an optional apodization scheme that we apply to the masks to smooth the sharp features introduced in the power spectrum of the masked map that enhance the high-ℓ power spectrum measurements; and iii) a mode mixing matrix, that propagates the effect of mode coupling due to the observational window.

As shown in Harnois-Déraps et al. (2016), steps (ii) and (iii) are not always necessary in the context of cross-correlation when the masks from both maps do not strongly correlate with the data. We have checked that this is indeed the case by measuring the cross-correlation signal from the cosmo-OWLS simulations with and without applying different sections of the RCSLenS masks, with and without apodization, and observed that changes in the results were minor. We therefore choose to remove the

steps (ii) and (iii) from the analysis pipeline. As the last step in our forward modelling, we re-bin the modelled pseudo-C_ℓ so that it matches the binning scheme of the data. Note that these steps have to be calculated separately for each individual field due to their distinct masks.

Fig. 3.3 shows our Fourier-space measurement for the y–κ cross-correlation, where halo model predictions for the WMAP-7yr and Planck cosmologies are also over-plotted. Our Fourier-space measurement is consistent with the configuration-space measurement overall. Namely, the data points provide a better match to WMAP-7yr cosmology prediction on small physical scales (large ℓ modes) and tend to move towards the Planck prediction on large physical scales (small ℓ modes). A more detailed comparison is non-trivial as different scales (ℓ modes) are mixed in the configuration-space measurements.

The details of error estimation and the significance of the detection are described in Section 3.4.

3.4 Estimation of covariance matrices and significance of detection

In this section, we describe the procedure for constructing the covariance matrix and the statistical analysis that we perform to estimate the significance of our measurements. We have investigated several methods for estimating the covariance matrix for the type of cross-correlations performed in this chapter.

3.4.1 Configuration-space covariance

To estimate the covariance matrix we follow the method of van Waerbeke et al. (2013). We first produce 300 random shear catalogues from each of the RCSLenS fields. We create these catalogs by randomly rotating the individual galaxies. This procedure will destroy the underlying lensing signal and create catalogs with pure statistical lensing noise. We then construct the y–γ_t covariance matrix, $\mathbf{C}^{y-\gamma_t}$, by cross-correlating the randomized shear maps for each field with the y map.

To construct the y–κ covariance matrix, we perform our standard mass reconstruction procedure on each of the 300 random shear catalogs to get a set of convergence noise maps. We then compute the covariance matrix by cross-correlating the y maps with these random convergence maps. We follow the same procedure of map making (masking, smoothing, etc.) in the measurements from random maps as we did for the actual measurement. This ensures that our error estimation is representative of the underlying covariance matrix.

Note that we also need to 'debias' the inverse covariance matrix by a debiasing factor as described in Hartlap et al. (2007):

$$\alpha = (n-p-2)/(n-1)\,, \tag{3.22}$$

where p is the number of data bins and n is the number of random maps used in the covariance estimation[2].

The correlation coefficients are shown in Fig. 3.4 for y–κ (left) and y–γ_t (right). As a characteristic of configuration-space, there is a high level of correlation between pairs of data points within each estimator. This is more pronounced for y–κ since the mass map construction is a non-local operation,

[2]In principle we should also implement the treatment of Sellentin et al. (2016), but the precision of our measurement is not high enough to worry about such errors.

and also that the maps are smoothed which creates correlation by definition. Having a lower level of bin-to-bin correlations is another reason why one might want to work with tangential shear measurements rather than mass maps in such cross-correlation studies.

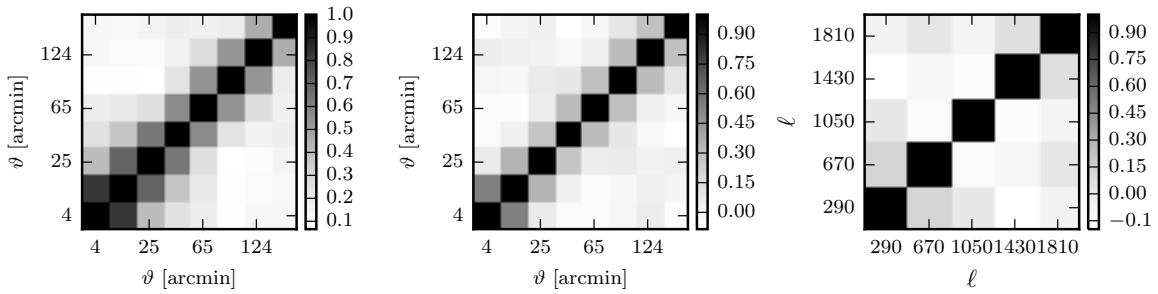

Figure 3.4: Cross-correlation coefficient matrix of the angular bins for the configuration-space $y-\kappa$ (left) and y–γ_t (middle), and the Fourier-space $y-\kappa$ (right) estimators. Angular bins are more correlated for the y–κ estimator compared to y–γ_t or the Fourier-space estimator.

3.4.2 Fourier-space covariance

For the covariance matrix estimation in Fourier space, we follow a similar procedure as in configuration space. We first Fourier transform the random convergence maps, and then follow the same analysis for the measurements (see Section 3.3). The resulting cross-correlation measurements create a large sample that can be used to construct the covariance matrix. Similar to the configuration space analysis, we also debias the computed covariance matrix.

Figure 3.4, right shows the cross-correlation coefficients for the ℓ bins (Note that we chose to work with 5 linearly-spaced bins between $\ell = 100$ and $\ell = 2000$). As expected, there is not much bin-to-bin correlation and the off-diagonal elements are small.

3.4.3 Estimating the contribution from the sampling variance

Constructing the covariance matrix as described above includes the statistical noise contribution only. There is, however, a considerable scatter in the cross-correlation signal between the individual fields. A comparison of the observed scatter to that among different lines of sight (LoS) of the (noise-free) simulations shows that the sampling variance contribution is non-negligible. We therefore need to include the contribution to the covariance matrix from sampling variance.

We are not able, however, to estimate a reliable covariance matrix that includes sampling variance since the number of samples we have access to is very limited and the resulting covariance matrix will be noisy and non-invertible. We only have a small number of fields from the lensing surveys (14 fields from RCSLenS is not nearly enough) and the same is true for the number of LoS maps from hydrodynamical

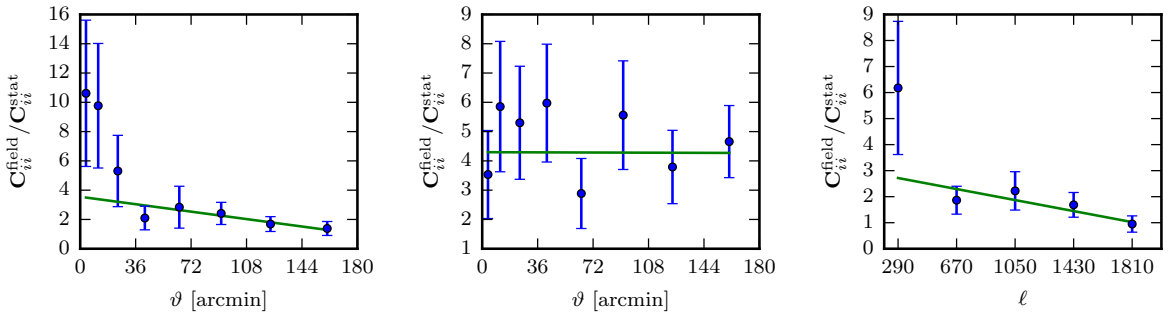

Figure 3.5: Ratios of the variance between the 14 RCSLenS fields and the variance estimated from random shear maps, as described in Sec. 3.4. The best-fitting linear model for the ratios are shown in green.

simulations (10 LoS). Instead, we can estimate the sampling variance contribution by quantifying by how much we need to 'inflate' our errors to account for the impact of sampling variance.

Note that the scatter in the cross-correlation signal from the individual fields is due to both statistical noise and sampling variance. We compare the scatter (or variance) in each angular bin to that of the diagonal elements of the reconstructed covariance matrix that we obtained from the previous section (which quantifies the statistical uncertainty alone). We estimate the scaling factor by which we should inflate the computed covariance matrix to match the observed scatter.

The ratio between the variance between the fields and the statistical covariance is scale-independent for the tangential shear but shows some scale dependence for the other two estimators. We therefore wish to find a simple description of the ratio r_i at some scale i between the field variance and statistical covariance, such that the statistical covariance $\mathbf{C}^{\rm stat}$ can be rescaled as

$$\mathbf{C}_{ij} = \mathbf{C}_{ij}^{\rm stat}\sqrt{r_i r_j}\,. \tag{3.23}$$

We model the ratio r_i as a liner function of the scale. The model is then fit to the observer ratios between the field variances and statistical covariance. The errors on the observed ratios are estimated by taking 1000 bootstrap resamplings of the 14 RCSLenS fields and calculating the ratio from the variance of those resampled fields. The errors are highly correlated themselves but the error covariance is not invertible for the same reason the data covariance of the 14 fields is not invertible; the number of independent fields is too small. The observed ratios and the best-fitting models r_i are shown on Fig. 3.5. We use these best-fitting models to rescale the statistical covariance according to Eq. (3.23) to obtained an estimate of the full covariance.

3.4.4 χ^2 analysis and significance of detection

We quantify the significance of our measurements using the SNR estimator as described below. We assume that the RCSLenS fields are sufficiently separated such that they can be treated as independent, ignoring field-to-field covariance.

Estimator	DoF	$\chi^2_{\rm null}$, stat. err. only	$\chi^2_{\rm null}$, adjusted
$\xi^{y-\kappa}$	8	193.5	56.2
$\xi^{y-\gamma_t}$	8	307.4	71.6
combined	16	328.7	124.2
$C_\ell^{y-\kappa}$	5	156.4	64.9

Table 3.2: Summary of the $\chi^2_{\rm null}$ values before and after including the sampling variance contribution according to the adjustment procedure of Section 3.4.3. There are 8 angular bins, or degrees of freedom (DoF), at which the individual estimators are computed. Combining the estimators increases the DoF accordingly.

First, we introduce the cross-correlation bias factor, $A_{\rm tSZ}$, through:

$$\mathscr{V} = \tilde{\xi} - A_{\rm tSZ}\,\hat{\xi}. \tag{3.24}$$

$A_{\rm tSZ}$ quantifies the difference in amplitude between the measured ($\tilde{\xi}$) and predicted ($\hat{\xi}$) cross-correlation function. The prediction can be from either the halo model or from hydrodynamical simulations. Using $\mathscr{V}$, we define the χ^2 as

$$\chi^2 = \mathscr{V}\mathbf{C}^{-1}\mathscr{V}^T, \tag{3.25}$$

where $\mathbf{C}$ is the covariance matrix.

We define $\chi^2_{\rm null}$ by setting $A_{\rm tSZ} = 0$. In addition, $\chi^2_{\rm min}$ is found by minimizing Eq. (3.25) with respect to $A_{\rm tSZ}$:

$$\chi^2_{\rm null} \quad : \quad A_{\rm tSZ} = 0\,; \tag{3.26}$$

$$\chi^2_{\rm min} \quad : \quad A_{\rm tSZ,min}\,. \tag{3.27}$$

In other words, $\chi^2_{\rm min}$ quantifies the goodness of fit between the measurements and our model prediction after marginalizing over $A_{\rm tSZ}$.

Table 3.2 summarizes the $\chi^2_{\rm null}$ values from the measurements before and after including the sampling variance contribution. The values are quoted for individual estimators as well as when they are combined. The $\chi^2_{\rm null}$ is always higher for y–γ_t estimator, demonstrating that it is a better estimator for our cross-correlation analysis. It also improves when we combine the estimators but we should consider that $\chi^2_{\rm null}$ increases at the expense of adding extra degrees of freedom. Namely, we have eight angular bins for each estimators and combining the two, there are 16 degrees of freedom which introduces a redundancy due to the correlation between the two estimators so that $\chi^2_{\rm null}$ does not increase by a factor of 2.

Finally, we define the SNR as follows. We wish to quantify how strongly we can reject the null hypothesis H_0, that no correlation exists between lensing and tSZ, in favour of the alternative hypothesis H_1, that the cross-correlation is well described by our fiducial model up to a scaling by the cross-

correlation bias $A_{\rm tSZ}$. To this end, we employ a likelihood ratio method. The deviance $\mathscr{D}$ is given by the logarithm of the likelihood ratio between H_0 and H_1:

$$\mathscr{D} = -2\log\frac{\mathscr{L}(\vec{d}|H_0)}{\mathscr{L}(\vec{d}|H_1)}. \tag{3.28}$$

For Gaussian likelihoods, the deviance can then be written as

$$\mathscr{D} = \chi^2_{\rm null} - \chi^2_{\rm min}\ . \tag{3.29}$$

If H_1 can be characterized by a single, linear parameter, $\mathscr{D}$ is distributed as χ^2 with one degree of freedom Williams (2001). The significance in units of standard deviations σ of the rejection of the null hypothesis, i.e., the significance of detection, is therefore given by:

$$\mathrm{SNR} = \sqrt{\chi^2_{\rm null} - \chi^2_{\rm min}}. \tag{3.30}$$

Table 3.3 summarizes the significance analysis of our measurements. We show the SNR and best-fit amplitude $A_{\rm tSZ}$, for the theoretical halo model predictions with WMAP-7yr and Planck cosmologies. The results are presented for each estimator independently as well as for their combination. Note that all the values in Table 3.3 are adjusted to account for the sampling variance, as described in Section 3.4.3. To estimate the combined covariance matrix, we place the covariance for individual estimators as block diagonal elements of combined matrix and compute the off-diagonal blocks (the covariance between the two estimators).

The predictions from WMAP-7yr cosmology are relatively favored in our analysis, which is consistent with the results of previous studies (e.g. McCarthy et al. 2014; Hojjati et al. 2015). We, however, find similar SNR values from both cosmologies because the effect of the different cosmologies on the halo model prediction can be largely accounted for by an overall rescaling ($A_{\rm tSZ}$). After rescaling, the remaining minor differences are due to the shape of the cross-correlation signal so that the SNR depends only weakly on the cosmology.

We obtain a 13.3σ and 16.8σ from y–κ and y–γ_t estimators, respectively, when we only consider the statistical noise in the covariance matrix (before the adjustment prescription of Section 3.4.3) [3].

The 13.3σ significance from y–κ estimator should be compared to the $\sim 6\sigma$ detection from the same estimator in van Waerbeke et al. (2014) where CFHTLenS data are used instead. As expected, RCSLenS yields an improvement in the SNR and y–γ_t improves it further. Including sampling variance in the covariance matrix decreases the detection significance from RCSLenS data to 7.1σ and 8.1σ for the y–κ and y–γ_t estimators, respectively.

We perform a similar analysis in Fourier space where the data vector is given by the pseudo-C_ℓs and the results are included in Table 3.3. The SNR values are in agreement with the configurations-space

[3] Note that we are quoting the detection levels from a statistical noise-only covariance matrix so that we can compare to the previous literature, including the results of van Waerbeke et al. (2014), where a similar approach is taken in the construction of the covariance matrix (i.e. only statistical noise is considered).

Estimator	SNR stat. err. only	SNR adjusted	$A_{\rm tsz}$, WMAP-7yr	$A_{\rm tsz}$, Planck
$\xi^{y-\kappa}$	13.3	7.1	1.18±0.17	0.64±0.09
$\xi^{y-\gamma_t}$	16.8	8.1	1.27±0.16	0.68±0.08
combined	17.1	10.6	1.23±0.12	0.66±0.06
$C_\ell^{y-\kappa}$	11.6	7.5	1.07±0.14	0.60±0.08

Table 3.3: Summary of the statistical analysis of the cross-correlation measurements. For the configuration-space estimators, the results are shown for each estimator independently and when they are combined. SNR quantifies the significance of detection after a fit to model predictions (halo model). SNR values are shown before (SNR, stat. err. only) and after (SNR, adjusted) adjustment for sampling variance uncertainties according to the description of Section 3.4.3, while $A_{\rm tSZ}$ values are quoted after the adjustment. The Planck cosmology predicts higher amplitude than WMAP-7yr cosmology so that overall, the WMAP-7yr cosmology predictions are in better agreement with the measurements.

analysis[4]. We see a similar trend as in the configuration-space analysis in that there is a better agreement with the WMAP-7yr halo model predictions ($A_{\rm tSZ}$ is closer to 1) while the Planck cosmology predicts a high amplitude.

Table 3.3 summarizes the predictions from the halo model framework with a fixed pressure profile for gas (UPP). In Section 3.5, we revisit this by comparing to predictions from hydrodynamical simulations where haloes with different mass and at different redshifts have a variety of gas pressure profiles. We show that we find better agreement with models where AGN feedback is present in haloes.

Impact of maximum angular separation

The two configuration-space estimators we use probe different dynamical scales by definition. This means that as we include cross-correlations at larger angular scales, information is captured at a different rate by the two estimators. For a survey with limited sky coverage, combining the two estimators will therefore improve the SNR of the measurements. In the following, we quantify this improvement of the SNR.

In Fig. 3.6, we plot the SNR values as a function of the maximum angular separation for both estimators. In addition, we also include the same quantities when debiased using Eq.3.22 to highlight the effect of increasing DoF on the debiasing factor. Each angular bin is 10 arcmin wide and adding more bins means including cross-correlation at larger angular scales.

We observe that the y–κ measurement starts off with a higher SNR relative to y–γ_t at small angular separations. The SNR in y–κ levels off very quickly with little information added above 1° separation. The shallow SNR slope of the y–κ curve is partly due to the Gaussian smoothing kernel that is used in reconstructing the mass maps which spreads the signal within the width of the kernel. The y–γ_t cross-correlation, on the other hand, has a higher rate of gain in SNR and catches up with the convergence rapidly. Eventually, the two estimators approach a plateau as the cross correlation signals drops to zero.

[4]Note that the Fourier-space analysis is performed by pipeline 3 in Harnois-Déraps et al. (2016). Different pipelines give slightly different but consistent results.

At that point, both contain the same amount of cross-correlation information.

Note that we limit ourselves to a maximum angular separation of 3 degrees in the RCSLenS measurements since the measurement is very noisy beyond that. Fig. 3.6 indicates that the two estimators might not have converged to the limit where the information is saturated (a plateau in the SNR curve). Since each estimator captures different information up to 3 degrees, combining them improves the measurement significance (see Table 3.3). With surveys like the Kilo-Degree Surveys (KiDS) de Jong et al. (2013a), the Dark Energy Survey (DES) Abbott et al. (2016) and the Hyper Suprime-Cam Survey (HSC) Miyazaki et al. (2012), where the coverage area is larger, we will be able to go to larger angular separations where the information from our estimators is saturated. The signal at such large scales is primarily dependent on cosmology and quite independent of the details of the astrophysical processes inside haloes (see Hojjati et al. 2015 for more details). This could, in principle, provide a new probe of cosmology based on the cross-correlation of baryons and lensing on distinct scales and redshifts.

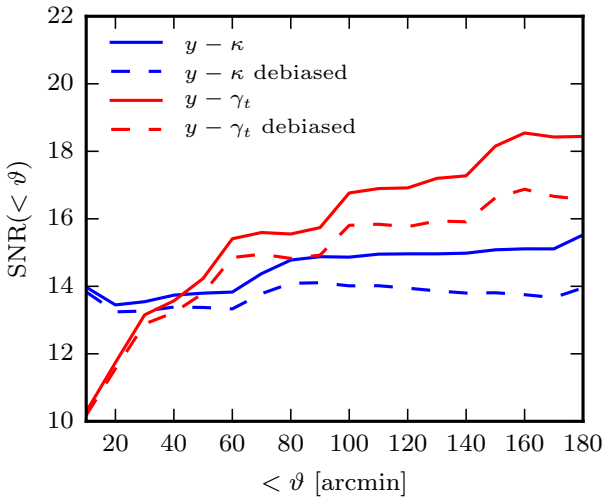

Figure 3.6: SNR as a function of the maximum angular separation for the two configuration-space estimators, with and without debiasing (as described in Sec. 3.4.1). The slope of the lines is different for the two estimators due to the different information they capture as a function of angular separation. For y–κ, most of the signal is in the first few bins making it a better candidate at small scales, while y–γ_t has a larger slope and catches up quickly. Eventually, the two estimators approach a plateau where they contain the same amount of cross-correlation information. Note that the plots show the SNR before the 'adjustment' procedure of Sec. 3.4.3.

3.5 Implications for cosmology and astrophysics

In Section 3.3 we compared our measurements to predictions from the theoretical halo model. The halo model approach, however, has limitations for the type of cross-correlation we are considering. For example, in our analysis we cross-correlate every source in the sky that produces a tSZ signal with every source that produces a lensing signal. A fundamental assumption of the halo model, however,

is that all the mass in the Universe is in spherical haloes, which is not an accurate description of the large-scale structure in the Universe. There are other structures such as filaments, walls or free flowing diffuse gas in the Universe, so that matching them with spherical haloes could lead to biased inference of results (see Hojjati et al. 2015). Another shortcoming is that our halo model analysis considers a fixed pressure profile for diffuse gas, while it has been demonstrated in various studies that the UPP does not necessarily describe the gas around low-mass haloes particularly well (e.g., Battaglia et al. 2012; Le Brun et al. 2015).

Here we employ the cosmo-OWLS suite of cosmological hydrodynamical simulations (see Section 3.2.4) which includes various simulations with different baryonic feedback models. The cosmo-OWLS suite provides a wide range of tSZ and lensing (convergence and shear) maps allowing us to study the impact of baryons on the cross-correlation signal. We follow the same steps as we did with the real data to extract the cross-correlation signal from the simulated maps.

Figure 3.7 compares our measured configuration-space cross-correlation signal to those from simulations with different feedback models. The plots are for the five baryon models using the WMAP-7yr cosmology and the AGN 8.0 model using the Planck cosmology is also plotted for comparison. Note that baryon models make the largest difference at small scales due to mechanisms that change the density and temperature of the gas inside clusters. For the (non-physical) NOCOOL model, the gas can reach very high densities near the centre of dark matter haloes and is very hot since there is no cooling mechanism in place. This leads to a high tSZ and hence a high cross-correlation signal. After including the main baryonic processes in the simulation (e.g. radiative cooling, star formation, SN winds), we see that the signal drops on small scales. Adding AGN feedback warms up the gas but also expels it to larger distances from the centre of haloes. This explains why we see a lower signal at small scales but a higher signal at intermediate scales for the AGN 8.7 model. Note that the scatter of the LoS signal varies for different models due to the details of the baryon processes so that, for example, the AGN 8.7 model creates a larger sampling variance. The mean signal of the feedback models is also affected by the cosmological parameters at all scales. Adopting a Planck cosmology produces a higher signal at all scales and for all models. This is mainly due to the larger values of $\Omega_{\rm b}$, $\Omega_{\rm M}$, and particularly σ_8, in the Planck 2013 cosmology compared to that of the WMAP-7yr cosmology.

We summarize in Table 3.4 our χ^2 analysis for feedback model predictions relative to our measurements. We find that the data prefers a WMAP-7yr cosmology to the Planck 2013 cosmology *for all of the baryon feedback models*. The best-fit models are underlined for both cosmologies.

Our measurements are limited by the relatively low resolution of the Planck tSZ maps. On small scales, our signal is diluted due to the convolution of the tSZ maps with the Planck beam (FWHM = 10 arcmin) which makes it hard to discriminate the feedback models with our configuration-space measurements. This highlights that high-resolution tSZ measurements can be particularly useful to overcome this limitation and open up the opportunity to discriminate the feedback models from tSZ-lensing cross-correlations.

The feedback models could be better discriminated in Fourier-space through their power spectra. We therefore repeat our measurements on the simulation in the Fourier-space. We apply the same procedure

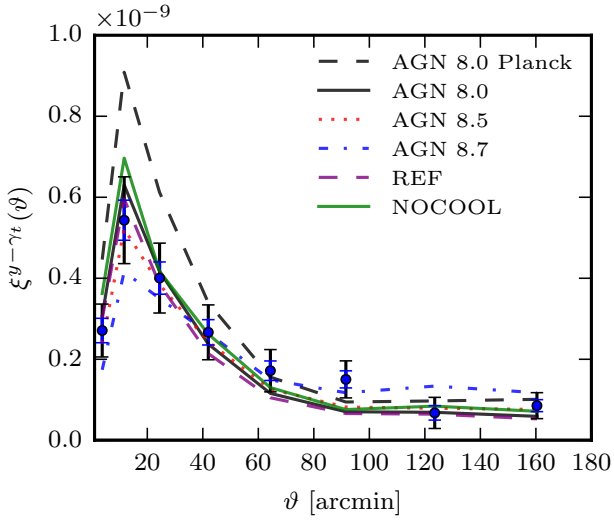

Figure 3.7: Comparisons of our cross-correlation measurement from RCSLenS to predictions from hydrodynamical simulations. The larger (smaller) error bars represent uncertainties after (before) including our estimate of the sampling variance contribution (see Section 3.4). Different baryon feedback models with WMAP-7yr cosmology are shown for y–γ_t estimator (we are not showing the plots for y–κ as they are very similar). Baryon feedback has an impact on the cross-correlation signal at small scales.

described in Section 3.3.2 to the simulated maps. Fig. 3.8 compares our power spectrum measurements to simulation predictions, and we have summarized the χ^2 analysis in Table 3.4.

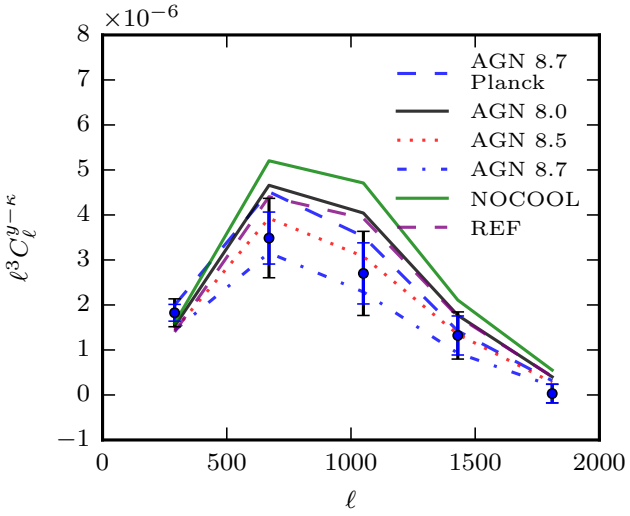

Figure 3.8: Same as Fig. 3.7 for the Fourier-space estimator, $C_\ell^{y-\kappa}$.

Our Fourier-space analysis follows a similar trend as the configuration-space analysis. Namely, there is a general over-prediction of the amplitude, which is worse for the Planck cosmology. For the

	Model	$\chi^2_{\rm min}$ WMAP-7yr	$A_{\rm tsz}$ WMAP-7yr	$\chi^2_{\rm min}$ Planck	$A_{\rm tsz}$ Planck
Config. Space	AGN 8.0	5.3	1.00±0.12	5.4	0.68±0.08
	AGN 8.5	3.2	1.10±0.13	5.9	0.74±0.09
	AGN 8.7	8.6	1.01±0.13	8.3	0.72±0.09
	NOCOOL	5.7	0.89±0.11	6.1	0.62±0.08
	REF	5.7	1.06±0.13	5.8	0.74±0.09
Fourier Space	AGN 8.0	6.1	0.83±0.11	6.5	0.57±0.07
	AGN 8.5	3.3	1.01±0.13	4.0	0.68±0.09
	AGN 8.7	1.4	1.20±0.15	1.7	0.83±0.10
	NOCOOL	8.7	0.72±0.10	8.2	0.50±0.07
	REF	7.2	0.86±0.11	7.2	0.61±0.08

Table 3.4: Summary of $\chi^2_{\rm min}$ analysis of the cross-correlation measurements from hydrodynamical simulations. The error on the best-fit amplitudes are adjusted according to description of Section 3.4.3. The best-fit models are underlined for both cosmologies. The WMAP-7yr predictions fit data better for all baryon models. The AGN 8.5 model is preferred by the configuration space measurements while the Fourier space measurements prefer the AGN 8.7 model.

best-fit WMAP-7yr models the fitted amplitude is consistent with 1. Our estimator prefers the AGN 8.7 model in all cases with a Planck cosmology that is different than configuration-space estimator where the AGN 8.5 was preferred.[5] There are a few reasons for these minor differences. For example, the binning schemes are different and give different weights to bins of angular separation. Furthermore, the Fourier-based result can change by small amounts depending on precisely which pipeline from Harnois-Déraps et al. (2016) is adopted.

When we fit the amplitude $A_{\rm tSZ}$ to obtain the $\chi^2_{\rm min}$ or SNR values, we are in fact factoring out the scaling of the model prediction and are left with the prediction of the shape of the cross-correlation signal. The shape depends on both the cosmological parameters (weakly) and details of the baryon model so that the values in Tables 3.3 and 3.4 are a measure of how well the model shape matches the measurement. By comparing the $\chi^2_{\rm min}$ values from the two cosmologies in Table 3.4, the general conclusion of our analysis is that significant AGN feedback in baryon models is required to match the measurements well. Note, however, that while there are differences in the amplitude (and shape) of the cross-correlation signal, the predictions from the two cosmology are not in tension with the measurements when one considers the current uncertainties in the values of the cosmological parameters (e.g., σ_8).

3.6 Summary and discussion

We have performed cross-correlations of the public Planck 2015 tSZ map with the public weak lensing shear data from the RCSLenS survey. We have demonstrated that such cross-correlation measurements

[5]We tested that if large-scale correlations ($\vartheta > 100$ arcmin), where uncertainties are large, are removed from the analysis, the AGN 8.7 model is also equally preferred by the configuration-space estimators.

between two independent data sets are free from contamination by residual systematics in each data set, allowing us to make an initial assessment of the implications of the measured cross-correlations for cosmology and ICM physics.

Our cross-correlations are performed at the map level where every object is contributing to the signal. In other words, this is not a stacking analysis where measurements are done around identified haloes. Instead, we are probing all the structure in the Universe (haloes, filaments etc) and the associated baryon distribution including diffuse gas in the intergalactic medium.

We performed our analysis using two configuration-space estimators, $\xi^{y-\gamma_t}$ and $\xi^{y-\kappa}$, and a Fourier-space analysis with $C_\ell^{y-\kappa}$ for completeness. Configuration-space estimators have the advantage that they are less affected by the details of map making processes (masks, appodization etc) and the analysis is straightforward. We showed that the estimators probe different dynamical scales so that combining them can improve the SNR of the measurement.

Based only on the estimation of statistical uncertainties, the cross-correlation using RCSLenS data is detected with a significance of 13.3σ and 16.8σ from the y–κ and y–γ_t estimators, respectively. Including a heuristic estimate of the sampling variance reduces the detection to 7.1σ and 8.1σ, respectively. We demonstrated that RCSLenS data improve the SNR of the measurements significantly compared to previous studies where CFHTLenS data were used.

The Fourier-space analysis, while requiring significant processing to account for masking effects, is more useful for probing the impact of physical effects at different scales. We work with $C_\ell^{y-\kappa}$ and test for consistency of the results with the configuration-space estimators. We reach similar conclusions for the $C_\ell^{y-\kappa}$ measurement as the configuration-space counterpart as well as the same level of significance of detection.

The high level of detection compared to similar measurements in van Waerbeke et al. (2014) is due to two main improvements: the larger sky coverage offered by RCSLenS survey has suppressed the statistical uncertainties of the measured signal; and the final tSZ map provided by the Planck team is also less noisy than that used in van Waerbeke et al. (2014).

We have compared our measurements against predictions from the halo model, which adopts the empirically-motivated 'universal pressure profile' to describe the pressure of the hot gas associated with haloes. We highlighted the difficulties in estimating the covariance matrix for the type of cross-correlation measurement we consider in this chapter. Our error analysis includes contributions from both statistical uncertainty and sampling variance. The large sampling variance in the cross-correlation signal originates mainly from the tSZ maps due to the dependence of the tSZ signal on the halo mass, AGN feedback and other stochastic processes. We estimated its contribution from field-to-field variance, but recognize that better estimation requires access to more data or more hydrodynamical simulations. Predictions from a WMAP-7yr best-fit cosmology match the data better than those based on the Planck cosmology, in agreement with previous studies (e.g., McCarthy et al. 2014).

Finally, we employed the cosmo-OWLS hydrodynamical simulations (Le Brun et al., 2014), using synthetic tSZ and weak lensing maps produced for a wide range of baryonic physics models in both the WMAP-7yr and Planck cosmologies. In agreement with the findings of the halo model results,

the comparison to the predictions of the simulations yields a preference for the WMAP-7yr cosmology regardless of which feedback model is adopted. This is noteworthy, given the vast differences in the models in terms of their predictions for the ICM properties of groups and clusters (which bracket the observed hot gas properties of local groups and clusters, see Le Brun et al., 2014). The detailed shape of the measured cross-correlations tend to prefer models that invoke significant feedback from AGN, consistent with what is found from the analysis of observed scaling relations, although there is still some degeneracy between the adopted cosmological parameters and the treatment of feedback physics. Future high-resolution CMB experiments combined with large sky area from a galaxy survey can in principle break the degeneracy between feedback models and place tighter constrains on the model parameters.

We highlighted the difficulties in estimating the covariance matrix for the type of cross-correlation measurement we consider in this chapter. The large sampling variance in the cross-correlation signal, which originates mainly from the tSZ maps, requires access to more data or more hydrodynamical simulations to be accurately estimated. With the limited data we have, the covariance matrix that contained the contribution from sampling variance was noisy, making it impossible to perform a robust significance analysis of the measurements. This is an area where further effort is required and we will pursue this in future work.

Chapter 4

Weak lensing corrections to tSZ-lensing cross-correlation

The cross-correlation between the thermal Sunyaev-Zeldovich (tSZ) effect and gravitational lensing in wide fields has recently been measured. This can be used to probe the distribution of the diffuse gas in large-scale structure, as well as inform us about the missing baryons. As for any lensing-based quantity, higher-order lensing effects can potentially affect the signal. Here, we extend previous higher-order lensing calculations to the case of tSZ-lensing cross-correlations. We derive terms analogous to corrections due to the Born approximation, lens-lens coupling, and reduced shear up to order $\mathscr{O}(\Phi^4)$ in the Newtonian potential. Redshift distortions and vector modes are shown to be negligible at this order. We find that the dominant correction due to the reduced shear exceeds the percent-level only at multipoles of $\ell \gtrsim 3000$.

4.1 Introduction

Even though both the direct detection of dark matter and its microscopic description have proven to be elusive so far, its macroscopic behaviour is thought to be well understood. The large-scale clustering of dark matter has been observed though gravitational lensing and has been found to agree with theoretical predictions; see Bartelmann (2010) for a review and Hildebrandt et al. (2014) for an overview of the recent results with the Canada France Hawaii Telescope Lensing Survey (CFHTLenS). On small scales its clustering behaviour has been modelled with N-body simulations to relatively high precision (e.g., Harnois-Déraps et al., 2015a). Conversely, even though the microscopic behaviour of baryons is fully understood, half of the Universe's baryon content is in a hitherto unobserved state (Fukugita et al., 2004; Bregman, 2007); the 'missing baryon problem'.

A significant fraction of these missing baryons might reside in a warm, low density phase beyond galactic halos (Anderson et al., 2010). By cross-correlating the thermal Sunyaev-Zeldovich (tSZ) effect maps, which traces warm electrons, and mass maps derived from weak gravitational lensing data, there is now observational support for the possibility that a significant fraction of the baryons indeed resides in such a phase (van Waerbeke et al., 2014; Ma et al., 2015; Hill et al., 2014).

Future surveys with large sky coverage (de Jong et al., 2013a; Sánchez et al., 2010) will produce data whose precision warrants a more sophisticated theoretical treatment than has been necessary so far. In this work we investigate the effect of higher-order lensing terms on the tSZ-lensing cross-correlation. There has been considerable effort to characterize higher-order contributions to correlations of lensing observables (Schneider et al., 1998; Cooray et al., 2002; Hirata et al., 2003; Dodelson et al., 2005b, 2006; Shapiro et al., 2006; Shapiro, 2009; Krause et al., 2010; Bernardeau et al., 2010; Vanderveld et al., 2011; Bernardeau et al., 2012; Andrianomena et al., 2014). Some of these higher-order effects, like the rotation power spectrum, have been successfully observed in high-resolution ray-tracing simulations (Hilbert et al., 2009; Becker, 2013). Building on this corpus of previous work, we derive analogous contributions to the tSZ-lensing cross-correlation.

In section 4.2 we introduce the notation and recapitulate the first-order results. In section 4.3 we investigate the higher-order corrections. The terms related to the Born approximation, i.e., the evaluation of the integrals along the unperturbed photon path, and lens-lens coupling are derived in section 4.3.1. The observed quantity in weak gravitational lensing is the reduced shear. Corrections due to the non-linear relation between the shear and the convergence are derived in section 4.3.2. We also consider redshift distortions in section 4.3.3 and vector modes in section 4.3.4 and show that they do not contribute at the order we are considering.

4.2 First order

In the Newtonian gauge the perturbed Robertson-Walker (RW) metric without anisotropic stresses can be written as

$$\mathrm{d}s^2 = a(\eta)^2\left[-(1+2\Phi)\mathrm{d}\eta^2 + (1-2\Phi)\left(\mathrm{d}\chi^2 + f_\mathrm{K}(\chi)^2\mathrm{d}\Omega^2\right)\right] , \tag{4.1}$$

with $f_\mathrm{K}(\chi)$ the comoving angular diameter distance and χ the comoving radial distance. We will henceforth work in units where $c = 1$. The potential Φ is assumed to be small, i.e., $\Phi \ll 1$. The first-order solution to the geodesic deviation equation at a comoving distance χ from the observer is then (Schneider et al., 1992; Schneider et al., 1998; Bartelmann, 2010)

$$x^i(\vec{\theta},\chi) = f_\mathrm{K}(\chi)\theta^i - 2\int_0^\chi \mathrm{d}\chi' f_\mathrm{K}(\chi-\chi')\Phi_{,i}(\vec{x}(\vec{\theta},\chi'),\chi') , \tag{4.2}$$

where $\vec{\theta}$ represents the angle between the perturbed and fiducial ray at the observer. Vector quantities are denoted by lowercase Latin indices and partial derivatives with respect to comoving transverse coordinates, i.e., those perpendicular to the line-of-sight, are denoted by a comma. We make use of the sum convention where repeated indices are summed over. Unless otherwise noted, this sum only includes the two transverse directions. The Jacobi map is defined as the derivative of the deflection angle $\frac{\vec{x}(\vec{\theta},\chi)}{f_\mathrm{K}(\chi)}$ with respect to $\vec{\theta}$, i.e.,

$$\mathscr{A}_{ij}(\vec{\theta},\chi) = \frac{\partial x^i(\vec{\theta},\chi)}{f_\mathrm{K}(\chi)\partial\theta^j} = \delta_{ij} - 2\int_0^\chi \mathrm{d}\chi' \frac{f_\mathrm{K}(\chi-\chi')f_\mathrm{K}(\chi')}{f_\mathrm{K}(\chi)}\Phi_{,ik}(\vec{x}(\vec{\theta},\chi'),\chi')\mathscr{A}_{kj}(\vec{\theta},\chi') . \tag{4.3}$$

It can be expressed in terms of the convergence κ, shear γ_1, γ_2, and rotation ω as

$$\mathscr{A}_{ij} = \begin{pmatrix} 1-\kappa-\gamma_1 & -\gamma_2-\omega \\ -\gamma_2+\omega & 1-\kappa+\gamma_1 \end{pmatrix} = \delta_{ij} - \psi_{ij} \ . \tag{4.4}$$

Here we have introduced the distortion tensor ψ_{ij} as a measure of the deviation from the identity map. The convergence is then given by the trace of the distortion tensor:

$$\kappa = \frac{1}{2}\psi_{ii} \ . \tag{4.5}$$

Using (4.3) and (4.5), we find for the first-order convergence

$$\kappa^{(1)}(\vec{\theta},\chi_s) = \int_0^{\chi_s} \mathrm{d}\chi' K(\chi_s,\chi')\Phi_{,ii}(f_\mathrm{K}(\chi')\vec{\theta},\chi') \ , \tag{4.6}$$

where we have defined the kernel

$$K(\chi_s,\chi') = \frac{f_\mathrm{K}(\chi_s-\chi')f_\mathrm{K}(\chi')}{f_\mathrm{K}(\chi_s)}\Theta(\chi_s-\chi') \ . \tag{4.7}$$

Equation (4.6) describes the convergence due to a single source at a comoving distance $\chi_s = \chi(z_s)$ from the observer. The convergence of a population of sources with redshift distribution $n(z)\mathrm{d}z$ is found by averaging over the sources with $n(z)$ as the weighting factor. One then finds

$$\kappa^{(1)}(\vec{\theta}) = \int_0^\infty \mathrm{d}\chi(z)p(z)\frac{\mathrm{d}z}{\mathrm{d}\chi}\kappa^{(1)}(\vec{\theta},\chi(z)) = \int_0^\infty \mathrm{d}\chi W^\kappa(\chi)\Phi_{,ii}(f_\mathrm{K}(\chi)\vec{\theta},\chi) \ , \tag{4.8}$$

with the kernel given by

$$W^\kappa(\chi) = \int_\chi^\infty \mathrm{d}\chi' p(z)\frac{\mathrm{d}z}{\mathrm{d}\chi'}K(\chi',\chi) \ . \tag{4.9}$$

The tSZ effect involves the inverse Compton scattering of CMB photons off relativistic electrons (Sunyaev et al., 1972). This introduces a frequency dependent temperature shift ΔT in the observed CMB temperature. The temperature shift at position $\vec{\theta}$ on the sky and frequency ν can be parameterized as

$$\frac{\Delta T}{T_0}(\vec{\theta},\nu) = y(\vec{\theta})S_{SZ}(\nu) \ , \tag{4.10}$$

where the Compton $y(\vec{\theta})$ parameter encodes the spatial and $S_{SZ}(\nu)$ the spectral dependence. The Compton y parameter is defined as the line-of-sight integral over the electron pressure. In this work we adapt the constant bias model of van Waerbeke et al. (2014) to simplify the analysis. It has been shown in Ma et al. (2015) that the constant bias model is consistent with a halo model approach, thus justifying the use of the simpler model. For a constant bias, the y parameter can be written as an integral over the

density contrast δ, i.e.,

$$y(\vec{\theta}) = \int_0^{\chi_H} \mathrm{d}\chi \tilde{W}^y(\chi)\delta(\vec{x}(\vec{\theta},\chi),\chi) \,, \tag{4.11}$$

where χ_H is the comoving distance to the surface of last scattering. We express the density contrast in terms of the Newtonian potential through the Poisson equation as

$$y(\vec{\theta}) = \int_0^{\chi_H} \mathrm{d}\chi \tilde{W}^y(\chi)\frac{2a\Delta\Phi(\vec{x}(\vec{\theta},\chi),\chi)}{3H_0^2\Omega_\mathrm{M}} = \int_0^{\chi_H} \mathrm{d}\chi W^y(\chi)\Delta\Phi(\vec{x}(\vec{\theta},\chi),\chi) \,, \tag{4.12}$$

where we have absorbed the factors from the Poisson equation into the new kernel $W^y(\chi)$.

Ultimately, we are interested in the angular cross-power spectrum $C_\ell^{y\kappa}$. In this work we assume that the convergence is derived from shear measurements of galaxy surveys. The sky coverage of these surveys is still relatively small (although this will not be the case of future surveys such as Euclid and LSST) allowing the analysis to proceed in the flat-sky approximation. Using the definition of the 2D Fourier transform (C.2), we can write the angular cross-power spectrum of $\hat{y}(\vec{\ell})$ and $\hat{\kappa}(\vec{\ell})$ as

$$\begin{aligned}\langle \hat{y}^{(1)}(\vec{\ell}_1)\hat{\kappa}^{(1)}(\vec{\ell}_2)\rangle &= (2\pi)^2\delta_\mathrm{D}^2(\vec{\ell}_1+\vec{\ell}_2)C_{\ell_1}^{(2)} \\ &= \int_0^{\chi_H} \mathrm{d}\chi\mathrm{d}\chi' W^y(\chi)W^\kappa(\chi')\frac{|\vec{\ell}_1|^2}{f_\mathrm{K}(\chi)^2}\frac{|\vec{\ell}_2|^2}{f_\mathrm{K}(\chi')^2}\langle\hat{\phi}(\vec{\ell}_1,\chi)\hat{\phi}(\vec{\ell}_2,\chi')\rangle \,,\end{aligned} \tag{4.13}$$

where we have dropped the contributions of the derivatives along the line-of-sight in (4.12). Under the Limber approximation (Limber, 1953; Kaiser, 1992) one assumes that the transverse modes are much large than the longitudinal modes, i.e., $\frac{\ell}{f_\mathrm{K}(\chi)} \gg k_3$. This ceases to be true on large scales, where extensions to the Limber approximation such as those described in LoVerde et al. (2008) or an exact full-sky treatment have to be employed. However, for the scales of interest in this work the Limber approximation is sufficient. In fact, it has been shown in Bernardeau et al. (2012) that the lowest-order Limber approximation is an excellent fit down to multipoles of $\ell \approx 20$. Expressing the two-point function in (4.13) in terms of the power spectrum (C.5) we find for the y–κ cross-power spectrum

$$\langle \hat{y}^{(1)}(\vec{\ell}_1)\hat{\kappa}^{(1)}(\vec{\ell}_2)\rangle = (2\pi)^2\delta_\mathrm{D}^2\left(\vec{\ell}_1+\vec{\ell}_2\right)\int_0^{\chi_H}\mathrm{d}\chi W^y(\chi)W^\kappa(\chi)\frac{|\vec{\ell}_1|^4}{f_\mathrm{K}(\chi)^4}\mathscr{P}_\Phi\left(\frac{|\vec{\ell}_1|}{f_\mathrm{K}(\chi)},\chi\right) \,. \tag{4.14}$$

Note that upon replacing the kernel for the y parameter W^y with W^κ, one recovers the well known expression for the angular power spectrum of the convergence.

4.3 Corrections

To consistently treat fourth-order corrections to the cross spectrum we need to include terms up to third order in Φ of the Compton y parameter and convergence κ (Cooray et al., 2002). Indeed, it has been shown in Krause et al. (2010) that divergences in second-second order cross terms cancel with corresponding divergences in first-third order cross terms. It is thus important to find expressions for the two fields y and κ up to third order. A full sky treatment of lensing observables to even second order is

already a formidable task (Bernardeau et al., 2010, 2012; Vanderveld et al., 2011); a full sky derivation to third order would be beyond the scope of this work. Fortunately, the calculations can be simplified greatly by restricting ourselves to small scales. We follow Dodelson et al. (2005b) to identify the terms that contribute dominantly at small scales and those that can be neglected.

Broadly speaking, on small scales terms with the most angular derivatives are expected to dominate. At second order this are: the well known Born approximation; lens-lens coupling; and reduced shear contributions (Bernardeau et al., 1997; Schneider et al., 1998; Cooray et al., 2002; Dodelson et al., 2005b, 2006; Shapiro, 2009; Krause et al., 2010). Third order terms derived from the aforementioned effects have at least the same number of angular derivatives and are therefore expected to be the dominant third-order contributions. We discuss these contributions in sections 4.3.1 and 4.3.2.

Recent work by Andrianomena et al. (2014) found that contributions from peculiar velocities to the convergence can be as large as the primary contribution from scalar modes in certain redshift ranges. Even though peculiar velocities formally affect the convergence at first order, they affect the shear only at second order (Bonvin, 2008). In the case where the convergence is derived from shear measurements, as we assume in this work, the effect of peculiar velocities enters only at second order. We investigate the effect of peculiar velocities in section 4.3.3. Vector modes induced by second-order perturbations have been shown to yield corrections of similar magnitude as traditional Born and lens-lens terms (Andrianomena et al., 2014). We show that vector modes do not contribute to the y–κ cross spectrum at fourth order in section 4.3.4.

To distinguish the different corrections to the convergence we denote them by subscripts: $\kappa_{\rm std}$ refers to corrections due to Born approximation and lens-lens coupling; $\kappa_{\rm rs}$ to corrections due to the reduced shear; and $\kappa_{\rm z}$ and $\kappa_{\rm v}$ to corrections due to redshift distortions and vector modes, respectively.

4.3.1 Born approximation and lens-lens coupling

For the derivation of the Born and lens-lens coupling terms we roughly follow Krause et al. (2010), in that we expand the solution to the geodesic deviation equation (4.2) systematically in powers of Φ. Alternatively, one could expand the terms in the distortion matrix (4.3), which makes the physical meaning of the terms more apparent.

We expand the comoving transverse displacement in powers of the potential Φ as

$$\vec{x} = \vec{x}^{(0)} + \vec{x}^{(1)} + \vec{x}^{(2)} + \vec{x}^{(3)} + \mathcal{O}(\Phi^4) \,, \tag{4.15}$$

where the superscript in parentheses denotes the order of the expansion. The zeroth and first-order contributions are given by

$$\vec{x}^{(0)} = f_{\rm K}(\chi)\vec{\theta}, \quad x^{(1)i}(\vec{\theta},\chi) = -2\int_0^\chi {\rm d}\chi' f_{\rm K}(\chi-\chi')\Phi_{,i}(f_{\rm K}(\chi')\vec{\theta},\chi') \,. \tag{4.16}$$

The higher-order contributions can be found by Taylor expanding $\Phi(\vec{x})$ in (4.2) around the zeroth order solution $\vec{x}^{(0)}(\vec{\theta},\chi) = f_{\rm K}(\chi)\vec{\theta}$. The potential can then be expanded as $\Phi = \Phi^{(1)} + \Phi^{(2)} + \Phi^{(3)} + \mathcal{O}(\Phi^4)$,

with

$$\begin{aligned}\Phi^{(1)}(\vec{x}) &= \Phi(\vec{x}^{(0)}) \\ \Phi^{(2)}(\vec{x}) &= \Phi_{,i}(\vec{x}^{(0)})x^{(1)i} \\ \Phi^{(3)}(\vec{x}) &= \frac{1}{2}\Phi_{,ij}(\vec{x}^{(0)})x^{(1)i}x^{(1)j} + \Phi_{,i}(\vec{x}^{(0)})x^{(2)i} \ .\end{aligned} \tag{4.17}$$

By replacing the Φ with $\Phi^{(2)}$ in (4.2), we can write the second-order deflection angle as

$$\begin{aligned}\frac{x^{(2)i}(\vec{\theta},\chi)}{f_{\rm K}(\chi)} &= -2\int_0^\chi \mathrm{d}\chi' \frac{f_{\rm K}(\chi-\chi')}{f_{\rm K}(\chi)}\Phi^{(2)}_{,i}(\vec{x}(\vec{\theta},\chi'),\chi') \\ &= 4\int_0^\chi \mathrm{d}\chi' \int_0^{\chi'} \mathrm{d}\chi'' K(\chi,\chi')\frac{K(\chi',\chi'')}{f_{\rm K}(\chi'')}\Phi_{,ij}(\chi')\Phi_{,j}(\chi'') \ ,\end{aligned} \tag{4.18}$$

where we have dropped the angular dependence of the potentials for brevity. We adapt this shorthand for the rest of this work, i.e., unless otherwise noted $\Phi(\vec{x}^{(0)}(\vec{\theta},\chi),\chi)$ is written as $\Phi(\chi)$. Analogously, the third-order deflection angle can be written as

$$\begin{aligned}\frac{x^{(3)i}(\vec{\theta},\chi)}{f_{\rm K}(\chi)} = -4\int_0^\chi \mathrm{d}\chi' \int_0^{\chi'} \mathrm{d}\chi'' \int_0^{\chi'} \mathrm{d}\chi''' K(\chi,\chi')\frac{K(\chi',\chi'')K(\chi',\chi''')f_{\rm K}(\chi')}{f_{\rm K}(\chi'')f_{\rm K}(\chi''')} \\ \times \Phi_{,ijk}(\chi')\Phi_{,j}(\chi'')\Phi_{,k}(\chi''') \\ -8\int_0^\chi \mathrm{d}\chi' \int_0^{\chi'} \mathrm{d}\chi'' \int_0^{\chi''} \mathrm{d}\chi''' K(\chi,\chi')K(\chi',\chi'')\frac{K(\chi'',\chi''')}{f_{\rm K}(\chi''')} \\ \times \Phi_{,ij}(\chi')\Phi_{,jk}(\chi'')\Phi_{,k}(\chi''') \ .\end{aligned} \tag{4.19}$$

Convergence

Equipped with second- and third-order expressions for the deflection angle it is straightforward to derive expressions for the convergence. Using the relation of the convergence to the trace of the distortion tensor (4.5), we can readily write down the second- and third-order expressions for the convergence. At second order this is

$$\begin{aligned}\kappa^{(2)}_{\rm std}(\vec{\theta},\chi_S) = -2\int_0^{\chi_S} \mathrm{d}\chi' \int_0^{\chi'} \mathrm{d}\chi'' K(\chi,\chi')K(\chi',\chi'') \\ \times \left(\frac{f_{\rm K}(\chi')}{f_{\rm K}(\chi'')}\Phi_{,iij}(\chi')\Phi_{,j}(\chi'') + \Phi_{,ij}(\chi')\Phi_{,ji}(\chi'')\right) \ .\end{aligned} \tag{4.20}$$

The first term in the bracket is the well known Born term, while the second is the lens-lens coupling term. The extra factors of the comoving angular distance $f_{\rm K}(\chi)$ arise because the derivative in (4.3) is with respect to the angular deviation $\vec{\theta}$, whereas the potential is a function of the comoving transverse distance $\vec{x}^{(0)} = f_{\rm K}(\chi)\vec{\theta}$.

The third-order expression for the convergence is analogously found to be

$$\begin{aligned}\kappa^{(3)}_{\rm std}(\vec{\theta},\chi_S) = 2\int_0^{\chi_S}\mathrm{d}\chi'\int_0^{\chi'}\mathrm{d}\chi''\int_0^{\chi'}\mathrm{d}\chi'''K(\chi,\chi')K(\chi',\chi'')K(\chi',\chi''')\\ \times\left(\frac{f_{\rm K}(\chi')^2}{f_{\rm K}(\chi'')f_{\rm K}(\chi''')}\Phi_{,iijk}(\chi')\Phi_{,j}(\chi'')\Phi_{,k}(\chi''')\right)\\ +4\int_0^{\chi_S}\mathrm{d}\chi'\int_0^{\chi'}\mathrm{d}\chi''\int_0^{\chi'}\mathrm{d}\chi'''K(\chi,\chi')K(\chi',\chi'')K(\chi',\chi''')\\ \times\left(\frac{f_{\rm K}(\chi')}{f_{\rm K}(\chi''')}\Phi_{,ijk}(\chi')\Phi_{,ji}(\chi'')\Phi_{,k}(\chi''')\right)\\ +4\int_0^{\chi_S}\mathrm{d}\chi'\int_0^{\chi'}\mathrm{d}\chi''\int_0^{\chi''}\mathrm{d}\chi'''K(\chi,\chi')K(\chi',\chi'')\frac{K(\chi'',\chi''')}{f_{\rm K}(\chi''')}\\ \times\frac{\partial}{\partial\theta^i}\left(\Phi_{,ij}(\chi')\Phi_{,jk}(\chi'')\Phi_{,k}(\chi''')\right)\ .\end{aligned} \tag{4.21}$$

The term on line 2 corresponds a second-order Born correction, the term on line 4 to a mixed Born-lens-coupling, and the three terms on line 6 to a second-order Born correction, Born-lens-coupling, second-order lens-lens coupling, respectively.

Compton y parameter

The second and third-order contributions to the Compton y parameter are somewhat easier to derive, as there are no lens-lens coupling terms. As in the case of the convergence, we replace Φ in (4.12) by its expansion (4.17). The second-order contribution to the y parameter is then

$$y^{(2)}(\vec{\theta}) = -2\int_0^{\chi_H}\mathrm{d}\chi'\int_0^{\chi'}\mathrm{d}\chi''W^y(\chi')K(\chi',\chi'')\frac{f_{\rm K}(\chi')}{f_{\rm K}(\chi'')}\Phi_{,iij}(\chi')\Phi_{,j}(\chi'')\ . \tag{4.22}$$

The third-order term follows analogously and is given by

$$\begin{aligned}y^{(3)}(\vec{\theta}) = 2\int_0^{\chi_H}\mathrm{d}\chi'\int_0^{\chi'}\mathrm{d}\chi''\int_0^{\chi'}\mathrm{d}\chi'''W^y(\chi')K(\chi',\chi'')K(\chi',\chi''')\frac{f_{\rm K}(\chi')^2}{f_{\rm K}(\chi'')f_{\rm K}(\chi''')}\\ \times\Phi_{,iijk}(\chi')\Phi_{,j}(\chi'')\Phi_{,k}(\chi''')\\ +4\int_0^{\chi_H}\mathrm{d}\chi'\int_0^{\chi'}\mathrm{d}\chi''\int_0^{\chi''}\mathrm{d}\chi'''W^y(\chi')K(\chi',\chi'')K(\chi'',\chi''')\frac{f_{\rm K}(\chi')}{f_{\rm K}(\chi''')}\\ \times\Phi_{,iij}(\chi')\Phi_{,jk}(\chi'')\Phi_{,k}(\chi''')\ .\end{aligned} \tag{4.23}$$

Both terms are due to the Born approximation. The term on line 2 stems from the $\frac{1}{2}\Phi_{,ij}(\vec{x}^{(0)})x^{(1)i}x^{(1)j}$ term in the third-order contribution to Φ in (4.17), whereas the term on line 4 in (4.23) is due to the $\Phi_{,i}(\vec{x}^{(0)})x^{(2)i}$ term in (4.17).

Cross correlations

The second-second-order contribution to the angular y–κ cross-power spectrum due to Born and lens-lens terms can be derived by taking the ensemble average of the product of the Fourier space expressions $\hat{y}^{(2)}(\vec{\ell}_1)$ and $\hat{\kappa}^{(2)}(\vec{\ell}_2)$. Using the results from appendix C.1, we find

$$\begin{aligned}\langle \hat{y}^{(2)}(\vec{\ell}_1)\hat{\kappa}^{(2)}_{\rm std}(\vec{\ell}_2)\rangle = 4\int_0^{\chi_H}\mathrm{d}\chi_y\mathrm{d}\chi_\kappa\int_0^{\chi_y}\mathrm{d}\chi'_y\int_0^{\chi_\kappa}\mathrm{d}\chi'_\kappa\frac{W^y(\chi_y)W^\kappa(\chi_\kappa)K(\chi_y,\chi'_y)K(\chi_\kappa,\chi'_\kappa)}{f_{\rm K}(\chi_y)^2 f_{\rm K}(\chi'_y)^2 f_{\rm K}(\chi_\kappa)^2 f_{\rm K}(\chi'_\kappa)^2}\\ \times\int\frac{\mathrm{d}^2\vec{\ell}'\mathrm{d}^2\vec{\ell}''}{(2\pi)^4}|\vec{\ell}'|^2\vec{\ell}'(\vec{\ell}_1-\vec{\ell}')\left[|\vec{\ell}''|^2\vec{\ell}''(\vec{\ell}_2-\vec{\ell}'')+\left(\vec{\ell}''(\vec{\ell}_2-\vec{\ell}'')\right)^2\right]\\ \times\langle\hat{\phi}(\vec{\ell}',\chi_y)\hat{\phi}(\vec{\ell}_1-\vec{\ell}',\chi'_y)\hat{\phi}(\vec{\ell}'',\chi_\kappa)\hat{\phi}(\vec{\ell}_2-\vec{\ell}'',\chi'_\kappa)\rangle\ ,\end{aligned} \tag{4.24}$$

where we used the kernel W^κ for a source distribution $n(z)$ instead of a single source at redshift z_S. The four-point function on the last line is made up of one connected and three unconnected terms. The connected term is proportional to the trispectrum (C.7). Under the Limber approximation this introduces a product of delta functions $\delta_{\rm D}(\chi_y-\chi'_y)\delta_{\rm D}(\chi_y-\chi_\kappa)\delta_{\rm D}(\chi_y-\chi'_\kappa)$, setting all comoving distances along the line-of-sight equal. The kernel $K(\chi,\chi')$ is zero for $\chi\leq\chi'$, thus eliminating the contribution from the connected part of the correlation function. The unconnected part can be decomposed into three products of two-point functions by Wick's theorem. Each of the two-point functions yields a delta function times a power spectrum. The term proportional to $\delta_{\rm D}(\chi_y-\chi'_y)\delta_{\rm D}(\chi_\kappa-\chi'_\kappa)$ is zero because $K(\chi,\chi)=0$. The term proportional to $\delta_{\rm D}(\chi_y-\chi'_\kappa)\delta_{\rm D}(\chi'_y-\chi_\kappa)$ is zero because $K(\chi,\chi')K(\chi',\chi)\equiv 0$. The only surviving term is proportional to $\delta_{\rm D}(\chi_y-\chi_\kappa)\delta_{\rm D}(\chi'_y-\chi'_\kappa)$, and upon evaluating the integrals gives for the angular cross-power spectrum

$$\begin{aligned}\langle \hat{y}^{(2)}(\vec{\ell}_1)\hat{\kappa}^{(2)}_{\rm std}(\vec{\ell}_2)\rangle = 4(2\pi)^2\delta^2_{\rm D}(\vec{\ell}_1+\vec{\ell}_2)\int_0^{\chi_H}\mathrm{d}\chi\int_0^{\chi}\mathrm{d}\chi'\frac{W^y(\chi)W^\kappa(\chi)K(\chi,\chi')^2}{f_{\rm K}(\chi)^6 f_{\rm K}(\chi')^6}\int\frac{\mathrm{d}^2\vec{\ell}'}{(2\pi)^2}\\ \times|\vec{\ell}'|^2\vec{\ell}_1\vec{\ell}'\left(\vec{\ell}'(\vec{\ell}_1-\vec{\ell}')\right)^2\mathscr{P}_\Phi\left(\frac{|\vec{\ell}'|}{f_{\rm K}(\chi)},\chi\right)\mathscr{P}_\Phi\left(\frac{|\vec{\ell}_1-\vec{\ell}'|}{f_{\rm K}(\chi')},\chi'\right)\ .\end{aligned} \tag{4.25}$$

The derivation for the first-third order contributions proceeds similarly. The connected correlation function drops out for the same reason as in the second-second-order case. Furthermore, terms in the third-order expressions for y and κ that include a line-of-sight kernel proportional to $K(\chi',\chi'')K(\chi'',\chi''')$, i.e., line 5 in (4.21) and line 3 in (4.23), do not contribute to the power spectra because the kernel is zero for all possible contractions of the correlation function.

The contribution from the second term in (4.21), i.e., line 4, to the cross-power spectrum is proportional to

$$\int\frac{\mathrm{d}^2\vec{\ell}'}{(2\pi)^2}\left(\vec{\ell}_1\vec{\ell}'\right)^3\mathscr{P}_\Phi\left(\frac{|\vec{\ell}_1|}{f_{\rm K}(\chi)},\chi\right)\mathscr{P}_\Phi\left(\frac{|\vec{\ell}'|}{f_{\rm K}(\chi')},\chi'\right)\ ,$$

which is zero due to the antisymmetry of the integral under the transformation $\vec{\ell}'\to-\vec{\ell}'$ (Krause et al.,

2010). Hence, only the first Born term in (4.21) contributes to $\langle \hat{y}^{(1)} \hat{\kappa}^{(3)} \rangle$. We find

$$\begin{aligned}\langle \hat{y}^{(1)}(\vec{\ell}_1)\hat{\kappa}^{(3)}_{\rm std}(\vec{\ell}_2)\rangle = -2(2\pi)^2\delta^2_{\rm D}(\vec{\ell}_1+\vec{\ell}_2)\int_0^{\chi_H}{\rm d}\chi\int_0^{\chi}{\rm d}\chi'\frac{W^y(\chi)W^\kappa(\chi)K(\chi,\chi')^2}{f_{\rm K}(\chi)^6 f_{\rm K}(\chi')^6} \\ \times\int\frac{{\rm d}^2\vec{\ell}'}{(2\pi)^2}\,|\vec{\ell}_1|^4\left(\vec{\ell}_1\vec{\ell}'\right)^2\mathscr{P}_\Phi\left(\frac{|\vec{\ell}_1|}{f_{\rm K}(\chi)},\chi\right)\mathscr{P}_\Phi\left(\frac{|\vec{\ell}'|}{f_{\rm K}(\chi')},\chi'\right)\,.\end{aligned} \tag{4.26}$$

Since the only contribution to $\langle \hat{y}^{(3)} \hat{\kappa}^{(1)} \rangle$ comes from the first term in (4.23), which is identical to the first term in (4.21) up to an interchange of the kernels $W^y(\chi)$ and $W^\kappa(\chi)$, the cross-power spectra $\langle \hat{y}^{(3)} \hat{\kappa}^{(1)} \rangle$ and $\langle \hat{y}^{(1)} \hat{\kappa}^{(3)} \rangle$ are identical.

4.3.2 Reduced shear

At first order the shear and convergence are related by

$$\hat{\kappa}(\vec{\ell}) = T^I(\vec{\ell})\hat{\gamma}_I(\vec{\ell})\,,\quad T^1(\vec{\ell}) = \cos 2\phi_\ell\,,\quad T^2(\vec{\ell}) = \sin 2\phi_\ell\,, \tag{4.27}$$

where ϕ_ℓ is the angle between the two-dimensional wave-vector $\vec{\ell}$ and some fixed reference axis. The components of the shear and other polar quantities are labeled by capital Latin indices. It can be shown that this relation holds exactly up to second order and under the Limber approximation up to third order (see appendix C.2 for details). In the weak lensing regime, the measured quantity is not the shear itself but the reduced shear, conventionally defined as

$$g_I = \frac{\gamma_I}{1-\kappa}\,,\quad I = 1,2\,. \tag{4.28}$$

This definition of the reduced shear is based on the assumption that the Jacobi map (4.3) is symmetric. In general the Jacobi map is not symmetric however, because lens-lens couplings generate the anti-symmetric contribution ω. Including the anti-symmetric terms in the Jacobi map, the generalized reduced shear in complex notation is given by (see appendix C.3)

$$g = \frac{\gamma_1+{\rm i}\gamma_2}{1-\kappa+{\rm i}\omega}\,. \tag{4.29}$$

Accounting for the reduced shear in the relation (4.27) amounts to replacing the shear γ_I with the reduced shear g_I. Using (C.22) and expanding systematically in Φ to third order we can express the observed convergence as

$$\begin{aligned}\hat{\kappa}_{obs} = T^I\hat{g}_I = T^I\Big(&\hat{\gamma}^{(1)}_I + (\hat{\gamma}^{(2)}_{\rm std})_I + (\hat{\gamma}^{(3)}_{\rm std})_I \\ &+\hat{\gamma}^{(1)}_I * \hat{\kappa}^{(1)} + \hat{\gamma}^{(1)}_I * \hat{\kappa}^{(1)} * \hat{\kappa}^{(1)} + \hat{\gamma}^{(1)}_I * \hat{\kappa}^{(2)}_{\rm std} + (\hat{\gamma}^{(2)}_{\rm std})_I * \hat{\kappa}^{(1)} \\ &+R(\hat{\omega}^{(2)}_{\rm std})_{IJ} * \hat{\gamma}^{(1)}_J\Big) + \mathscr{O}(\Phi^4)\,,\end{aligned} \tag{4.30}$$

where $*$ stands for a convolution in Fourier space. As shown in appendix C.2, the first line is equivalent to $\hat{\kappa}^{(1)} + \hat{\kappa}^{(2)}_{\rm std} + \hat{\kappa}^{(3)}_{\rm std}$, where $\hat{\kappa}^{(2)}_{\rm std}$ and $\hat{\kappa}^{(3)}_{\rm std}$ denote the corrections due to Born approximation and lens-lens coupling. The second line includes the well known contributions from the reduced shear (Schneider et al., 1998; Dodelson et al., 2006; Shapiro, 2009; Krause et al., 2010), while the third line is a novel contribution due to second-order induced rotations. The sole second-order correction due to reduced shear to the convergence is

$$\begin{aligned}\hat{\kappa}^{(2)}_{\rm rs}(\vec{\ell}) &= [T^I(\vec{\ell})\hat{\gamma}^{(1)}_I * \hat{\kappa}^{(1)}](\vec{\ell}) = \int \frac{{\rm d}^2\vec{\ell}'}{(2\pi)^2} T^I(\vec{\ell})\hat{\gamma}^{(1)}_I(\vec{\ell}')\hat{\kappa}^{(1)}(\vec{\ell}-\vec{\ell}') \\ &= \int \frac{{\rm d}^2\vec{\ell}'}{(2\pi)^2} \cos(2\phi_{\ell'} - 2\phi_\ell)\hat{\kappa}^{(1)}(\vec{\ell}')\hat{\kappa}^{(1)}(\vec{\ell}-\vec{\ell}') \ ,\end{aligned} \tag{4.31}$$

where we used the identity $T^I(\vec{\ell})T_I(\vec{\ell}') = \cos(2\phi_{\ell'} - 2\phi_\ell)$. Since the reduced shear is an intrinsic lensing effect, it does not affect the Compton y parameter. The lowest-order contribution to the cross-power spectrum is therefore formed by the first-order y parameter (4.12) and second-order reduced shear correction (4.31), i.e.,

$$\begin{aligned}\langle \hat{y}^{(1)}(\vec{\ell}_1)\hat{\kappa}^{(2)}_{\rm rs}(\vec{\ell}_2)\rangle = &-(2\pi)^2\delta^2_{\rm D}(\vec{\ell}_1+\vec{\ell}_2)\int {\rm d}\chi \frac{W^y(\chi)\left(W^\kappa(\chi)\right)^2}{f_{\rm K}(\chi)^{10}} \int \frac{{\rm d}^2\vec{\ell}'}{(2\pi)^2} \\ &\times |\vec{\ell}_1|^2|\vec{\ell}'|^2|\vec{\ell}_2-\vec{\ell}'|^2\cos(2\phi_{\ell'}-2\phi_{\ell_2})\mathscr{B}_\Phi\left(\frac{|\vec{\ell}_1|}{f_{\rm K}(\chi)}, \frac{|\vec{\ell}'|}{f_{\rm K}(\chi)}, \frac{|\vec{\ell}_2-\vec{\ell}'|}{f_{\rm K}(\chi)}\right) \ ,\end{aligned} \tag{4.32}$$

where we used the definition (C.6) of the bispectrum. Unlike in the case of the Born and lens-lens terms, there is a third-order contribution to the cross-power spectrum. As a consistency check, one can show that upon replacing W^y by W^κ, and using the fact that to first order the convergence is the same as the E-mode of the shear, one recovers the expression for the correction to the E-mode shear due to reduced shear in Dodelson et al. (2006).

To analyze the first-third-order contributions, we split the third-order contribution to the convergence due to the reduced shear in (4.30) into three components:

$$\hat{\kappa}^{(3,A)}_{\rm rs}(\vec{\ell}) = T^I(\vec{\ell})[\hat{\gamma}^{(1)}_I * \hat{\kappa}^{(1)} * \hat{\kappa}^{(1)}](\vec{\ell}) \ ; \tag{4.33a}$$

$$\hat{\kappa}^{(3,B)}_{\rm rs}(\vec{\ell}) = T^I(\vec{\ell})[\hat{\gamma}^{(1)}_I * \hat{\kappa}^{(2)}_{\rm std} + (\hat{\gamma}^{(2)}_{\rm std})_I * \hat{\kappa}^{(1)}](\vec{\ell}) \ ; \tag{4.33b}$$

$$\hat{\kappa}^{(3,C)}_{\rm rs}(\vec{\ell}) = T^I(\vec{\ell})[R(\hat{\omega}^{(2)}_{\rm std})_{IJ} * \hat{\gamma}^{(1)}_J](\vec{\ell}) \ . \tag{4.33c}$$

The cross-power spectrum of $\hat{\kappa}^{(3,A)}_{\rm rs}$ with y is then

$$\begin{aligned}\langle \hat{y}^{(1)}(\vec{\ell}_1)\hat{\kappa}^{(3,A)}_{\rm rs}(\vec{\ell}_2)\rangle = &\int {\rm d}\chi_y \frac{W^y(\chi_y)}{f_{\rm K}(\chi_y)^2}\prod_{i=1}^3 {\rm d}\chi_i \frac{W^\kappa(\chi_i)}{f_{\rm K}(\chi_i)^2}\int \frac{{\rm d}^2\vec{\ell}'{\rm d}^2\vec{\ell}''}{(2\pi)^4}\cos(2\phi_{\ell_2}-2\phi_{\ell'}) \\ &\times |\vec{\ell}_1|^2|\vec{\ell}'|^2|\vec{\ell}''|^2|\vec{\ell}_2-\vec{\ell}'-\vec{\ell}''|^2 \\ &\times \langle\hat{\phi}(\vec{\ell}_1,\chi_y)\hat{\phi}(\vec{\ell}',\chi_1)\hat{\phi}(\vec{\ell}'',\chi_2)\hat{\phi}(\vec{\ell}_2-\vec{\ell}'-\vec{\ell}'',\chi_3)\rangle \ .\end{aligned} \tag{4.34}$$

Because the line-of-sight integral does not include the kernel $K(\chi,\chi')$, like in the case of the third-order cross-power spectrum (4.32), the connected part of the four-point function does not vanish. The connected and unconnected contributions to the cross-power spectrum are found to be

$$\begin{aligned}\langle\hat{y}^{(1)}(\vec{\ell}_1)\hat{\kappa}_{\rm rs}^{(3,A)}(\vec{\ell}_2)\rangle_{\rm c} &= (2\pi)^2\delta_{\rm D}^2\left(\vec{\ell}_1+\vec{\ell}_2\right)\int{\rm d}\chi\,\frac{W^y(\chi)W^\kappa(\chi)^3}{f_{\rm K}(\chi)^{14}}\int\frac{{\rm d}^2\vec{\ell}'{\rm d}^2\vec{\ell}''}{(2\pi)^4}\cos(2\phi_{\ell_2}-2\phi_{\ell'})\\ &\quad\times|\vec{\ell}_1|^2|\vec{\ell}'|^2|\vec{\ell}''|^2|\vec{\ell}_1+\vec{\ell}'+\vec{\ell}''|^2\mathscr{T}_\Phi\left(\frac{\vec{\ell}_1}{f_{\rm K}(\chi)},\frac{\vec{\ell}'}{f_{\rm K}(\chi)},\frac{\vec{\ell}''}{f_{\rm K}(\chi)},-\frac{\vec{\ell}_1+\vec{\ell}'+\vec{\ell}''}{f_{\rm K}(\chi)},\chi\right)\end{aligned} \tag{4.35a}$$

$$\langle\hat{y}^{(1)}(\vec{\ell}_1)\hat{\kappa}_{\rm rs}^{(3,A)}(\vec{\ell}_2)\rangle_{\rm g} = \langle\hat{y}^{(1)}(\vec{\ell}_1)\hat{\kappa}^{(1)}(\vec{\ell}_2)\rangle\int\frac{{\rm d}^2\vec{\ell}'}{(2\pi)^2}C_{\ell'}^{\kappa\kappa,2}\,, \tag{4.35b}$$

where the connected and unconnected parts are denoted by the subscript c and g, respectively. For the derivation of the connected part we have used the definition of the trispectrum C.7. Replacing the kernel W^y by W^κ we recover again the same expression as found in Krause et al. (2010).

The two other third-order contributions to the convergence due the reduced shear (4.33b) and (4.33c) involve second-order Born and lens-lens corrections, i.e., include the coupling kernel $K(\chi,\chi')$ in their line-of-sight integrals. Hence, only their unconnected parts contribute to the cross-power spectrum. The derivation proceeds as for the other terms discussed so far, albeit with somewhat more complicated expressions, as there are now two contractions of the four-point function that survive. The contribution involving $\hat{\kappa}_{\rm rs}^{(3,B)}$ is

$$\begin{aligned}\langle\hat{y}^{(1)}(\vec{\ell}_1)\hat{\kappa}_{\rm rs}^{(3,B)}(\vec{\ell}_2)\rangle &= -2(2\pi)^2\delta_{\rm D}^2\left(\vec{\ell}_1+\vec{\ell}_2\right)\int{\rm d}\chi{\rm d}\chi'\,\frac{W^y(\chi)W^\kappa(\chi')}{f_{\rm K}(\chi)^6 f_{\rm K}(\chi')^6}\int\frac{{\rm d}^2\vec{\ell}'}{(2\pi)^2}\\ &\quad\times|\vec{\ell}_1|^2|\vec{\ell}'|^2\vec{\ell}_1\vec{\ell}'\,\mathscr{P}_\Phi\left(\frac{|\vec{\ell}_1|}{f_{\rm K}(\chi)},\chi\right)\mathscr{P}_\Phi\left(\frac{|\vec{\ell}'|}{f_{\rm K}(\chi')},\chi'\right)\\ &\quad\times\Big\{\cos(2\phi_{\ell_2}-2\phi_{\ell'})\vec{\ell}_1\vec{\ell}'\left[W^\kappa(\chi)K(\chi,\chi')+W^\kappa(\chi')K(\chi',\chi)\right]\\ &\qquad\cos(2\phi_{\ell_2}-2\phi_{\vec{\ell}'+\vec{\ell}_1})\left[\vec{\ell}_1(\vec{\ell}'+\vec{\ell}_1)W^\kappa(\chi)K(\chi,\chi')+\vec{\ell}'(\vec{\ell}'+\vec{\ell}_1)W^\kappa(\chi')K(\chi',\chi)\right]\Big\}\,.\end{aligned} \tag{4.36}$$

The azimuthal integral of the third line can be done analytically and is equal to $\frac{\pi}{2}$. Note that our result differs from that obtained in Krause et al. (2010) by an extra factor of $\cos(2\phi_{\ell_2}-2\phi_{\vec{\ell}'+\vec{\ell}_1})$ on the fourth line.

Using the definition of the matrix $R(\omega)$ in (C.23), the contribution $\hat{\kappa}_{\rm rs}^{(3,C)}$ can be written as

$$\begin{aligned}\hat{\kappa}_{\rm rs}^{(3,C)}(\vec{\ell}) &= T^1(\vec{\ell})[\gamma_2^{(1)}*\hat{\omega}_{\rm std}^{(2)}](\vec{\ell})-T^2(\vec{\ell})[\gamma_1^{(1)}*\hat{\omega}_{\rm std}^{(2)}](\vec{\ell})\\ &= \int\frac{{\rm d}^2\vec{\ell}'}{(2\pi)^2}\sin(2\phi_{\ell'}-2\phi_\ell)\hat{\kappa}^{(1)}(\vec{\ell}')\hat{\omega}_{\rm std}^{(2)}(\vec{\ell}-\vec{\ell}')\,.\end{aligned} \tag{4.37}$$

The cross-power spectrum is therefore

$$\begin{aligned}\langle\hat{y}^{(1)}(\vec{\ell}_1)\hat{\kappa}_{\rm rs}^{(3,C)}(\vec{\ell}_2)\rangle = -2(2\pi)^2\delta_{\rm D}^2\left(\vec{\ell}_1+\vec{\ell}_2\right)\int {\rm d}\chi{\rm d}\chi' \frac{W^y(\chi)W^\kappa(\chi')}{f_{\rm K}(\chi)^6 f_{\rm K}(\chi')^6}\int\frac{{\rm d}^2\vec{\ell}'}{(2\pi)^2} \\ \times|\vec{\ell}_1|^3|\vec{\ell}'|^3\vec{\ell}_1\vec{\ell}'\sin(\phi_{\ell_2}-\phi_{\ell'})\sin(2\phi_{\ell'}-2\phi_{\ell_2})\mathscr{P}_\Phi\left(\frac{|\vec{\ell}_1|}{f_{\rm K}(\chi)},\chi\right)\mathscr{P}_\Phi\left(\frac{|\vec{\ell}'|}{f_{\rm K}(\chi')},\chi'\right) \\ \times\left[W^\kappa(\chi)K(\chi,\chi')+W^\kappa(\chi')K(\chi',\chi)\right]\,.\end{aligned} \tag{4.38}$$

The mode-coupling term can be reduced to $|\vec{\ell}_1|^4|\vec{\ell}'|^4\frac{\sin(2\phi_{\ell'}-2\phi_{\ell_2})^2}{2}$. The azimuthal integral then evaluates to $\frac{\pi}{2}$. The contributions from $\hat{\kappa}_{\rm rs}^{(3,C)}$ and from the first term in $\hat{\kappa}_{\rm rs}^{(3,B)}$ are therefore identical.

Finally, we find the only second-second-order contribution due to the reduced shear to the cross-power spectrum to be

$$\begin{aligned}\langle\hat{y}^{(2)}(\vec{\ell}_1)\hat{\kappa}_{\rm rs}^{(2)}(\vec{\ell}_2)\rangle = -2(2\pi)^2\delta_{\rm D}^2\left(\vec{\ell}_1+\vec{\ell}_2\right)\int {\rm d}\chi{\rm d}\chi' \frac{W^y(\chi)K(\chi,\chi')W^\kappa(\chi)W^\kappa(\chi')}{f_{\rm K}(\chi)^6 f_{\rm K}(\chi')^6}\int\frac{{\rm d}^2\vec{\ell}'}{(2\pi)^2} \\ \times|\vec{\ell}'|^4|\vec{\ell}_1-\vec{\ell}'|^2\left[\vec{\ell}'\left(\vec{\ell}_1-\vec{\ell}'\right)\right]\mathscr{P}_\Phi\left(\frac{|\vec{\ell}'|}{f_{\rm K}(\chi)},\chi\right)\mathscr{P}_\Phi\left(\frac{|\vec{\ell}_1-\vec{\ell}'|}{f_{\rm K}(\chi')},\chi'\right) \\ \times\left[\cos(2\phi_{\ell_2}-2\phi_{\vec{\ell}'})+\cos(2\phi_{\ell_2}-2\phi_{\vec{\ell}_1-\vec{\ell}'})\right]\,.\end{aligned} \tag{4.39}$$

The dominant contribution is the third-order correction (4.32), by virtue of being of a lower order than the other contributions considered in this work, which are all of fourth order.

4.3.3 Redshift distortions

The comoving line-of-sight distance to a source is usually not an observable quantity. Instead it is derived from the measured redshift, which is affected by the peculiar motions of the source and observer, Sachs-Wolfe, and integrated Sachs-Wolfe effects. The second-order contribution to the convergence due to a perturbation of the cosmological redshift is

$$\kappa_{\rm z}^{(2)}(\chi) = \frac{{\rm d}\kappa^{(1)}(\chi)}{{\rm d}z}\delta z^{(1)} = \frac{{\rm d}\kappa^{(1)}(\chi)}{{\rm d}\chi}\frac{{\rm d}\chi}{{\rm d}z}\delta z^{(1)}\,. \tag{4.40}$$

The dependence of the convergence on comoving distance of the source is

$$\frac{{\rm d}\kappa^{(1)}(\chi)}{{\rm d}\chi} = \frac{1}{f_{\rm K}(\chi)^2}\int_0^\chi {\rm d}\chi'\frac{\Phi_{,ii}(\chi')}{f_{\rm K}(\chi')^2}\,, \tag{4.41}$$

while the redshift perturbation due to peculiar motion of the source, Sachs-Wolfe, and integrated Sachs-Wolfe effects is given by (Bernardeau et al., 2010)

$$\delta z^{(1)} = \frac{1}{a}\left(-2\int_0^\chi {\rm d}\chi'\frac{\partial\Phi(\chi')}{\partial\chi'}+\Phi(\chi)-n^i v_i^{(1)}(\chi)\right)\,, \tag{4.42}$$

where the potential at the observer and the peculiar motion of the observer have been set to zero, as they would only contribute at the very largest scales. The peculiar motion from first-order perturbation theory is (Bernardeau et al., 2012)

$$v_i^{(1)}(\chi) = -\frac{2a}{3H_0^2\Omega_m}\partial_i\left(-\frac{\partial\Phi(\chi')}{\partial\chi'} + \mathscr{H}(\chi)\Phi(\chi)\right) . \tag{4.43}$$

From (4.42) and (4.43) we can already see that only the term corresponding to the peculiar motion would contribute appreciably, as it involves an angular derivative. Restricting ourselves to the contribution due to the peculiar motion, the second-order convergence can be written as

$$\kappa_{\mathrm{z}}^{(2)}(\chi) = \frac{-n^i v_i^{(1)}(\chi)}{\mathscr{H}(\chi) f_{\mathrm{K}}(\chi)^2}\int_0^\chi \mathrm{d}\chi' \frac{\Phi_{,ii}(\chi')}{f_{\mathrm{K}}(\chi')^2} . \tag{4.44}$$

The photon trajectory $\vec{n}$ projects the peculiar velocity along the line-of-sight, i.e., the angular derivatives are projected out. Thus all redshift distortions that contribute to (4.40) have only two angular derivatives and can be safely neglected on small scales.

4.3.4 Vector modes

In Andrianomena et al. (2014) it was shown that fourth-order contributions from vector modes to lensing observables can be of comparable magnitude as other fourth-order contributions considered in this work. It would thus be conceivable that there are large third-order contributions involving vector modes. The lowest-order cross-correlation that includes vector modes is $\langle\hat{y}^{(1)}(\vec{\ell}_1)\hat{\kappa}_{\mathrm{v}}^{(2)}(\vec{\ell}_2)\rangle$, where the second-order contribution to the convergence is (Andrianomena et al., 2014; Thomas et al., 2015)

$$\kappa_{\mathrm{v}}^{(2)}(\chi) = \int_0^\chi \mathrm{d}\chi' K(\chi,\chi') n_j V^j_{,ii}(\chi') . \tag{4.45}$$

The contraction of the line-of-sight direction $\vec{n}$ with the vector potential V^i is proportional to

$$n_i V^i(\chi) \propto \sin\vartheta\, \mathrm{e}^{\pm\mathrm{i}\varphi} , \tag{4.46}$$

where ϑ and φ denote the spherical coordinates on the sky. This expression is manifestly of odd parity and does not contribute if one correlates it with the even parity field y. The lowest-order vector contribution to the cross-power spectrum has to be quadratic in the vector potential. Since the vector potential is already of second order in the scalar potential Φ, and the lowest vector contribution to y is of third order, there are no fourth-order vector contribution to the cross-power spectrum.

4.4 Discussion

In Fig. 4.1 we have plotted the cross-power spectrum (4.14) and the various higher-order contributions considered in this work. The underlying non-linear matter power spectrum was computed with CAMB,[1]

[1] http://camb.info

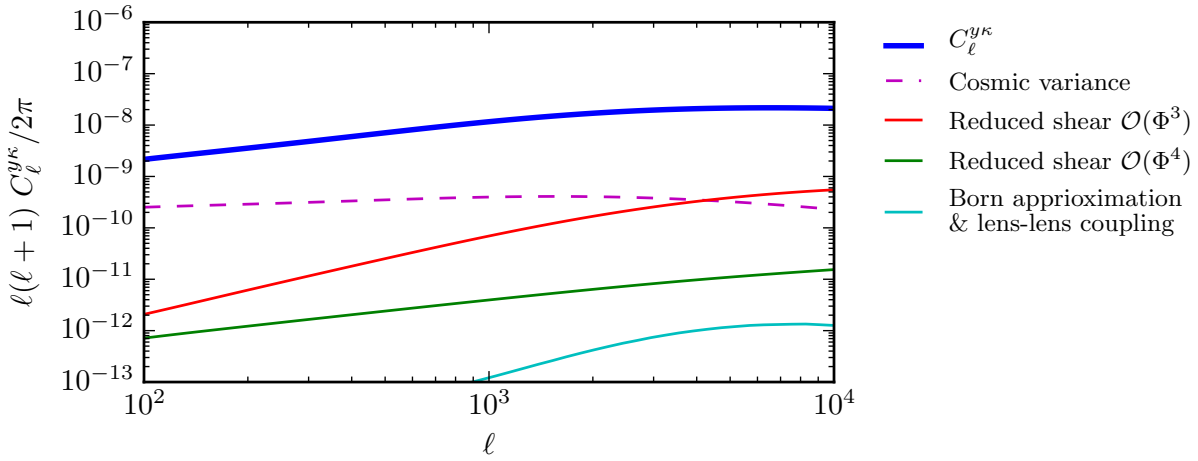

Figure 4.1: The different contributions to the angular cross-power spectrum $C_\ell^{y\kappa}$. The first-order result (4.14)(bold blue), third-order reduced shear (4.32)(red), fourth-order Born and lens-lens terms (4.25) and (4.26)(cyan), and fourth-order reduced shear contributions (4.35), (4.36), (4.38), (4.39) (green).

using the best fit Planck cosmological parameters (Planck Collaboration XVI, 2014) and the extension to HALOFIT by Takahashi et al. (2012). For the source redshift distribution $n(z)$ we use the fitting formula of the redshift distribution of CFHTLenS (van Waerbeke et al., 2013). We computed the non-linear bispectrum using the fitting formulae of both Scoccimarro et al. (2001) and Gil-Marín et al. (2012). It was found in Fu et al. (2014) that the fitting formula in Gil-Marín et al. (2012) slightly overestimates the bispectrum on small scales compared to that of Scoccimarro et al. (2001). For clarity, we only show the reduced shear contribution computed with the fitting formula of Scoccimarro et al. (2001) in Fig. 4.1. The relative contributions to the cross-power spectrum due to the third-order term (4.32) with both fitting formulae is shown in Fig. 4.2. We find that the third-order contribution (4.32) gives the largest correction to the cross-power spectrum. At multipoles of $\ell \approx 4000$ it begins to dominate over the cosmic variance $\left((C_\ell^{y\kappa})^2 + C_\ell^{yy} C_\ell^{\kappa\kappa}\right)/(2\ell+1)$ (Kamionkowski et al., 1997) and reaches several percent of the second-order result (4.14) at multipoles of $\ell \approx 10^4$. The fourth-order contributions are over an order of magnitude lower at small scales. Furthermore, the difference between the two fitting formulae for the bispectrum of Scoccimarro et al. (2001) and Gil-Marín et al. (2012) are at least an order of magnitude larger on small scales than the fourth-order corrections. It is thus justified to approximate the fourth-order contribution (4.34) by its unconnected part, as it is expected to dominate over the connected part at all but the smallest scales (Krause et al., 2010).

4.5 Conclusion

We have calculated all contributions up to fourth order due to weak lensing to the tSZ-lensing cross-correlation in the small angle approximation. We have found that only the third-order term (4.32) due to the reduced shear contributes appreciably. At multipoles of $\ell \approx 3000$ the contribution reaches the percent

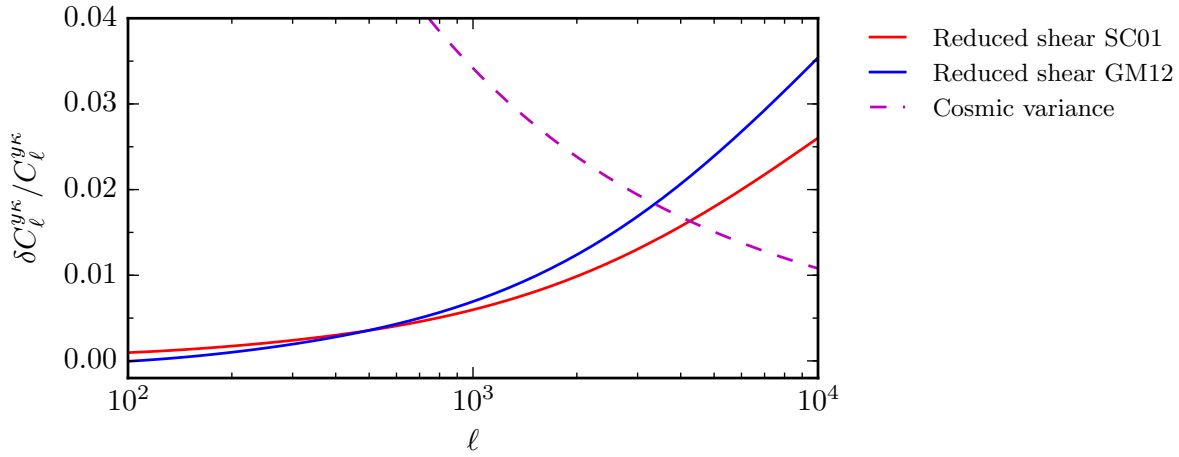

Figure 4.2: The third-order contribution (4.32) to the cross-power spectrum computed using the fitting formulae for the bispectrum from Scoccimarro et al. (2001) and Gil-Marín et al. (2012). The corrections begin to dominate over cosmic variance above $\ell \sim 4000$.

level and rises strongly from there. The effect might thus be observable in future high-resolution surveys, in particular for cluster samples where the tSZ-lensing cross-correlation signal will be measured around clusters and stacked. However, baryon physics can have similar — or even stronger — effects on the tSZ-lensing cross-correlation at small scales, such that the contributions calculated in this chapter might remain unobservable for the foreseeable future. For upcoming large-area surveys such as LSST[2] and Euclid[3], a full-sky treatment will be necessary. As is evident from the large amount of terms in even the second-order shear in Bernardeau et al. (2010, 2012), a derivation to the same order as considered in this work will be a formidable task.

Even though the simple bias model employed in this work is compatible with a halo model approach (Ma et al., 2015), a treatment of the corrections considered in this work in the context of the halo model would be of interest. It should be noted that even within the framework of the halo model there is still considerable uncertainty in the modelling of the pressure profile, exemplifying the complications one encounters once baryonic physics are introduced.

Beyond its explicit application to the cross-correlation between lensing and tSZ, our work can be used to calculate high order lensing corrections to cross-correlation signals other than tSZ. For instance one can envision measuring the cross-correlation between the cosmic infrared background and lower redshift structures, which in principles could require similar corrections to the cross-correlation with tSZ presented in this chapter.

[2] http://www.lsst.org
[3] http://sci.esa.int/euclid/

Chapter 5

KiDS-450: tomographic cross-correlation of galaxy shear with Planck lensing

We present the tomographic cross-correlation between galaxy lensing measured in the Kilo-Degree Survey (KiDS-450) with overlapping lensing measurements of the cosmic microwave background (CMB), as detected by Planck (2015 data release). We compare our joint probe measurement to the theoretical expectation for a flat ΛCDM cosmology, assuming the best-fitting cosmological parameters from the KiDS-450 cosmic shear and Planck CMB analyses. We find that our results are consistent within 1σ with the KiDS-450 cosmology, with an amplitude re-scaling parameter $A_{\rm KiDS} = 0.86 \pm 0.19$. Adopting a Planck cosmology, we find our results are consistent within 2σ, with $A_{\rm Planck} = 0.68 \pm 0.15$. We show that the agreement is improved in both cases when the contamination of the signal by intrinsic galaxy alignments is accounted for, increasing A by approximately 0.1. This is the first tomographic analysis of the galaxy lensing – CMB lensing cross-correlation signal, and is based on five photometric redshift bins. We use this measurement as an independent validation of the multiplicative shear calibration and of the calibrated source redshift distribution at high redshifts. We find that constraints on these two quantities are strongly correlated when obtained from this technique, which should therefore not be considered as a stand-alone competitive calibration tool.

5.1 Introduction

Recent observations of distinct cosmological probes are closing in on the few parameters that enter the standard model of cosmology (see for example Planck Collaboration XIII, 2016, and references therein). Although there is clear evidence that the Universe is well described by the ΛCDM model, some tensions are found between probes. For instance, the best fit cosmology inferred from the observation of the Cosmic Microwave Background (CMB) in Planck Collaboration XIII (2016) is in tension with some cosmic shear analyses (MacCrann et al., 2015; Hildebrandt et al., 2017; Joudaki et al., 2016, 2017), while both direct and strong lensing measurements of today's Hubble parameter H_0 are more than 3σ away from the values inferred from the CMB (Bernal et al., 2016; Bonvin et al., 2017). At face value, these discrepancies either point towards new physics (for a recent example, see Joudaki et al., 2016) or

un-modelled systematics in any of those probes. In this context, cross-correlation of different cosmic probes stands out as a unique tool, as many residual systematics that could contaminate one data set are unlikely to correlate also with the other (e.g. 'additive biases'). This type of measurement can therefore be exempt from un-modelled biases that might otherwise source the tension. Another point of interest is that the systematic effects that do not fully cancel, for example 'multiplicative biases' or the uncertainty on the photometric redshifts, will often impact differently the cosmological parameters compared to the stand-alone probe, allowing for degeneracy breaking or improved calibration.

In this chapter, we present the first tomographic cross-correlation measurement between CMB lensing and galaxy lensing, based on the lensing map described in Planck Collaboration XV (2016) and the lensing data from the Kilo-Degree Survey[1] presented in Kuijken et al. (2015, KiDS hereafter) and in the KiDS-450 cosmic shear analysis (Hildebrandt et al., 2017). The main advantage in this sort of measurement resides in it being free of uncertainty on galaxy bias, which otherwise dominates the error budget in CMB lensing - galaxy position cross-correlations (Omori et al., 2015; Giannantonio et al., 2016; Baxter et al., 2016). Over the last two years, the first lensing-lensing cross-correlations were used to measure σ_8 and Ω_m (Hand et al., 2015; Liu et al., 2015), by combining the CMB lensing data from the Atacama Cosmology Telescope (Das et al., 2014) with the lensing data from the Canada-France-Hawaii Telescope Stripe 82 Survey (Moraes et al., 2014), and from the Planck lensing data and the Canada-France-Hawaii Telescope Lensing Survey (Erben et al., 2013, CFHTLenS hereafter). Since then, additional effects were found to contribute to the measurement, introducing extra complications in the interpretation of the signal. For instance, Hall et al. (2014) and Troxel et al. (2014) showed that the measurement is likely to be contaminated by the intrinsic alignment of galaxies with the tidal field in which they live. At the same time, Liu et al. (2016) argued that this measurement could point instead to residual systematics in the multiplicative shear bias and proposed that the measurement itself could be used to set constraints on the shear bias (see also Das et al., 2013). Their results showed that large residuals are favoured, despite the calibration accuracy claimed by the analysis of image simulations tailored for the same survey (Miller et al., 2013). A recent analysis from Harnois-Déraps et al. (2016, HD16 hereafter) suggested instead that the impact of catastrophic redshift outliers could be causing this apparent discrepancy, since these dominate the uncertainty in the modelling. They also showed that choices concerning the treatment of the masks can lead to biases in the measured signal, and that the current estimators should therefore be thoroughly calibrated on full light-cone mocks.

Although these pioneering works were based on Fourier space cross-correlation techniques, more recent analyses presented results from configuration-space measurements, which are cleaner due to their insensitivity to masking. Kirk et al. (2016, K16 hereafter) combined the CMB lensing maps from Planck and from the South Pole Telescope (van Engelen et al., 2012, SPT) with the Science Verification Data from the Dark Energy Survey[2]. Their measurement employed the POLSPICE numerical tool (Szapudi et al., 2001a; Chon et al., 2004), which starts off with a pseudo-C_ℓ measurement that is converted into configuration space to deal with masks, then is turned back into a Fourier space estimator. Soon after,

[1] KiDS: http://kids.strw.leidenuniv.nl

[2] DES: www.darkenergysurvey.org

HD16 showed consistency between pseudo-C_ℓ analyses and configuration space analyses of two-point correlation functions, combining the Planck lensing maps with both CFHTLenS and the Red-sequence Cluster Lensing Survey (Hildebrandt et al., 2016, RCSLenS hereafter). A similar configuration space estimator was recently used with Planck lensing and SDSS shear data (Singh et al., 2017), although the signal was subject to higher noise levels.

This chapter directly builds on the K16 and HD16 analyses, utilising tools and methods described therein, but on a new suite of lensing data. The additional novelty here is that we perform the first tomographic cross-correlation analysis between CMB lensing and galaxy lensing, where we split the galaxy sample into five redshift bins and examine the redshift evolution. This is made possible by the high quality of the KiDS photometric redshift data, by the extent of the spectroscopic matched sample, and consequently by the precision achieved on the calibrated source redshift distribution (see Hildebrandt et al., 2017, for more details). It provides a new test of cosmology within the ΛCDM model, including the redshift evolution of the growth of structure, and also offers an opportunity to examine the tension between the KiDS and Planck cosmologies (reported in Hildebrandt et al., 2017). With the upcoming lensing surveys such as LSST[3] and Euclid[4], it is expected that this type of cross-correlation analysis will be increasingly used to validate the data calibration (Schaan et al., 2017) and extract cosmological information in a manner that complements the cosmic shear and clustering data.

The basic theoretical background upon which we base our work is laid out in Section 5.2. We then describe the data sets and our measurement strategies in Sections 5.3 and 5.4, respectively. Our cosmological results are presented in Section 5.5. We also describe therein a calibration analysis along the lines of Liu et al. (2016), this time focussing on high redshift galaxies for which the photometric redshifts and shear calibration are not well measured. Informed on cosmology from lower redshift measurement, this self-calibration technique has the potential to constraint jointly the shear bias and the photo-z distribution, where other methods fail. We conclude in Section 5.6.

The fiducial cosmology that we adopt in our analysis corresponds to the flat WMAP9+SN+BAO cosmology[5] (Hinshaw et al., 2013), in which the matter density, the dark energy density, the baryonic density, the amplitude of matter fluctuations, the Hubble parameter and the tilt of the matter power spectrum are described by $(\Omega_\mathrm{m}, \Omega_\Lambda, \Omega_\mathrm{b}, \sigma_8, h, n_\mathrm{s}) = (0.2905, 0.7095, 0.0473, 0.831, 0.6898, 0.969)$. Aside from determining the overall amplitude of the theoretical signal from the $(\sigma_8, \Omega_\mathrm{m})$ pair, this choice has little impact on our analysis, as we later demonstrate. Future surveys will have the statistical power to constrain the complete cosmological set, but this is currently out of reach for a survey the size of KiDS-450. We note that our fiducial cosmology is a convenient choice that is consistent within 2σ with the Planck, KiDS-450, CFHTLenS, and WMAP9+ACT+SPT analyses in the $(\sigma_8, \Omega_\mathrm{m})$ plane. As such, it minimizes the impact of residual tension across data sets.

[3] www.lsst.org

[4] sci.esa.int/euclid

[5] Our fiducial cosmology consists of a flat ΛCDM universe in which the dark energy equation of state is set to $w = -1$.

5.2 Theoretical background

Photons from the surface of last scattering are gravitationally lensed by large-scale structures in the Universe before reaching the observer. Similarly, photons emitted by observed galaxies are lensed by the low redshift end of the same large-scale structures. The signal expected from a cross-correlation measurement between the two lenses can be related to the fluctuations in their common foreground matter field, more precisely by the matter power spectrum $P(k,z)$. The lensing signal is obtained from an extended first-order Limber integration over the past light cone up to the horizon distance $\chi_{\rm H}$, weighted by geometrical factors $W^i(\chi)$, assuming a flat cosmology (Limber, 1954; LoVerde et al., 2008; Kilbinger et al., 2017):

$$C_\ell^{\kappa_{\rm CMB}\kappa_{\rm gal}} = \int_0^{\chi_{\rm H}} d\chi W^{\rm CMB}(\chi) W^{\rm gal}(\chi) P\left(\frac{\ell+1/2}{\chi}; z\right). \tag{5.1}$$

In the above expression, χ is the comoving distance from the observer, ℓ is the angular multipole, and z is the redshift. The lensing kernels are given by

$$W^i(\chi) = \frac{3\Omega_{\rm m} H_0^2}{2c^2} \chi g^i(\chi)(1+z), \tag{5.2}$$

with

$$g^{\rm gal}(\chi) = \int_\chi^{\chi_H} {\rm d}\chi' \tilde{n}(\chi') \frac{\chi'-\chi}{\chi'} \quad \text{and}$$

$$g^{\rm CMB}(\chi) = \left[1 - \frac{\chi}{\chi_*}\right] {\rm H}(\chi_* - \chi). \tag{5.3}$$

Here the constant c is the speed of light in vacuum and χ_* is the comoving distance to the surface of last scattering. The term $\tilde{n}(\chi)$ is related to the redshift distribution of the observed galaxy sources, $n(z)$, by $\tilde{n}(\chi) = n(z){\rm d}z/{\rm d}\chi$, which depends on the depth of the survey. The Heaviside function ${\rm H}(x)$ guarantees that no contribution comes from beyond the surface of last scattering as the integration in equation 5.1 approaches the horizon.

The angular cross-spectrum described by equation 5.1 is related to correlation functions in configuration space, in particular between the CMB lensing map and the tangential shear (Miralda-Escude, 1991):

$$\xi^{\kappa_{\rm CMB}\gamma_{\rm t}}(\vartheta) = \frac{1}{2\pi} \int_0^\infty {\rm d}\ell\, \ell\, C_\ell^{\kappa_{\rm CMB}\kappa_{\rm gal}} J_2(\ell\vartheta), \tag{5.4}$$

where, J_2 is the Bessel function of the first kind of order 2, and the quantity ϑ represents the angular separation on the sky. Details about measurements of $C_\ell^{\kappa_{\rm CMB}\kappa_{\rm gal}}$ and the tangential shear $\gamma_{\rm t}$ – relevant for equations 5.1 and 5.4 respectively – are provided in Section 5.4.

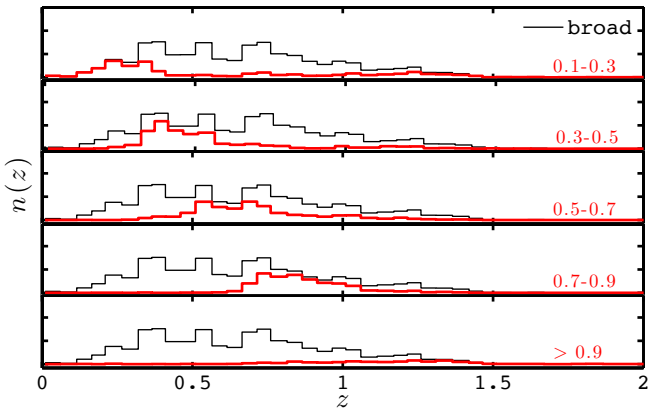

Figure 5.1: Redshift distribution of the selected KiDS-450 sources in the tomographic bins (unnormalized), calibrated using the DIR method described in Hildebrandt et al. (2017). The $n(z)$ of the broad $z_B \in [0.1, 0.9]$ bin is shown in black in all panels for reference, while the $n(z)$ for the five tomographic bins are shown in red. The mean redshift and effective number of galaxies in each tomographic bin are summarized in Table 5.1.

Our predictions are obtained from the NICAEA[6] cosmological tool (Kilbinger et al., 2009), assuming a non-linear power spectrum described by the Takahashi et al. (2012) revision of the HALOFIT model (Smith et al., 2003).

5.3 The data sets

5.3.1 KiDS-450 lensing data

The KiDS-450 lensing data that we use for our measurements are based on the third data release of dedicated KiDS observations from the VLT Survey Telescope at Paranal, in Chile, and are described in Kuijken et al. (2015), Hildebrandt et al. (2017) and de Jong (2017 in prep.). These references describe the reduction and analysis pipelines leading to the shear catalogues, and present a rigorous and extensive set of systematic verifications. Referring to these papers for more details, we summarise here the properties of the data that directly affect our measurement.

Although the full area of the KiDS survey will consist of two large patches on the celestial equator and around the South Galactic Pole, the observing strategy was optimized to prioritize the coverage of the GAMA fields (Liske et al., 2015). The footprint of the KiDS-450 data is consequently organized in five fields, G9, G12, G15, G23 and GS, covering a total of 449.7 deg^2 While the multiband imaging data are processed by Astro-WISE (de Jong et al., 2015), the lensing r-band data are processed by the THELI reduction method described in Erben et al. (2013). Shape measurements are determined using the self-calibrated LENSFIT algorithm (based on Miller et al., 2013) detailed in Fenech Conti et al. (2017).

As described in Hildebrandt et al. (2017), each galaxy is assigned a photometric redshift probability

[6] www.cosmostat.org/software/nicaea/

Table 5.1: Summary of the data properties in the different tomographic bins. The effective number of galaxies assumes the estimation method of Heymans et al. (2012).

z_B cut	$\bar{z}$	n_{eff} (gal/arcmin^2)	σ_e
[0.1, 0.9]	0.72	7.54	0.28
[0.1, 0.3]	0.75	2.23	0.29
[0.3, 0.5]	0.59	2.03	0.28
[0.5, 0.7]	0.72	1.81	0.27
[0.7, 0.9]	0.87	1.49	0.28
>0.9	1.27	0.90	0.33

distribution provided by the software BPZ (Benítez, 2000). The position of the maximum value of this distribution, labelled z_B, serves only to divide the data into redshift bins. Inspired by the KiDS-450 cosmic shear measurement, we split the galaxy sample into five redshift bins: $z_B \in [0.1,0.3]$, $[0.3,0.5]$, $[0.5,0.7]$, $[0.7,0.9]$ and > 0.9. We also define a broad redshift bin by selecting all galaxies falling in the range $z_B \in [0.1,0.9]$. The KiDS-450 cosmic shear measurement did not include the $z_B > 0.9$ bin because the photo-z and the shear calibration were poorly constrained there. For this reason, we do not use this bin in our cosmological analysis either. Instead, we estimate these calibration quantities directly from our measurement in Section 5.5.7.

For each tomographic bin, the estimate of the redshift distribution of our galaxy samples, $n(z)$, is not obtained from the stacked BPZ-PDF, but from a magnitude-weighted scheme (in 4-dimensional *ugri* magnitude space) of a spectroscopically matched sub-sample. In Hildebrandt et al. (2017), this 'weighted direct calibration' or 'DIR' method was demonstrated to be the most precise covering our redshift range, among four independent $n(z)$ estimation techniques. Figure 5.1 shows these weighted $n(z)$ distributions, which enter the theoretical predictions through equation 5.1, along with the effective number density per bin. In order to preserve the full description of the data in the high redshift tail, from where most of the signal originates, we do not fit the distributions with analytical functions, as was done in previous work (Hand et al., 2015; Liu et al., 2015, K16, HD16). Fitting functions tend to capture well the region where $n(z)$ is maximal, however they attribute almost no weight to the (noisy) high redshift tail. This is of lesser importance in the galaxy lensing auto-correlation measurements, but becomes highly relevant for the CMB lensing cross-correlation. Instead, we use the actual histograms in the calculation (as in Liu et al., 2015), recalling that their apparent spikes are smoothed by the lensing kernels in equation 5.3. What is apparent from Fig. 5.1, and of importance for this analysis, is that all tomographic bins have a long tail that significantly overlaps with the CMB lensing kernel, especially the first tomographic bin. These tails are caused by inherent properties to the *ugri*-band photo-z of the KiDS-450 data, and given the wavelength range and SNR, some high-z tails are expected (Hildebrandt et al., 2017). This feature is well captured by the mean redshift distributions, which are listed in Table 5.1.

Based on the quality of the ellipticity measurement, each galaxy is assigned a LENSFIT weight w,

plus a multiplicative shear calibration factor – often referred to as the m-correction or the shear bias – that is obtained from image simulations (Fenech Conti et al., 2017). This calibration is accurate to better than 1% for objects with $z_B < 0.9$, but the precision quickly degrades at higher redshifts. As recommended, we do not correct for shear bias in each galaxy, but instead compute the average correction for each tomographic bin (see equation 5.7). In the fifth tomographic bin, we expect to find residual biases in the m-correction, but apply it nevertheless, describing in Section 5.5.7 how this correction can be self-calibrated. To be absolutely clear, we reiterate that we do not include this fifth bin in our main cosmological analysis. The effective number density and the shape noise in each tomographic bin are also listed in Table 5.1.

Following Hildebrandt et al. (2017), we apply a c-correction by subtracting the weighted mean ellipticity in each field and each tomographic bin, but this has no impact on our analysis since this c term does not correlate with the CMB lensing data.

5.3.2 Planck $\kappa_{\rm CMB}$ maps

The CMB lensing data that enter our measurements are the $\kappa_{\rm CMB}$ map obtained from the 2015 public data release,[7] thoroughly detailed in Planck Collaboration XV (2016). The map-making procedure is based on the quadratic estimator described in Okamoto et al. (2003), which is applicable to a suite of multi-frequency temperature and polarization maps. Frequencies are combined so as to remove foreground contamination, while other sources of secondary signal (mainly emissions from the Galactic plane, from point sources and hot clusters) are masked in the CMB maps, prior to the reconstruction. If some of these are not fully removed from the lensing maps, they will create systematic effects in the $\kappa_{\rm CMB}$ map that show up differently in the cross-correlation measurement compared to the auto-spectrum analysis. For example, there could be leakage in the CMB map coming from, e.g., residual thermal Sunyaev-Zel'dovich signal that is most likely located near massive clusters. These same clusters are highly efficient at lensing background galaxies, hence our cross-correlation measurement would be sensitive to this effect. Indeed, the $\langle {\rm tSZ} \times \gamma_t \rangle$ correlation, as recently measured in Hojjati et al. (2016), has a very large signal to noise and could possibly be detected in a targeted analysis. Although it is difficult to assess the exact level of the tSZ signal in our $\kappa_{\rm CMB}$ map, the cleaning made possible from the multi-frequency observations from Planck is thorough, reducing the residual contaminants to a very small fraction. No quantitative evidence of such leakage has been reported as of yet, and we therefore ignore this in our analysis.

Regions from the full sky lensing map that overlap with the five KiDS footprints are extracted, including a 4° extension to optimise the signal-to-noise ratio of the measurement (see HD16). The Planck release of lensing data also provides the analysis mask, which we apply to the $\kappa_{\rm CMB}$ map prior to carrying out our measurement.[8]

[7] Planck Legacy Archive: pla.esac.esa.int/pla/#cosmology

[8] This procedure does not entirely capture the masking analysis since the mask was applied on the temperature field, not on the lensing map. The reconstruction process inevitably leaks some of the masked regions into unmasked area, and vice versa. Applying this mask will therefore only remove the most problematic regions.

5.4 The measurements

This section presents the cross-correlation measurements, which are performed with two independent estimators: $\xi^{\kappa_{\rm CMB}\gamma_{\rm t}}$ (equation 5.4); and the POLSPICE measurement of $C_\ell^{\kappa_{\rm CMB}\kappa_{\rm gal}}$ (equation 5.1). These techniques were used and rigorously validated in previous work and we refer the interested reader to HD16, K16, and references therein for more details. The reasons for conducting our analysis with these two estimators instead of only one are two fold: firstly, they do not probe identical physical scales, which makes them complementary when carried out on surveys covering patchy regions; secondly, being completely independent codes, residual systematics arising from inaccuracies in the analysis could be identified through their different effect on these two statistics.

5.4.1 The $\xi^{\kappa_{\rm CMB}\gamma_{\rm t}}$ estimation

The first estimator presented in this chapter, $\xi^{\kappa_{\rm CMB}\gamma_{\rm t}}$, was recently introduced in HD16, and used later in Singh et al. (2017). It is a full configuration-space measurement that involves minimal manipulation of the data. The calculation simply loops over each pixel of the $\kappa_{\rm CMB}$ maps and defines concentric annuli with different radii ϑ, therein measuring the average tangential component of the shear, $\gamma_{\rm t}$, from the KiDS galaxy shapes. For this reason, it is arguably the cleanest route to performing such a cross-correlation measurement, even though there appears to be a limit to its accuracy at large angles in some cases due to the finite support of the observation window (Mandelbaum et al., 2013). That being said, it nevertheless bypasses a number of potential issues that are encountered with other estimators (see HD16 for a discussion). The $\xi^{\kappa_{\rm CMB}\gamma_{\rm t}}$ estimator is given by

$$\xi^{\kappa_{\rm CMB}\gamma_{\rm t}}(\vartheta) = \frac{\sum_{ij}\kappa^i_{\rm CMB}e^{ij}_{\rm t}w^j\Delta_{ij}(\vartheta)}{\sum_{ij}w^j\Delta_{ij}(\vartheta)}\frac{1}{1+K(\vartheta)}\,, \tag{5.5}$$

where the sum first runs over the $\kappa_{\rm CMB}$ pixels 'i', then over all galaxies 'j' found in an annulus of radius ϑ and width Δ, centred on the pixel i. In this local coordinate system, $e^{ij}_{\rm t}$ is the tangential component of the LENSFIT ellipticity from the jth galaxy relative to pixel i. The exact binning scheme is described by $\Delta_{ij}(\vartheta)$, the binning operator:

$$\Delta_{ij}(\vartheta) = \begin{cases} 1, \text{if}\left|\theta_i-\theta_j\right| < \vartheta \pm \frac{\Delta}{2}\,, \\ 0, \text{otherwise}\,, \end{cases} \tag{5.6}$$

where θ_i and θ_j are the observed positions of the pixel i and galaxy j. Following HD16, the bin width Δ is set to 30 arcmin, equally spanning the angular range [1, 181] arcmin with six data points. Larger angular scales capture very little signal with the current level of statistical noise. We verified that our analysis results are independent of our choice of binning scheme. In equation 5.5, w^j is the LENSFIT weight of the galaxy j and $K(\vartheta)$ corrects for the shape multiplicative bias m^j that must be applied to

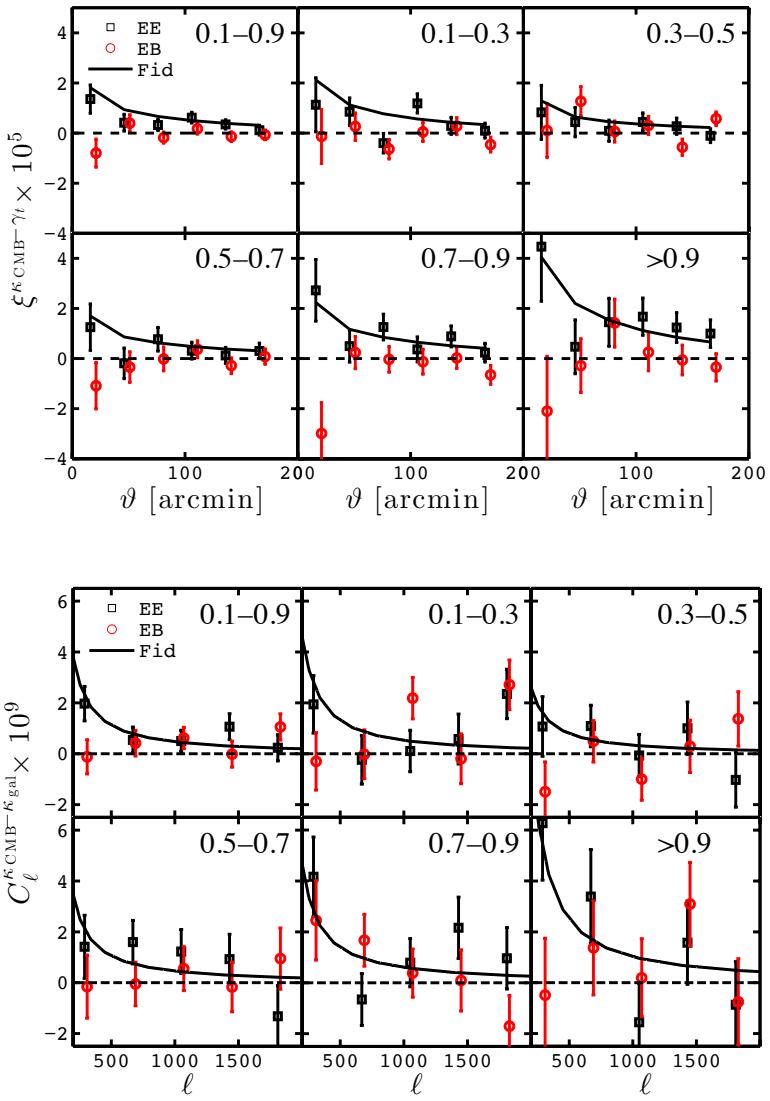

Figure 5.2: Cross-correlation measurement between Planck 2015 $\kappa_{\rm CMB}$ maps and KiDS-450 lensing data. The upper part presents results from the $\xi^{\kappa_{\rm CMB}\gamma_t}$ estimator, while the lower part shows the estimation of $C_\ell^{\kappa_{\rm CMB}\kappa_{\rm gal}}$. Different panels show the results in different tomographic bins, with predictions (solid curve) given by equations 5.1 and 5.4 in our fiducial cosmology. The black squares show the signal, whereas the red circles present the *EB* null test described in Section 5.5.2, slightly shifted horizontally to improve the clarity in this figure. The error bars are computed from 100 CMB lensing simulations.

the lensing data (Fenech Conti et al., 2017):

$$\frac{1}{1+K(\vartheta)} = \frac{\sum_{ij} w^j \Delta_{ij}(\vartheta)}{\sum_{ij} w^j (1+m^j) \Delta_{ij}(\vartheta)} \,. \tag{5.7}$$

The theoretical predictions for $\xi^{\kappa_{\rm CMB}\gamma_{\rm t}}$ are provided by equation 5.4. We apply the same binning as with the data, averaging the continuous theory lines inside each angular bin. We show in the upper panel of Fig. 5.2 the measurements in all tomographic bins, compared to theoretical predictions given by our fiducial WMAP9+BAO+SN cosmology. The estimation of our error bars is described in Section 5.4.3.

We also project the galaxy shape components onto $e_\times$, which is rotated by 45° compared to $e_{\rm t}$. This effectively constitutes a nulling operation that can inform us of systematic leakage, in analogy to the *EB* test performed in the context of cosmic shear. For this reason, we loosely refer to '*EE*' and '*EB*' tests in this chapter, when we are in fact comparing $\kappa_{\rm CMB} \times e_{\rm t}$ and $\kappa_{\rm CMB} \times e_\times$, respectively. We note that the past literature referred to such an *EB* measurement as the '*B*-mode test', which can be misleading for the non-expert. Indeed, the proper *B*-mode test refers to the *BB* measurement in weak lensing analyses, a non-lensing signal that can be caused by astrophysics and systematics. The *EB* signal test asserts something more fundamental: since *B* changes sign under parity, and *E* does not, a non-zero *EB* means a violation of the parity of the shear/ellipticity field (Schneider, 2003). That is not expected from lensing alone, so could only come from a systematic effect that does not vanish under averaging. Our *EB* measurement is shown with the red symbols in Fig. 5.2. We find by visual inspection that in most tomographic bins, these seem closely centred on zero, but not in all cases. To quantify the significance of this *EB* measurement, we estimate the confidence level with which these red points deviate from zero. We detail in Section 5.5.2 how we carry out that test and show that they are consistent with noise.

We have carried out an additional null test presented in HD16, which consists in randomly rotating the shapes of the galaxies before the measurement ($\kappa_{\rm CMB} \times$ random). This test is sensitive to the noise levels in the galaxy lensing data and hence affected by the shape noise $\sigma_{\rm e}$ listed in Table 5.1. We find that the resulting signal is fully consistent with zero in all tomographic bins.

5.4.2 The $C_\ell^{\kappa_{\rm CMB}\kappa_{\rm gal}}$ estimation

The second estimator uses the same data as our $\xi^{\kappa_{\rm CMB}\gamma_{\rm t}}$ analysis, namely the $\kappa_{\rm CMB}$ map and the KiDS shear catalogues, but requires additional operations on the data, including harmonic space transforms. This is accomplished with the POLSPICE numerical code (Szapudi et al., 2001a; Chon et al., 2004) running in polarization mode, where the $\{T, Q, U\}$ triplets are replaced by $\{\kappa_{\rm CMB}, 0, 0\}$ and $\{0, -e_1, e_2\}$. The code first computes the pseudo-C_ℓ of the maps and of the masks, then transforms the results into configuration space quantities, that are finally combined and transformed back into Fourier space. The output of POLSPICE is therefore an estimate of the cross-spectrum $C_\ell^{\kappa_{\rm CMB}\kappa_{\rm gal}}$. While POLSPICE is frequently used for CMB analyses, it was applied for the first time in the context of CMB lensing $\times$ galaxy lensing by K16 and serves as a good comparison to the configuration-space estimator described in Section 5.4.1. One main advantage of this estimator is that in principle different ℓ bands are largely uncorrelated, which makes the covariance matrix almost diagonal and hence easier to estimate.

The POLSPICE measurement[9] is presented in the lower panel of Fig. 5.2, plotted against the theoretical predictions given by equation 5.1. The *EB* data points are directly obtained from the temperature/*B*-mode output provided by the polarization version of the code, and are further discussed in Section 5.5.2.

Note that our choice of the γ_t and POLSPICE estimators was motivated by our desire to avoid producing $\kappa_{\rm gal}$ maps in order to reduce the risks of errors and systematic biases that can arise in the map making stage in the presence of a mask as inhomogeneous as that of the KiDS-450 data. These two estimators produce correlated measurements, but they probe different scales. The γ_t estimator is accurate at the few percent level, as verified on full mock data in HD16, and the POLSPICE code has been thoroughly verified and validated on the same mocks as well. We refer the reader to K16 and HD16 for details of these tests.

5.4.3 Covariance estimation

The $\kappa_{\rm CMB}$ map reconstructed from the Planck data is noise dominated for most Fourier modes (Planck Collaboration XV, 2016). It is only by combining the full sky temperature and polarization maps that the Planck Collaboration could achieve a lensing detection of 40σ.

Since the noise $N_{\rm CMB}$ is larger than the signal $\kappa_{\rm CMB}$ at every scale included in our analysis (HD16), we can evaluate the covariance matrix from cross-correlation measurements between the 100 Planck simulated lensing maps (also provided in their 2015 public data release) and the tomographic KiDS data:

$$\mathrm{Cov}^{\kappa_{\rm CMB}\,\kappa_{\rm gal}}_{\ell\ell'} \simeq \langle \Delta\hat{C}^{N_{\rm CMB}\,\kappa_{\rm gal}}_{\ell}\, \Delta\hat{C}^{N_{\rm CMB}\,\kappa_{\rm gal}}_{\ell'} \rangle \;; \tag{5.8}$$

and

$$\mathrm{Cov}^{\kappa_{\rm CMB}\,\gamma_t}_{\vartheta\,\vartheta'} \simeq \langle \Delta\hat{\xi}^{N_{\rm CMB}\,\gamma_t}_{\vartheta}\, \Delta\hat{\xi}^{N_{\rm CMB}\,\gamma_t}_{\vartheta'} \rangle \;, \tag{5.9}$$

where the 'hats' refer to measured quantities, $\Delta\hat{x} = \hat{x} - \bar{x}$, and the brackets represent the average over the 100 realizations. This method assumes that the covariance is completely dominated by the CMB lensing and neglects the contribution from the shear covariance. This is justified by the fact that the signal from the former is about an order of magnitude larger, and hence completely drives the statistical uncertainty (HD16). The error bars shown in Fig. 5.2 are obtained from these matrices (from the square root of the diagonals). For each tomographic bin, the $\mathrm{Cov}^{\kappa_{\rm CMB}\,\kappa_{\rm gal}}_{\ell\ell'}$ matrix has 25 elements, whereas the $\mathrm{Cov}^{\kappa_{\rm CMB}\,\gamma_t}_{\vartheta\,\vartheta'}$ matrix has 36. The 100 realizations are enough to invert these matrices one at a time with a controllable level of noise bias, and the numerical convergence on this inverse is guaranteed (Lu et al., 2010). Note that this strategy fails to capture the correlation between tomographic bins, which are not required by our cosmological analysis presented in Section 5.5.6. If needed in future analyses, these could be estimated from full light-cone mock simulations.

[9]POLSPICE has adjustable internal parameters, and we use THETAMAX = 60°, APODIZESIGMA = 60° and NLMAX = 3000.

For both estimators, the covariance matrix is dominated by its diagonal, with most off-diagonal elements of the cross-correlation coefficient matrix being under $\pm 10\%$. Some elements reach larger values, $\pm 40\%$ correlation at the most, but these are isolated, not common to all tomographic bins, and are consistent with being noise fluctuations, given that we are measuring many elements from 'only' 100 simulations. This partly explains why our cosmological results are not based on a joint tomographic analysis. We keep the full matrices in the analysis, even though we could, in principle, include only the diagonal part in the POLSPICE measurement. Nevertheless, we have checked that our final results are only negligibly modified if we use this approximation in the χ^2 calculation, suggesting that one could reliably use a Gaussian approximation to the error estimation in this type of measurement (see equation 23 in HD16).

5.5 Cosmological inference

Given the relatively low signal-to-noise ratio of our measurement (Fig. 5.2), we do not fit our signal for the six parameter ΛCDM cosmological model. Instead, we follow the strategy adopted in earlier studies: we compare the measured signal to our fiducial cosmological predictions, treating the normalization as a free parameter 'A'. If the assumed fiducial cosmology is correct and in absence of other systematic effects, A is expected to be consistent with unity. As discussed in previous studies, A is affected by a number of effects that can similarly modulate the overall amplitude of the signal. Aside from its sensitivity to cosmology – our primary science target – this rescaling term will absorb contributions from residual systematic errors in the estimation of $n(z)$, from mis-modelling of the galaxy intrinsic alignments, from residual systematic bias in the shear multiplicative term m (equation 5.7), from astrophysical phenomena such as massive neutrinos and/or baryonic feedback, and from residual systematics in the cross-correlation estimators themselves (K16 and HD16).

In this section, we first present our constraints on A; we then quantify how the different effects listed above can impact our measurements, and finally present our cosmological interpretation. Our primary results assume the fiducial WMAP9+BAO+SN cosmology, i.e. we first place constraints on $A_{\rm fid}$, however we also report constraints on $A_{\rm KiDS}$ and $A_{\rm Planck}$, obtained by assuming different baseline cosmologies.

5.5.1 Significance

To measure A, we first compute the χ^2 statistic:

$$\chi^2 = \Delta \mathrm{x}^{\mathrm{T}}\, \mathrm{Cov}^{-1}\, \Delta \mathrm{x}\ , \tag{5.10}$$

with

$$\Delta \mathrm{x} = \hat{\xi}^{\kappa_{\rm CMB}\gamma_{\rm t}} - A\xi^{\kappa_{\rm CMB}\gamma_{\rm t}} \text{ or } \Delta \mathrm{x} = \hat{C}^{\kappa_{\rm CMB}\kappa_{\rm gal}} - AC^{\kappa_{\rm CMB}\kappa_{\rm gal}} \tag{5.11}$$

for the configuration-space and POLSPICE estimators, respectively. As before, quantities with 'hats' are measured, and the predictions assume the fiducial cosmology, unless stated otherwise. The signal-to-noise ratio (SNR) is given by the likelihood ratio test, which measures the confidence at which we can reject the null hypothesis (i.e., that there is no signal, simply noise) in favour of an alternative hypothesis described by our theoretical model with a single parameter A (see Hojjati et al., 2016, for a recent derivation in a similar context). We can write SNR $= \sqrt{\chi^2_{\rm null} - \chi^2_{\rm min}}$, where $\chi^2_{\rm null}$ is computed by setting $A = 0$, and $\chi^2_{\rm min}$ corresponds to the best-fit value for A. The error on A is obtained by varying the value of A until $\chi^2_A - \chi^2_{\rm min} = 1$ (see, e.g. Wall et al., 2003).

We include two additional statistical corrections to this calculation. The first is a correction factor that multiplies the inverse covariance matrix, $\alpha = (N_{\rm sim} - N_{\rm bin} - 2)/(N_{\rm sim} - 1) = 0.94$, to account for biases inherent to matrix inversion in the presence of noise (Hartlap et al., 2007). Here $N_{\rm bin}$ is the number of data bins (five for $C^{\kappa_{\rm CMB}\kappa_{\rm gal}}$ and six for $\xi^{\kappa_{\rm CMB}\gamma_{\rm t}}$) and $N_{\rm sim}$ is the number of simulations (100) used in the covariance estimation. There exists an improved version of this calculation based on assuming a t-distribution in the likelihood, however with our values of $N_{\rm bin}$ and $N_{\rm sim}$, the differences in the inverted matrix would be of order 10–20% (Sellentin et al., 2016), a correction on the error that we ignore given the relatively high level of noise in our measurement.

The second correction was first used in HD16, and consists of an additional error on A due to the propagated uncertainty coming from the noise in the covariance matrix (Taylor et al., 2014). This effectively maps $\sigma_A \to \sigma_A(1+\varepsilon/2)$, where $\varepsilon = \sqrt{2/N_{\rm sim} + 2(N_{\rm bin}/N^2_{\rm sim})} = 0.145$. These two correction factors are included in the analysis. The results from our statistical investigation are reported in Table 5.2, where we list $\chi^2_{\rm min}$, $\chi^2_{\rm null}$, SNR and A for every tomographic bin. The theoretical predictions provide a good fit to the data given that for our number of degrees of freedom $\nu = N_{\rm bin} - 1$, $\nu - \sqrt{2\nu} < \chi^2_{\rm min} < \nu + \sqrt{2\nu}$. In other words, all our measured χ^2 fall within the expected 1σ error. We also compute the p-value for all these χ^2 measurements at the best-fitting A in order to estimate the confidence at which we can accept or reject the assumed model. Assuming Gaussian statistics, p-values smaller than 0.01 correspond to a 99% confidence in the rejection of the model (the null hypothesis) by the data, and are considered 'problematic'. Our measured p-values, also listed in Table 5.2, are always larger than 0.12, meaning that the model provides a good fit to the data in all cases.

These tomographic measurements are re-grouped in Fig. 5.3, where we compare the redshift evolution of A for both estimators. We mark the 1σ region of the broad bin $n(z)$ with the solid horizontal lines, and see that all points overlap with this region within 1σ. This is an indication that the relative growth of structure between the tomographic bins is consistent with the assumed ΛCDM model. For the broad $n(z)$, the signal prefers an amplitude that is $23-31$ percent lower than the fiducial cosmology, i.e., the 1σ region shown by the horizontal solid lines in Fig. 5.3 is offset from unity by that amount. The main cosmological result that we quote from the $z_{\rm B} \in [0.1, 0.9]$ measurement is that of the $\gamma_{\rm t}$ estimator due to its higher SNR, as seen from comparing the top two rows of Table 5.2. For our fiducial cosmology, we find

$$A_{\rm fid} = 0.69 \pm 0.15 \; . \tag{5.12}$$

Table 5.2: Summary of χ^2, SNR and p-values obtained with the two different pipelines. The $C_\ell^{\kappa_{\rm CMB}\kappa_{\rm gal}}$ measurements have 4 degrees of freedom (5 ℓ bins $-$ 1 free parameter), whereas the configuration space counterpart $\xi^{\kappa_{\rm CMB}\gamma_t}(\vartheta)$ has one more, with 6 ϑ-bins. $A_{\rm fid}$ is the best-fit amplitude that scales the theoretical signals in the fiducial cosmology, according to equation 5.11, also shown in Fig. 5.3. The numbers listed here include the covariance debiasing factor α and the extra error ε due to the noise in the covariance (see main text of Section 5.5.1 for more details).

$z_{\rm B}$	Estimator	$\chi^2_{\rm min}$	$\chi^2_{\rm null}$	SNR	p-values	$A_{\rm fid}$
[0.1, 0.9]	$C_\ell^{\kappa_{\rm CMB}\kappa_{\rm gal}}$	2.80	18.21	3.93	0.53	0.77 ± 0.19
	$\xi^{\kappa_{\rm CMB}\gamma_t}$	2.88	22.94	4.48	0.64	0.69 ± 0.15
[0.1, 0.3]	$C_\ell^{\kappa_{\rm CMB}\kappa_{\rm gal}}$	5.48	8.89	1.85	0.20	0.55 ± 0.30
	$\xi^{\kappa_{\rm CMB}\gamma_t}$	7.93	13.38	2.34	0.12	0.53 ± 0.24
[0.3, 0.5]	$C_\ell^{\kappa_{\rm CMB}\kappa_{\rm gal}}$	2.95	4.95	1.42	0.50	0.71 ± 0.51
	$\xi^{\kappa_{\rm CMB}\gamma_t}$	1.44	4.19	1.66	0.84	0.60 ± 0.37
[0.5, 0.7]	$C_\ell^{\kappa_{\rm CMB}\kappa_{\rm gal}}$	4.00	10.13	2.47	0.35	0.87 ± 0.35
	$\xi^{\kappa_{\rm CMB}\gamma_t}$	2.00	6.45	2.11	0.77	0.55 ± 0.26
[0.7, 0.9]	$C_\ell^{\kappa_{\rm CMB}\kappa_{\rm gal}}$	5.12	10.04	2.22	0.23	0.79 ± 0.36
	$\xi^{\kappa_{\rm CMB}\gamma_t}$	2.78	15.41	3.55	0.65	1.02 ± 0.29
> 0.9	$C_\ell^{\kappa_{\rm CMB}\kappa_{\rm gal}}$	4.70	12.92	2.87	0.26	0.83 ± 0.29
	$\xi^{\kappa_{\rm CMB}\gamma_t}$	4.68	22.64	4.24	0.38	0.95 ± 0.22

Varying the cosmology to the best fit KiDS-450 and Planck cosmologies[10,11,12], we obtain

$$A_{\rm KiDS} = 0.86 \pm 0.19 \qquad \text{and} \qquad A_{\rm Planck} = 0.68 \pm 0.15 \; . \tag{5.13}$$

The relative impact of these different cosmologies on our signal is presented in Fig. 5.4, where we see that the KiDS-450 cosmology prediction mostly differ from the other two at large scales. The signal from our fiducial cosmology agrees with that assuming the best-fit Planck cosmology to better than 5% in all tomographic bins.

Figure 5.3 demonstrates there are small differences between the two estimators at fixed cosmology, especially at high redshift. As mentioned in Section 5.4.2, the scales being probed are not identical, and therefore some differences in the recovered values of A are expected. Nevertheless, within the current statistical accuracy, the two estimators are fully consistent with one another.

Visually, the $\xi^{\kappa_{\rm CMB}\gamma_t}(\vartheta)$ estimator seems to show a mild trend for decreasing values of A in lower redshift bins. Although such an effect could point towards a number of interesting phenomena suppressing power for source galaxies at $z \lesssim 0.7$ (e.g., modification to the growth history compared to

[10]Fiducial $(\Omega_{\rm m}, \Omega_\Lambda, \Omega_{\rm b}, \sigma_8, h, n_{\rm s}) = (0.29, 0.71, 0.047, 0.83, 0.69, 0.97)$.
[11]KiDS-450 $(\Omega_{\rm m}, \Omega_\Lambda, \Omega_{\rm b}, \sigma_8, h, n_{\rm s}) = (0.25, 0.75, 0.047, 0.85, 0.75, 1.09)$.
[12]Planck $(\Omega_{\rm m}, \Omega_\Lambda, \Omega_{\rm b}, \sigma_8, h, n_{\rm s}) = (0.32, 0.68, 0.049, 0.80, 0.67, 0.97)$.

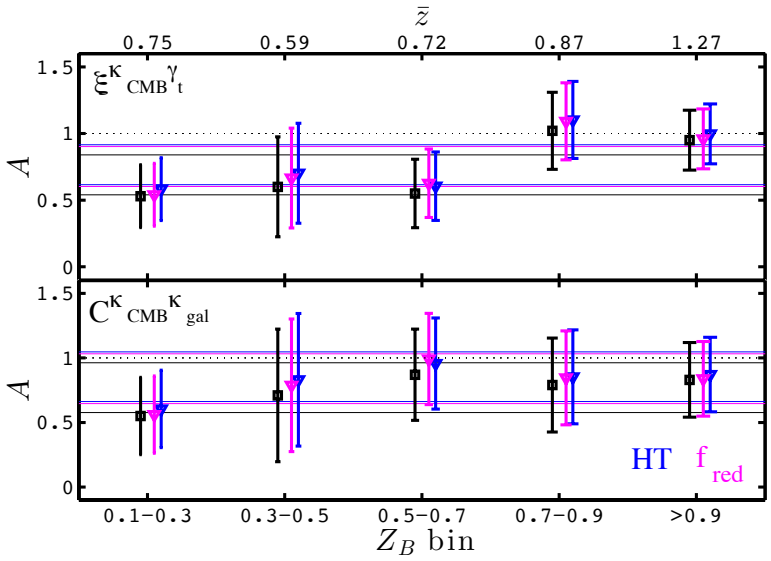

Figure 5.3: Tomographic measurement of $A_{\rm fid}$, defined in equation 5.11, assuming our fiducial cosmology. The two panels present results from the two cross-correlation estimators (labelled in the top left corner). Black symbols assume no IA, while colour symbols include correction factors from two IA models ($f_{\rm red}$ in magenta and HT in blue, see Sec. 5.5.3). The horizontal solid lines of a given colour enclose the 1σ region measured in the broad $z_{\rm B} \in [0.1, 0.9]$ bin, while the dotted horizontal lines indicate the fiducial values ($A_{\rm fid} = 1$). The mean source redshift in each bin is indicated at the top and summarized in Table 5.1. The mean in the first bin is high because of the long tail, visible in Fig. 5.1. The best-fit values in different cosmologies are $A_{\rm fid} = 0.69 \pm 0.15$, $A_{\rm KiDS} = 0.86 \pm 0.19$ and $A_{\rm Planck} = 0.68 \pm 0.15$.

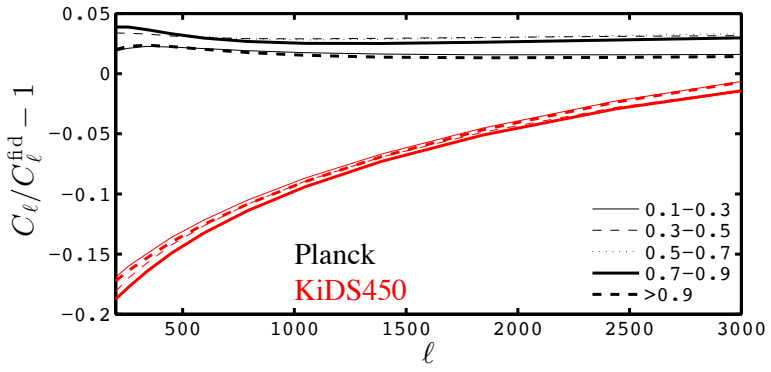

Figure 5.4: Fractional effect on the signal when changing the fiducial cosmology to Planck or KiDS-450. Different symbols show the impact in different tomographic bins, relative to the fiducial predictions. Current measurements are limited to $\ell < 2000$.

Table 5.3: p-values for the *EB* test obtained for the 6 tomographic bins. Highlighted in bold is the p-value ≤ 0.01. The column labelled C_{10} refers to POLSPICE measurements in which the data are organized in 10 bins instead of five. These calculations assume t-distributed likelihoods (following Sellentin et al., 2016).

$z_{\rm B}$	$C^{t-\rm dist}$	$C_{10}^{t-\rm dist}$	$\xi^{t-\rm dist}$
[0.1, 0.9]	0.20	0.09	0.58
[0.1, 0.3]	**0.01**	0.09	0.52
[0.3, 0.5]	0.39	0.63	0.08
[0.5, 0.7]	0.94	0.57	0.78
[0.7, 0.9]	0.21	0.20	0.16
> 0.9	0.53	0.54	0.68

the fiducial cosmology, additional feedback processes from baryons or massive neutrinos, or redshift-dependent contamination from IA) the significance of this redshift dependence is too low to draw any robust conclusions.

What is significantly seen from Fig. 5.3 is that the signal is generally low compared to the fiducial and Planck cosmologies. Our measurements of the amplitude A prefer instead the KiDS-450 cosmology, which also aligns with the CFHTLenS cosmic shear results (Kilbinger et al., 2013). We further quantify this comparison in Section 5.5.6, first presenting results from our set of null tests, and then examining three sources of contamination and systematic biases that potentially affect our signal. In this work, we neglect the effect of source-lens coupling (Bernardeau, 1998), which could possibly act as another secondary signal, biasing the signal low. As it is the case for cosmic shear, this effect should be too small ($< 10\%$) to affect our results significantly, and further investigation will be required to interpret correctly the measurements from future surveys.

5.5.2 Null tests

We have shown in Section 5.4 and in Fig. 5.2 (red circles) that the parity violation *EB* test seems consistent with noise in most tomographic bins, but occasionally this is not obvious. In this section, we investigate the significance of these measurements. Statistically, this is accomplished by measuring the confidence at which we can reject the null hypothesis '*parity is not violated*'. We therefore re-run the full χ^2 statistical analysis[13] and measure the p-value about the model with $A = 0$. Low p-values correspond to high confidence of rejection, i.e., that some residual systematic effect might be causing and apparent parity violation. This type of measurement strongly probes the tail of the χ^2 distribution, hence assuming a Gaussian likelihood would provide inaccurate estimations of the p-values, even when including the Hartlap et al. (2007) debiasing α factor. Instead, we follow Sellentin et al. (2016) and assume a t-distribution for the likelihood, which better models the tail of the likelihood. Table 5.3 lists

[13]Due to the absence of parameters in the null hypothesis, the *EB* case has one additional degree of freedom compared to the *EE* case.

all these p-values, highlighting in bold one that seems slightly problematic (p-value ≤ 0.01). Since this single low p-value is only seen in one of the two estimators, we conclude that it must originate from expected noise fluctuations, and not from the data themselves. This conclusion is additionally supported by the fact that the level of B-modes in the KiDS data (i.e., the BB measurement) is consistent with zero on the scales we are probing (Hildebrandt et al., 2017).

For the sake of testing the robustness of the EB POLSPICE measurement, we have additionally investigated the effect of changing the number of bins from 5 to 10. In the EE case, the recovered values of A and the SNR are similar to those presented in Table 5.2, from which we conclude that this comes with no gain. However, when applied to the EB null test, something interesting happens: the 'problematic' measurement (p-value = 0.01 in the $z_{\rm B} \in [0.1, 0.3]$ bin, Table 5.3) relaxes to 0.09, as seen in the column labelled C_{10}. This is another indication that the cause of the low p-value originates from fluctuations in the noise – which is affected in the binning process – without pointing to residual systematic effects in the data.

We have verified that our measurement of A is robust against the removal of some scales. When we exclude the largest or the smallest angular bin in the $\xi^{\kappa_{\rm CMB}\gamma_t}$ measurement, results change by at most 0.7σ, generally by less than 0.2σ. This gives us confidence in the robustness of our measurement. The same holds when removing the highest ℓ bin from the POLSPICE measurement, but not for the lowest ℓ bin, which captures the peak of the signal, and therefore contributes significantly to the SNR. At the same time, this test illustrates that we are currently not sensitive to the effect of massive neutrinos nor to baryonic feedback, which mainly affect these non-linear scales.

5.5.3 Effect of intrinsic alignments

Intrinsic alignments (IA) are a known secondary effect in the cross-correlation of galaxy lensing and CMB lensing that lowers the amplitude of the measured signal (Hall et al., 2014; Troxel et al., 2014; Chisari et al., 2015). It is therefore important to investigate how much IA could contribute to the observed low values of A reported in Table 5.2. To estimate the contamination level, we compare two different models, which we then apply equally to both estimators, $C_\ell^{\kappa_{\rm CMB}\kappa_{\rm gal}}$ and $\xi^{\kappa_{\rm CMB}\gamma_t}(\vartheta)$.

First, we follow Hall et al. (2014, 'HT-IA' model hereafter) in using the 'linear non-linear alignment' model of Bridle et al. (2007) with the SuperCOSMOS normalization found in Brown et al. (2002). We recall that this prescription comes from constraints at $z = 0.1$ that are independent of galaxy type or colour, and that the effect of IA in this model is to reduce the amplitude of the observed signal, as the galaxies tend to align radially towards each other. The scale-dependence of the alignment contribution is similar to the lensing signal, as seen in Hall et al. (2014) and in Fig. 5.5, hence we only quote the percentage of contamination at $\ell = 1000$ for reference. This also allows us to confidently use the same IA contamination levels for the configuration space estimator, since rescaling $C_\ell^{\kappa_{\rm CMB}\kappa_{\rm gal}}$ by a constant rescales $\xi^{\kappa_{\rm CMB}\gamma_t}$ by the same constant (as per equation 5.1). For each of the five redshift bins considered in this chapter, starting from the lower redshift, we estimate a $\{10, 17, 10, 8, 5\}\%$ contamination to the signal, respectively. For the broader tomographic bin $z_{\rm B} \in [0.1, 0.9]$, we estimate an 11% contamination. In other words, within the HT-IA model, the measured value of $A_{\rm fid}$ in the broad bin (equation 5.12)

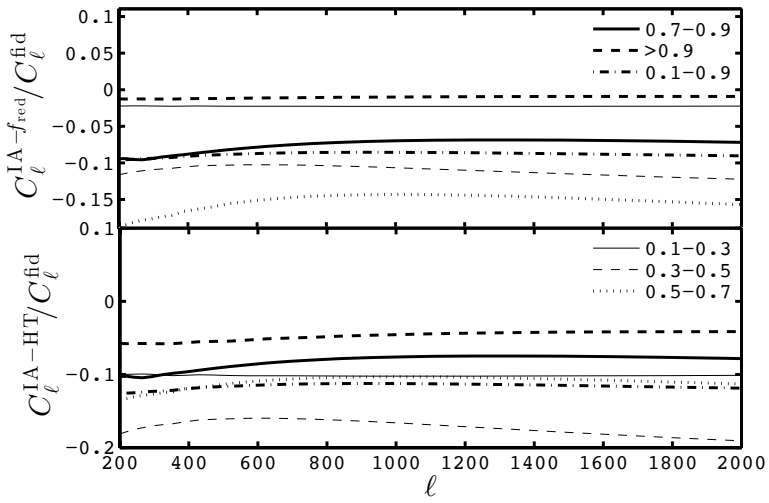

Figure 5.5: Strength of the contamination by intrinsic galaxy alignments for different tomographic bins, assuming our fiducial cosmology and the linear non-linear alignment model. The difference between lines is caused by changes in $n(z)$ (and in the red fraction in the $f_{\rm red}$-IA model).

should be corrected to

$$A_{\rm fid}^{\rm HT} = 0.77 \pm 0.15 \; . \tag{5.14}$$

The error bars here are not modified compared to the no-IA case since this contamination signal is additive. This model is the simplest as it assumes no luminosity or redshift dependence of the alignment normalization, and adopts the same alignment prescription for all galaxies regardless of morphological type or colour.

Second, we estimate the contamination from the alignment model of Chisari et al. (2015, '$f_{\rm red}$-IA' model hereafter) that allows for differential contributions based on galaxy colour/morphology. We assume that blue galaxies do not contribute at all, consistent with observations (Heymans et al., 2013; Mandelbaum et al., 2011), even though this null measurement remains poorly constrained. We estimate the red fraction directly from the data in each redshift bin using the best-fit spectral template returned by BPZ for each source, referred to as $\rm T_B$. Motivated by Simon et al. (2015), we identify red galaxies as objects with $\rm T_B < 1.5$.

For the five tomographic bins, we obtain fractions of red galaxies $f_{\rm red} = \{0.04, 0.12, 0.27, 0.18, 0.04\}$; we estimate $f_{\rm red} = 0.15$ for the broad bin. We then use the alignment amplitude for the red galaxies from Heymans et al. (2013) to obtain an estimate of alignment contamination given our red fractions. These results are presented in the upper panel of Fig. 5.5. With this method, we estimate a $\{2, 11, 14, 7, 1\}\%$ contamination from intrinsic alignments in the

tomographic bins, and a 9% contamination in the $z_{\rm B} \in [0.1, 0.9]$ bin.[14] Then we can estimate

$$A_{\rm fid}^{f_{\rm red}} = 0.75 \pm 0.15 \ . \tag{5.15}$$

One caveat with this model is that the K-correction and evolutionary corrections are uncertain at high redshift, which could result in biased estimates of the red fraction (see discussion in Chisari et al., 2015). This has an impact on the exact level of intrinsic alignment contamination by red galaxies, but we neglect this effect in this work.

Both methods are broadly consistent even though they differ in details, especially in the lowest redshift bin. For instance, the second method captures the redshift differences observed in the data and takes into account the split in contributions arising from different galaxy types, which introduces a slightly different redshift dependence of the IA signal. Nevertheless, the overall trends between the HT and the $f_{\rm red}$-IA models are similar, although that is not the case for all IA models (see, for example, the tidal torque theory from Codis et al., 2015, in which the sign of the IA effect on the signal is the opposite). There remains a large uncertainty in the modelling of the IA contamination, and we do not know which model, if any, should enter in our cosmological interpretation.

According to these estimations, both the HT-IA and $f_{\rm red}$-IA models help to bring A closer to unity. From the contamination levels listed above, at most 17% of the observed cross-correlation signal can be canceled by IA contamination in our tomographic bins. After correcting for this effect in each tomographic bin, most points agree with $A_{\rm fid} = 1$ within 1σ. This is shown with the colour symbols in Fig. 5.3.

Finally, we note that the uncertainty on the level of IA contamination quoted in the section is high, especially because of the unknown signal from the blue galaxies. For instance, at the 1σ level and assuming the linear non-linear alignment model, the IA contamination from blue galaxies could range from $-\{10, 15, 8, 6, 4\}$% to $+\{6, 9, 5, 4, 3\}$% in each tomographic bin, and from -10% to +6% in the $z_{\rm B} \in [0.1, 0.9]$ bin.

5.5.4 Effect of $n(z)$ errors

We investigate here the impact on our measurement of A from the uncertainty on the source redshift distribution. This is estimated from 100 bootstrap resamplings of the source catalogue, as detailed in Hildebrandt et al. (2017, the DIR method described therein). These samples consist of internal fluctuations in the $n(z)$, which we turn into fluctuations in the signal using equations 5.1–5.3. We present in the top panel of Fig. 5.6 the fractional error on the signal, i.e. $\sigma_{C_\ell}^{\rm boot}/C_\ell$. According to this error estimate, the uncertainty on $n(z)$ is up to 8% of the signal in the first redshift bin, then 4, 2 and 1% for the others, and about 3% for the $z_{\rm B} \in [0.1, 0.9]$ bin.

Note that this quantity is a measure of how the DIR $n(z)$ varies – and how it impacts the signal – across subsamples of the re-weighted spectroscopically-matched catalogue. This catalogue is by itself

[14] We measured the field-to-field variance in $f_{\rm red}$ and observed that it hardly varies except in the highest redshift bin, where the scatter could turn the 1% IA contamination into a 0.0–2.5% contamination. This remains small and should have a negligible impact on our results.

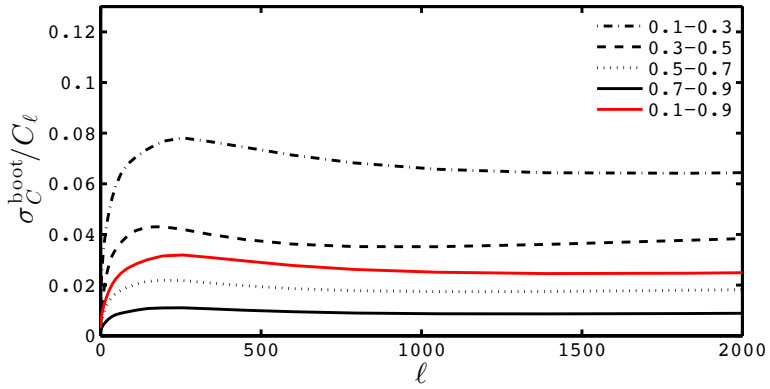

Figure 5.6: Fractional effect on the $C_\ell^{\kappa_{\rm CMB}\kappa_{\rm gal}}$ signal when varying the $n(z)$ between 100 bootstrap resamplings, for the four tomographic bins with $z_{\rm B} < 0.9$. Shown here is the 1σ scatter divided by the signal.

subsampling the full KiDS sources, and hence is subject to sampling variance. It is therefore likely that the error quoted above slightly under-estimates the true error on the signal due to the $n(z)$, as discussed in Section C3.1 of Hildebrandt et al. (2017). However, this is sub-dominant compared to our statistical uncertainty and is therefore not expected to affect our results.

For comparison purposes, we also investigated estimates of the redshift distribution determined using the cross-correlation between spectroscopic and photometric samples (known as the CC method in Hildebrandt et al., 2017; Morrison et al., 2017). This scheme has a high level of noise compared to the fiducial DIR method and we find that the error on the recovered C_ℓ in our analysis increases from $\sim$5% in the DIR case to $\sim$30% in the CC case. From this we can draw the same conclusion as the KiDS-450 cosmic shear analysis, namely that determining the redshift distribution using the cross-correlation CC method will remove any discrepancy with a Planck cosmology through inflation of the error bars. We believe, however, that the error on the CC estimate is not representative of our actual knowledge of the $n(z)$ in the KiDS data, and refer instead to the redshift distribution defined using the DIR method in the rest of this chapter.

Precision on the KiDS source redshift distribution will soon increase thanks to the ongoing processing of near-IR VIKING data (Hildebrandt et al. in prep.), which primarily impacts the high redshift tail so crucial to our measurement. Finally note that in the DIR method we are using a calibrated $n(z)$, estimated from weighted spectroscopic data, hence we do not have to worry nearly as much about catastrophic photo-z outliers. This was not the case for the analysis presented in HD16, which showed that for $n(z)$ estimated directly from photometric data (for e.g., CFHTLenS and RCSLenS), these can easily dominate the error budget, with systematic effects on the signal of the order of 15%. If our measurement contains more high-redshift objects than our $n(z)$ suggests, our predictions are too low; correcting for this would lower A.

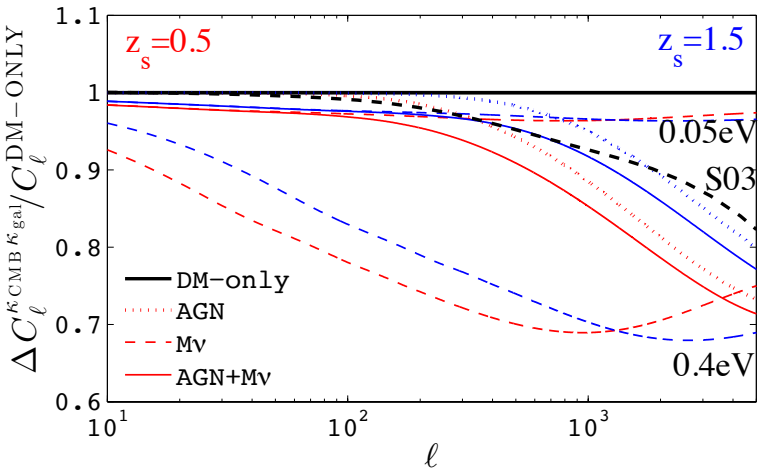

Figure 5.7: Fractional effect of the AGN baryon feedback and massive neutrinos on the cross-spectra, for different combinations of source planes. The red solid line shows the combined effect on the cross-spectrum for sources placed on a single plane at $z_s = 0.5$. The effect of 0.05 eV massive neutrinos and AGN feedback are shown separately by the upper dashed and dotted lines (also in red). The lower dashed red line shows the impact of 0.4 eV neutrinos. Blue lines show the same quantities, but for sources placed at $z_s = 1.5$. The dashed black line shows the ratio between the predictions from Smith et al. (2003) and that of Takahashi et al. (2012).

5.5.5 Baryon feedback, massive neutrinos and non-linear modelling

As shown in HD16, baryonic feedback and massive neutrinos can cause an important decrease of the cross-correlation signal, which would translate into lower values of A when compared to a fiducial dark matter only cosmology. To investigate how this could affect our cosmological results, we modify the $P(k,z)$ term in equation 5.1 to include 'massive neutrino bias' and 'baryon feedback bias', as detailed in Harnois-Déraps et al. (2015b). The baryon bias was extracted from the OWL simulations, assuming the AGN model (van Daalen et al., 2011), while the neutrino bias was extracted from the recalibrated HALOFIT code (Takahashi et al., 2012) with total neutrino masses M_ν = 0.05, 0.2, 0.4 and 0.6 eV. Our results are presented in Fig. 5.7 for two simplified cases, in which the source galaxy populations are placed on single planes at $z_s = 0.5$ (in red) and at $z_s = 1.5$ (in blue). The figure focuses on the 0.05 eV scenario, showing the suppression of power caused by massive neutrinos (3.5% effect on A for both z_s planes, averaged over the ℓ modes that we measured), by baryonic feedback (5.0% for $z_s = 1.5$ and 10.6% for $z_s = 0.5$), and by the combination of both (8.2% and 13.7% for $z_s = 1.5$ and 0.5 respectively). The reason why the effect of baryons is larger on the lower redshift source plane is simply a projection effect: the same physical scales subtend different angles on the sky, which contribute differently to our measurement restricted to the $\ell \in [20-2000]$ range. We also show the effect of 0.4 eV neutrinos (28% and 30% in the two z_s slices), which demonstrates a scaling of 7% per 0.1 eV. We note that Mead et al. (2015) proposed an alternative method to account simultaneously for baryons and neutrinos based on the halo model, which might prove useful in future work.

These two effects contribute at some level to the measurement of A, but it is too early to put constraints on them based on our measurement. Firstly, the cosmology is not guaranteed to be that of Planck, secondly the exact feedback mechanism that is at play in the Universe remains largely unknown, and thirdly other effects (e.g., IA contamination or errors in $n(z)$) could explain why our measured $A_{\rm fid}$ is low. However, if the fiducial cosmology is correct and if the intrinsic alignments are well described by the HT model outlined in Section 5.5.3, then $A_{\rm fid}$ would be brought to unity with $M_\nu = 0.33 \pm 0.22$ eV in the absence of baryonic feedback, and $M_\nu = 0.19 \pm 0.22$ eV within the AGN model.

We have verified that the uncertainty in the non-linear modelling does not affect our measurement of A significantly. This is mainly because the angles and redshifts probed by our measurement correspond to scales that are mostly in the linear and mildly non-linear regimes. Replacing the non-linear power spectrum from the Takahashi et al. (2012) model with that of Smith et al. (2003), corresponding to a radical change in the non-linear predictions at small scales shown in Fig. 5.7 (black dashed line), affects our measurement of A by only 1–2%. This is well within the statistical uncertainty and can be safely neglected. Figure 5.7 shows that there is a clear degeneracy between differences in the two models, and the effects of baryonic feedback. However, the Smith et al. (2003) predictions are known to suffer from a significant loss of power at small scales, visible in Fig. 5.7, and the state-of-the-art precision on the non-linear power spectrum, from e.g., the Cosmic Emulator (Heitmann et al., 2014) deviates from the Takahashi et al. (2012) model by less than 5% (Mead et al., 2015). This alleviates the degeneracy between modelling and baryonic feedback effects and further supports our (model-dependent) neutrino mass constraints presented above.

5.5.6 Cosmology from broad $n(z)$

In this section, we investigate how our cross-correlation measurement can constrain cosmology, and specifically compute confidence regions in the $(\sigma_8, \Omega_{\rm m})$ plane. For this calculation we assume massless neutrinos and no baryonic feedback; we also ignore the error on $n(z)$, but examine our results for the two IA models (as well as the 'no-IA' case) described in Section 5.5.3.

It was shown in Liu et al. (2015) that the amplitude of the cross-correlation signal scales approximately with $\sigma_8^2\Omega_{\rm m}^{-0.5}$ at large, linear scales ($\ell <$ few hundred), and as $\sigma_8^3\Omega_{\rm m}^{1.3}$ at small scales ($\ell > 1000$). Most of our constraints come from small scales, but our measurement includes some large modes down to $\ell \approx 200$. For this reason, we strike a compromise: we keep the $\Omega_{\rm m}^{1.3}$ dependence, as suggested by Liu et al. (2015), but use a $\sigma_8^{2.5}$ dependence, to capture the gradual transition between both. Future measurements will require Monte Carlo algorithms to be run to better capture these dependencies, but this is unnecessary in our case given the relatively large uncertainty on A.

As discussed before, we use the $\xi^{\kappa_{\rm CMB}\gamma_{\rm t}}$ results in the broad $z_{\rm B} \in [0.1, 0.9]$ tomographic bin because it has the highest signal to noise; however, our results would not change significantly if we used the $C_\ell^{\kappa_{\rm CMB}\kappa_{\rm gal}}$ measurement instead. We could also have used the tomographic results, i.e., the $A(z)$ varies in the four bins. However, these measurements are all correlated, probing common low-redshift lenses. Such an approach would require us to calculate and include cross-correlation coefficients between the different tomographic bins when solving for the best-fit cosmology. These could be evaluated from

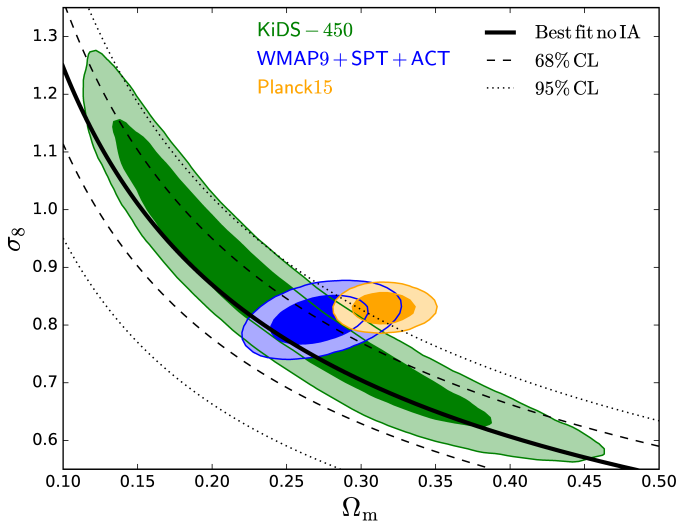

Figure 5.8: Constraints on σ_8 and Ω_m as estimated from the cross-correlation measurement, ignoring potential contamination by intrinsic galaxy alignments (shown in black). The solid line shows the best fit, while the dashed and dotted lines indicate the 68% and 95% confidence level (CL) regions, respectively. The cross-correlation results can be compared to KiDS-450 (green, where IA effects are accounted for), Planck (orange), and WMAP9+SPT+ACT (blue).

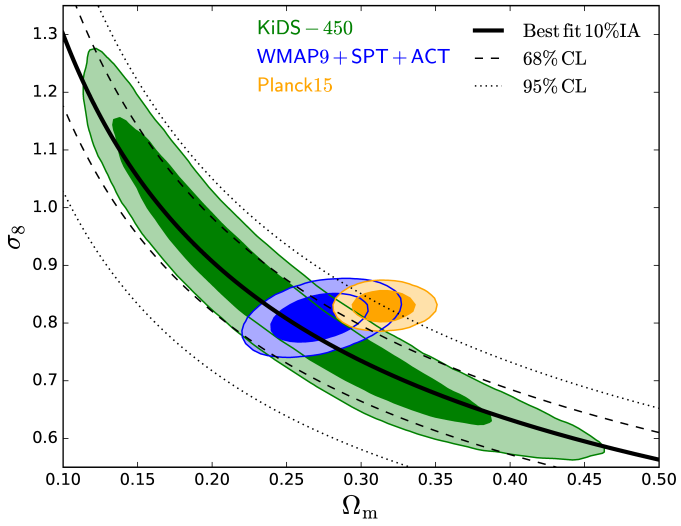

Figure 5.9: Same as Fig. 5.8, but here assuming 10% contamination from IA in the cross-correlation measurement (equation 5.17), consistent with both the 'HT-IA' and the 'f_{red}-IA' models.

mock data, but this is not required when working with a single data point for A. Combining this scaling relation with equations 5.12–5.14, we obtain

$$A = A_{\rm fid}\left(\frac{\sigma_8}{0.831}\right)^{2.5}\left(\frac{\Omega_{\rm m}}{0.2905}\right)^{1.3} = 0.69 \pm 0.15 \tag{5.16}$$

and

$$A = A_{\rm fid}^{\rm HT}\left(\frac{\sigma_8}{0.831}\right)^{2.5}\left(\frac{\Omega_{\rm m}}{0.2905}\right)^{1.3} = 0.77 \pm 0.15, \tag{5.17}$$

which we use to propagate the error on A into confidence regions in the $(\sigma_8, \Omega_{\rm m})$ plane. We show in Figs. 5.8 and 5.9 how these constraints compare to the results from KiDS-450 cosmic shear (with IA), *Planck* and pre-Planck experiments.[15] Our cross-correlation measurement has a larger overlap with the KiDS-450 constraints, but is still consistent with the Planck cosmology in the sense that their $\lesssim 95\%$ confidence regions overlap. Including IA reduces the offset from Planck.

Given that our signal has different dependences on cosmological (e.g., $\Omega_{\rm m}$ and σ_8) and nuisance (e.g., m, $n(z)$) parameters, we can see how this can provide new insights into resolving tensions between the cosmic shear and CMB measurements. For example, whereas the KiDS-450 and CFHTLenS cosmic shear results scale as $(1+m)^2 n^2(z)$, our KiDS-450 $\times$ Planck lensing measurement scales as $(1+m)\,n(z)$. This difference could therefore allow us to break the degeneracy in a joint probe analysis. Also note that in general, we should not exclude the possibility that there could be residual systematics left over in a CMB temperature and polarization analysis — driving the cosmology to higher $(\sigma_8, \Omega_{\rm m})$ values — that do not make their way to the CMB lensing map or into the joint probes measurement, in analogy with the cosmic shear c-term. This is certainly the case for the additive shear bias (the c-correction) described in Kuijken et al. (2015). Having this new kind of handle can help to identify the cause of disagreements between different probes, and will be central to the cosmological analyses of future surveys. We explore further how cross-correlation analyses can be turned into a calibration tool in the next section.

5.5.7 Application: photo-z and m-calibration

The CMB lensing–galaxy lensing cross-correlation signal has been identified as a promising alternative to calibrate cosmic shear data without relying completely on image simulations (Das et al., 2013; Liu et al., 2016; Schaan et al., 2017). This statement relies on the fact that A absorbs all phenomena that affect the amplitude of the measurement, i.e., cosmology, intrinsic alignment, $n(z)$, and shear calibration, and that we can marginalize over some of these in order to solve for others.

Most of the attention so far has been directed towards the multiplicative term in the cosmic shear calibration — the m^j factor in equation 5.7 — which has an important impact on the cosmological interpretation. In the case of the KiDS-450 data, the shear calibration is known at the percent level

[15] The MCMC chains entering these contour plots can be found on the KiDS-450 website: kids.strw.leidenuniv.nl/cosmicshear2016.php Note also that the WMAP9+SPT+ACT cosmology presented in Figs. 5.8 and 5.9 differ from the fiducial WMAP9+BAO+SN cosmology.

from image simulations for objects with $z_B < 0.9$ (see Fig. 5.11), but the precision on m^j quickly degrades at higher redshifts (Fenech Conti et al., 2017). Similar conclusions can be drawn from the photometric redshift estimation, which becomes unreliable at high redshift when only using optical bands (Hildebrandt et al., 2017). We see in our cross-correlation measurement a unique opportunity to place a joint-constraint on these two quantities in the highest redshift bin, informed by our measurements at lower redshift. We ignore the contribution from IA due to the high level of statistical noise in our measurement. However, this will need to be included in similar analyses of upcoming surveys with higher statistical precision.[16]

Our approach is to fix the scaling term A to the value preferred by the $z_B \in [0.1, 0.9]$ data, which we label $A_{\mathrm{low}z}$ here for clarity, and to jointly fit for the mean shear bias and mean redshift distribution in the $z_B > 0.9$ bin. Forcing A to this value in the high redshift bin provides constraints on $\langle 1 + m_{\mathrm{high}z} \rangle$ and $\langle n_{\mathrm{high}z}(z) \rangle$, which we extract by varying these quantities in the predictions.

The correction to the shear bias is trivial to implement as it scales linearly with A, so we simply write $A_{\mathrm{high}z} = A_{\mathrm{low}z}(1 + \delta_m) = 0.95 \pm 0.22$ (from Table 5.2) and solve for δ_m. If this was the only correction, we could write $\delta_m = A_{\mathrm{high}z}/A_{\mathrm{low}z} - 1 = 0.38 \pm 0.44$, which is consistent with zero but not well constrained.

Corrections to the photometric distribution can be slightly more complicated, since the full redshift distribution that enters our calculation is not simple, as seen in Fig. 5.1. There are a number ways in which we could alter the $n(z)$ and propagate the effect onto the signal, e.g., by modifying the overall shape, the mean or the tail of the distribution. We opted for arguably the simplest prescription, which consists of shifting the $n(z)$ along the z direction by applying the mapping $z \to z + \delta_z$ (thereby shifting $\langle n_{\mathrm{high}z}(z) \rangle$ by the same amount). We propagate this new $n(z)$ through equation 5.1 and solve for values of δ_z that satisfy constraints on A. In this process, we allow δ_z to vary by up to 0.5, which is rather extreme.

Following the simple reasoning described for the shear calibration, we can see that if m was trusted at the percent level in this high redshift bin, constraints on the redshift distribution could be simply derived by computing $A_{\mathrm{high}z}/A_{\mathrm{low}z} = C_{\delta_z}/C_{\mathrm{fid}} = (1 + \delta_z)$. We therefore obtain the exact same constraints as for δ_m, namely: $\delta_z = 0.38 \pm 0.44$. We place constraints on the (δ_m, δ_z) plane by requiring $(1 + \delta_m)(1 + \delta_z) = A_{\mathrm{high}z}/A_{\mathrm{low}z}$, and present the 1σ constraints in Fig. 5.10. The data are still consistent with $\delta_m = \delta_z = 0$, but these two biases are not currently well constrained.

We also show in Fig. 5.10 the results from the $C_\ell^{\kappa_{\mathrm{CMB}}\kappa_{\mathrm{gal}}}$ estimator (red dashed lines), but these have a lower SNR hence are not included in the analysis. At first sight, the difference observed between the results from the two estimators might appear worrisome. Given that these constraints on (δ_m, δ_z) are obtained from the same data, and that the only difference is the analysis method, it is justified to question whether we could use this measurement for precise self-calibration if two methods on the

[16] One might well object that the uncertainty in IA modelling and its evolution is already larger than the uncertainty in shear calibration, and hence that our strategy is flawed to start with; instead, we should be placing simultaneous constraints on the photo-z, m-calibration and IA. A full MCMC approach will certainly be required in the future to disentangle these effects, exploiting their different shape dependence to break the degeneracy between these parameters. As an illustration of this strategy, however, we present a simple case here and assume no IA contamination in this rest of this section.

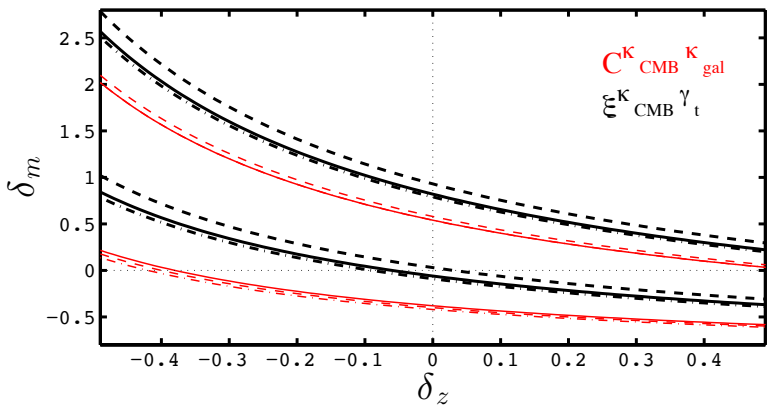

Figure 5.10: 1σ contour regions on the shear calibration correction δ_m and the redshift distribution correction δ_z in the bin $z_{\rm B} > 0.9$, from the cross-correlation measurements. Black and red lines correspond to constraints from $\xi^{\kappa_{\rm CMB}\gamma_{\rm t}}$ and $C_\ell^{\kappa_{\rm CMB}\kappa_{\rm gal}}$ respectively. The multiple lines present the results in three different cosmologies (fiducial is solid, KiDS-450 is dot-dashed, Planck is dashed), which are shown here to have a small impact on the constraints. Other independent measurements and improved image simulations could tighten the region of allowed values. The upper red solid and dot-dashed lines perfectly overlap.

same data give such different values for δ_m and δ_z. We recall that differences are expected, since both techniques are probing different scales, however, the calibration technique presented here is sensitive to these differences. The calibration is only weakly sensitive to the fiducial cosmology adopted, as shown in Fig. 5.10 using different line styles.

A significant improvement will come from future data sets (advanced-ACT, SPT-3G, LSST, Euclid), in which the noise will be much lower, allowing for more accurate measurements of $\xi^{\kappa_{\rm CMB}\gamma_{\rm t}}$ and $C_\ell^{\kappa_{\rm CMB}\kappa_{\rm gal}}$ to start with. In addition, including other measurements in this self-calibration approach will greatly enhance the achievable precision. For example, one could measure the galaxy-galaxy lensing signal from the same KiDS-450 source galaxies, using, e.g., the GAMA galaxies as lenses (van Uitert et al., 2016), selecting the sources in the same tomographic bin (i.e., $z_{\rm B} \in [0.1, 0.9]$ and $z_{\rm B} > 0.9$). Fixing the cosmology from the low redshift bin, one could then similarly constrain (δ_m, δ_z) in the high redshift bin. The idea here is that the trend can be made *opposite* to that seen in Fig. 5.10: an increase in δ_z pushes the sources away from the lenses, which, depending on the geometry, could reduce the signal. To compensate for this, the m-calibration would need to increase as well. In such a setup, the preferred region in parameter space would inevitably intersect with ours, and exploiting this complementarity might lead to competitive constraints. Further investigation of this combined measurement will be explored in upcoming work.

We are aware that our bi-linear modelling of the m and $n(z)$ calibration is an over-simplification of our knowledge (and uncertainty) about these quantities in the highest redshift bin, and one could envision improving this strategy in the future. For instance, the high-redshift objects are often the hardest to measure spectroscopically, hence there are greater chances that the DIR method fails at higher

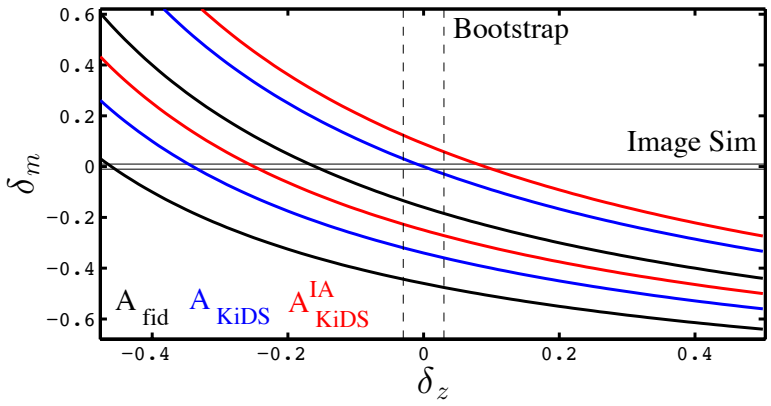

Figure 5.11: 1σ contour regions on the shear calibration correction δ_m and the redshift distribution correction δ_z derived from the $z_B \in [0.1, 0.9]$ measurement of A in three different cases. Results from $A_{\rm fid}$ (no-IA) are shown in solid black, results from $A_{\rm KiDS}$ (no IA) are shown in solid blue, and results from $A_{\rm KiDS}$ with 10% IA are shown in solid red. The pair of solid horizontal lines show the region of δ_m values allowed from image simulations, while the pair of dashed vertical lines show the region of δ_z values allowed from bootstrap resampling the $n(z)$.

redshifts. To capture this effect, instead of shifting the $n(z)$, one could modify only the high-redshift tail, moving 1%, 5% or 10% of our source galaxies from (very) low redshifts to $z > 1$, propagating the effect on the signal, and use our measurement of A to constrain the fraction of such 'missing' high-redshift galaxies. However, given the size of our error bars, it is not clear that we would learn more from this approach at the moment.

This situation will improve significantly with future CMB and galaxy surveys. According to Schaan et al. (2017), the lensing data provided by a Stage-4 CMB experiment, combined with 10 tomographic bins for LSST, will enable an m-calibration that is accurate to better than 0.5%. This comes from marginalising over a number of nuisance parameters that unfortunately does not include catastrophic photometric redshift outliers, so the actual accuracy will likely degrade compared to this impressive benchmark. Nevertheless, this is an avenue that is certainly worth exploiting with the upcoming data.

The $z_B < 0.9$ redshift data in the KiDS survey has been calibrated on image simulations whose precision on δ_m largely surpasses that of the cross-correlation technique presented in this section. Figure 5.11 shows the 1σ constraints in the (δ_m, δ_z) plane in the $z_B \in [0.1, 0.9]$ bin assuming the fiducial cosmology without IA (black), the KiDS-450 cosmology without IA (blue), and the KiDS-450 with 10% IA (red), consistent with both the HT-IA and $f_{\rm red}$-IA models. For comparison, the 1% precision on δ_m obtained from image simulations and the 3% precision on δ_z obtained from bootstrap resampling the $n(z)$, described in Section 5.5.4, are shown as the pairs of horizontal and vertical lines, respectively. For these redshifts at least, the measurement provides interesting constraints on the cosmology, IA and δ_z, but not on the m-calibration.

5.6 Conclusions

We perform the first tomographic lensing-lensing cross-correlation by combining the Planck 2015 lensing map with the KiDS-450 shear data. Our measurement is based on two independent estimators, the POLSPICE measurement of $C_\ell^{\kappa_{\rm CMB}\kappa_{\rm gal}}$, and the configuration-space measurement of $\xi^{\kappa_{\rm CMB}\gamma_t}(\vartheta)$. The two techniques agree within 1σ in all tomographic bins, although the former exhibits a lower signal to noise ratio.

We compare our tomographic results against a two-dimensional lensing analysis of a single broad redshift bin ($z_{\rm B} \in [0.1, 0.9]$), and fit the measured amplitude of the signal with a single multiplicative parameter A that scales the predictions. We obtain $A_{\rm fid} = 0.69 \pm 0.15$ in our fiducial cosmology, and show that the constraints on the $(\sigma_8, \Omega_{\rm m})$ plane are consistent with the flat ΛCDM Planck cosmology at the 95% level, with $A_{\rm Planck} = 0.68 \pm 0.15$, and with all previous results (Hand et al., 2015; Liu et al., 2015; Singh et al., 2017, K16 & HD16). The KiDS-450 cosmology is preferred, however, and in this case we obtain $A_{\rm KiDS} = 0.86 \pm 0.19$.

Photometric redshifts have been examined carefully and are unlikely to be affecting these results significantly ($< 8\%$ effect on the signal), unless the spectroscopic sample that is used to estimate the $n(z)$ distribution suffers from significant sampling variance. Multiplicative shear calibration is also highly unlikely to be affecting A, since it is known to be accurate at the percent level over the redshift range that enters our cosmological measurement. However, including different models of intrinsic alignment, massive neutrinos and baryon feedback in the predictions all affect the signal by tens of percent, pushing the recovered A to higher values.

Fixing the cosmology to that favoured by our low-redshift measurements ($z_{\rm B} < 0.9$), we calibrate the high-redshift ($z_{\rm B} > 0.9$) photometric $n(z)$ and the multiplicative shear calibration, which are not robustly constrained. We find that the high redshift data are consistent with no residual systematics, but that these are still allowed and only weakly constrained. Improved results on this high-redshift calibration will come in the future from larger data sets, from improved image simulations and from the combination with other independent measurements.

Tomographic measurements such as that presented in this chapter are insensitive to galaxy bias, and hence open the possibility of obtaining cosmological constraints from measurements of the growth factor. Upcoming and future lensing surveys will provide excellent opportunities for combining probes and improving their cosmological constraints.

Chapter 6

Concluding remarks

The fundamental question underlying all work presented in this thesis is the nature of dark matter. The work explores different facets of this question, relying on the cross-correlation of gravitational lensing with other cosmological probes.

In Chapter 2 we investigate the microscopic nature of dark matter by measuring the cross-correlation between gamma rays from Fermi-LAT and weak gravitational lensing from CFHTLenS, RCSLenS, and KiDS. We do not observe a cross-correlation signal and use this non-detection to constrain the mass, annihilation cross-section, and decay rate of WIMP dark matter. Accounting for astrophysical sources of gamma rays and assuming strong clustering of dark matter at small scales, we are able to exclude the thermal relic cross-section for dark matter particle masses of $m_{\rm DM} \lesssim 20\,{\rm GeV}$. This constraint is comparable to other analyses of the extra-galactic gamma-ray flux, such as those of its isotropic intensity energy spectrum (Ackermann et al., 2015d) or its auto-power spectrum (Fornasa et al., 2016). Exclusion limits derived from local probes, such as dSphs, are stronger, however (Ackermann et al., 2015c). However, since our analysis is based on a cross-correlation with lensing, it probes different structures and is less affected by systematics. The work also presented the first use of tomography in a weak lensing cross-correlation, pushing the boundaries of this versatile technique.

Baryon physics can significantly affect the matter distribution, especially at small scales (e.g., van Daalen et al., 2011). Since gravitational lensing probes the total matter distribution, gravitational lensing measurements are affected by these baryonic processes (Semboloni et al., 2011; Harnois-Déraps et al., 2015b). It is therefore important to understand the behaviour of baryonic matter if we wish to make solid inference on the dark matter distribution from gravitational lensing. Chapter 3 presents the analysis of the cross-correlation of the thermal Sunyaev-Zeldovich (tSZ) effect, a direct tracer of hot, diffuse gas, and weak gravitational lensing from RCSLenS. A cross-correlation signal is detected at 8σ significance. The measured signal is then compared to predictions from the cosmo-OWLS suite of hydrodynamical simulations, where we find that the data prefer models with significant active galactic nuclei (AGN) feedback. The scatter of the simulations and the limited range of angular scales we have access to in the data currently hide the scale-dependence of the different feedback models, making the effect of AGN feedback degenerate with that of σ_8. However, upcoming data and simulation products will be able to break this degeneracy and produce much tighter constraints using this technique.

The modelling of the cross-correlations signals uses a number of approximations to connect the three-dimensional matter distribution to the two-dimensional angular power spectrum, such as the Born approximation and neglecting other higher order terms of the gravitational potential. In Chapter 4 we examine these approximations in detail for the case of the cross-correlation of lensing and tSZ. We consider terms up to fourth order in the potential, including a new term due to rotation in the reduced shear. The standard second order expressions for the angular power spectrum are found to be sufficiently accurate for current and upcoming surveys. Certain third-order effects might become important at very small scales in future surveys, such as cross-correlations with a tSZ map from a CMB Stage 4 (Abazajian et al., 2016) experiment.

Chapter 5 studies the tomographic cross-correlation of CMB lensing from Planck with galaxy lensing from KiDS. The tomographic measurement allows the analysis of the growth of structure, which shows no deviation from the prediction based on a Universe made of cold dark matter and dark energy. Furthermore, we search for residual systematics in the galaxy lensing data. We find no evidence for multiplicative bias of the ellipticity estimate nor of errors in the estimate of the source distribution. With current data, the constraints on these biases from cross-correlation are still significantly weaker than those from direct methods (e.g, Fenech Conti et al., 2017; Hildebrandt et al., 2017), but future data sets will be able provide comparable and complementary constraints.

6.1 Future prospects

All analyses presented in this thesis are based on cross-correlation between essentially full-sky maps and relatively small regions of weak lensing data. The small sky fraction of the weak lensing data sets – combined they reach about 1000 deg^2 or 2.5% of the sky – restrict the power of these analyses. However, it also demonstrates the potential of these techniques for next-generation lensing surveys, such as full area KiDS, DES, LSST, and Euclid. For example, extrapolating our measurement of the cross-correlation between gamma rays and lensing suggests that a 4000 deg^2 lensing survey with KiDS characteristics would be able to detect a cross-correlation with astrophysical gamma-ray sources at 3σ significance. A cross-correlation between full-depth DES and 10 years of Fermi-LAT data could potentially detect a dark matter gamma-ray signal at $\gtrsim 5\sigma$ significance (Camera et al., 2015).

In the analysis of the cross-correlation between gravitational lensing and gamma rays the astrophysical contribution to the extra-galactic gamma-ray flux was considered a contaminant to our primary signal, the gamma-ray flux from dark matter annihilations and decays. However, the astrophysical signal is interesting in its own right. It is believed to be dominated by blazars – AGN with their jets pointed towards us – and thus probes similar physical processes to those considered in Chapter 3. High-energy emissions such as gamma rays could therefore be used as an additional lever to calibrate simulations.

The different cross-correlations have been analysed in isolation so far. Jointly analysing multiple, complementary probes is expected to break degeneracies and ensures that the different measurements are consistent. In fact, a joint analysis of the three cross-correlations between galaxy lensing, tSZ, and CMB lensing is currently being performed by the author of this thesis. The primary aims are to constrain baryon physics and the mass of the neutrinos. Since baryon physics affects the matter distribution in

the non-linear regime, the amplitude and scale-dependence of baryon physic effects on galaxy lensing and CMB lensing is not the same. The tSZ effect, by probing the gas directly, exhibits a different dependence on baryonic processes again. The effects of massive neutrinos and cosmological parameters, such as σ_8, on the matter distribution, and hence lensing, differs from that on the tSZ effect as well. By exploiting the different effects of baryon physics, massive neutrinos, and cosmological parameters on the different probes and their cross-correlations, we will be able to break the degeneracies we observed in the analyses of the single cross-correlations by themselves. In a similar vein, the joint analysis will allow us to constrain systematics, such as m-corrections, redshift distribution uncertainties, and intrinsic alignment more efficiently, thus making the analysis and its inferences more robust. Including upcoming CMB data sets, such as from ACTPol (Thornton et al., 2016) will reduce the noise in the reconstruction of the lensing of the CMB and improve the resolution of the tSZ map at small scales, increasing the overall SNR of the measurements and allowing us to further break degeneracies through access to smaller scales. The joint analysis of the cross-correlations between galaxy lensing, tSZ, and CMB lensing can be augmented by the auto-correlations of the three probes and inclusions of external data sets at the likelihood level, such as the primary CMB and BAO data, allowing us to further increase our understanding of baryon physics, massive neutrinos, and cosmology, while tightening constraints on systematics.

If one only cares about cosmological parameters, such as the dark energy equation of state, a complimentary approach to modelling baryon physics is to marginalise over a suitable set of parameters describing the effects of baryonic processes (Zentner et al., 2008, 2013; Eifler et al., 2015). However, this approach also benefits from including probes that are sensitive to baryon physics, as they allow us to find better sets of parameters describing baryonic effects and hence tighten their priors.

A recurring difficulty in the works presented in this thesis has been the accurate estimation of the data covariance. While the covariance of the power spectrum in the linear regime is diagonal and only depends on power spectra, non-linear processes cause the different modes to couple and the trispectrum contribution becomes non-negligible. Modelling the trispectrum is difficult, considering that finding accurate models for the power spectrum is often a formidable task in itself. An alternative approach is to create many realisations of the data from simulations and estimate the data covariance directly from the covariance of these realisations. To reduce the noise in the covariance, large numbers of realisations are required (Hartlap et al., 2007; Taylor et al., 2013, 2014). The computational cost can be prohibitively expensive when hydrodynamical simulations are required, like in the case of the tSZ effect. Reducing the size of the data vector through data compression schemes, such as Karhunen-Loéve methods (Tegmark et al., 1997), can reduce the number of required realisations but the effectiveness of this approach is still a topic of ongoing research. A third approach is to rely on internal covariance estimators, such as the jackknife and bootstrap methods. These methods are computationally cheap and require no modelling. However, the simple implementations used in cosmology are known to yield biased covariance estimates. Developing methods to correct for these biases would make it possible to take full advantage of the benefits of internal covariance estimators and is therefore a worthwhile endeavour.

Bibliography

K. N. Abazajian, P. Adshead, Z. Ahmed, S. W. Allen, D. Alonso, K. S. Arnold, C. Baccigalupi, J. G. Bartlett, N. Battaglia, B. A. Benson, C. A. Bischoff, J. Borrill, V. Buza, E. Calabrese, R. Caldwell, J. E. Carlstrom, C. L. Chang, T. M. Crawford, F.-Y. Cyr-Racine, F. De Bernardis, T. de Haan, S. di Serego Alighieri, J. Dunkley, C. Dvorkin, J. Errard, G. Fabbian, S. Feeney, S. Ferraro, J. P. Filippini, R. Flauger, G. M. Fuller, V. Gluscevic, D. Green, D. Grin, E. Grohs, J. W. Henning, J. C. Hill, R. Hlozek, G. Holder, W. Holzapfel, W. Hu, K. M. Huffenberger, R. Keskitalo, L. Knox, A. Kosowsky, J. Kovac, E. D. Kovetz, C.-L. Kuo, A. Kusaka, M. Le Jeune, A. T. Lee, M. Lilley, M. Loverde, M. S. Madhavacheril, A. Mantz, D. J. E. Marsh, J. McMahon, P. D. Meerburg, J. Meyers, A. D. Miller, J. B. Munoz, H. N. Nguyen, M. D. Niemack, M. Peloso, J. Peloton, L. Pogosian, C. Pryke, M. Raveri, C. L. Reichardt, G. Rocha, A. Rotti, E. Schaan, M. M. Schmittfull, D. Scott, N. Sehgal, S. Shandera, B. D. Sherwin, T. L. Smith, L. Sorbo, G. D. Starkman, K. T. Story, A. van Engelen, J. D. Vieira, S. Watson, N. Whitehorn, and W. L. Kimmy Wu. CMB-S4 Science Book, First Edition. *ArXiv e-prints*, Oct. 2016. → pages 118

T. Abbott et al. The Dark Energy Survey: more than dark energy - an overview. *Mon. Not. Roy. Astron. Soc.*, 2016. doi: 10.1093/mnras/stw641. → pages 68

F. Acero, M. Ackermann, M. Ajello, A. Albert, W. B. Atwood, M. Axelsson, L. Baldini, J. Ballet, G. Barbiellini, D. Bastieri, A. Belfiore, R. Bellazzini, E. Bissaldi, R. D. Blandford, E. D. Bloom, J. R. Bogart, R. Bonino, E. Bottacini, J. Bregeon, R. J. Britto, P. Bruel, R. Buehler, T. H. Burnett, S. Buson, G. A. Caliandro, R. A. Cameron, R. Caputo, M. Caragiulo, P. A. Caraveo, J. M. Casandjian, E. Cavazzuti, E. Charles, R. C. G. Chaves, A. Chekhtman, C. C. Cheung, J. Chiang, G. Chiaro, S. Ciprini, R. Claus, J. Cohen-Tanugi, L. R. Cominsky, J. Conrad, S. Cutini, F. D'Ammando, A. de Angelis, M. DeKlotz, F. de Palma, R. Desiante, S. W. Digel, L. Di Venere, P. S. Drell, R. Dubois, D. Dumora, C. Favuzzi, S. J. Fegan, E. C. Ferrara, J. Finke, A. Franckowiak, Y. Fukazawa, S. Funk, P. Fusco, F. Gargano, D. Gasparrini, B. Giebels, N. Giglietto, P. Giommi, F. Giordano, M. Giroletti, T. Glanzman, G. Godfrey, I. A. Grenier, M.-H. Grondin, J. E. Grove, L. Guillemot, S. Guiriec, D. Hadasch, A. K. Harding, E. Hays, J. W. Hewitt, A. B. Hill, D. Horan, G. Iafrate, T. Jogler, G. Jóhannesson, R. P. Johnson, A. S. Johnson, T. J. Johnson, W. N. Johnson, T. Kamae, J. Kataoka, J. Katsuta, M. Kuss, G. La Mura, D. Landriu, S. Larsson, L. Latronico, M. Lemoine-Goumard, J. Li, L. Li, F. Longo, F. Loparco, B. Lott, M. N. Lovellette, P. Lubrano, G. M. Madejski, F. Massaro, M. Mayer, M. N. Mazziotta, J. E. McEnery, P. F. Michelson, N. Mirabal, T. Mizuno, A. A. Moiseev, M. Mongelli, M. E. Monzani, A. Morselli, I. V. Moskalenko, S. Murgia, E. Nuss, M. Ohno, T. Ohsugi, N. Omodei, M. Orienti, E. Orlando, J. F. Ormes, D. Paneque, J. H. Panetta, J. S. Perkins, M. Pesce-Rollins, F. Piron, G. Pivato, T. A. Porter, J. L. Racusin, R. Rando, M. Razzano, S. Razzaque, A. Reimer, O. Reimer, T. Reposeur, L. S. Rochester, R. W. Romani, D. Salvetti, M. Sánchez-Conde, P. M. Saz Parkinson, A. Schulz, E. J. Siskind, D. A. Smith, F. Spada, G. Spandre, P. Spinelli, T. E. Stephens, A. W. Strong, D. J. Suson, H. Takahashi, T. Takahashi, Y. Tanaka, J. G. Thayer, J. B. Thayer, D. J. Thompson, L. Tibaldo, O. Tibolla, D. F.

Torres, E. Torresi, G. Tosti, E. Troja, B. Van Klaveren, G. Vianello, B. L. Winer, K. S. Wood, M. Wood, S. Zimmer, and Fermi-LAT Collaboration. Fermi Large Area Telescope Third Source Catalog. ApJS, 218:23, June 2015. doi: 10.1088/0067-0049/218/2/23. → pages 29, 34

M. Ackermann, M. Ajello, A. Allafort, L. Baldini, J. Ballet, D. Bastieri, K. Bechtol, R. Bellazzini, B. Berenji, E. D. Bloom, E. Bonamente, A. W. Borgland, A. Bouvier, J. Bregeon, M. Brigida, P. Bruel, R. Buehler, S. Buson, G. A. Caliandro, R. A. Cameron, P. A. Caraveo, J. M. Casandjian, C. Cecchi, E. Charles, A. Chekhtman, C. C. Cheung, J. Chiang, A. N. Cillis, S. Ciprini, R. Claus, J. Cohen-Tanugi, J. Conrad, S. Cutini, F. de Palma, C. D. Dermer, S. W. Digel, E. d. C. e. Silva, P. S. Drell, A. Drlica-Wagner, C. Favuzzi, S. J. Fegan, P. Fortin, Y. Fukazawa, S. Funk, P. Fusco, F. Gargano, D. Gasparrini, S. Germani, N. Giglietto, F. Giordano, T. Glanzman, G. Godfrey, I. A. Grenier, S. Guiriec, M. Gustafsson, D. Hadasch, M. Hayashida, E. Hays, R. E. Hughes, G. Jóhannesson, A. S. Johnson, T. Kamae, H. Katagiri, J. Kataoka, J. Knödlseder, M. Kuss, J. Lande, F. Longo, F. Loparco, B. Lott, M. N. Lovellette, P. Lubrano, G. M. Madejski, P. Martin, M. N. Mazziotta, J. E. McEnery, P. F. Michelson, T. Mizuno, C. Monte, M. E. Monzani, A. Morselli, I. V. Moskalenko, S. Murgia, S. Nishino, J. P. Norris, E. Nuss, M. Ohno, T. Ohsugi, A. Okumura, N. Omodei, E. Orlando, M. Ozaki, D. Parent, M. Persic, M. Pesce-Rollins, V. Petrosian, M. Pierbattista, F. Piron, G. Pivato, T. A. Porter, S. Rainò, R. Rando, M. Razzano, A. Reimer, O. Reimer, S. Ritz, M. Roth, C. Sbarra, C. Sgrò, E. J. Siskind, G. Spandre, P. Spinelli, Ł. Stawarz, A. W. Strong, H. Takahashi, T. Tanaka, J. B. Thayer, L. Tibaldo, M. Tinivella, D. F. Torres, G. Tosti, E. Troja, Y. Uchiyama, J. Vandenbroucke, G. Vianello, V. Vitale, A. P. Waite, M. Wood, and Z. Yang. GeV Observations of Star-forming Galaxies with the Fermi Large Area Telescope. ApJ, 755:164, Aug. 2012. doi: 10.1088/0004-637X/755/2/164. → pages 30

M. Ackermann, M. Ajello, A. Albert, W. B. Atwood, L. Baldini, J. Ballet, G. Barbiellini, D. Bastieri, K. Bechtol, R. Bellazzini, E. Bissaldi, R. D. Blandford, E. D. Bloom, E. Bottacini, T. J. Brandt, J. Bregeon, P. Bruel, R. Buehler, S. Buson, G. A. Caliandro, R. A. Cameron, M. Caragiulo, P. A. Caraveo, E. Cavazzuti, C. Cecchi, E. Charles, A. Chekhtman, J. Chiang, G. Chiaro, S. Ciprini, R. Claus, J. Cohen-Tanugi, J. Conrad, A. Cuoco, S. Cutini, F. D'Ammando, A. de Angelis, F. de Palma, C. D. Dermer, S. W. Digel, E. d. C. e. Silva, P. S. Drell, C. Favuzzi, E. C. Ferrara, W. B. Focke, A. Franckowiak, Y. Fukazawa, S. Funk, P. Fusco, F. Gargano, D. Gasparrini, S. Germani, N. Giglietto, P. Giommi, F. Giordano, M. Giroletti, G. Godfrey, G. A. Gomez-Vargas, I. A. Grenier, S. Guiriec, M. Gustafsson, D. Hadasch, K. Hayashi, E. Hays, J. W. Hewitt, P. Ippoliti, T. Jogler, G. Jóhannesson, A. S. Johnson, W. N. Johnson, T. Kamae, J. Kataoka, J. Knödlseder, M. Kuss, S. Larsson, L. Latronico, J. Li, L. Li, F. Longo, F. Loparco, B. Lott, M. N. Lovellette, P. Lubrano, G. M. Madejski, A. Manfreda, F. Massaro, M. Mayer, M. N. Mazziotta, J. E. McEnery, P. F. Michelson, W. Mitthumsiri, T. Mizuno, A. A. Moiseev, M. E. Monzani, A. Morselli, I. V. Moskalenko, S. Murgia, R. Nemmen, E. Nuss, T. Ohsugi, N. Omodei, E. Orlando, J. F. Ormes, D. Paneque, J. H. Panetta, J. S. Perkins, M. Pesce-Rollins, F. Piron, G. Pivato, T. A. Porter, S. Rainò, R. Rando, M. Razzano, S. Razzaque, A. Reimer, O. Reimer, T. Reposeur, S. Ritz, R. W. Romani, M. Sánchez-Conde, M. Schaal, A. Schulz, C. Sgrò, E. J. Siskind, G. Spandre, P. Spinelli, A. W. Strong, D. J. Suson, H. Takahashi, J. G. Thayer, J. B. Thayer, L. Tibaldo, M. Tinivella, D. F. Torres, G. Tosti, E. Troja, Y. Uchiyama, G. Vianello, M. Werner, B. L. Winer, K. S. Wood, M. Wood, G. Zaharijas, and S. Zimmer. The Spectrum of Isotropic Diffuse Gamma-Ray Emission between 100 MeV and 820 GeV. ApJ, 799:86, Jan. 2015a. doi: 10.1088/0004-637X/799/1/86. → pages 28, 29, 44

M. Ackermann, M. Ajello, W. B. Atwood, L. Baldini, J. Ballet, G. Barbiellini, D. Bastieri, J. Becerra Gonzalez, R. Bellazzini, E. Bissaldi, R. D. Blandford, E. D. Bloom, R. Bonino, E. Bottacini, T. J.

Brandt, J. Bregeon, R. J. Britto, P. Bruel, R. Buehler, S. Buson, G. A. Caliandro, R. A. Cameron, M. Caragiulo, P. A. Caraveo, B. Carpenter, J. M. Casandjian, E. Cavazzuti, C. Cecchi, E. Charles, A. Chekhtman, C. C. Cheung, J. Chiang, G. Chiaro, S. Ciprini, R. Claus, J. Cohen-Tanugi, L. R. Cominsky, J. Conrad, S. Cutini, R. D'Abrusco, F. D'Ammando, A. de Angelis, R. Desiante, S. W. Digel, L. Di Venere, P. S. Drell, C. Favuzzi, S. J. Fegan, E. C. Ferrara, J. Finke, W. B. Focke, A. Franckowiak, L. Fuhrmann, Y. Fukazawa, A. K. Furniss, P. Fusco, F. Gargano, D. Gasparrini, N. Giglietto, P. Giommi, F. Giordano, M. Giroletti, T. Glanzman, G. Godfrey, I. A. Grenier, J. E. Grove, S. Guiriec, J. W. Hewitt, A. B. Hill, D. Horan, R. Itoh, G. Jóhannesson, A. S. Johnson, W. N. Johnson, J. Kataoka, T. Kawano, F. Krauss, M. Kuss, G. La Mura, S. Larsson, L. Latronico, C. Leto, J. Li, L. Li, F. Longo, F. Loparco, B. Lott, M. N. Lovellette, P. Lubrano, G. M. Madejski, M. Mayer, M. N. Mazziotta, J. E. McEnery, P. F. Michelson, T. Mizuno, A. A. Moiseev, M. E. Monzani, A. Morselli, I. V. Moskalenko, S. Murgia, E. Nuss, M. Ohno, T. Ohsugi, R. Ojha, N. Omodei, M. Orienti, E. Orlando, A. Paggi, D. Paneque, J. S. Perkins, M. Pesce-Rollins, F. Piron, G. Pivato, T. A. Porter, S. Rainò, R. Rando, M. Razzano, S. Razzaque, A. Reimer, O. Reimer, R. W. Romani, D. Salvetti, M. Schaal, F. K. Schinzel, A. Schulz, C. Sgrò, E. J. Siskind, K. V. Sokolovsky, F. Spada, G. Spandre, P. Spinelli, L. Stawarz, D. J. Suson, H. Takahashi, T. Takahashi, Y. Tanaka, J. G. Thayer, J. B. Thayer, L. Tibaldo, D. F. Torres, E. Torresi, G. Tosti, E. Troja, Y. Uchiyama, G. Vianello, B. L. Winer, K. S. Wood, and S. Zimmer. The Third Catalog of Active Galactic Nuclei Detected by the Fermi Large Area Telescope. ApJ, 810:14, Sept. 2015b. doi: 10.1088/0004-637X/810/1/14. → pages 29

M. Ackermann, A. Albert, B. Anderson, W. B. Atwood, L. Baldini, G. Barbiellini, D. Bastieri, K. Bechtol, R. Bellazzini, E. Bissaldi, R. D. Blandford, E. D. Bloom, R. Bonino, E. Bottacini, T. J. Brandt, J. Bregeon, P. Bruel, R. Buehler, G. A. Caliandro, R. A. Cameron, R. Caputo, M. Caragiulo, P. A. Caraveo, C. Cecchi, E. Charles, A. Chekhtman, J. Chiang, G. Chiaro, S. Ciprini, R. Claus, J. Cohen-Tanugi, J. Conrad, A. Cuoco, S. Cutini, F. D'Ammando, A. de Angelis, F. de Palma, R. Desiante, S. W. Digel, L. Di Venere, P. S. Drell, A. Drlica-Wagner, R. Essig, C. Favuzzi, S. J. Fegan, E. C. Ferrara, W. B. Focke, A. Franckowiak, Y. Fukazawa, S. Funk, P. Fusco, F. Gargano, D. Gasparrini, N. Giglietto, F. Giordano, M. Giroletti, T. Glanzman, G. Godfrey, G. A. Gomez-Vargas, I. A. Grenier, S. Guiriec, M. Gustafsson, E. Hays, J. W. Hewitt, D. Horan, T. Jogler, G. Jóhannesson, M. Kuss, S. Larsson, L. Latronico, J. Li, L. Li, M. Llena Garde, F. Longo, F. Loparco, P. Lubrano, D. Malyshev, M. Mayer, M. N. Mazziotta, J. E. McEnery, M. Meyer, P. F. Michelson, T. Mizuno, A. A. Moiseev, M. E. Monzani, A. Morselli, S. Murgia, E. Nuss, T. Ohsugi, M. Orienti, E. Orlando, J. F. Ormes, D. Paneque, J. S. Perkins, M. Pesce-Rollins, F. Piron, G. Pivato, T. A. Porter, S. Rainò, R. Rando, M. Razzano, A. Reimer, O. Reimer, S. Ritz, M. Sánchez-Conde, A. Schulz, N. Sehgal, C. Sgrò, E. J. Siskind, F. Spada, G. Spandre, P. Spinelli, L. Strigari, H. Tajima, H. Takahashi, J. B. Thayer, L. Tibaldo, D. F. Torres, E. Troja, G. Vianello, M. Werner, B. L. Winer, K. S. Wood, M. Wood, G. Zaharijas, S. Zimmer, and Fermi-LAT Collaboration. Searching for Dark Matter Annihilation from Milky Way Dwarf Spheroidal Galaxies with Six Years of Fermi Large Area Telescope Data. *Physical Review Letters*, 115(23):231301, Dec. 2015c. doi: 10.1103/PhysRevLett.115.231301. → pages 23, 48, 49, 117

M. Ackermann et al. Limits on dark matter annihilation signals from the Fermi LAT 4-year measurement of the isotropic gamma-ray background. J. Cosmology Astropart. Phys., 9:008, Sept. 2015d. doi: 10.1088/1475-7516/2015/09/008. → pages 23, 34, 46, 49, 117

M. Ajello, D. Gasparrini, M. Sánchez-Conde, G. Zaharijas, M. Gustafsson, J. Cohen-Tanugi, C. D. Dermer, Y. Inoue, D. Hartmann, M. Ackermann, K. Bechtol, A. Franckowiak, A. Reimer, R. W. Romani, and A. W. Strong. The Origin of the Extragalactic Gamma-Ray Background and

Implications for Dark Matter Annihilation. ApJ, 800:L27, Feb. 2015. doi: 10.1088/2041-8205/800/2/L27. → pages 29

L. Anderson, E. Aubourg, S. Bailey, F. Beutler, A. S. Bolton, J. Brinkmann, J. R. Brownstein, C.-H. Chuang, A. J. Cuesta, K. S. Dawson, D. J. Eisenstein, S. Ho, K. Honscheid, E. A. Kazin, D. Kirkby, M. Manera, C. K. McBride, O. Mena, R. C. Nichol, M. D. Olmstead, N. Padmanabhan, N. Palanque-Delabrouille, W. J. Percival, F. Prada, A. J. Ross, N. P. Ross, A. G. Sánchez, L. Samushia, D. J. Schlegel, D. P. Schneider, H.-J. Seo, M. A. Strauss, D. Thomas, J. L. Tinker, R. Tojeiro, L. Verde, D. Wake, D. H. Weinberg, X. Xu, and C. Yeche. The clustering of galaxies in the SDSS-III Baryon Oscillation Spectroscopic Survey: measuring D_A and H at z = 0.57 from the baryon acoustic peak in the Data Release 9 spectroscopic Galaxy sample. MNRAS, 439:83–101, Mar. 2014. doi: 10.1093/mnras/stt2206. → pages 22

M. E. Anderson and J. N. Bregman. Do Hot Halos Around Galaxies Contain the Missing Baryons? *ApJ*, 714:320–331, May 2010. doi: 10.1088/0004-637X/714/1/320. → pages 74

S. Ando and K. Ishiwata. Constraining particle dark matter using local galaxy distribution. J. Cosmology Astropart. Phys., 6:045, June 2016. doi: 10.1088/1475-7516/2016/06/045. → pages 23, 46

S. Ando and E. Komatsu. Anisotropy of the cosmic gamma-ray background from dark matter annihilation. Phys. Rev. D, 73(2):023521, Jan. 2006. doi: 10.1103/PhysRevD.73.023521. → pages 25, 27

S. Ando and E. Komatsu. Constraints on the annihilation cross section of dark matter particles from anisotropies in the diffuse gamma-ray background measured with Fermi-LAT. Phys. Rev. D, 87(12): 123539, June 2013. doi: 10.1103/PhysRevD.87.123539. → pages 23, 27

S. Ando, A. Benoit-Lévy, and E. Komatsu. Mapping dark matter in the gamma-ray sky with galaxy catalogs. Phys. Rev. D, 90(2):023514, July 2014. doi: 10.1103/PhysRevD.90.023514. → pages 23

S. Andrianomena, C. Clarkson, P. Patel, O. Umeh, and J.-P. Uzan. Non-linear relativistic contributions to the cosmological weak-lensing convergence. *Journal of Cosmology and Astroparticle Physics*, 2014(06):023–023, June 2014. doi: 10.1088/1475-7516/2014/06/023. → pages 75, 78, 86

M. Arnaud, G. W. Pratt, R. Piffaretti, H. Böhringer, J. H. Croston, and E. Pointecouteau. The universal galaxy cluster pressure profile from a representative sample of nearby systems (REXCESS) and the Y_{SZ} - M_{500} relation. A&A, 517:A92, July 2010. doi: 10.1051/0004-6361/200913416. → pages 57

W. B. Atwood, A. A. Abdo, M. Ackermann, W. Althouse, B. Anderson, M. Axelsson, L. Baldini, J. Ballet, D. L. Band, G. Barbiellini, and et al. The Large Area Telescope on the Fermi Gamma-Ray Space Telescope Mission. ApJ, 697:1071–1102, June 2009. doi: 10.1088/0004-637X/697/2/1071. → pages 23

M. G. Baring, T. Ghosh, F. S. Queiroz, and K. Sinha. New limits on the dark matter lifetime from dwarf spheroidal galaxies using Fermi-LAT. Phys. Rev. D, 93(10):103009, May 2016. doi: 10.1103/PhysRevD.93.103009. → pages 48

M. Bartelmann. TOPICAL REVIEW Gravitational lensing. *Classical and Quantum Gravity*, 27(23): 233001, Dec. 2010. doi: 10.1088/0264-9381/27/23/233001. → pages 5, 25, 74, 75

M. Bartelmann and P. Schneider. Weak gravitational lensing. *Physics Reports*, 340(4-5):291–472, Jan. 2001. doi: 10.1016/S0370-1573(00)00082-X. → pages 5

N. Battaglia, J. R. Bond, C. Pfrommer, and J. L. Sievers. On the Cluster Physics of Sunyaev-Zel'dovich and X-Ray Surveys. II. Deconstructing the Thermal SZ Power Spectrum. ApJ, 758:75, Oct. 2012. doi: 10.1088/0004-637X/758/2/75. → pages 69

N. Battaglia, J. C. Hill, and N. Murray. Deconstructing Thermal Sunyaev-Zel'dovich - Gravitational Lensing Cross-correlations: Implications for the Intracluster Medium. ApJ, 812:154, Oct. 2015. doi: 10.1088/0004-637X/812/2/154. → pages 51

E. Baxter, J. Clampitt, T. Giannantonio, S. Dodelson, B. Jain, D. Huterer, L. Bleem, T. Crawford, G. Efstathiou, P. Fosalba, D. Kirk, J. Kwan, C. Sánchez, K. Story, M. A. Troxel, T. M. C. Abbott, F. B. Abdalla, R. Armstrong, A. Benoit-Lévy, B. Benson, G. M. Bernstein, R. A. Bernstein, E. Bertin, D. Brooks, J. Carlstrom, A. C. Rosell, M. Carrasco Kind, J. Carretero, R. Chown, M. Crocce, C. E. Cunha, L. N. da Costa, S. Desai, H. T. Diehl, J. P. Dietrich, P. Doel, A. E. Evrard, A. Fausti Neto, B. Flaugher, J. Frieman, D. Gruen, R. A. Gruendl, G. Gutierrez, T. de Haan, G. Holder, K. Honscheid, Z. Hou, D. J. James, K. Kuehn, N. Kuropatkin, M. Lima, M. March, J. L. Marshall, P. Martini, P. Melchior, C. J. Miller, R. Miquel, J. J. Mohr, B. Nord, Y. Omori, A. A. Plazas, C. Reichardt, A. K. Romer, E. S. Rykoff, E. Sanchez, I. Sevilla-Noarbe, E. Sheldon, R. C. Smith, M. Soares-Santos, F. Sobreira, E. Suchyta, A. Stark, M. E. C. Swanson, G. Tarle, D. Thomas, A. R. Walker, and R. H. Wechsler. Joint measurement of lensing-galaxy correlations using SPT and DES SV data. MNRAS, 461:4099–4114, Oct. 2016. doi: 10.1093/mnras/stw1584. → pages 90

M. R. Becker. CALCLENS: weak lensing simulations for large-area sky surveys and second-order effects in cosmic shear power spectra. *Monthly Notices of the Royal Astronomical Society*, 435(1): 115–132, Aug. 2013. doi: 10.1093/mnras/stt1352. → pages 75

N. Benítez. Bayesian Photometric Redshift Estimation. ApJ, 536:571–583, June 2000. doi: 10.1086/308947. → pages 54, 94

L. Bergström, J. Edsjö, and P. Ullio. Spectral Gamma-Ray Signatures of Cosmological Dark Matter Annihilations. *Physical Review Letters*, 87(25):251301, Dec. 2001. doi: 10.1103/PhysRevLett.87.251301. → pages 20

J. L. Bernal, L. Verde, and A. G. Riess. The trouble with H_0. *JCAP*, 10:019, Oct. 2016. doi: 10.1088/1475-7516/2016/10/019. → pages 89

F. Bernardeau. The effects of source clustering on weak lensing statistics. A&A, 338:375–382, Oct. 1998. → pages 104

F. Bernardeau, L. van Waerbeke, and Y. Mellier. Weak lensing statistics as a probe of {OMEGA} and power spectrum. A&A, 322:1–18, June 1997. → pages 78

F. Bernardeau, C. Bonvin, and F. Vernizzi. Full-sky lensing shear at second order. *Physical Review D*, 81(8):083002, Apr. 2010. doi: 10.1103/PhysRevD.81.083002. → pages 75, 78, 85, 88

F. Bernardeau, C. Bonvin, N. Van de Rijt, and F. Vernizzi. Cosmic shear bispectrum from second-order perturbations in general relativity. *Physical Review D*, 86(2):023001, July 2012. doi: 10.1103/PhysRevD.86.023001. → pages 4, 75, 77, 78, 86, 88

G. Bertone, D. Hooper, and J. Silk. Particle dark matter: evidence, candidates and constraints. Phys. Rep., 405:279–390, Jan. 2005. doi: 10.1016/j.physrep.2004.08.031. → pages 23

R. D. Blandford, A. B. Saust, T. G. Brainerd, and J. V. Villumsen. The distortion of distant galaxy images by large-scale structure. *Monthly Notices of the Royal Astronomical Society (ISSN 0035-8711)*, 251:600–627, 1991. → pages 5

C. Bonvin. Effect of peculiar motion in weak lensing. *Physical Review D*, 78(12):123530, Dec. 2008. doi: 10.1103/PhysRevD.78.123530. → pages 78

V. Bonvin, F. Courbin, S. H. Suyu, P. J. Marshall, C. E. Rusu, D. Sluse, M. Tewes, K. C. Wong, T. Collett, C. D. Fassnacht, T. Treu, M. W. Auger, S. Hilbert, L. V. E. Koopmans, G. Meylan, N. Rumbaugh, A. Sonnenfeld, and C. Spiniello. H0LiCOW - V. New COSMOGRAIL time delays of HE 0435-1223: H_0 to 3.8 per cent precision from strong lensing in a flat ΛCDM model. MNRAS, 465:4914–4930, Mar. 2017. doi: 10.1093/mnras/stw3006. → pages 89

C. M. Booth and J. Schaye. Cosmological simulations of the growth of supermassive black holes and feedback from active galactic nuclei: method and tests. MNRAS, 398:53–74, Sept. 2009. doi: 10.1111/j.1365-2966.2009.15043.x. → pages 59

J. N. Bregman. The Search for the Missing Baryons at Low Redshift. *Annual Review of Astronomy and Astrophysics*, 45(1):221–259, Sept. 2007. doi: 10.1146/annurev.astro.45.051806.110619. → pages 74

S. Bridle and L. King. Dark energy constraints from cosmic shear power spectra: impact of intrinsic alignments on photometric redshift requirements. *New Journal of Physics*, 9:444, Dec. 2007. doi: 10.1088/1367-2630/9/12/444. → pages 105

T. Bringmann. Particle models and the small-scale structure of dark matter. *New Journal of Physics*, 11(10):105027, Oct. 2009. doi: 10.1088/1367-2630/11/10/105027. → pages 27

M. L. Brown, A. N. Taylor, N. C. Hambly, and S. Dye. Measurement of intrinsic alignments in galaxy ellipticities. *MNRAS*, 333:501–509, July 2002. → pages 105

S. Camera, M. Fornasa, N. Fornengo, and M. Regis. A Novel Approach in the Weakly Interacting Massive Particle Quest: Cross-correlation of Gamma-Ray Anisotropies and Cosmic Shear. ApJ, 771:L5, July 2013. doi: 10.1088/2041-8205/771/1/L5. → pages 24

S. Camera, M. Fornasa, N. Fornengo, and M. Regis. Tomographic-spectral approach for dark matter detection in the cross-correlation between cosmic shear and diffuse γ-ray emission. J. Cosmology Astropart. Phys., 6:029, June 2015. doi: 10.1088/1475-7516/2015/06/029. → pages 24, 30, 31, 44, 46, 118

S. M. Carroll. *Spacetime and geometry. An introduction to general relativity*. Addison Wesley, 2004. → pages 2

J. A. R. Cembranos, A. de La Cruz-Dombriz, A. Dobado, R. A. Lineros, and A. L. Maroto. Photon spectra from WIMP annihilation. Phys. Rev. D, 83(8):083507, Apr. 2011. doi: 10.1103/PhysRevD.83.083507. → pages 26

E. Charles, M. Sánchez-Conde, B. Anderson, R. Caputo, A. Cuoco, M. Di Mauro, A. Drlica-Wagner, G. A. Gomez-Vargas, M. Meyer, L. Tibaldo, M. Wood, G. Zaharijas, S. Zimmer, M. Ajello, A. Albert, L. Baldini, K. Bechtol, E. D. Bloom, F. Ceraudo, J. Cohen-Tanugi, S. W. Digel, J. Gaskins, M. Gustafsson, N. Mirabal, and M. Razzano. Sensitivity projections for dark matter searches with the Fermi large area telescope. Phys. Rep., 636:1–46, June 2016. doi: 10.1016/j.physrep.2016.05.001. → pages 23

N. E. Chisari, J. Dunkley, L. Miller, and R. Allison. Contamination of early-type galaxy alignments to galaxy lensing-cmb lensing cross-correlation. MNRAS, 453:682–689, Oct. 2015. doi: 10.1093/mnras/stv1655. → pages 105, 106, 107

A. Choi, C. Heymans, C. Blake, H. Hildebrandt, C. A. J. Duncan, T. Erben, R. Nakajima, L. Van Waerbeke, and M. Viola. CFHTLenS and RCSLenS: testing photometric redshift distributions using angular cross-correlations with spectroscopic galaxy surveys. MNRAS, 463:3737–3754, Dec. 2016. doi: 10.1093/mnras/stw2241. → pages 32

G. Chon, A. Challinor, S. Prunet, E. Hivon, and I. Szapudi. Fast estimation of polarization power spectra using correlation functions. MNRAS, 350:914–926, May 2004. doi: 10.1111/j.1365-2966.2004.07737.x. → pages 90, 98

M. Cirelli, G. Corcella, A. Hektor, G. Hütsi, M. Kadastik, P. Panci, M. Raidal, F. Sala, and A. Strumia. PPPC 4 DM ID: a poor particle physicist cookbook for dark matter indirect detection. J. Cosmology Astropart. Phys., 3:051, Mar. 2011. doi: 10.1088/1475-7516/2011/03/051. → pages 26, 28

S. Codis, C. Pichon, and D. Pogosyan. Spin alignments within the cosmic web: a theory of constrained tidal torques near filaments. MNRAS, 452:3369–3393, Oct. 2015. doi: 10.1093/mnras/stv1570. → pages 107

A. Cooray and R. Sheth. Halo models of large scale structure. Phys. Rep., 372:1–129, Dec. 2002. doi: 10.1016/S0370-1573(02)00276-4. → pages 15, 30, 75, 77, 78

J. Coupon, S. Arnouts, L. van Waerbeke, T. Moutard, O. Ilbert, E. van Uitert, T. Erben, B. Garilli, L. Guzzo, C. Heymans, H. Hildebrandt, H. Hoekstra, M. Kilbinger, T. Kitching, Y. Mellier, L. Miller, M. Scodeggio, C. Bonnett, E. Branchini, I. Davidzon, G. De Lucia, A. Fritz, L. Fu, P. Hudelot, M. J. Hudson, K. Kuijken, A. Leauthaud, O. Le Fèvre, H. J. McCracken, L. Moscardini, B. T. P. Rowe, T. Schrabback, E. Semboloni, and M. Velander. The galaxy-halo connection from a joint lensing, clustering and abundance analysis in the CFHTLenS/VIPERS field. MNRAS, 449: 1352–1379, May 2015. doi: 10.1093/mnras/stv276. → pages 32, 54

A. Cuoco, J.-Q. Xia, M. Regis, E. Branchini, N. Fornengo, and M. Viel. Dark Matter Searches in the Gamma-ray Extragalactic Background via Cross-correlations with Galaxy Catalogs. ApJS, 221:29, Dec. 2015. doi: 10.1088/0067-0049/221/2/29. → pages 23, 28, 47, 49

C. Dalla Vecchia and J. Schaye. Simulating galactic outflows with kinetic supernova feedback. MNRAS, 387:1431–1444, July 2008. doi: 10.1111/j.1365-2966.2008.13322.x. → pages 59

S. Das, J. Errard, and D. Spergel. Can CMB Lensing Help Cosmic Shear Surveys? *ArXiv e-prints*, Nov. 2013. → pages 90, 112

S. Das, T. Louis, M. R. Nolta, G. E. Addison, E. S. Battistelli, J. R. Bond, E. Calabrese, D. Crichton, M. J. Devlin, S. Dicker, J. Dunkley, R. Dünner, J. W. Fowler, M. Gralla, A. Hajian, M. Halpern, M. Hasselfield, M. Hilton, A. D. Hincks, R. Hlozek, K. M. Huffenberger, J. P. Hughes, K. D. Irwin, A. Kosowsky, R. H. Lupton, T. A. Marriage, D. Marsden, F. Menanteau, K. Moodley, M. D. Niemack, L. A. Page, B. Partridge, E. D. Reese, B. L. Schmitt, N. Sehgal, B. D. Sherwin, J. L. Sievers, D. N. Spergel, S. T. Staggs, D. S. Swetz, E. R. Switzer, R. Thornton, H. Trac, and E. Wollack. The atacama cosmology telescope: temperature and gravitational lensing power spectrum measurements from three seasons of data. *JCAP*, 4:014, Apr. 2014. doi: 10.1088/1475-7516/2014/04/014. → pages 90

J. T. A. de Jong, K. Kuijken, D. Applegate, K. Begeman, A. Belikov, C. Blake, J. Bout, D. Boxhoorn, H. Buddelmeijer, A. Buddendiek, M. Cacciato, M. Capaccioli, A. Choi, O. Cordes, G. Covone, M. Dall'Ora, A. Edge, T. Erben, J. Franse, F. Getman, A. Grado, J. Harnois-Deraps, E. Helmich, R. Herbonnet, C. Heymans, H. Hildebrandt, H. Hoekstra, Z. Huang, N. Irisarri, B. Joachimi, F. Köhlinger, T. Kitching, F. La Barbera, P. Lacerda, J. McFarland, L. Miller, R. Nakajima, N. R. Napolitano, M. Paolillo, J. Peacock, B. Pila-Diez, E. Puddu, M. Radovich, A. Rifatto, P. Schneider, T. Schrabback, C. Sifon, G. Sikkema, P. Simon, W. Sutherland, A. Tudorica, E. Valentijn, R. van der Burg, E. van Uitert, L. van Waerbeke, M. Velander, G. V. Kleijn, M. Viola, and W.-J. Vriend. The Kilo-Degree Survey. *The Messenger*, 154:44–46, Dec. 2013a. → pages 68, 75

J. T. A. de Jong, G. A. Verdoes Kleijn, K. H. Kuijken, and E. A. Valentijn. The Kilo-Degree Survey. *Experimental Astronomy*, 35:25–44, Jan. 2013b. doi: 10.1007/s10686-012-9306-1. → pages 24

J. T. A. de Jong, G. A. Verdoes Kleijn, D. R. Boxhoorn, H. Buddelmeijer, M. Capaccioli, F. Getman, A. Grado, E. Helmich, Z. Huang, N. Irisarri, K. Kuijken, F. La Barbera, J. P. McFarland, N. R. Napolitano, M. Radovich, G. Sikkema, E. A. Valentijn, K. G. Begeman, M. Brescia, S. Cavuoti, A. Choi, O.-M. Cordes, G. Covone, M. Dall'Ora, H. Hildebrandt, G. Longo, R. Nakajima, M. Paolillo, E. Puddu, A. Rifatto, C. Tortora, E. van Uitert, A. Buddendiek, J. Harnois-Déraps, T. Erben, M. B. Eriksen, C. Heymans, H. Hoekstra, B. Joachimi, T. D. Kitching, D. Klaes, L. V. E. Koopmans, F. Köhlinger, N. Roy, C. Sifón, P. Schneider, W. J. Sutherland, M. Viola, and W.-J. Vriend. The first and second data releases of the Kilo-Degree Survey. A&A, 582:A62, Oct. 2015. doi: 10.1051/0004-6361/201526601. → pages 93

M. Di Mauro, F. Calore, F. Donato, M. Ajello, and L. Latronico. Diffuse γ-Ray Emission from Misaligned Active Galactic Nuclei. ApJ, 780:161, Jan. 2014. doi: 10.1088/0004-637X/780/2/161. → pages 29

S. Dodelson and P. Zhang. Weak lensing bispectrum. *Physical Review D*, 72(8):083001, Oct. 2005a. doi: 10.1103/PhysRevD.72.083001. → pages 152

S. Dodelson, E. Kolb, S. Matarrese, A. Riotto, and P. Zhang. Second order geodesic corrections to cosmic shear. *Physical Review D*, 72(10):103004, Nov. 2005b. doi: 10.1103/PhysRevD.72.103004. → pages 75, 78

S. Dodelson, C. Shapiro, and M. White. Reduced shear power spectrum. *Physical Review D*, 73(2): 023009, Jan. 2006. doi: 10.1103/PhysRevD.73.023009. → pages 75, 78, 83

B. Efron. Bootstrap methods: Another look at the jackknife. *Ann. Statist.*, 7(1):1–26, 01 1979. doi: 10.1214/aos/1176344552. → pages 19

T. Eifler, E. Krause, S. Dodelson, A. R. Zentner, A. P. Hearin, and N. Y. Gnedin. Accounting for baryonic effects in cosmic shear tomography: determining a minimal set of nuisance parameters using PCA. MNRAS, 454:2451–2471, Dec. 2015. doi: 10.1093/mnras/stv2000. → pages 119

T. Erben, H. Hildebrandt, L. Miller, L. van Waerbeke, C. Heymans, H. Hoekstra, T. D. Kitching, Y. Mellier, J. Benjamin, C. Blake, C. Bonnett, O. Cordes, J. Coupon, L. Fu, R. Gavazzi, B. Gillis, E. Grocutt, S. D. J. Gwyn, K. Holhjem, M. J. Hudson, M. Kilbinger, K. Kuijken, M. Milkeraitis, B. T. P. Rowe, T. Schrabback, E. Semboloni, P. Simon, M. Smit, O. Toader, S. Vafaei, E. van Uitert, and M. Velander. CFHTLenS: the Canada-France-Hawaii Telescope Lensing Survey - imaging data and catalogue products. MNRAS, 433:2545–2563, Aug. 2013. doi: 10.1093/mnras/stt928. → pages 32, 54, 90, 93

I. Fenech Conti, R. Herbonnet, H. Hoekstra, J. Merten, L. Miller, and M. Viola. Calibration of weak-lensing shear in the Kilo-Degree Survey. MNRAS, 467:1627–1651, May 2017. doi: 10.1093/mnras/stx200. → pages 33, 93, 95, 98, 113, 118

C. Feng, A. Cooray, and B. Keating. Planck Lensing and Cosmic Infrared Background Cross-correlation with Fermi-LAT: Tracing Dark Matter Signals in the Gamma-ray Background. ApJ, 836:127, Feb. 2017. doi: 10.3847/1538-4357/836/1/127. → pages 23

J. L. Feng. Dark Matter Candidates from Particle Physics and Methods of Detection. ARA&A, 48: 495–545, Sept. 2010. doi: 10.1146/annurev-astro-082708-101659. → pages 23

M. Fornasa and M. A. Sánchez-Conde. The nature of the Diffuse Gamma-Ray Background. Phys. Rep., 598:1–58, Oct. 2015. doi: 10.1016/j.physrep.2015.09.002. → pages 23, 28

M. Fornasa, J. Zavala, M. A. Sánchez-Conde, J. M. Siegal-Gaskins, T. Delahaye, F. Prada, M. Vogelsberger, F. Zandanel, and C. S. Frenk. Characterization of dark-matter-induced anisotropies in the diffuse gamma-ray background. MNRAS, 429:1529–1553, Feb. 2013. doi: 10.1093/mnras/sts444. → pages 25

M. Fornasa, A. Cuoco, J. Zavala, J. M. Gaskins, M. A. Sánchez-Conde, G. Gomez-Vargas, E. Komatsu, T. Linden, F. Prada, F. Zandanel, and A. Morselli. Angular power spectrum of the diffuse gamma-ray emission as measured by the Fermi Large Area Telescope and constraints on its dark matter interpretation. Phys. Rev. D, 94(12):123005, Dec. 2016. doi: 10.1103/PhysRevD.94.123005. → pages 23, 39, 41, 47, 49, 117

N. Fornengo and M. Regis. Particle dark matter searches in the anisotropic sky. *Frontiers in Physics*, 2:6, 2014. doi: 10.3389/fphy.2014.00006. → pages 25, 27

N. Fornengo, L. Pieri, and S. Scopel. Neutralino annihilation into γ rays in the Milky Way and in external galaxies. Phys. Rev. D, 70(10):103529, Nov. 2004. doi: 10.1103/PhysRevD.70.103529. → pages 26

N. Fornengo, L. Perotto, M. Regis, and S. Camera. Evidence of Cross-correlation between the CMB Lensing and the γ-Ray Sky. ApJ, 802:L1, Mar. 2015. doi: 10.1088/2041-8205/802/1/L1. → pages 23, 30

A. Franceschini, G. Rodighiero, and M. Vaccari. Extragalactic optical-infrared background radiation, its time evolution and the cosmic photon-photon opacity. A&A, 487:837–852, Sept. 2008. doi: 10.1051/0004-6361:200809691. → pages 26

L. Fu, M. Kilbinger, T. Erben, C. Heymans, H. Hildebrandt, H. Hoekstra, T. D. Kitching, Y. Mellier, L. Miller, E. Semboloni, P. Simon, L. Van Waerbeke, J. Coupon, J. Harnois-Déraps, M. J. Hudson, K. Kuijken, B. Rowe, T. Schrabback, S. Vafaei, and M. Velander. CFHTLenS: cosmological constraints from a combination of cosmic shear two-point and three-point correlations. MNRAS, 441:2725–2743, July 2014. doi: 10.1093/mnras/stu754. → pages 87

M. Fukugita and P. J. E. Peebles. The Cosmic Energy Inventory. *The Astrophysical Journal*, 616(2): 643–668, Dec. 2004. doi: 10.1086/425155. → pages 74

L. Gao, C. S. Frenk, A. Jenkins, V. Springel, and S. D. M. White. Where will supersymmetric dark matter first be seen? MNRAS, 419:1721–1726, Jan. 2012. doi: 10.1111/j.1365-2966.2011.19836.x. → pages 27

T. Giannantonio, P. Fosalba, R. Cawthon, Y. Omori, M. Crocce, F. Elsner, B. Leistedt, S. Dodelson, A. Benoit-Lévy, E. Gaztañaga, G. Holder, H. V. Peiris, W. J. Percival, D. Kirk, A. H. Bauer, B. A. Benson, G. M. Bernstein, J. Carretero, T. M. Crawford, R. Crittenden, D. Huterer, B. Jain, E. Krause, C. L. Reichardt, A. J. Ross, G. Simard, B. Soergel, A. Stark, K. T. Story, J. D. Vieira, J. Weller, T. Abbott, F. B. Abdalla, S. Allam, R. Armstrong, M. Banerji, R. A. Bernstein, E. Bertin, D. Brooks, E. Buckley-Geer, D. L. Burke, D. Capozzi, J. E. Carlstrom, A. Carnero Rosell, M. Carrasco Kind, F. J. Castander, C. L. Chang, C. E. Cunha, L. N. da Costa, C. B. D'Andrea, D. L. DePoy, S. Desai, H. T. Diehl, J. P. Dietrich, P. Doel, T. F. Eifler, A. E. Evrard, A. F. Neto, E. Fernandez, D. A. Finley, B. Flaugher, J. Frieman, D. Gerdes, D. Gruen, R. A. Gruendl, G. Gutierrez, W. L. Holzapfel, K. Honscheid, D. J. James, K. Kuehn, N. Kuropatkin, O. Lahav, T. S. Li, M. Lima, M. March, J. L. Marshall, P. Martini, P. Melchior, R. Miquel, J. J. Mohr, R. C. Nichol, B. Nord, R. Ogando, A. A. Plazas, A. K. Romer, A. Roodman, E. S. Rykoff, M. Sako, B. R. Saliwanchik, E. Sanchez, M. Schubnell, I. Sevilla-Noarbe, R. C. Smith, M. Soares-Santos, F. Sobreira, E. Suchyta, M. E. C. Swanson, G. Tarle, J. Thaler, D. Thomas, V. Vikram, A. R. Walker, R. H. Wechsler, and J. Zuntz. CMB lensing tomography with the DES Science Verification galaxies. MNRAS, 456:3213–3244, Mar. 2016. doi: 10.1093/mnras/stv2678. → pages 90

H. Gil-Marín, C. Wagner, F. Fragkoudi, R. Jimenez, and L. Verde. An improved fitting formula for the dark matter bispectrum. *Journal of Cosmology and Astroparticle Physics*, 2012(02):047–047, Feb. 2012. doi: 10.1088/1475-7516/2012/02/047. → pages 87, 88

D. G. Gilbank, M. D. Gladders, H. K. C. Yee, and B. C. Hsieh. The Red-sequence Cluster Survey-2 (RCS-2): survey details and photometric catalog construction. *Astron. J.*, 141:94, 2011. doi: 10.1088/0004-6256/141/3/94. → pages 54

K. M. Górski, E. Hivon, A. J. Banday, B. D. Wandelt, F. K. Hansen, M. Reinecke, and M. Bartelmann. HEALPix: A Framework for High-Resolution Discretization and Fast Analysis of Data Distributed on the Sphere. ApJ, 622:759–771, Apr. 2005. doi: 10.1086/427976. → pages 33

C. Gruppioni, F. Pozzi, G. Rodighiero, I. Delvecchio, S. Berta, L. Pozzetti, G. Zamorani, P. Andreani, A. Cimatti, O. Ilbert, E. Le Floc'h, D. Lutz, B. Magnelli, L. Marchetti, P. Monaco, R. Nordon, S. Oliver, P. Popesso, L. Riguccini, I. Roseboom, D. J. Rosario, M. Sargent, M. Vaccari, B. Altieri, H. Aussel, A. Bongiovanni, J. Cepa, E. Daddi, H. Domínguez-Sánchez, D. Elbaz, N. Förster Schreiber, R. Genzel, A. Iribarrem, M. Magliocchetti, R. Maiolino, A. Poglitsch, A. Pérez García, M. Sanchez-Portal, E. Sturm, L. Tacconi, I. Valtchanov, A. Amblard, V. Arumugam, M. Bethermin, J. Bock, A. Boselli, V. Buat, D. Burgarella, N. Castro-Rodríguez, A. Cava, P. Chanial, D. L. Clements, A. Conley, A. Cooray, C. D. Dowell, E. Dwek, S. Eales, A. Franceschini, J. Glenn, M. Griffin, E. Hatziminaoglou, E. Ibar, K. Isaak, R. J. Ivison, G. Lagache, L. Levenson, N. Lu, S. Madden, B. Maffei, G. Mainetti, H. T. Nguyen, B. O'Halloran, M. J. Page, P. Panuzzo, A. Papageorgiou, C. P. Pearson, I. Pérez-Fournon, M. Pohlen, D. Rigopoulou, M. Rowan-Robinson, B. Schulz, D. Scott, N. Seymour, D. L. Shupe, A. J. Smith, J. A. Stevens, M. Symeonidis, M. Trichas, K. E. Tugwell, L. Vigroux, L. Wang, G. Wright, C. K. Xu, M. Zemcov, S. Bardelli, M. Carollo, T. Contini, O. Le Févre, S. Lilly, V. Mainieri, A. Renzini, M. Scodeggio, and E. Zucca. The Herschel PEP/HerMES luminosity function - I. Probing the evolution of PACS selected Galaxies to z $\simeq$ 4. MNRAS, 432:23–52, June 2013. doi: 10.1093/mnras/stt308. → pages 30

J. E. Gunn, B. W. Lee, I. Lerche, D. N. Schramm, and G. Steigman. Some astrophysical consequences of the existence of a heavy stable neutral lepton. ApJ, 223:1015–1031, Aug. 1978. doi: 10.1086/156335. → pages 23

A. Hall and A. Taylor. Intrinsic alignments in the cross-correlation of cosmic shear and cosmic microwave background weak lensing. MNRAS, 443:L119–L123, Sept. 2014. doi: 10.1093/mnrasl/slu094. → pages 90, 105

N. Hand, A. Leauthaud, S. Das, B. D. Sherwin, G. E. Addison, J. R. Bond, E. Calabrese, A. Charbonnier, M. J. Devlin, J. Dunkley, T. Erben, A. Hajian, M. Halpern, J. Harnois-Déraps, C. Heymans, H. Hildebrandt, A. D. Hincks, J.-P. Kneib, A. Kosowsky, M. Makler, L. Miller, K. Moodley, B. Moraes, M. D. Niemack, L. A. Page, B. Partridge, N. Sehgal, H. Shan, J. L. Sievers, D. N. Spergel, S. T. Staggs, E. R. Switzer, J. E. Taylor, L. Van Waerbeke, C. Welker, and E. J. Wollack. First measurement of the cross-correlation of CMB lensing and galaxy lensing. Phys. Rev. D, 91(6):062001, Mar. 2015. doi: 10.1103/PhysRevD.91.062001. → pages 90, 94, 116

J. Harnois-Déraps and L. van Waerbeke. Simulations of weak gravitational lensing - II. Including finite support effects in cosmic shear covariance matrices. MNRAS, 450:2857–2873, July 2015a. doi: 10.1093/mnras/stv794. → pages 74, 142

J. Harnois-Déraps, L. van Waerbeke, M. Viola, and C. Heymans. Baryons, neutrinos, feedback and weak gravitational lensing. MNRAS, 450:1212–1223, June 2015b. doi: 10.1093/mnras/stv646. → pages 51, 109, 117

J. Harnois-Déraps, T. Tröster, A. Hojjati, L. van Waerbeke, M. Asgari, A. Choi, T. Erben, C. Heymans, H. Hildebrandt, T. D. Kitching, L. Miller, R. Nakajima, M. Viola, S. Arnouts, J. Coupon, and T. Moutard. CFHTLenS and RCSLenS cross-correlation with Planck lensing detected in fourier and configuration space. MNRAS, 460:434–457, July 2016. doi: 10.1093/mnras/stw947. → pages 21, 32, 35, 54, 55, 61, 67, 71, 90

J. Hartlap, P. Simon, and P. Schneider. Why your model parameter confidences might be too optimistic. Unbiased estimation of the inverse covariance matrix. A&A, 464:399–404, Mar. 2007. doi: 10.1051/0004-6361:20066170. → pages 37, 41, 62, 101, 104, 119

K. Heitmann, E. Lawrence, J. Kwan, S. Habib, and D. Higdon. The Coyote Universe Extended: Precision Emulation of the Matter Power Spectrum. ApJ, 780:111, Jan. 2014. doi: 10.1088/0004-637X/780/1/111. → pages 110

C. Heymans, L. Van Waerbeke, L. Miller, T. Erben, H. Hildebrandt, H. Hoekstra, T. D. Kitching, Y. Mellier, P. Simon, C. Bonnett, J. Coupon, L. Fu, J. Harnois Déraps, M. J. Hudson, M. Kilbinger, K. Kuijken, B. Rowe, T. Schrabback, E. Semboloni, E. van Uitert, S. Vafaei, and M. Velander. CFHTLenS: the Canada-France-Hawaii Telescope Lensing Survey. MNRAS, 427:146–166, Nov. 2012. doi: 10.1111/j.1365-2966.2012.21952.x. → pages 32, 39, 54, 55, 94

C. Heymans, E. Grocutt, A. Heavens, M. Kilbinger, T. D. Kitching, F. Simpson, J. Benjamin, T. Erben, H. Hildebrandt, H. Hoekstra, Y. Mellier, L. Miller, L. Van Waerbeke, M. L. Brown, J. Coupon, L. Fu, J. Harnois-Déraps, M. J. Hudson, K. Kuijken, B. Rowe, T. Schrabback, E. Semboloni, S. Vafaei, and M. Velander. CFHTLenS tomographic weak lensing cosmological parameter constraints: Mitigating the impact of intrinsic galaxy alignments. MNRAS, 432:2433–2453, July 2013. doi: 10.1093/mnras/stt601. → pages 106

S. Hilbert, J. Hartlap, S. D. M. White, and P. Schneider. Ray-tracing through the Millennium Simulation: Born corrections and lens-lens coupling in cosmic shear and galaxy-galaxy lensing. *Astronomy and Astrophysics*, 499(1):31–43, May 2009. doi: 10.1051/0004-6361/200811054. → pages 75

H. Hildebrandt and on behalf of the CFHTLenS collaboration. An overview of the completed Canada-France-Hawaii Telescope Lensing Survey (CFHTLenS). *ArXiv e-prints*, June 2014. → pages 74

H. Hildebrandt, T. Erben, K. Kuijken, L. van Waerbeke, C. Heymans, J. Coupon, J. Benjamin, C. Bonnett, L. Fu, H. Hoekstra, T. D. Kitching, Y. Mellier, L. Miller, M. Velander, M. J. Hudson, B. T. P. Rowe, T. Schrabback, E. Semboloni, and N. Benítez. CFHTLenS: improving the quality of photometric redshifts with precision photometry. MNRAS, 421:2355–2367, Apr. 2012. doi: 10.1111/j.1365-2966.2012.20468.x. → pages 32, 54

H. Hildebrandt, A. Choi, C. Heymans, C. Blake, T. Erben, L. Miller, R. Nakajima, L. van Waerbeke, M. Viola, A. Buddendiek, J. Harnois-Déraps, A. Hojjati, B. Joachimi, S. Joudaki, T. D. Kitching, C. Wolf, S. Gwyn, N. Johnson, K. Kuijken, Z. Sheikhbahaee, A. Tudorica, and H. K. C. Yee. RCSLenS: The Red Cluster Sequence Lensing Survey. MNRAS, 463:635–654, Nov. 2016. doi: 10.1093/mnras/stw2013. → pages 32, 51, 54, 60, 91, 147, 149

H. Hildebrandt, M. Viola, C. Heymans, S. Joudaki, K. Kuijken, C. Blake, T. Erben, B. Joachimi, D. Klaes, L. Miller, C. B. Morrison, R. Nakajima, G. Verdoes Kleijn, A. Amon, A. Choi, G. Covone, J. T. A. de Jong, A. Dvornik, I. Fenech Conti, A. Grado, J. Harnois-Déraps, R. Herbonnet, H. Hoekstra, F. Köhlinger, J. McFarland, A. Mead, J. Merten, N. Napolitano, J. A. Peacock, M. Radovich, P. Schneider, P. Simon, E. A. Valentijn, J. L. van den Busch, E. van Uitert, and L. Van Waerbeke. KiDS-450: cosmological parameter constraints from tomographic weak gravitational lensing. MNRAS, 465:1454–1498, Feb. 2017. doi: 10.1093/mnras/stw2805. → pages 22, 33, 89, 90, 91, 93, 94, 95, 105, 107, 108, 113, 118

J. C. Hill and D. N. Spergel. Detection of thermal SZ-CMB lensing cross-correlation in Planck nominal mission data. J. Cosmology Astropart. Phys., 2:030, Feb. 2014. doi: 10.1088/1475-7516/2014/02/030. → pages 51, 74

G. Hinshaw, D. Larson, E. Komatsu, D. N. Spergel, C. L. Bennett, J. Dunkley, M. R. Nolta, M. Halpern, R. S. Hill, N. Odegard, L. Page, K. M. Smith, J. L. Weiland, B. Gold, N. Jarosik, A. Kogut, M. Limon, S. S. Meyer, G. S. Tucker, E. Wollack, and E. L. Wright. Nine-year Wilkinson Microwave Anisotropy Probe (WMAP) Observations: Cosmological Parameter Results. ApJS, 208: 19, Oct. 2013. doi: 10.1088/0067-0049/208/2/19. → pages 22, 91

C. Hirata and U. Seljak. Reconstruction of lensing from the cosmic microwave background polarization. *Physical Review D*, 68(8):083002, Oct. 2003. doi: 10.1103/PhysRevD.68.083002. → pages 75

H. Hoekstra, R. Herbonnet, A. Muzzin, A. Babul, A. Mahdavi, M. Viola, and M. Cacciato. The Canadian Cluster Comparison Project: detailed study of systematics and updated weak lensing masses. MNRAS, 449:685–714, May 2015. doi: 10.1093/mnras/stv275. → pages 22, 43

A. Hojjati, I. G. McCarthy, J. Harnois-Déraps, Y.-Z. Ma, L. Van Waerbeke, G. Hinshaw, and A. M. C. Le Brun. Dissecting the thermal Sunyaev-Zeldovich-gravitational lensing cross-correlation with hydrodynamical simulations. J. Cosmology Astropart. Phys., 10:047, Oct. 2015. doi: 10.1088/1475-7516/2015/10/047. → pages 51, 58, 59, 66, 68, 69

A. Hojjati, T. Tröster, J. Harnois-Déraps, I. G. McCarthy, L. van Waerbeke, A. Choi, T. Erben, C. Heymans, H. Hildebrandt, G. Hinshaw, Y.-Z. Ma, L. Miller, M. Viola, and H. Tanimura. Cross-correlating Planck tSZ with RCSLenS weak lensing: Implications for cosmology and AGN feedback. *ArXiv e-prints*, Aug. 2016. → pages 32, 35, 95, 101

D. Hooper and S. Profumo. Dark matter and collider phenomenology of universal extra dimensions. *Physics Reports*, 453(2-4):29–115, Dec. 2007. doi: 10.1016/j.physrep.2007.09.003. → pages 23

W. Hu and T. Okamoto. Mass reconstruction with cosmic microwave background polarization. ApJ, 574:566–574, Aug. 2002. doi: 10.1086/341110. → pages 8

A. Ibarra, D. Tran, and C. Weniger. Indirect Searches for Decaying Dark Matter. *International Journal of Modern Physics A*, 28:1330040, Oct. 2013. doi: 10.1142/S0217751X13300408. → pages 27

D. Jeong, E. Komatsu, and B. Jain. Galaxy-CMB and galaxy-galaxy lensing on large scales: Sensitivity to primordial non-Gaussianity. Phys. Rev. D, 80(12):123527, Dec. 2009. doi: 10.1103/PhysRevD.80.123527. → pages 53

S. Joudaki, A. Mead, C. Blake, A. Choi, J. de Jong, T. Erben, C. Heymans, H. Hildebrandt, H. Hoekstra, B. Joachimi, D. Klaes, F. Köhlinger, K. Kuijken, J. McFarland, L. Miller, P. Schneider, and M. Viola. KiDS-450: Testing extensions to the standard cosmological model. *ArXiv e-prints*, Oct. 2016. → pages 89

S. Joudaki, C. Blake, C. Heymans, A. Choi, J. Harnois-Deraps, H. Hildebrandt, B. Joachimi, A. Johnson, A. Mead, D. Parkinson, M. Viola, and L. van Waerbeke. CFHTLenS revisited: assessing concordance with Planck including astrophysical systematics. MNRAS, 465:2033–2052, Feb. 2017. doi: 10.1093/mnras/stw2665. → pages 89

G. Jungman, M. Kamionkowski, and K. Griest. Supersymmetric dark matter. Phys. Rep., 267: 195–373, Mar. 1996. doi: 10.1016/0370-1573(95)00058-5. → pages 20, 23

N. Kaiser. Weak gravitational lensing of distant galaxies. *The Astrophysical Journal*, 388:272, Apr. 1992. doi: 10.1086/171151. → pages 77, 152

M. Kamionkowski, A. Kosowsky, and A. Stebbins. Statistics of cosmic microwave background polarization. Phys. Rev. D, 55:7368–7388, June 1997. doi: 10.1103/PhysRevD.55.7368. → pages 87

G. Kaufman. Some bayesian moment formulae. *Center for Operations Research and Econometrics, Catholic University of Louvain, Heverlee, Belgium*, Report No. 6710, 1967. → pages 37, 41

M. Kilbinger, K. Benabed, J. Guy, P. Astier, I. Tereno, L. Fu, D. Wraith, J. Coupon, Y. Mellier, C. Balland, F. R. Bouchet, T. Hamana, D. Hardin, H. J. McCracken, R. Pain, N. Regnault, M. Schultheis, and H. Yahagi. Dark-energy constraints and correlations with systematics from CFHTLS weak lensing, SNLS supernovae Ia and WMAP5. A&A, 497:677–688, Apr. 2009. doi: 10.1051/0004-6361/200811247. → pages 93

M. Kilbinger, L. Fu, C. Heymans, F. Simpson, J. Benjamin, T. Erben, J. Harnois-Déraps, H. Hoekstra, H. Hildebrandt, T. D. Kitching, Y. Mellier, L. Miller, L. Van Waerbeke, K. Benabed, C. Bonnett, J. Coupon, M. J. Hudson, K. Kuijken, B. Rowe, T. Schrabback, E. Semboloni, S. Vafaei, and M. Velander. CFHTLenS: combined probe cosmological model comparison using 2D weak gravitational lensing. *MNRAS*, 430:2200–2220, Apr. 2013. doi: 10.1093/mnras/stt041. → pages 32, 104

M. Kilbinger, C. Heymans, M. Asgari, S. Joudaki, P. Schneider, P. Simon, L. Van Waerbeke, J. Harnois-Déraps, H. Hildebrandt, F. Köhlinger, K. Kuijken, and M. Viola. Precision calculations of the cosmic shear power spectrum projection. *ArXiv e-prints*, Feb. 2017. → pages 11, 92

D. Kirk, Y. Omori, A. Benoit-Lévy, R. Cawthon, C. Chang, P. Larsen, A. Amara, D. Bacon, T. M. Crawford, S. Dodelson, P. Fosalba, T. Giannantonio, G. Holder, B. Jain, T. Kacprzak, O. Lahav, N. MacCrann, A. Nicola, A. Refregier, E. Sheldon, K. T. Story, M. A. Troxel, J. D. Vieira, V. Vikram, J. Zuntz, T. M. C. Abbott, F. B. Abdalla, M. R. Becker, B. A. Benson, G. M. Bernstein, R. A. Bernstein, L. E. Bleem, C. Bonnett, S. L. Bridle, D. Brooks, E. Buckley-Geer, D. L. Burke, D. Capozzi, J. E. Carlstrom, A. C. Rosell, M. C. Kind, J. Carretero, M. Crocce, C. E. Cunha, C. B. D'Andrea, L. N. da Costa, S. Desai, H. T. Diehl, J. P. Dietrich, P. Doel, T. F. Eifler, A. E. Evrard, B. Flaugher, J. Frieman, D. W. Gerdes, D. A. Goldstein, D. Gruen, R. A. Gruendl, K. Honscheid, D. J. James, M. Jarvis, S. Kent, K. Kuehn, N. Kuropatkin, M. Lima, M. March, P. Martini, P. Melchior, C. J. Miller, R. Miquel, R. C. Nichol, R. Ogando, A. A. Plazas, C. L. Reichardt, A. Roodman, E. Rozo, E. S. Rykoff, M. Sako, E. Sanchez, V. Scarpine, M. Schubnell, I. Sevilla-Noarbe, G. Simard, R. C. Smith, M. Soares-Santos, F. Sobreira, E. Suchyta, M. E. C. Swanson, G. Tarle, D. Thomas, R. H. Wechsler, and J. Weller. Cross-correlation of gravitational lensing from DES Science Verification data with SPT and Planck lensing. MNRAS, 459:21–34, June 2016. doi: 10.1093/mnras/stw570. → pages 90

E. Komatsu, K. M. Smith, J. Dunkley, C. L. Bennett, B. Gold, G. Hinshaw, N. Jarosik, D. Larson, M. R. Nolta, L. Page, D. N. Spergel, M. Halpern, R. S. Hill, A. Kogut, M. Limon, S. S. Meyer, N. Odegard, G. S. Tucker, J. L. Weiland, E. Wollack, and E. L. Wright. Seven-year Wilkinson Microwave Anisotropy Probe (WMAP) Observations: Cosmological Interpretation. ApJS, 192:18, Feb. 2011. doi: 10.1088/0067-0049/192/2/18. → pages 58

E. Krause and C. M. Hirata. Weak lensing power spectra for precision cosmology. *Astronomy & Astrophysics*, 523:A28, Nov. 2010. doi: 10.1051/0004-6361/200913524. → pages 4, 75, 77, 78, 81, 83, 84, 87

K. Kuijken, C. Heymans, H. Hildebrandt, R. Nakajima, T. Erben, J. T. A. de Jong, M. Viola, A. Choi, H. Hoekstra, L. Miller, E. van Uitert, A. Amon, C. Blake, M. Brouwer, A. Buddendiek, I. F. Conti, M. Eriksen, A. Grado, J. Harnois-Déraps, E. Helmich, R. Herbonnet, N. Irisarri, T. Kitching, D. Klaes, F. La Barbera, N. Napolitano, M. Radovich, P. Schneider, C. Sifón, G. Sikkema, P. Simon, A. Tudorica, E. Valentijn, G. Verdoes Kleijn, and L. van Waerbeke. Gravitational lensing analysis of the Kilo-Degree Survey. MNRAS, 454:3500–3532, Dec. 2015. doi: 10.1093/mnras/stv2140. → pages 24, 90, 93, 112

A. M. C. Le Brun, I. G. McCarthy, J. Schaye, and T. J. Ponman. Towards a realistic population of simulated galaxy groups and clusters. MNRAS, 441:1270 (L14)–1290, June 2014. doi: 10.1093/mnras/stu608. → pages 59, 72, 73

A. M. C. Le Brun, I. G. McCarthy, and J.-B. Melin. Testing Sunyaev-Zel'dovich measurements of the hot gas content of dark matter haloes using synthetic skies. MNRAS, 451:3868–3881, Aug. 2015. doi: 10.1093/mnras/stv1172. → pages 69

B. W. Lee and S. Weinberg. Cosmological lower bound on heavy-neutrino masses. *Physical Review Letters*, 39:165–168, July 1977. doi: 10.1103/PhysRevLett.39.165. → pages 23

D. N. Limber. The Analysis of Counts of the Extragalactic Nebulae in Terms of a Fluctuating Density Field. *The Astrophysical Journal*, 117:134, Jan. 1953. doi: 10.1086/145672. → pages 11, 24, 77, 152

D. N. Limber. The analysis of counts of the extragalactic nebulae in terms of a fluctuating density field. ii. ApJ, 119:655–+, May 1954. doi: 10.1086/145870. → pages 92

J. Liske, I. K. Baldry, S. P. Driver, R. J. Tuffs, M. Alpaslan, E. Andrae, S. Brough, M. E. Cluver, M. W. Grootes, M. L. P. Gunawardhana, L. S. Kelvin, J. Loveday, A. S. G. Robotham, E. N. Taylor, S. P. Bamford, J. Bland-Hawthorn, M. J. I. Brown, M. J. Drinkwater, A. M. Hopkins, M. J. Meyer, P. Norberg, J. A. Peacock, N. K. Agius, S. K. Andrews, A. E. Bauer, J. H. Y. Ching, M. Colless, C. J. Conselice, S. M. Croom, L. J. M. Davies, R. De Propris, L. Dunne, E. M. Eardley, S. Ellis, C. Foster, C. S. Frenk, B. Häußler, B. W. Holwerda, C. Howlett, H. Ibarra, M. J. Jarvis, D. H. Jones, P. R. Kafle, C. G. Lacey, R. Lange, M. A. Lara-López, Á. R. López-Sánchez, S. Maddox, B. F. Madore, T. McNaught-Roberts, A. J. Moffett, R. C. Nichol, M. S. Owers, D. Palamara, S. J. Penny, S. Phillipps, K. A. Pimbblet, C. C. Popescu, M. Prescott, R. Proctor, E. M. Sadler, A. E. Sansom, M. Seibert, R. Sharp, W. Sutherland, J. A. Vázquez-Mata, E. van Kampen, S. M. Wilkins, R. Williams, and A. H. Wright. Galaxy And Mass Assembly (GAMA): end of survey report and data release 2. MNRAS, 452:2087–2126, Sept. 2015. doi: 10.1093/mnras/stv1436. → pages 93

J. Liu and J. C. Hill. Cross-correlation of Planck CMB lensing and CFHTLenS galaxy weak lensing maps. Phys. Rev. D, 92(6):063517, Sept. 2015. doi: 10.1103/PhysRevD.92.063517. → pages 90, 94, 110, 116

J. Liu, A. Ortiz-Vazquez, and J. C. Hill. Constraining multiplicative bias in CFHTLenS weak lensing shear data. Phys. Rev. D, 93(10):103508, May 2016. doi: 10.1103/PhysRevD.93.103508. → pages 90, 91, 112

M. LoVerde and N. Afshordi. Extended Limber approximation. *Physical Review D*, 78(12):123506, Dec. 2008. doi: 10.1103/PhysRevD.78.123506. → pages 77, 92

T. Lu, U.-L. Pen, and O. Doré. Dark energy from large-scale structure lensing information. Phys. Rev. D, 81(12):123015–+, June 2010. doi: 10.1103/PhysRevD.81.123015. → pages 99

Y.-Z. Ma, L. Van Waerbeke, G. Hinshaw, A. Hojjati, D. Scott, and J. Zuntz. Probing the diffuse baryon distribution with the lensing-tSZ cross-correlation. J. Cosmology Astropart. Phys., 9:046, Sept. 2015. doi: 10.1088/1475-7516/2015/09/046. → pages 51, 53, 57, 74, 76, 88

N. MacCrann, J. Zuntz, S. Bridle, B. Jain, and M. R. Becker. Cosmic discordance: are Planck CMB and CFHTLenS weak lensing measurements out of tune? MNRAS, 451:2877–2888, Aug. 2015. doi: 10.1093/mnras/stv1154. → pages 89

R. Mandelbaum, C. Blake, S. Bridle, F. B. Abdalla, S. Brough, M. Colless, W. Couch, S. Croom, T. Davis, M. J. Drinkwater, K. Forster, K. Glazebrook, B. Jelliffe, R. J. Jurek, I.-H. Li, B. Madore, C. Martin, K. Pimbblet, G. B. Poole, M. Pracy, R. Sharp, E. Wisnioski, D. Woods, and T. Wyder. The wigglez dark energy survey: direct constraints on blue galaxy intrinsic alignments at intermediate redshifts. *MNRAS*, 410:844–859, January 2011. → pages 106

R. Mandelbaum, A. Slosar, T. Baldauf, U. Seljak, C. M. Hirata, R. Nakajima, R. Reyes, and R. E. Smith. Cosmological parameter constraints from galaxy-galaxy lensing and galaxy clustering with the SDSS DR7. MNRAS, 432:1544–1575, June 2013. doi: 10.1093/mnras/stt572. → pages 96

A. B. Mantz, A. von der Linden, S. W. Allen, D. E. Applegate, P. L. Kelly, R. G. Morris, D. A. Rapetti, R. W. Schmidt, S. Adhikari, M. T. Allen, P. R. Burchat, D. L. Burke, M. Cataneo, D. Donovan, H. Ebeling, S. Shandera, and A. Wright. Weighing the giants - IV. Cosmology and neutrino mass. MNRAS, 446:2205–2225, Jan. 2015. doi: 10.1093/mnras/stu2096. → pages 22

I. G. McCarthy, A. M. C. Le Brun, J. Schaye, and G. P. Holder. The thermal Sunyaev-Zel'dovich effect power spectrum in light of Planck. MNRAS, 440:3645–3657, June 2014. doi: 10.1093/mnras/stu543. → pages 59, 66, 72

A. J. Mead, J. A. Peacock, C. Heymans, S. Joudaki, and A. F. Heavens. An accurate halo model for fitting non-linear cosmological power spectra and baryonic feedback models. MNRAS, 454: 1958–1975, Dec. 2015. doi: 10.1093/mnras/stv2036. → pages 17, 109, 110

A. J. Mead, C. Heymans, L. Lombriser, J. A. Peacock, O. I. Steele, and H. A. Winther. Accurate halo-model matter power spectra with dark energy, massive neutrinos and modified gravitational forces. MNRAS, 459:1468–1488, June 2016. doi: 10.1093/mnras/stw681. → pages 17

L. Miller, C. Heymans, T. D. Kitching, L. van Waerbeke, T. Erben, H. Hildebrandt, H. Hoekstra, Y. Mellier, B. T. P. Rowe, J. Coupon, J. P. Dietrich, L. Fu, J. Harnois-Déraps, M. J. Hudson, M. Kilbinger, K. Kuijken, T. Schrabback, E. Semboloni, S. Vafaei, and M. Velander. Bayesian galaxy shape measurement for weak lensing surveys - III. Application to the Canada-France-Hawaii Telescope Lensing Survey. MNRAS, 429:2858–2880, Mar. 2013. doi: 10.1093/mnras/sts454. → pages 32, 54, 59, 90, 93

J. Miralda-Escude. The correlation function of galaxy ellipticities produced by gravitational lensing. ApJ, 380:1–8, Oct. 1991. → pages 92

S. Miyazaki, Y. Komiyama, H. Nakaya, Y. Kamata, Y. Doi, T. Hamana, H. Karoji, H. Furusawa, S. Kawanomoto, T. Morokuma, Y. Ishizuka, K. Nariai, Y. Tanaka, F. Uraguchi, Y. Utsumi, Y. Obuchi, Y. Okura, M. Oguri, T. Takata, D. Tomono, T. Kurakami, K. Namikawa, T. Usuda, H. Yamanoi, T. Terai, H. Uekiyo, Y. Yamada, M. Koike, H. Aihara, Y. Fujimori, S. Mineo, H. Miyatake, N. Yasuda, J. Nishizawa, T. Saito, M. Tanaka, T. Uchida, N. Katayama, S.-Y. Wang, H.-Y. Chen, R. Lupton, C. Loomis, S. Bickerton, P. Price, J. Gunn, H. Suzuki, Y. Miyazaki, M. Muramatsu, K. Yamamoto, M. Endo, Y. Ezaki, N. Itoh, Y. Miwa, H. Yokota, T. Matsuda, R. Ebinuma, and K. Takeshi. Hyper Suprime-Cam. In *Ground-based and Airborne Instrumentation for Astronomy IV*, volume 8446 of Proc. SPIE, page 84460Z, Sept. 2012. doi: 10.1117/12.926844. → pages 68

H. J. Mo and S. D. M. White. An analytic model for the spatial clustering of dark matter haloes. MNRAS, 282:347–361, Sept. 1996. doi: 10.1093/mnras/282.2.347. → pages 15

Á. Moliné, M. A. Sánchez-Conde, S. Palomares-Ruiz, and F. Prada. Characterization of subhalo structural properties and implications for dark matter annihilation signals. MNRAS, 466(4):4974, Jan. 2017. doi: 10.1093/mnras/stx026. → pages 27, 28

B. Moraes, J.-P. Kneib, A. Leauthaud, M. Makler, L. Van Waerbeke, K. Bundy, T. Erben, C. Heymans, H. Hildebrandt, L. Miller, H. Y. Shan, D. Woods, A. Charbonnier, and M. E. Pereira. The cfht/megacam stripe-82 survey. In *Revista Mexicana de Astronomia y Astrofisica Conference Series*, volume 44 of *Revista Mexicana de Astronomia y Astrofisica Conference Series*, pages 202–203, Oct. 2014. → pages 90

C. B. Morrison, H. Hildebrandt, S. J. Schmidt, I. K. Baldry, M. Bilicki, A. Choi, T. Erben, and P. Schneider. the-wizz: clustering redshift estimation for everyone. MNRAS, 467:3576–3589, May 2017. doi: 10.1093/mnras/stx342. → pages 108

D. Nagai, A. V. Kravtsov, and A. Vikhlinin. Effects of Galaxy Formation on Thermodynamics of the Intracluster Medium. ApJ, 668:1–14, Oct. 2007. doi: 10.1086/521328. → pages 58

J. F. Navarro, C. S. Frenk, and S. D. M. White. A Universal Density Profile from Hierarchical Clustering. ApJ, 490:493–508, Dec. 1997. → pages 13, 27

T. Okamoto and W. Hu. Cosmic microwave background lensing reconstruction on the full sky. Phys. Rev. D, 67(8):083002, Apr. 2003. doi: 10.1103/PhysRevD.67.083002. → pages 95

Y. Omori and G. Holder. Cross-correlation of cfhtlens galaxy number density and planck cmb lensing. *ArXiv e-prints*, Feb. 2015. → pages 90

Planck Collaboration XVI. *Planck* 2013 results. XVI. Cosmological parameters. A&A, 571:A16, 2014. doi: 10.1051/0004-6361/201321591. → pages 58, 87

Planck Collaboration XIII. *Planck* 2015 results. XIII. Cosmological parameters. A&A, 594:A13, 2016. doi: 10.1051/0004-6361/201525830. → pages 10, 20, 22, 24, 89

Planck Collaboration XV. *Planck* 2015 results. XV. Gravitational lensing. A&A, 594:A15, 2016. doi: 10.1051/0004-6361/201525941. → pages 90, 95, 99

Planck Collaboration XXII. *Planck* 2015 results. XXII. A map of the thermal Sunyaev-Zeldovich effect. A&A, 594:A22, 2016. doi: 10.1051/0004-6361/201525826. → pages 51, 56

Planck Collaboration Int. V. *Planck* intermediate results. V. Pressure profiles of galaxy clusters from the Sunyaev-Zeldovich effect. A&A, 550:A131, 2013. doi: 10.1051/0004-6361/201220040. → pages 58

F. Prada, A. A. Klypin, A. J. Cuesta, J. E. Betancort-Rijo, and J. Primack. Halo concentrations in the standard Λ cold dark matter cosmology. MNRAS, 423:3018–3030, July 2012. doi: 10.1111/j.1365-2966.2012.21007.x. → pages 27, 28

S. Profumo, K. Sigurdson, and M. Kamionkowski. What Mass Are the Smallest Protohalos? *Physical Review Letters*, 97(3):031301, July 2006. doi: 10.1103/PhysRevLett.97.031301. → pages 27

T. Pyne and M. Birkinshaw. Beyond the Thin Lens Approximation. *The Astrophysical Journal*, 458: 46, Feb. 1996. doi: 10.1086/176791. → pages 5

M. Regis, J.-Q. Xia, A. Cuoco, E. Branchini, N. Fornengo, and M. Viel. Particle Dark Matter Searches Outside the Local Group. *Physical Review Letters*, 114(24):241301, June 2015. doi: 10.1103/PhysRevLett.114.241301. → pages 23, 27, 48, 49

J. Ripken, A. Cuoco, H.-S. Zechlin, J. Conrad, and D. Horns. The sensitivity of Cherenkov telescopes to dark matter and astrophysical anisotropies in the diffuse gamma-ray background. J. Cosmology Astropart. Phys., 1:049, Jan. 2014. doi: 10.1088/1475-7516/2014/01/049. → pages 49

A. J. Ross, L. Samushia, C. Howlett, W. J. Percival, A. Burden, and M. Manera. The clustering of the SDSS DR7 main Galaxy sample - I. A 4 per cent distance measure at z = 0.15. MNRAS, 449: 835–847, May 2015. doi: 10.1093/mnras/stv154. → pages 22

R. Sachs. Gravitational Waves in General Relativity. VI. The Outgoing Radiation Condition. *Proceedings of the Royal Society A Mathematical Physical and Engineering Sciences*, 264(1318): 309–338, 1961. doi: 10.1098/rspa.1961.0202. → pages 5

E. Sánchez and Des Collaboration. The Dark Energy Survey. *Journal of Physics Conference Series*, 259(1):012080, Nov. 2010. doi: 10.1088/1742-6596/259/1/012080. → pages 75

M. A. Sánchez-Conde and F. Prada. The flattening of the concentration-mass relation towards low halo masses and its implications for the annihilation signal boost. MNRAS, 442:2271–2277, Aug. 2014. doi: 10.1093/mnras/stu1014. → pages 27

E. Schaan, E. Krause, T. Eifler, O. Doré, H. Miyatake, J. Rhodes, and D. N. Spergel. Looking through the same lens: Shear calibration for LSST, Euclid, and WFIRST with stage 4 CMB lensing. Phys. Rev. D, 95(12):123512, June 2017. doi: 10.1103/PhysRevD.95.123512. → pages 91, 112, 115

J. Schaye and C. Dalla Vecchia. On the relation between the Schmidt and Kennicutt-Schmidt star formation laws and its implications for numerical simulations. MNRAS, 383:1210–1222, Jan. 2008. doi: 10.1111/j.1365-2966.2007.12639.x. → pages 59

J. Schaye, C. Dalla Vecchia, C. M. Booth, R. P. C. Wiersma, T. Theuns, M. R. Haas, S. Bertone, A. R. Duffy, I. G. McCarthy, and F. van de Voort. The physics driving the cosmic star formation history. MNRAS, 402:1536–1560, Mar. 2010. doi: 10.1111/j.1365-2966.2009.16029.x. → pages 58

R. J. Scherrer and E. Bertschinger. Statistics of primordial density perturbations from discrete seed masses. ApJ, 381:349–360, Nov. 1991. doi: 10.1086/170658. → pages 13

M. Schmaltz and D. Tucker-Smith. Little Higgs Theories. *Annual Review of Nuclear and Particle Science*, 55:229–270, Dec. 2005. doi: 10.1146/annurev.nucl.55.090704.151502. → pages 23

P. Schneider. The consequences of parity symmetry for higher-order statistics of cosmic shear and other polar fields. A&A, 408:829–834, Sept. 2003. doi: 10.1051/0004-6361:20031035. → pages 98

P. Schneider and C. Seitz. Steps towards nonlinear cluster inversion through gravitational distortions. 1: Basic considerations and circular clusters. A&A, 294:411–431, Feb. 1995. → pages 155

P. Schneider, J. Ehlers, and E. E. Falco. *Gravitational Lenses*. Springer-Verlag Berlin Heidelberg New York, 1992. doi: 10.1007/978-3-662-03758-4. → pages 75

P. Schneider, L. van Waerbeke, B. Jain, and G. Kruse. A new measure for cosmic shear. *Monthly Notices of the Royal Astronomical Society*, 296(4):873–892, June 1998. doi: 10.1046/j.1365-8711.1998.01422.x. → pages 75, 78, 83, 149

P. Schneider, L. van Waerbeke, M. Kilbinger, and Y. Mellier. Analysis of two-point statistics of cosmic shear. I. Estimators and covariances. A&A, 396:1–19, Dec. 2002. doi: 10.1051/0004-6361:20021341. → pages 36

R. Scoccimarro and H. M. P. Couchman. A fitting formula for the non-linear evolution of the bispectrum. *Monthly Notices of the Royal Astronomical Society*, 325(4):1312–1316, Aug. 2001. doi: 10.1046/j.1365-8711.2001.04281.x. → pages 87, 88

R. Scoccimarro, R. K. Sheth, L. Hui, and B. Jain. How Many Galaxies Fit in a Halo? Constraints on Galaxy Formation Efficiency from Spatial Clustering. ApJ, 546:20–34, Jan. 2001. doi: 10.1086/318261. → pages 13

C. Seitz and P. Schneider. Steps towards nonlinear cluster inversion through gravitational distortions. III. Including a redshift distribution of the sources. A&A, 318:687–699, Feb. 1997. → pages 155

S. Seitz, P. Schneider, and J. Ehlers. Light propagation in arbitrary spacetimes and the gravitational lens approximation. *Classical and Quantum Gravity*, 11(9):2345–2373, Sept. 1994. doi: 10.1088/0264-9381/11/9/016. → pages 5

E. Sellentin and A. F. Heavens. Parameter inference with estimated covariance matrices. MNRAS, 456:L132–L136, Feb. 2016. doi: 10.1093/mnrasl/slv190. → pages 37, 41, 62, 101, 104

E. Semboloni, H. Hoekstra, J. Schaye, M. P. van Daalen, and I. G. McCarthy. Quantifying the effect of baryon physics on weak lensing tomography. MNRAS, 417:2020–2035, Nov. 2011. doi: 10.1111/j.1365-2966.2011.19385.x. → pages 50, 117

C. Shapiro. BIASED DARK ENERGY CONSTRAINTS FROM NEGLECTING REDUCED SHEAR IN WEAK-LENSING SURVEYS. *The Astrophysical Journal*, 696(1):775–784, May 2009. doi: 10.1088/0004-637X/696/1/775. → pages 75, 78, 83

C. Shapiro and A. Cooray. The Born and lens–lens corrections to weak gravitational lensing angular power spectra. *Journal of Cosmology and Astroparticle Physics*, 2006(03):007–007, Mar. 2006. doi: 10.1088/1475-7516/2006/03/007. → pages 75

R. K. Sheth and G. Tormen. Large-scale bias and the peak background split. MNRAS, 308:119–126, Sept. 1999. doi: 10.1046/j.1365-8711.1999.02692.x. → pages 15, 27, 30

M. Shirasaki, S. Horiuchi, and N. Yoshida. Cross correlation of cosmic shear and extragalactic gamma-ray background: Constraints on the dark matter annihilation cross section. Phys. Rev. D, 90 (6):063502, Sept. 2014. doi: 10.1103/PhysRevD.90.063502. → pages 23, 24, 35, 40, 43, 47, 49

M. Shirasaki, S. Horiuchi, and N. Yoshida. Cross-correlation of the extragalactic gamma-ray background with luminous red galaxies. Phys. Rev. D, 92(12):123540, Dec. 2015. doi: 10.1103/PhysRevD.92.123540. → pages 23

M. Shirasaki, O. Macias, S. Horiuchi, S. Shirai, and N. Yoshida. Cosmological constraints on dark matter annihilation and decay: Cross-correlation analysis of the extragalactic γ -ray background and cosmic shear. Phys. Rev. D, 94(6):063522, Sept. 2016. doi: 10.1103/PhysRevD.94.063522. → pages 23, 24, 34, 41, 43, 47, 49

P. Simon, E. Semboloni, L. van Waerbeke, H. Hoekstra, T. Erben, L. Fu, J. Harnois-Déraps, C. Heymans, H. Hildebrandt, M. Kilbinger, T. D. Kitching, L. Miller, and T. Schrabback. CFHTLenS: a Gaussian likelihood is a sufficient approximation for a cosmological analysis of third-order cosmic shear statistics. MNRAS, 449:1505–1525, May 2015. doi: 10.1093/mnras/stv339. → pages 106

S. Singh, R. Mandelbaum, and J. R. Brownstein. Cross-correlating Planck CMB lensing with SDSS: lensing-lensing and galaxy-lensing cross-correlations. MNRAS, 464:2120–2138, Jan. 2017. doi: 10.1093/mnras/stw2482. → pages 91, 96, 116

T. Sjöstrand, S. Mrenna, and P. Skands. A brief introduction to PYTHIA 8.1. *Computer Physics Communications*, 178:852–867, June 2008. doi: 10.1016/j.cpc.2008.01.036. → pages 25

R. E. Smith, J. A. Peacock, A. Jenkins, S. D. M. White, C. S. Frenk, F. R. Pearce, P. A. Thomas, G. Efstathiou, and H. M. P. Couchman. Stable clustering, the halo model and non-linear cosmological power spectra. *Monthly Notices of the Royal Astronomical Society*, 341(4):1311–1332, June 2003. doi: 10.1046/j.1365-8711.2003.06503.x. → pages 17, 93, 109, 110

G. Steigman, B. Dasgupta, and J. F. Beacom. Precise relic WIMP abundance and its impact on searches for dark matter annihilation. Phys. Rev. D, 86(2):023506, July 2012. doi: 10.1103/PhysRevD.86.023506. → pages 45, 46

R. A. Sunyaev and Y. B. Zeldovich. Small-Scale Fluctuations of Relic Radiation. *Astrophysics and Space Science*, 7:3–19, Apr. 1970. doi: 10.1007/BF00653471. → pages 52

R. A. Sunyaev and Y. B. Zeldovich. The Observations of Relic Radiation as a Test of the Nature of X-Ray Radiation from the Clusters of Galaxies. *Comments on Astrophysics and Space Physics*, 4, 1972. → pages 20, 76

I. Szapudi, S. Prunet, and S. Colombi. Fast Analysis of Inhomogenous Megapixel Cosmic Microwave Background Maps. ApJ, 561:L11–L14, Nov. 2001a. doi: 10.1086/324312. → pages 90, 98

I. Szapudi, S. Prunet, D. Pogosyan, A. S. Szalay, and J. R. Bond. Fast Cosmic Microwave Background Analyses via Correlation Functions. ApJ, 548:L115–L118, Feb. 2001b. doi: 10.1086/319105. → pages 36

R. Takahashi, M. Sato, T. Nishimichi, A. Taruya, and M. Oguri. Revising the halofit model for the nonlinear matter power spectrum. ApJ, 761:152, Dec. 2012. doi: 10.1088/0004-637X/761/2/152. → pages 17, 87, 93, 109, 110

A. Taylor and B. Joachimi. Estimating cosmological parameter covariance. MNRAS, 442:2728–2738, Aug. 2014. doi: 10.1093/mnras/stu996. → pages 41, 101, 119

A. Taylor, B. Joachimi, and T. Kitching. Putting the precision in precision cosmology: How accurate should your data covariance matrix be? MNRAS, 432:1928–1946, July 2013. doi: 10.1093/mnras/stt270. → pages 37, 119

M. Tegmark, A. N. Taylor, and A. F. Heavens. Karhunen-Loève Eigenvalue Problems in Cosmology: How Should We Tackle Large Data Sets? ApJ, 480:22–35, May 1997. → pages 119

D. B. Thomas, M. Bruni, and D. Wands. Relativistic weak lensing from a fully non-linear cosmological density field. J. Cosmology Astropart. Phys., 9:021, Sept. 2015. doi: 10.1088/1475-7516/2015/09/021. → pages 86

R. J. Thornton, P. A. R. Ade, S. Aiola, F. E. Angilè, M. Amiri, J. A. Beall, D. T. Becker, H.-M. Cho, S. K. Choi, P. Corlies, K. P. Coughlin, R. Datta, M. J. Devlin, S. R. Dicker, R. Dünner, J. W. Fowler, A. E. Fox, P. A. Gallardo, J. Gao, E. Grace, M. Halpern, M. Hasselfield, S. W. Henderson, G. C. Hilton, A. D. Hincks, S. P. Ho, J. Hubmayr, K. D. Irwin, J. Klein, B. Koopman, D. Li, T. Louis, M. Lungu, L. Maurin, J. McMahon, C. D. Munson, S. Naess, F. Nati, L. Newburgh, J. Nibarger, M. D. Niemack, P. Niraula, M. R. Nolta, L. A. Page, C. G. Pappas, A. Schillaci, B. L. Schmitt, N. Sehgal, J. L. Sievers, S. M. Simon, S. T. Staggs, C. Tucker, M. Uehara, J. van Lanen, J. T. Ward, and E. J. Wollack. The Atacama Cosmology Telescope: The Polarization-sensitive ACTPol Instrument. ApJS, 227:21, Dec. 2016. doi: 10.3847/1538-4365/227/2/21. → pages 119

T. Tröster and L. Van Waerbeke. Weak lensing corrections to tSZ-lensing cross correlation. J. Cosmology Astropart. Phys., 11:008, Nov. 2014. doi: 10.1088/1475-7516/2014/11/008. → pages 53

M. Troxel and M. Ishak. Cross-correlation between cosmic microwave background lensing and galaxy intrinsic alignment as a contaminant to gravitational lensing cross-correlated probes of the universe. Phys. Rev. D, 89:063528, 2014. → pages 90, 105

J. W. Tukey. Bias and confidence in not-quite large samples. *Ann. Math. Statist.*, 29:614–623, 1958. → pages 19

P. Ullio, L. Bergström, J. Edsjö, and C. Lacey. Cosmological dark matter annihilations into γ rays: A closer look. Phys. Rev. D, 66(12):123502, Dec. 2002. doi: 10.1103/PhysRevD.66.123502. → pages 20

M. P. van Daalen, J. Schaye, C. M. Booth, and C. Dalla Vecchia. The effects of galaxy formation on the matter power spectrum: a challenge for precision cosmology. MNRAS, 415:3649–3665, Aug. 2011. doi: 10.1111/j.1365-2966.2011.18981.x. → pages 20, 50, 109, 117

A. van Engelen, R. Keisler, O. Zahn, K. A. Aird, B. A. Benson, L. E. Bleem, J. E. Carlstrom, C. L. Chang, H. M. Cho, T. M. Crawford, A. T. Crites, T. de Haan, M. A. Dobbs, J. Dudley, E. M. George, N. W. Halverson, G. P. Holder, W. L. Holzapfel, S. Hoover, Z. Hou, J. D. Hrubes, M. Joy, L. Knox, A. T. Lee, E. M. Leitch, M. Lueker, D. Luong-Van, J. J. McMahon, J. Mehl, S. S. Meyer, M. Millea, J. J. Mohr, T. E. Montroy, T. Natoli, S. Padin, T. Plagge, C. Pryke, C. L. Reichardt, J. E. Ruhl, J. T. Sayre, K. K. Schaffer, L. Shaw, E. Shirokoff, H. G. Spieler, Z. Staniszewski, A. A. Stark, K. Story, K. Vanderlinde, J. D. Vieira, and R. Williamson. A measurement of gravitational lensing of the microwave background using south pole telescope data. ApJ, 756:142, Sept. 2012. doi: 10.1088/0004-637X/756/2/142. → pages 90

E. van Uitert, H. Hoekstra, M. Velander, D. G. Gilbank, M. D. Gladders, and H. K. C. Yee. Galaxy-galaxy lensing constraints on the relation between baryons and dark matter in galaxies in the Red Sequence Cluster Survey 2. *Astronomy & Astrophysics*, 534:A14, Sept. 2011. doi: 10.1051/0004-6361/201117308. → pages 43

E. van Uitert, M. Cacciato, H. Hoekstra, M. Brouwer, C. Sifón, M. Viola, I. Baldry, J. Bland-Hawthorn, S. Brough, M. J. I. Brown, A. Choi, S. P. Driver, T. Erben, C. Heymans, H. Hildebrandt, B. Joachimi, K. Kuijken, J. Liske, J. Loveday, J. McFarland, L. Miller, R. Nakajima, J. Peacock, M. Radovich, A. S. G. Robotham, P. Schneider, G. Sikkema, E. N. Taylor, and G. Verdoes Kleijn. The stellar-to-halo mass relation of GAMA galaxies from 100 deg^2 of KiDS weak lensing data. MNRAS, 459:3251–3270, July 2016. doi: 10.1093/mnras/stw747. → pages 114

L. van Waerbeke, J. Benjamin, T. Erben, C. Heymans, H. Hildebrandt, H. Hoekstra, T. D. Kitching, Y. Mellier, L. Miller, J. Coupon, J. Harnois-Déraps, L. Fu, M. Hudson, M. Kilbinger, K. Kuijken, B. Rowe, T. Schrabback, E. Semboloni, S. Vafaei, E. van Uitert, and M. Velander. CFHTLenS: mapping the large-scale structure with gravitational lensing. MNRAS, 433:3373–3388, Aug. 2013. doi: 10.1093/mnras/stt971. → pages 55, 56, 62, 87, 147

L. van Waerbeke, G. Hinshaw, and N. Murray. Detection of warm and diffuse baryons in large scale structure from the cross correlation of gravitational lensing and the thermal Sunyaev-Zeldovich effect. Phys. Rev. D, 89(2):023508, Jan. 2014. doi: 10.1103/PhysRevD.89.023508. → pages 51, 52, 56, 66, 72, 74, 76

R. A. Vanderveld, R. R. Caldwell, and J. Rhodes. Second-order weak lensing from modified gravity. *Physical Review D*, 84(12):123510, Dec. 2011. doi: 10.1103/PhysRevD.84.123510. → pages 75, 78

M. Viola, M. Cacciato, M. Brouwer, K. Kuijken, H. Hoekstra, P. Norberg, A. S. G. Robotham, E. van Uitert, M. Alpaslan, I. K. Baldry, A. Choi, J. T. A. de Jong, S. P. Driver, T. Erben, A. Grado, A. W. Graham, C. Heymans, H. Hildebrandt, A. M. Hopkins, N. Irisarri, B. Joachimi, J. Loveday, L. Miller, R. Nakajima, P. Schneider, C. Sifón, and G. Verdoes Kleijn. Dark matter halo properties of GAMA galaxy groups from 100 square degrees of KiDS weak lensing data. MNRAS, 452: 3529–3550, Oct. 2015. doi: 10.1093/mnras/stv1447. → pages 12

R. M. Wald. *General relativity*. University of Chicago Press, 1984. → pages 2

J. V. Wall and C. R. Jenkins. *Practical Statistics for Astronomers*. Cambridge University Press, Nov. 2003. → pages 101

R. P. C. Wiersma, J. Schaye, and B. D. Smith. The effect of photoionization on the cooling rates of enriched, astrophysical plasmas. MNRAS, 393:99–107, Feb. 2009a. doi: 10.1111/j.1365-2966.2008.14191.x. → pages 59

R. P. C. Wiersma, J. Schaye, T. Theuns, C. Dalla Vecchia, and L. Tornatore. Chemical enrichment in cosmological, smoothed particle hydrodynamics simulations. MNRAS, 399:574–600, Oct. 2009b. doi: 10.1111/j.1365-2966.2009.15331.x. → pages 59

D. Williams. *Weighing the Odds,A Course in Probability and Statistics*. Cambridge University Press, 2001. → pages 66

J.-Q. Xia, A. Cuoco, E. Branchini, and M. Viel. Tomography of the Fermi-LAT γ-Ray Diffuse Extragalactic Signal via Cross Correlations with Galaxy Catalogs. ApJS, 217:15, Mar. 2015. doi: 10.1088/0067-0049/217/1/15. → pages 20, 28, 43

A. R. Zentner, D. H. Rudd, and W. Hu. Self-calibration of tomographic weak lensing for the physics of baryons to constrain dark energy. Phys. Rev. D, 77(4):043507, Feb. 2008. doi: 10.1103/PhysRevD.77.043507. → pages 119

A. R. Zentner, E. Semboloni, S. Dodelson, T. Eifler, E. Krause, and A. P. Hearin. Accounting for baryons in cosmological constraints from cosmic shear. Phys. Rev. D, 87(4):043509, Feb. 2013. doi: 10.1103/PhysRevD.87.043509. → pages 119

Appendix A

Supplementary material to Chapter 2

A.1 Fourier-space estimator performance

To check the ability of the power spectrum estimator based on the integration of the tangential shear correlation function, given by Eq. (2.12), to recover the true underlying power spectrum, we test it on a suite of mock simulations. We wish to make a generic test of the accuracy of the power spectrum estimation. To this end, we compare the auto-spectrum of the convergence with the estimated cross-spectrum between the convergence and the shear, which are expected to yield the same result on the flat patches of the simulations. This is analogous to the cross-spectrum of the gamma rays and shear in the analysis of Chapter 2 but easier to handle, as high-resolution simulation products for convergence and shear are readily available.

The simulation products we use are part of the Scinet LIght Cone Simulation suite (Harnois-Déraps et al., 2015a, SLICS hereafter), which consist of 930 realizations of lensing data over $10^\circ \times 10^\circ$ patches in a WMAP9+SN+BAO cosmology ($\{\Omega_{\rm M}, \Omega_\Lambda, \Omega_{\rm b}, \sigma_8, h, n_{\rm s}\} = \{0.2905, 0.7095, 0.0473, 0.826, 0.6898, 0.969\}$). The convergence and two shear components are constructed by ray-tracing up to 18 density planes between redshift zero and 3, and finally mapped on to 7745^2 pixels (see the SLICS reference for details about how this is implemented numerically). For our particular setup, we use the maps constructed while assuming that the galaxy sources are all placed at redshift 0.582. This is of course not representative of the real galaxy distribution of the data, but closely matches the mean of the distribution, which is sufficient for the purpose of calibration.

For the verification of our estimator in Eq. (2.12), we use a subset of 100 realizations. The convergence and shear maps are cropped to 7700^2 pixels and then down-sampled by a factor of 10 to closer resemble the pixel size encountered in the gamma-ray analysis.

We measure the tangential shear correlation function between the convergence and shear maps using the same binning scheme as the gamma-ray cross-correlation measurement, i.e., 300 linearly spaced bins between 1 and 301 arcmin. The power spectrum estimated using Eq. (2.12) is then expected to agree with the auto-power spectrum of the convergence map $C_\ell^{\kappa\kappa}$. The power spectra measured on the simulations are shown in Fig. A.1. For the scales of interest in the analysis of Chapter 2 the estimator

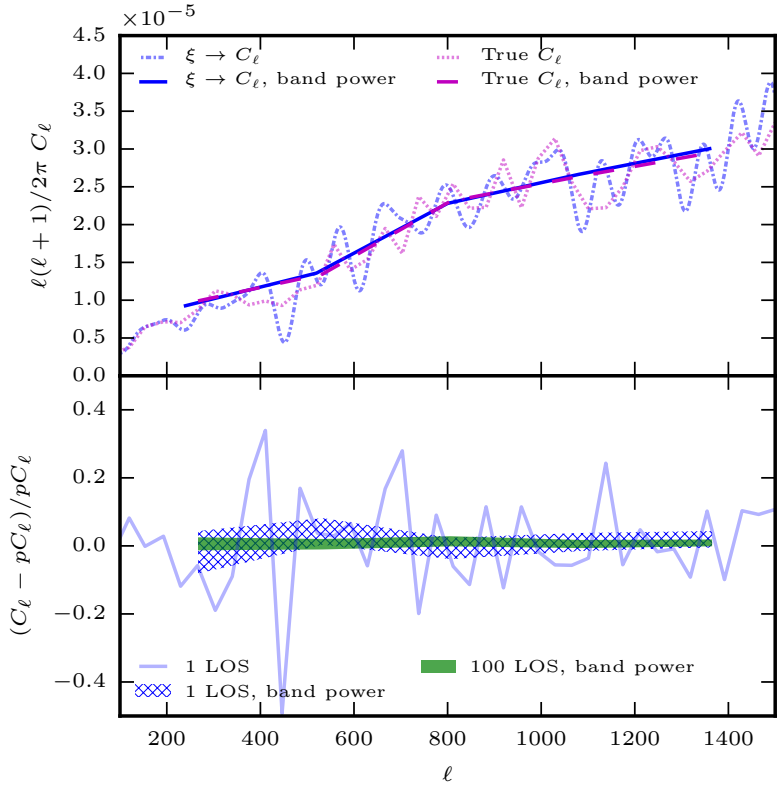

Figure A.1: *Top*: power spectrum estimated using Eq. (2.12) ($\xi \to C_\ell$, dash-dotted blue), $\xi \to C_\ell$ band power (solid blue), true power spectrum from SLICS (dotted magenta), and true band power from SLICS (dashed magenta) for one line-of-sight. *Bottom*: difference between estimated and true power spectrum from SLICS (light solid blue) for one line-of-sight, difference between the estimated and true band power from SLICS for one line-of-sight (hashed blue) and 100 lines-of-sight (solid green).

recovers the power spectrum to within 5 percent on individual line-of-sights, which is within the error on the mean per ℓ-bin of the true power spectrum. The agreement is within 1 per cent for 100 lines-of-sight, which is less than the error on the mean of the 100 true power spectra, showing that the fluctuations seen on individual lines-of-sight average out.

One caveat is that the range of integration in Eq. (2.12) is formally from 0 to infinite angular separation. By restricting the integration to some finite range $\vartheta_{\rm min}$ to $\vartheta_{\rm max}$, the resulting power spectrum estimate can become biased.

To estimate the effect of restricting the angular range of the two-point correlation function on the power spectrum estimate we produce a high-resolution measurement of the convergence power spectrum $C_\ell^{\kappa\kappa}$. Using the relation in Eq. (2.2) between the power spectrum $C_\ell^{\kappa\kappa}$ and the tangential shear correlation function $\xi^{\kappa\gamma_t}(\vartheta)$, we compute a theory estimate $\xi_{\rm th}^{\kappa\gamma_t}(\vartheta)$ from the measured high-resolution convergence power spectrum. Alternatively, we could also have used an analytical model for the power spectrum or correlation function. However, since we have access to the true power spectrum from SLICS and in

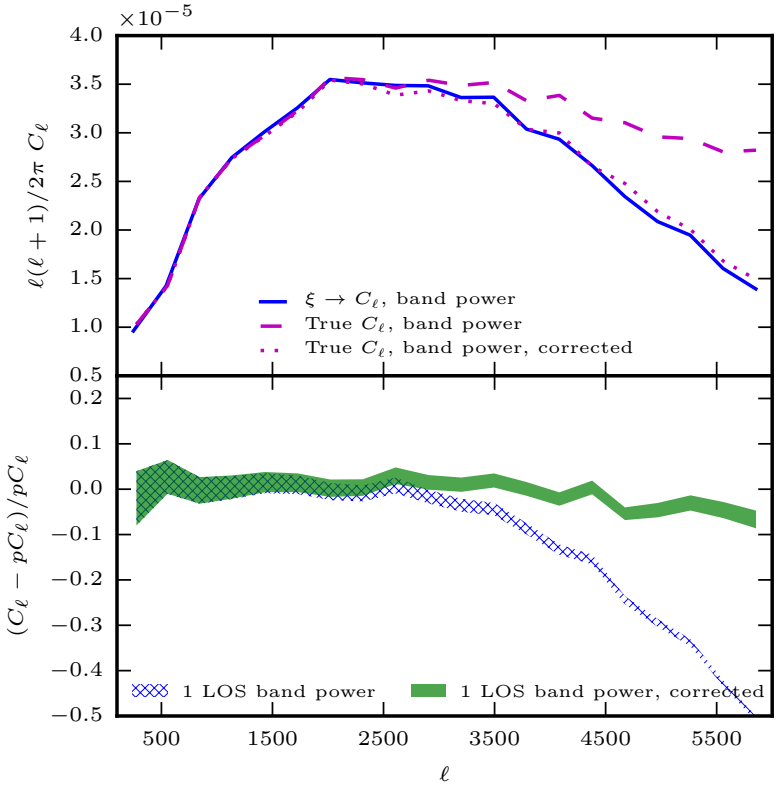

Figure A.2: *Top*: band power spectrum estimated using Eq. (2.12) ($\xi \to C_\ell$, solid blue), true band power from SLICS (dashed magenta), and true band power from SLICS including the effect of finite $\vartheta_{\rm min}$ in Eq. (A.1)(dotted magenta). *Bottom*: difference between estimated band power and true band power from SLICS (solid green) and adjusted for finite $\vartheta_{\rm min}$ (hashed blue).

order to make the comparison between the different power spectrum estimates as direct as possible, we chose to minimize the amount of external information.

Finally, to estimate the effect of restricting the range of integration we compute the corrections terms

$$C_\ell^{\vartheta_{\rm min}} = 2\pi \int_0^{\vartheta_{\rm min}} {\rm d}\vartheta' \; \vartheta J_2(\ell\vartheta')\xi_{\rm th}^{\kappa\gamma_t}(\vartheta') \tag{A.1}$$

and

$$C_\ell^{\vartheta_{\rm max}} = 2\pi \int_{\vartheta_{\rm max}}^{\infty} {\rm d}\vartheta' \; \vartheta J_2(\ell\vartheta')\xi_{\rm th}^{\kappa\gamma_t}(\vartheta') \; . \tag{A.2}$$

The effect of the minimum angular separation $\vartheta_{\rm min}$ is a suppression of power at small scales, restricting the range of scales where the power spectrum estimate is unbiased. However, by forward modelling, i.e., accounting for the effect of the minimum angular separation when comparing the measurements to models, the effective range can be increased significantly. This can be seen in Fig. A.2, where

accounting for $C_\ell^{\vartheta_{\rm min}}$ increases the range of validity from $\ell \approx 2000$ to $\ell \approx 6000$. On the scales considered in the analysis of Chapter 2 ($\ell \leq 1500$) the effect of a finite ϑ is negligible and no forward modelling of this effect was conducted.

A finite maximum angular separation $\vartheta_{\rm max}$ does not lead to a systematic bias in the power spectrum estimation like the effect of $\vartheta_{\rm min}$. The oscillatory nature of the estimated power spectrum requires the use of band powers, however. The width of the bins results in an effective lower limit on the scales that can be estimated. For fixed ϑ', the Bessel function in Eq. (2.12) oscillates with period of $\frac{2\pi}{\vartheta'}$. The shortest period that can be probed is therefore around $\frac{2\pi}{\vartheta'_{\rm max}}$. Requiring two to three periods per ℓ-bin, the minimum reliable bin width for a maximum angular separation of $\vartheta_{\rm max} = 301$ arcmin is therefore $\Delta_\ell \approx 200$. The bin-width chosen in Chapter 2 is $\Delta_\ell = 260$ and can thus be assumed to yield a reliable estimate of the power spectrum.

The accuracy of the estimator is thus sufficient for the analysis in Chapter 2. Applications to higher SNR probes, such as cosmic shear, or future surveys, such as LSST, would require further testing, however. At large scales, the effect of the finite maximum angular separation $\vartheta_{\rm max}$ could become important enough to require inclusion in the forward modelling. The effect of using the flat-sky approximation also needs to quantified and might warrant a reformulation to a full-sky formalism.

Appendix B

Supplementary material to Chapter 3

B.1 Extra considerations in κ-map reconstruction

In the following, we describe the set of extra processing steps we have performed in our κ-map reconstruction pipeline to improve the SNR of our cross correlation measurements. These include the selection function applied to the lensing shear catalogue, adjustments in the reconstruction process, and proper masking of the contamination in the tSZ y maps.

Magnitude Selection

One of the parameters that we can optimize to increase the SNR is the magnitude selection function with which we select galaxies from the shear catalogue (and then make convergence maps from). This is not trivial, as it is not obvious whether including faint sources with a noisy shear signal would improve our signal or not. To investigate this, we apply different magnitude cuts to our shear catalogue and compute the SNR of the correlation function measurement in each case.

In Fig. B.1, we compare the correlation functions from three different r-band magnitude cuts: 21–23.5; 18–24; and ≥ 18 (all of the objects). We find that the variations in the mean signal due to different magnitude cuts are relatively small. However, there is still considerable difference in the scatter around the mean signal, which results in different SNR for the cuts. We consistently found that including all the objects (no cut) leads to a higher SNR.

Impact of smoothing

Another factor that can change the SNR of the measurements is the smoothing kernel we apply to the lensing maps. Note that in our analysis, the resolution of the cross-correlation (the smallest angular separation) is limited by the resolution of the tSZ maps, which matches the observational beam scale from the Planck satellite (FWHM$=$ 10 arcmin). On the other hand, lensing maps could have a much higher resolution and the interesting question is how the smoothing scale of the lensing maps affects the SNR.

As described before, the configuration-space y–γ_t cross-correlation works at the catalogue level

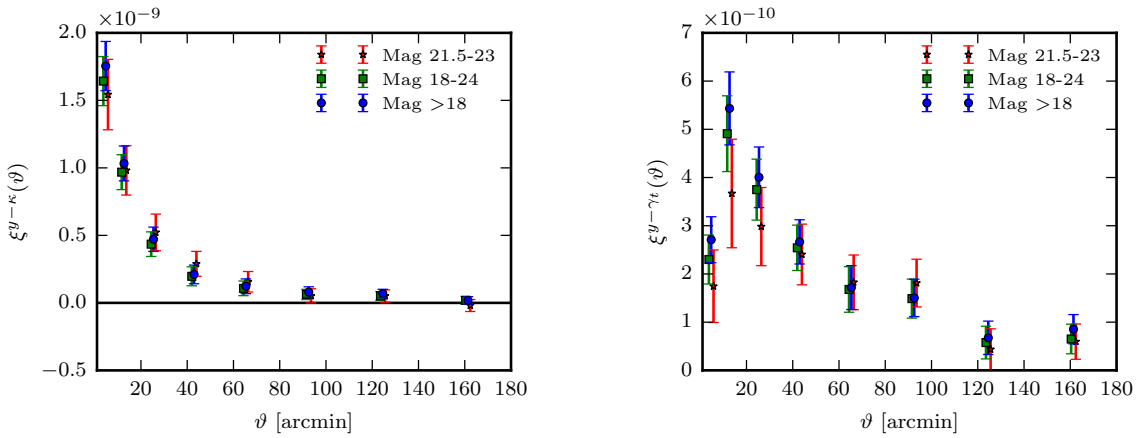

Figure B.1: Impact of different magnitude cuts on the y–κ (left) and y–γ_t (right) cross-correlation signals. Including all the sources in the lensing surveys yields the highest SNR.

without any smoothing involved. However, in making the convergence maps, we apply a smoothing kernel as described in van Waerbeke et al. (2013). One has therefore the freedom to smooth the convergence maps with an arbitrary kernel. We consider three different smoothing scales and evaluate the SNR of the cross-correlations.

Figure B.2 demonstrates the impact of applying different smoothing scales (FWHM = 3.3, 10 and 16.5 arcmin) to the convergence maps used for the y–κ cross-correlation. Note that while narrower smoothing kernels results in a higher cross-correlation amplitude, the uncertainties also increase and it lowers the SNR. We concluded that smoothing the maps with roughly the same scale as the y maps (FWHM $\approx$ 9.5 arcmin) leads to the highest SNR.

Masks on the y maps

Since we work with tSZ maps provided by the Planck collaboration, there is a minimal processing of the y maps for our analysis. We apply the masks provided by the Planck collaboration to remove point sources and Galactic contamination. Note that the Galactic mask does not significantly affect our measurements since all the RCSLenS fields are at high enough latitude. Cross-correlations are not sensitive to uncorrelated sources such as Galactic diffuse emission and point sources either. We have checked that our signal is robust against the masking of the point sources (see Fig. B.3).

B.2 Null tests and other effects

We have performed several consistency checks to verify our map reconstruction procedures and the robustness of the measurements. As mentioned before, an advantage of a cross-correlation analysis is that those sources of systematics that are unrelated to the measured signal will be suppressed in the measurement. This is particularly useful in the case of RCSLenS. As described below, there are residual systematics in the RCSLenS shear data (see Hildebrandt et al., 2016, for details). It is therefore

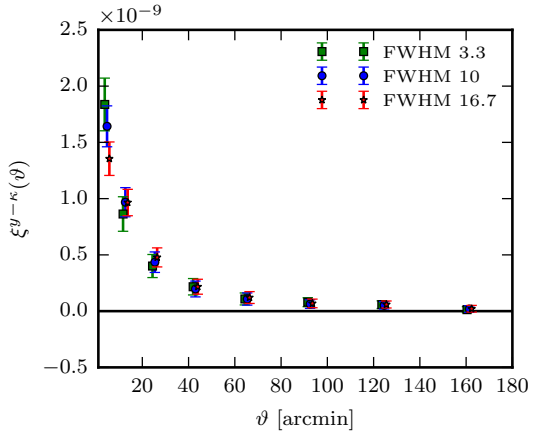

Figure B.2: Impact of varying the smoothing of the convergence maps on the y–κ cross-correlation signal. We apply three different smoothing scales of FWHM = 3.3, 10 and 16.7 arcmin during the mass map making process. While smaller scales result in a higher cross-correlation signal, the SNR is best for a smoothing scale of the same order as that of the y maps (FWHM = 10 arcmin).

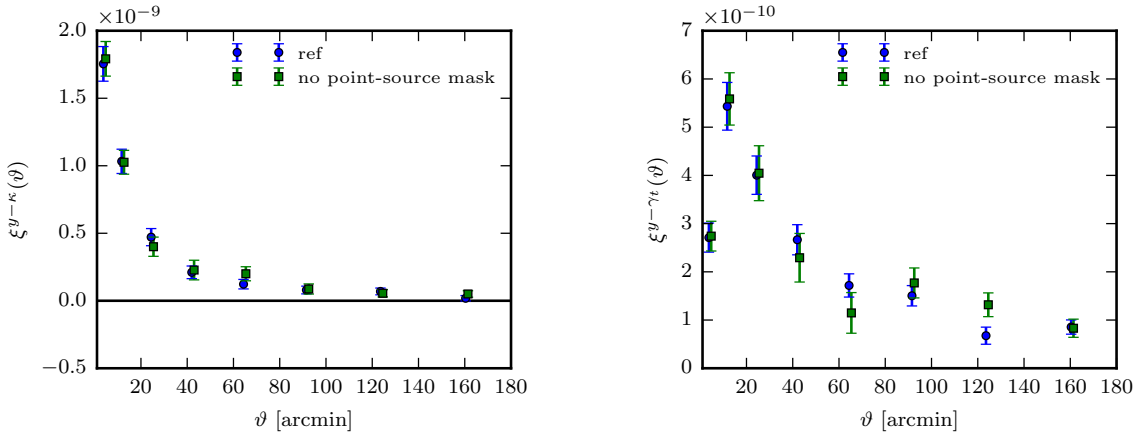

Figure B.3: The impact of masking point sources in the y map on the y–κ (left) and y–γ_t (right) cross correlation analysis. The measurements are fairly robust against such contamination.

important to check if these systematics contaminate our cross-correlation. We start with a description of lensing B-mode residuals in RCSLenS data.

Lensing B-mode residuals

In the absence of residual systematics, the scalar nature of the gravitational potential should lead to a vanishing convergence B-mode signal. As one of the important systematic checks in a weak lensing survey, one should investigate the level of the B-mode present in the constructed mass maps.

To check for B-mode residuals in the RCSLenS data, we first create a new shear catalogue by rotating

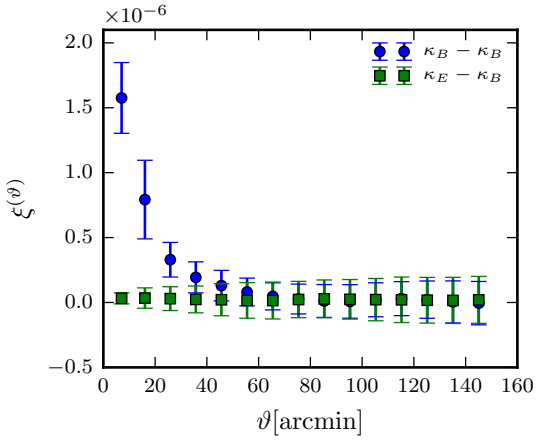

Figure B.4: The stacked B-mode residual from the RCSLenS fields represented through the auto-correlation function, after subtracting the statistical noise contribution. The signal is not consistent with zero due to residual systematics in the shape measurements. The $\kappa_E - \kappa_B$ cross-correlation is also shown which is consistent with zero.

each galaxy in the original RCSLenS catalogue by 45° in the observation plane. This is equivalent to applying a transformation of shear components from (γ_1, γ_2) to $(-\gamma_2, \gamma_1)$ (Schneider et al., 1998). We then follow our standard mass map making procedure to construct B-mode convergence maps, $\kappa_B^{\rm obs}$, from the new catalogue. Similar to the original maps, these maps are noisy and consists of the true underlying convergence, κ_B, and additional statistical noise, $\kappa_{\rm ran}$:

$$\kappa_B^{\rm obs} = \kappa_B + \kappa_{\rm ran}. \tag{B.1}$$

It is, therefore, necessary to distinguish between the two components when searching for residual B-modes.

To estimate $\kappa_{\rm ran}$, we produce many 'noise' catalogue where this time the orientations of galaxies are randomly changed (these are essentially the same maps that are used to construct the covariance matrix as described in Section 3.4). The constructed mass maps from these catalogue would only contain statistical noise. We estimate an average statistical noise auto-correlation function, $\bar{\xi}_{\kappa_{\rm ran}}$, for each RCSLenS field by averaging over the auto-correlation function from the random mass map realizations of the field. Finally, we estimate the residual B-mode signal in each of the RCSLenS fields by subtracting the statistical noise contribution computed for that field from the *observed* auto-correlation function.

Figure B.4 shows the weighted average of the residual B-mode correlation function computed from the 14 RCSLenS fields after subtracting the contribution from statistical noise. The error bars represent the error on the mean value in each angular bin. Note that there is an excess of residual B-modes at angular separations of ≤ 40 arcmin. Independent analysis of projected 3D shear power spectrum also confirms presence of excess residual B-mode signal at the corresponding scales (Hildebrandt et al., 2016), consistent with our finding. The existence of such residual systematics could be problematic for our studies and needs to be checked as we describe in the following.

In Fig. B.4, we show E- and B-mode mass map cross-correlation from RCSLenS. The cross-correlation signal is consistent with zero which shows that any possible leakage of the systematic B-mode residuals to E-mode does not correlate with the true E-mode signal.

Residual tSZ-lensing systematic correlation

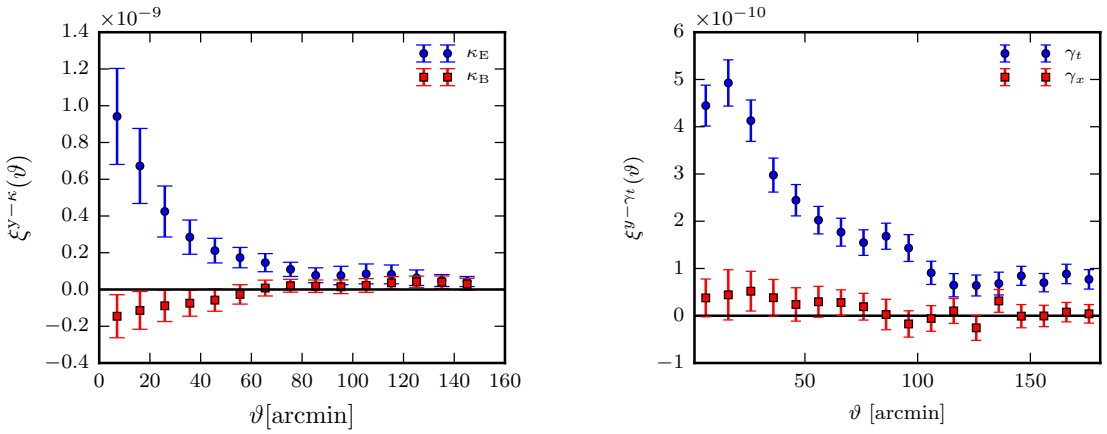

Figure B.5: Summary of the null tests performed on the y–κ (left) and y–γ_t (right) estimators. The red squares show the B-mode κ (right) and $\gamma_\times$ cross-correlations which are consistent with zero as expected (the blue circles show the E-mode κ (right) and γ_t cross-correlations for comparison). The null tests are validated in all cases confirming that the level of contaminating systematics in RCSLenS are under control in the cross-correlation analysis.

In the following, we demonstrate that while there is significant B-mode signal in the RCSLenS data, the lensing-tSZ cross-correlation signal is not contaminated. This serves as a good example of how cross-correlating different probes can suppress significant systematic residuals and make it useful for further studies.

As the first step, we cross-correlate the y maps with the random noise maps constructed for each RCSLenS field. We computed the mean cross-correlation and the error on the mean from these random noise maps. Consistency with zero insures that there is not any unexpected correlation between the y signal in the absence of a true lensing signal and insures that the field masks do not create any artefacts.

As the next step, we correlate the y maps with the constructed κ_B maps. This cross-correlation should also be consistent with zero to ensure that there is no unexpected correlation between the tSZ signal and the systematic lensing B-mode. Note that we can perform a similar consistency check using the shear data instead. The analogue to the κ_B mode for shear is the cross (or radial) shear quantity, $\gamma_\times$, defined as

$$\gamma_\times(\theta) = -\gamma_1 \cos(2\phi) + \gamma_2 \sin(2\phi), \tag{B.2}$$

which can be constructed by 45° rotation of galaxy orientation in the shear catalogue. With this estimator, we expect the y–$\gamma_\times$ cross correlations to be consistent with zero as another check of systematics in our measurements.

Fig. B.5 summarizes the null tests described above. In the left panel, cross-correlations of y with reconstructed κ_B maps are shown with the y–κ_E curve over-plotted for comparison. Correlation with κ_B maps slightly deviates from zero at smaller scales due to residual systematics, but is still insignificant considering the high level of bin-to-bin correlation. In the right panel, we show cross-correlation with $\gamma_\times$ with the y–γ_t curve over-plotted for comparison. We do not see any inconsistency in the y–$\gamma_\times$ correlation. Both estimators are also perfectly consistent with zero when cross-correlated with random maps.

We therefore conclude that the systematic residuals are sufficiently under control and do not affect our measurements at a measurable level for this data set.

Appendix C

Supplementary material to Chapter 4

C.1 Fourier space identities

Adapting the notation of Dodelson et al. (2005a), we define the 2D Fourier transform on the plane perpendicular to the line-of-sight as

$$\Phi(f_{\rm K}(\chi)\vec{\theta},\chi) = \int \frac{{\rm d}^2\ell'}{(2\pi)^2}\hat{\phi}(\vec{\ell}',\chi){\rm e}^{{\rm i}\vec{\ell}'\vec{\theta}} \ , \tag{C.1}$$

with the angular transform of the field Φ given by

$$\hat{\phi}(\vec{\ell},\chi) = \int \frac{{\rm d}k_3}{2\pi}\frac{1}{f_{\rm K}(\chi)^2}\hat{\Phi}\left(\frac{\vec{\ell}}{f_{\rm K}(\chi)},k_3\right){\rm e}^{{\rm i}k_3\chi} \ . \tag{C.2}$$

The higher order expressions for y and κ involve products of the potential Φ. In Fourier space, these products become convolutions. For two fields F and G we have

$$\widehat{[FG]}(\vec{\ell}) = \left[\hat{F}*\hat{G}\right](\vec{\ell}) = \int \frac{{\rm d}^2\ell'}{(2\pi)^2}\hat{F}(\vec{\ell}')\hat{G}(\vec{\ell}-\vec{\ell}') \ . \tag{C.3}$$

This generalizes straightforwardly to the case of three fields F, G, and K as

$$\widehat{[FGK]}(\vec{\ell}) = \left[\hat{F}*\hat{G}*\hat{K}\right](\vec{\ell}) = \int \frac{{\rm d}^2\ell'{\rm d}^2\ell''}{(2\pi)^4}\hat{F}(\vec{\ell}')\hat{G}(\vec{\ell}'')\hat{K}(\vec{\ell}-\vec{\ell}'-\vec{\ell}'') \ . \tag{C.4}$$

The two-point correlation function of the fields $\hat{\phi}(\vec{\ell},\chi)$ is directly related to the power spectrum of the potential Φ. Assuming homogeneity, isotropy, and using the Limber approximation (Limber, 1953; Kaiser, 1992), i.e., assuming that $|\vec{\ell}| \gg k_3$, thus justifying neglecting the longitudinal modes, the two-

point function can be written as

$$\begin{aligned}\langle\hat{\phi}(\vec{\ell}_1,\chi_1)\hat{\phi}(\vec{\ell}_2,\chi_2)\rangle &= (2\pi)^2\delta_{\rm D}(\chi_1-\chi_2)\delta_{\rm D}(\vec{\ell}_1+\vec{\ell}_2)C_\ell^{\phi\phi}\\ &= (2\pi)^2\delta_{\rm D}(\chi_1-\chi_2)\frac{\delta_{\rm D}^2\left(\vec{\ell}_1+\vec{\ell}_2\right)}{f_{\rm K}(\chi_1)^2}\mathscr{P}_\Phi\left(\frac{|\vec{\ell}_1|}{f_{\rm K}(\chi_1)},\chi_1\right)\,.\end{aligned} \tag{C.5}$$

Similarly, the three-point function of $\hat{\phi}(\vec{\ell},\chi)$ is related to the bispectrum $\mathscr{B}_\Phi(\vec{k}_1,\vec{k}_2,\vec{k}_3,\chi)$ by

$$\begin{aligned}\langle\hat{\phi}(\vec{\ell}_1,\chi_1)\hat{\phi}(\vec{\ell}_2,\chi_2)\hat{\phi}(\vec{\ell}_3,\chi_3)\rangle = (2\pi)^2\delta_{\rm D}(\chi_1-\chi_2)\delta_{\rm D}(\chi_1-\chi_3)&\frac{\delta_{\rm D}^2\left(\vec{\ell}_1+\vec{\ell}_2+\vec{\ell}_3\right)}{f_{\rm K}(\chi_1)^4}\\ &\times\mathscr{B}_\Phi\left(\frac{|\vec{\ell}_1|}{f_{\rm K}(\chi_1)},\frac{|\vec{\ell}_2|}{f_{\rm K}(\chi_1)},\frac{|\vec{\ell}_3|}{f_{\rm K}(\chi_1)},\chi_1\right)\,.\end{aligned} \tag{C.6}$$

The four-point function can be expressed in terms of the trispectrum as

$$\begin{aligned}\langle\hat{\phi}(\vec{\ell}_1,\chi_1)\hat{\phi}(\vec{\ell}_2,\chi_2)\hat{\phi}(\vec{\ell}_3,\chi_3)\hat{\phi}(\vec{\ell}_4,\chi_4)\rangle &= (2\pi)^2\delta_{\rm D}(\chi_1-\chi_2)\delta_{\rm D}(\chi_1-\chi_3)\delta_{\rm D}(\chi_1-\chi_4)\\ &\times\frac{\delta_{\rm D}^2\left(\vec{\ell}_1+\vec{\ell}_2+\vec{\ell}_3+\vec{\ell}_4\right)}{f_{\rm K}(\chi_1)^6}\\ &\times\mathscr{T}_\Phi\left(\frac{|\vec{\ell}_1|}{f_{\rm K}(\chi_1)},\frac{|\vec{\ell}_2|}{f_{\rm K}(\chi_1)},\frac{|\vec{\ell}_3|}{f_{\rm K}(\chi_1)},\frac{|\vec{\ell}_4|}{f_{\rm K}(\chi_1)},\chi_1\right)\,.\end{aligned} \tag{C.7}$$

Using the definition of the Fourier transform (C.1), partial derivatives with respect to comoving transverse coordinates can be written as

$$\Phi_{,i_1\ldots i_N}(f_{\rm K}(\chi)\vec{\theta},\chi) = \int\frac{{\rm d}^2\ell'}{(2\pi)^2}\frac{{\rm i}^N}{f_{\rm K}(\chi)^N}\ell'_{i_1}\ldots\ell'_{i_N}\hat{\phi}(\vec{\ell}',\chi){\rm e}^{{\rm i}\vec{\ell}'\vec{\theta}}\,. \tag{C.8}$$

C.2 Convergence - shear relation

In this appendix we show that the relation (4.27) holds even beyond first order, justifying the use of the convergence as the fundamental quantity instead of the shear. The second-order expressions of the convergence and shear due to Born approximation and lens-lens couplings in Fourier space are

$$\begin{aligned}\hat{\kappa}^{(2)}_{\rm std}(\vec{\ell},\chi) = -2\int_0^\chi{\rm d}\chi'\int_0^{\chi'}{\rm d}\chi''&\frac{K(\chi,\chi')K(\chi',\chi'')}{f_{\rm K}(\chi')^2f_{\rm K}(\chi'')^2}\\ &\times\int\frac{{\rm d}^2\ell'}{(2\pi)^2}|\vec{\ell}'||\vec{\ell}|\cos(\phi_\ell-\phi_{\ell'})\left[\vec{\ell}'(\vec{\ell}-\vec{\ell}')\right]\hat{\phi}(\vec{\ell}',\chi')\hat{\phi}(\vec{\ell}-\vec{\ell}',\chi'')\end{aligned} \tag{C.9}$$

and

$$(\hat{\gamma}^{(2)}_{\rm std})_I(\vec{\ell},\chi) = -2\int_0^{\chi} \mathrm{d}\chi' \int_0^{\chi'} \mathrm{d}\chi'' \frac{K(\chi,\chi')K(\chi',\chi'')}{f_{\rm K}(\chi')^2 f_{\rm K}(\chi'')^2} \\ \times \int \frac{\mathrm{d}^2\ell'}{(2\pi)^2} |\vec{\ell}'||\vec{\ell}| U_I(\vec{\ell},\vec{\ell}') \left[\vec{\ell}'(\vec{\ell}-\vec{\ell}')\right] \hat{\phi}(\vec{\ell}',\chi')\hat{\phi}(\vec{\ell}-\vec{\ell}',\chi'') \,, \tag{C.10}$$

where the couplings U_I are given by

$$U^1(\vec{\ell},\vec{\ell}') = \cos(\phi_\ell + \phi_{\ell'}) \,, \quad U^2(\vec{\ell},\vec{\ell}') = \sin(\phi_\ell + \phi_{\ell'}) \,. \tag{C.11}$$

Using the identity

$$T^I(\vec{\ell}) U_I(\vec{\ell},\vec{\ell}') = \cos(\phi_\ell - \phi_{\ell'}) \,, \tag{C.12}$$

where T^I is given in (4.27), we have thus shown that $\hat{\kappa}^{(2)}_{\rm std} = T^I(\hat{\gamma}^{(2)}_{\rm std})_I$.

Generally, the relation does not hold anymore at third order. As we are only concerned with correlation functions in this work, it is sufficient to show that the relation holds within correlation functions, i.e., $\langle \hat{y}^{(1)} \hat{\kappa}^{(3)}_{\rm std} \rangle = \langle \hat{y}^{(1)} T^I(\hat{\gamma}^{(3)}_{\rm std})_I \rangle$. To do so we first note that the third term in the third-order expression for the convergence (4.21) does not contribute to the correlation function under the Limber approximation. This also applies to the third-order shear, since the line-of-sight integrals are the same for both the convergence and the shear. The mode coupling terms of the angular cross-power spectra are

$$\langle \hat{y}^{(1)}(\vec{\ell}_1) \hat{\kappa}^{(3)}_{\rm std}(\vec{\ell}_2) \rangle \propto \int \frac{\mathrm{d}^2\ell'}{(2\pi)^2} \left(|\vec{\ell}_2|^2 + 2\vec{\ell}_2\vec{\ell}' \right) |\vec{\ell}_1|^2 \left[\vec{\ell}_2\vec{\ell}'\right]^2 \tag{C.13}$$

and

$$\langle \hat{y}^{(1)}(\vec{\ell}_1) T^I(\vec{\ell}_2) (\hat{\gamma}^{(3)}_{\rm std})_I(\vec{\ell}_2) \rangle \propto T^I(\vec{\ell}_2) \int \frac{\mathrm{d}^2\ell'}{(2\pi)^2} \left(|\vec{\ell}_2|^2 T_I(\vec{\ell}_2) - 2|\vec{\ell}_2||\vec{\ell}'| U_I(\vec{\ell}_2,\vec{\ell}') \right) |\vec{\ell}_1|^2 \left[\vec{\ell}_2\vec{\ell}'\right]^2 \,. \tag{C.14}$$

Applying the two identities $T^I(\vec{\ell}) T_I(\vec{\ell}') = \cos(2\phi_{\ell'} - 2\phi_\ell)$ and (C.12) we see that the two above expressions are equal. We have thus proven that it is justified to use the convergence in cross-power spectra instead of terms of the from $T^I(\vec{\ell})\hat{\gamma}_I(\vec{\ell})$, up to third order. To second order, the relation $\hat{\kappa} = T^I \hat{\gamma}_I$ even holds exactly.

C.3 Induced rotation

Let $S(\vec{\theta})$ be the surface brightness distribution of an extended source. The first and second moments of the brightness distributions are then defined as (Schneider et al., 1995)

$$\theta_i^0 = \frac{\int \mathrm{d}^2\vec{\theta}\ \theta_i S(\vec{\theta})}{\int \mathrm{d}^2\vec{\theta}\ S(\vec{\theta})}\ , \tag{C.15a}$$

$$Q_{ij} = \frac{\int \mathrm{d}^2\vec{\theta}\ (\theta_i - \theta_i^0)(\theta_j - \theta_j^0) S(\vec{\theta})}{\int \mathrm{d}^2\vec{\theta}\ S(\vec{\theta})}\ . \tag{C.15b}$$

Following Seitz et al. (1997), we introduce the complex ellipticity parameter

$$\varepsilon = \frac{Q_{11} - Q_{22} + 2\mathrm{i}Q_{12}}{Q_{11} + Q_{22} + 2\sqrt{Q_{11}Q_{22} - Q_{12}^2}}\ . \tag{C.16}$$

For an elliptical source with semi-major and semi-minor axis a and b, rotated by an angle α with respect to a fixed coordinate system, the ellipticity parameter (C.16) is given by

$$\varepsilon = \frac{a-b}{a+b}\mathrm{e}^{2\mathrm{i}\alpha}\ . \tag{C.17}$$

The Jacobi map (4.3) relates an infinitesimal distance on the source plane to an infinitesimal distance on the image plane by $\mathrm{d}\vec{\theta}^{\mathrm{S}} = \mathscr{A}(\vec{\theta}^{\mathrm{S}})\ \mathrm{d}\vec{\theta}^{\mathrm{O}}$. Assuming the source is sufficiently small such that the Jacobi map does not vary over the extend of the source, the second brightness moment (C.15b) of the source Q^S can be approximately related to the observed second brightness moment Q^O by

$$Q^{\mathrm{S}} = \mathscr{A}\ Q^{\mathrm{O}} \mathscr{A}^{\mathrm{T}}\ . \tag{C.18}$$

We generalize previous work by allowing $\mathscr{A}(\vec{\theta})$ to have an anti-symmetric part. This anti-symmetric contribution ω can be thought of as a rotation induced by lens-lens coupling. Given an elliptical source, the observed ellipticity can be written as

$$\varepsilon^{\mathrm{O}} = \frac{g + \varepsilon^{\mathrm{S}\prime}}{1 + g^*\varepsilon^{\mathrm{S}\prime}}\ , \tag{C.19}$$

where the generalized reduced shear g and rotated source ellipticity $\varepsilon^{\mathrm{S}\prime}$ are given by

$$g = \frac{\gamma_1 + \mathrm{i}\gamma_2}{1 - \kappa + \mathrm{i}\omega}\ , \quad \varepsilon^{\mathrm{S}\prime} = \varepsilon^{\mathrm{S}}\ \mathrm{e}^{-2\mathrm{i}\vartheta}\ , \quad \tan\vartheta = \frac{\omega}{1-\kappa}\ . \tag{C.20}$$

The reduced shear now includes a contribution from the anti-symmetric term ω of the general Jacobi map. Furthermore, the source ellipticity is rotated by an angle ϑ. However, assuming the sources are distributed isotropically, this rotation is not observable. In particular, the ensemble average $\langle\varepsilon^{\mathrm{O}}\rangle = g$, i.e., the observed ellipticity remains an unbiased estimator of the reduced shear despite the rotation ω. In the limit of a symmetric Jacobi map $\omega \to 0$ one recovers eq. (3.2) of Seitz et al. (1997).

Finally, we express the generalized reduced shear in vector notation to facilitate the use in section 4.3.2. The two components are

$$g_1 = \Re(g) = \frac{\gamma_1(1-\kappa)+\gamma_2\omega}{(1-\kappa)^2+\omega^2} \ , \quad g_2 = \Im(g) = \frac{\gamma_2(1-\kappa)-\gamma_1\omega}{(1-\kappa)^2+\omega^2} \ . \tag{C.21}$$

Because ω is necessarily of at least second order, the generalized reduced shear to third order can be written as

$$g_I = \frac{\gamma_I}{1-\kappa} + R(\omega)_{IJ}\gamma_J + \mathscr{O}(\Phi^4) \ , \tag{C.22}$$

where the matrix $R(\omega)$ is defined as

$$R(\omega)_{IJ} = \begin{pmatrix} 0 & \omega \\ -\omega & 0 \end{pmatrix} \ . \tag{C.23}$$

This can be understood as an infinitesimal rotation of the shear by an angle ω.